

**CHARACTERIZATION AND NUMERICAL
MODELLING OF FROST HEAVE**

THE EXPERIMENTAL CHARACTERIZATION AND NUMERICAL MODELLING OF FROST HEAVE

by

ERIC TIEDJE, B.ENG

A thesis Submitted to the School of Graduate Studies in Partial Fulfillment of the
Requirements for the Degree Doctor of Philosophy

McMaster University
© Copyright Eric Tiedje, February 2015

DOCTOR OF PHILOSOPHY (2015)

McMaster University

(Civil Engineering)

Hamilton, Ontario

TITLE: The Experimental Characterization and Numerical Modelling of Frost
Heave

AUTHOR: Eric Tiedje

B.Eng. (McMaster University)

SUPERVISOR: Peijun Guo

NUMBER OF PAGES: xxiii, 243

LAY ABSTRACT

An experimental investigation was conducted and a numerical model was developed to predict the effects of frost heave in freezing soils. Frost heave is the expansion of soils caused by the formation of a specific type of ice, called ice lenses. This expansion can cause damage and lead to failure in roads, foundations, buried pipelines and other infrastructure exposed to heaving soils. The research developed a model capable of providing engineers with the information necessary to account for, and possibly avoid, these effects when designing such infrastructure. A series of experiments were conducted to produce frost heave in soils in a laboratory. The information gained from these tests was used to both develop and confirm the performance of a frost heave model using established numerical techniques. Finally, the model was used to simulate the upward movement of a buried natural gas pipeline exposed to frost heave in a cold region.

ABSTRACT

Frost heave is the expansion of soil upon freezing due to the formation and growth of segregated ice lenses. Because of the large stresses and displacements associated with frost heave, it is an important design consideration for geotechnical structures such as roads, foundations, and buried pipelines, particularly in cold regions. The objective of this research was to characterize frost heave expansion within the context of design and analysis applications.

A series of laboratory-scale frost heave experiments were conducted to examine frost heave under one-dimensional freezing. The previously established segregation potential concept (*SP*) was utilized to characterize both the intrinsic frost heave behavior of two reference soils. A novel modification was proposed to account for the observed variation of *SP* with freezing rate; it was noted that ignoring this influence would lead to under-predictions of the heave expansion.

The thermal properties of frozen soils were explored. A method for characterizing the anisotropic thermal conductivity was proposed utilizing existing composite models in a multi-level homogenization. Ultimately it was determined that for ice lens-rich soils, a simpler and isotropic expression may provide similar performance, namely the geometric mean approximation. Additionally, a method was proposed to characterize the thermal conductivity of composite materials containing discrete particle phases using numerical simulations of complex phase geometries. This method was used to develop a specified characterization of discrete particle composites.

A two-dimensional, fully coupled thermal-mechanical and implicitly coupled hydraulic frost heave model was formulated from thermodynamic principles. The model included the proposed form of SP to characterize the mass transport process. The finite element method was used to implement the model and its performance was validated in one-dimension through comparative analysis with the laboratory frost heave tests. Finally, the model was applied to a two-dimensional, full-scale problem involving the frost heave-induced displacement of a chilled natural gas problem.

ACKNOWLEDGEMENTS

In presenting this work I would like to express my sincere appreciation for the following. To my supervisor, Dr. Peijun Guo for his guidance and support during the research and preparation of this thesis. I am grateful for his steadfast optimism and personal encouragement in addition to his considerable technical expertise. To Dr. Dieter Stolle, member of the supervisory committee, for his invaluable advice, particularly regarding numerical analysis and geotechnical experimentation. Dr. Stolle's personal support has been both remarkably consistent and most assuredly welcomed throughout my time at McMaster. To Dr. Samir Chidiac, supervisory committee member, for his support, insight, and honesty. To Mr. Peter Koudys for his practical expertise, remarkable fabrication skills, and friendship. The experimental investigation was due in no small part to his support and assistance.

Financial support was provided by McMaster University through the Department of Civil Engineering and the Province of Ontario through the QEII-GSST scholarship.

Furthermore, I would like to thank my family. To my parents for their unconditional love. To Emma and Wallace for their respective warmth and support. Finally, I would like to acknowledge that this work would not have been possible without the strength, patience, and support of my wife and partner, Marianne.

TABLE OF CONTENTS

ABSTRACT.....	iii
ACKNOWLEDGEMENTS.....	v
TABLE OF CONTENTS.....	vi
LIST OF FIGURES.....	x
LIST OF TABLES.....	xviii
LIST OF SYMBOLS.....	xix
PREFACE.....	xxiii
1 INTRODUCTION.....	1
1.1 BACKGROUND.....	1
1.2 OBJECTIVE.....	2
1.3 THESIS OUTLINE.....	3
2 LITERATURE REVIEW.....	6
2.1 INTRODUCTION.....	6
2.2 PHYSICAL DYNAMICS OF FROST HEAVE.....	7
2.2.1 Thermodynamic Characteristics of Water.....	8
2.2.2 Unfrozen Water in Soil.....	8
2.2.3 Cryogenic Potential.....	10
2.2.4 Frozen Hydraulic Conductivity.....	11
2.2.5 Ice Lens Initiation.....	13
2.2.6 Frost Heave Susceptibility.....	14
2.3 EXPERIMENTAL INVESTIGATIONS.....	16
2.3.1 Laboratory Frost Heave Experiments.....	16
2.3.2 Full-Scale Frost Heave Studies.....	19
2.4 FROST HEAVE MODELS.....	22
2.4.1 Empirical Frost Heave Models.....	23
2.4.2 Physical Frost Heave Models.....	25
2.4.3 Thermal Analysis.....	29

2.5 MECHANICAL PROPERTIES OF FROZEN SOIL.....	30
2.6 SUMMARY AND CONCLUSIONS	36
3 EXPERIMENTAL FROST HEAVE INVESTIGATION	38
3.1 INTRODUCTION	38
3.2 EXPERIMENTAL METHODOLOGY	38
3.2.1 Description of the Experimental Apparatus	38
3.3 MATERIALS AND SAMPLE PREPARATION.....	40
3.4 EXPERIMENTAL PROGRAM	43
3.5 TEST RESULTS	45
3.5.1 Thermal Boundary Conditions.....	46
3.5.2 Material Comparison.....	51
3.5.3 Segregation Potential	53
3.5.4 Influence of the Hydraulic Boundary Conditions	64
3.6 DISCUSSION.....	70
3.7 SUMMARY AND CONCLUSIONS	74
4 THERMAL PROPERTIES OF FROZEN SOIL	77
4.1 INTRODUCTION	77
4.2 HEAT CAPACITY OF FROZEN SOIL	77
4.3 THERMAL CONDUCTIVITY OF FROZEN SOIL	78
4.3.1 Review of Isotropic Thermal Conductivity Models.....	78
4.3.2 Multi-level Homogenization	84
4.3.3 Model Evaluation	87
4.3.4 Anisotropic Thermal Conductivity	93
4.3.5 Further Composite Thermal Conductivity	97
4.4 SUMMARY AND CONCLUSIONS	98
5 FROST HEAVE MODEL	100
5.1 INTRODUCTION	100

5.2 MODEL FORMULATION	101
5.2.1 Physical Governing Equations	101
5.2.1.1 Energy Conservation	101
5.2.1.2 Mass Conservation	106
5.2.2 Deformation	110
5.2.2.1 Mechanical Deformation	110
5.2.2.2 Anisotropic Ice Lens Growth	111
5.2.3 Numerical Considerations	114
5.2.3.1 Model Implementation	114
5.2.3.2 Solution Framework	116
5.3 SIMULATIONS OF LABORATORY TEST	117
5.3.1 Material Properties	118
5.3.2 Boundary Conditions	122
5.3.3 Evaluation of Model Performance	123
5.5 SUMMARY AND CONCLUSIONS	132
6 MODELLING OF THE CALGARY PIPELINE TEST	136
6.1 INTRODUCTION	136
6.1.1 Description of the Calgary Pipeline tests	136
6.2 MODEL FORMULATION	139
6.2.1 Geometry and Boundary Conditions	139
6.2.2 Material Properties	142
6.2.2.1 Frost Susceptibility	142
6.2.2.2 Mechanical Properties	143
6.3 RESULTS	148
6.3.1 Base Analysis	148
6.3.2 Parametric Sensitivity	153
6.3.3 Operational Parameters	159
6.4 SUMMARY AND CONCLUSIONS	161
7 CONCLUSION	163
7.1 RECOMMENDATIONS	166
APPENDIX A FROST HEAVE TEST RESULTS	168
APPENDIX B THERMAL CONDUCTIVITY OF DISCRETE PARTICLE COMPOSITES	182

B.1 ABSTRACT	182
B.2 INTRODUCTION	182
B.3 COMPOSITE CONDUCTIVITY MODELS	183
B.4 APPROACH	187
B.4.1 Numerical Modelling of Composite Thermal Conductivities	188
B.4.2 Finite Element Analysis	193
B.5 RESULTS AND ANALYSIS	194
B.5.1 Single Particle Simulations	194
B.5.2 Multiple Particle Simulations	200
B.5.3 Influence of the Relative Particle Size	201
B.5.4 Thermal conductivity anisotropy of multiple particle composites	204
B.5.5 Isotropic Multiple Particle Composites	208
B.6 CONCLUSIONS	210
APPENDIX C THE THERMAL CONDUCTIVITY OF BENTONITE GROUT CONTAINING GRAPHITE OR CHOPPED CARBON FIBRES	211
C.1 ABSTRACT	211
C.2 INTRODUCTION	211
C.3 EXPERIMENTAL STUDY	214
C.3.1 Materials	214
C.3.2 Thermal Conductivity Measurements	216
C.3.3 Grout Mix Preparation Method	217
C.4 RESULTS	218
C.5 DISCUSSION	219
APPENDIX D FROST HEAVE MODEL SUBROUTINE	222
APPENDIX E NUMERICAL SENSITIVITY OF THE ONE-DIMENSIONAL MODEL IMPLEMENTATION	227
APPENDIX F CALGARY PIPELINE SIMULATION FIGURES	234
REFERENCES	240

LIST OF FIGURES

Figure 2.1: A schematic diagram of the relevant components of the frost heave process...	7
Figure 2.2: The reported hydraulic conductivities of select frozen soils (Nixon 1991)	13
Figure 2.3: The frost susceptibility of soils based on the Unified Soil Classification System (Andersland and Ladanyi 1994).....	15
Figure 2.4: An illustration of the stepped and ramped freezing boundary conditions used in 1D laboratory frost heave tests and the typical soil response	18
Figure 2.5: The variation of the 50% peak strength modulus with temperature and the applied strain rate for a frozen Fairbanks silt (Zhu and Carbee 1984)	31
Figure 2.6: Variation in the angle of friction, φ , and cohesion, c , with the volumetric ice content of an ice-rich granular permafrost (Arenson and Springman 2005)	35
Figure 2.7: The variation in compressive and tensile strength of pure ice as a function of the applied strain rate at -10 °C (Schulson 1999)	36
Figure 3.1: Frost heave test apparatus schematic.....	40
Figure 3.2: Particle size distribuion of the two examined soils	41
Figure 3.3: Ice lens formation at 72 and 212 hours of freezing for BS-2 and BS-3, respectively	45
Figure 3.4: The observed temperature profile and surface heave during step freezing of FS-3.....	47
Figure 3.5: The observed temperature profile and surface heave during ramped-freezing of FR-1	48
Figure 3.6: Temperature profile of FR-3, FHC tested under ramped conditions	50
Figure 3.7: Comparison of the observed displacement between step tests on FHC (FS-3) and BSM (BS-1). For both tests $\sigma_0 = 20.0$ kPa, $T_{min} = -2.9$ °C, $T_{max} = 3.8$ °C.....	51
Figure 3.8: Comparison of the observed displacement between the ramped tests on FHC (FS-3) and BSM (BS-1). For both tests $\sigma_0 = 20.0$ kPa, $dT/dz = 20.0$ °C/m, $dT/dt = 0.036$ °C/hr.....	52

Figure 3.9: The observed <i>SP</i> of FHC under a step test FS-3 (a) and a ramped test FR-3 (b).....	56
Figure 3.10: Comparison of the observed <i>SP</i> under step conditions between FHC (FS-3) and BSM (BS-1).	57
Figure 3.11: Comparison of the observed <i>SP</i> under ramped conditions between FHC (FR-3) and BSM (BR-3).....	57
Figure 3.12: The variation in observed <i>SP</i> with the overburden stress for the FHC step-freezing tests.	58
Figure 3.13: The variation of <i>SP</i> with the frost penetration rate for FHC under step freezing. The solid lines indicate the general observed trends..	60
Figure 3.14: The variation of the slope of the $SP - \frac{\partial z_f}{\partial t}$ relationship of FHC with the overburden stress level, obtained from Figure 3.12.....	61
Figure 3.15: The variation of <i>SP</i> with the frost penetration rate of FS-3 and BS-1, which correspond to FHC and BSM.....	61
Figure 3.16: The displacement response of BSM under step freezing with an external water supply (BS-1) and without an external water supply (BS-2 and BS-3).	66
Figure 3.17: The observed <i>SP</i> of BSM with an external water supply (BS-1) and without an external water supply (BS-2 and BS-3).	66
Figure 3.18: The variation in the water content in the unfrozen soil post testing of BS-1, BS-2, and BS-3.	67
Figure 3.19: The temporal variation in the basal pore pressure of step freezing tests BS-2 and BS-3 (without a water supply)..	69
Figure 3.20: The consolidation curve of the prepared BSM samples.....	70
Figure 3.21: Illustration of the pore pressure profile during frost heave	72
Figure 3.22: The variation in the pore pressure profile as the frost front advances.....	73
Figure 4.1: An illustration of assumptions made regarding geometric distribution of phases.....	82
Figure 4.2: Comparison of the thermal conductivity models discussed for a two phase composite material	83

Figure 4.3: Illustration of the composite pore phase medium.	85
Figure 4.4: Variation of reported volumetric composition of the silty-clay referred to in Figure 4.6 (Penner 1970).	88
Figure 4.5: Comparison of the reported thermal conductivities of a gravel material at a porosity of 0.18 (Coté and Konrad 2005), with modeled values	90
Figure 4.6: Comparison of the reported thermal conductivities of a gravel material at a porosity of 0.30 (Coté and Konrad 2005), with modeled values.	91
Figure 4.7: Comparison of the reported thermal conductivities of a frozen, saturated silty-clay (Penner 1970), with modeled values.	92
Figure 4.8: Conceptual representation of the multi-level homogenization of frozen soil containing segregated ice lenses.	94
Figure 4.9: The orientation of the ice lens plane to the thermal gradient	95
Figure 5.1: Illustration of frozen fringe and heave orientation.....	113
Figure 5.2: Illustration of the definition of the proportionality parameter, ξ , used to distribute volumetric strains due to ice lens growth within a FEM element.	115
Figure 5.3: Flowchart of the model procedure.....	116
Figure 5.4: Schematic and boundary conditions of the 1D simulations (a) and the corresponding FEM mesh utilized (b).	118
Figure 5.5: The modeled variation in soil thermal conductivity with temperature.....	121
Figure 5.6: The simulated and observed heave, (a), frost penetration, (b), and segregation potential (c) of test BS1.	124
Figure 5.7: The simulated temperature (a) and porosity (b) profiles corresponding to select time points in test BS-1.....	125
Figure 5.8: The observed and simulated frost heave profiles of BS-1 at varying SP_0 by 9.4% ($\beta = 5.95 \times 10^{-6}$ s/mm).	126
Figure 5.9: The observed and simulated frost heave development with time of BS-1 when β varies by 10.1% ($(SP_0 = 26.5 \times 10^5 \text{ mm}^2/\text{s}^\circ\text{C})$).	127
Figure 5.10: The variation in the simulated results of BS-1 with constant soil heat capacity and the base-line variable case.	128

Figure 5.11: The observed and simulated frost heave profiles of FHC under overburden stress levels of: 15 kPa, 45 kPa, 75 kPa, and 125 kPa. The simulations include three values of SP_0 .	129
Figure 5.12: The simulated and observed heave evaluations of tests BR-2 (a) and FR-3 (b) and the simulated and observed apparent SP values of the same materials (c) and (d)...	131
Figure 6.1: Schematic of the three examined pipe configurations (Slusarchuk et al. 1978).	138
Figure 6.2: Geometry and mechanical boundary conditions used to represent the control configuration	140
Figure 6.3: Monthly mean air temperature in Calgary, Alberta during the first 5 years of the pipeline experiment (Environment Canada 2013).	141
Figure 6.4: The variation of SP with applied surcharge for Calgary silt obtained from laboratory frost heave tests conducted under step-freezing conditions (Konrad and Morgenstern 1984).	142
Figure 6.5: Assumed variation in cohesion at the Calgary pipeline test site. The active zones of the three configurations are noted on the left.	146
Figure 6.6: The simulated and observed (Slusarchuk et al. 1978) vertical pipe displacements due to frost heave	149
Figure 6.7: The simulated and observed (Slusarchuk et al. 1978) frost penetration below pipeline, defined as the distance between the bottom of the pipe and the 0°C isotherm.	150
Figure 6.8: The simulated maximum in-plane plastic strain (a) developed by day 1042 and the corresponding temperature profile (b) of the control section.	151
Figure 6.9: The simulated porosity on day 1042 for the control configuration. Initial porosity in the frost susceptible and non-susceptible soil was 0.341	152
Figure 6.10: The variation in the simulated pipe displacement with SP_0	154
Figure 6.11: The variation in the simulated pipe displacement with β , the parameter expressing heave rate sensitivity to the freezing rate.	155
Figure 6.12: The absolute, (a), and relative, (b), variation in the simulated pipe displacement with fractional anisotropy parameter, ζ	156

Figure 6.13: The variation in the simulated pipe displacement with the Mohr-Coulomb failure parameters of the soil for the three sections	157
Figure 6.14: The variation in the pipe displacement with elastic modulus of the soil for the control configuration.....	158
Figure 6.15: Variation in the simulated pipe displacement with the dilation angle of soil for the control configuration	159
Figure 6.16: The variation in simulated pipe displacement with the applied surcharge..	160
Figure 6.17: The variation in the simulated pipe displacement with pipe temperature. .	161
Figure A.1: FS-3 results.....	169
Figure A.2: FS-7 results.....	170
Figure A.3: FS-8 results.....	171
Figure A.4: FS-9 results.....	172
Figure A.5: FS-10 results.....	173
Figure A.6: BS-1 results.	174
Figure A.7: BS-2 results.	175
Figure A.8: BS-3 results	176
Figure A.9: FR-1 results.	177
Figure A.10: FR-2 results	178
Figure A.11: FR-3 results.	179
Figure A.12: BR-1 results.....	180
Figure A.13: BR-2 results.....	181
Figure B.1: Schematic representation of a single, rectangular particle composite simulation.....	189
Figure B.2: Illustration of the periodic particle distribution scheme	192

Figure B.3: The variation of the simulated composite conductivity, k_E/k_I , with the number of nodes of a reference composite.	193
Figure B.4: Variation of composite thermal conductivity of a single rectangular particle composite with relative orientation and elongation	195
Figure B.5: Variation of the composite thermal conductivity of a single particle composite averaged across all orientations	195
Figure B.6: The variation of the effective thermal conductivity, k_E/k_I , and the geometric distribution factor, ζ , with AR and orientation for a single, rectangular, particle composite with $\phi_2 = 0.01$ and $k_2/k_1 = 100$	196
Figure B.7: Select results of the variation of ζ with AR for perfectly aligned rectangular particles. The line of best fit in this equation corresponds to equation B.13.	198
Figure B.8: Variation of ζ with F_x for select aspect ratios. Figures (a), (b), and (c) correspond to rectangular, elliptical and rhomboidal particles, respectively.	199
Figure B.9: Variation of the mean relative composite thermal conductivity, k_E/k_I , with aspect ratio and volumetric fraction for multi-particle composites. Figure (a) corresponds to a periodic particle distribution while (b) corresponds to a random distribution. For both cases the composite contained mono-sized rectangular particles with a conductivity ratio of $k_2/k_1 = 100$	200
Figure B.10: Variation of the mean composite thermal conductivity with the constituent conductivity ratio for select results of the multiple particle simulations using a periodic particle distribution.	201
Figure B.11: Variation of the simulated composite thermal conductivities with relative particle size for the random distributions. The symbols μ and σ refer to the arithmetic mean and standard deviation, respectively.	203
Figure B.12: Variation of relative composite properties with associated components (F_x or F_y ,) of the fabric tensor orientation parameter for multi-particle simulations using the periodic distribution method.	205
Figure B.13: Comparison of the simulated variation of ζ with F_i and equation B.16. In all figures the periodic particle distribution method was used and $k_2/k_1 = 100$. In total 50 unique distributions were analyzed with the global gradient in both the x and y axes. ...	206
Figure B.14: Thermal conductivity anisotropy in the multi-particle simulations. In this case 50 periodic distributions were analyzed with the global gradient in both the x and y directions at $k_2/k_1 = 100$	207

Figure B.15: Comparison of the mean results of the multi-particle simulations with periodic distributions and $\phi_2= 0.01$ to the predictions utilizing equation B.20	209
Figure B.16: Comparison of the mean results of the multi-particle simulations with random distributions and $k_2/k_1 = 100$ to the predictions utilizing equation B.20.	209
Figure C.1: Particle size distribution of the two forms graphite and the silica sand.	215
Figure C.2: Illustration of the needle probe used to measure the thermal conductivity of the grout	216
Figure C.3: Variation of thermal conductivity of bentonite grout with additive concentration for the four materials examined; the error bars indicate the 95% confidence interval assuming a normal distribution.....	219
Figure E.1: The variation in the model results of FH-7 with the value of the fixed time step. The reference simulation used an alternate time stepping scheme dictated by dT . 229	
Figure E.2: The variation in the model results of FH-7 with the size of the maximum allowable temperature increment. The dashed line corresponds to the reference case of 0.1 °C.	230
Figure E.3: The variation in the model results of FH-7 with the element size (all elements in these simulations were square). The dashed line corresponds to the reference case of 0.02 m.	231
Figure E.4: The variation in the model results of FH-7 with the element aspect ratio, defined as l_y/l_x where heat transfer occurs in the y -orientation. The dashed line corresponds to the reference case of 1.	231
Figure E.5: The variation in the model results of FH-7 with the dimensionless fractional anisotropy parameter. The dashed line corresponds to the reference case of 0.09.	233
Figure F.1: Control configuration representation (a) and corresponding finite element discretization (b) of the Calgary pipeline problem.	234
Figure F.2: Deep burial configuration representation (a) and corresponding finite element discretization (b) of the Calgary pipeline problem.	235
Figure F.3: Gravel configuration representation (a) and corresponding finite element discretization (b) of the Calgary pipeline problem.	236

Figure F.4: Temperature profile (a), porosity profile (b), and plastic strain (c) on day 1042 for the control configuration	237
Figure F.5: Temperature profile (a), porosity profile (b), and plastic strain (c) on day 1042 for the deep burial configuration.....	238
Figure F.6: Temperature profile (a), porosity profile (b), and plastic strain (c) on day 1042 for the gravel configuration	239

LIST OF TABLES

Table 3.1: Soil properties.....	41
Table 3.2: Step-freezing testing matrix.....	43
Table 3.3: Ramped-freezing testing matrix.....	44
Table 3.4: The frost heave characterizing parameters from equation 3.8 observed for FHC and BSM	64
Table 4.1: Assumed thermal conductivity values of the constituent soil phases.....	88
Table 4.2: Difference between thermal conductivity of the strong, λ_s , and weak, λ_w , orientation for a soil with a 10% ice lens volume fraction.	97
Table 5.1: The range in parameter values in equation 5.1 that may be expected under natural conditions.....	104
Table 5.2: The range in heat transfer mechanisms implied by the parameter values in Table 5.1	105
Table 5.3: Material properties defining the thermal conductivity of FHC and BSM.....	120
Table 5.4: Frost heave characterizing parameters.....	121
Table 6.1: The assumed cohesion, c' , and friction angle, ϕ_0 , of each soil region.....	146
Table 6.2: The assumed thermal properties of each soil constituent phase (Michalowski 1993).	147
Table 6.3: Input parameters for the base case simulations	153
Table A.1: Step-freezing testing matrix.....	168
Table A.2: Ramped-freezing testing matrix.....	168
Table B.1: Select values of ζ used to predict the bulk modulus of discrete particle composites using the Halpin-Tsai equation	187
Table B.2: The range of variables examined in the single particle composite simulations.	190

Table B.3: The shape parameters in equation B.13 for the three different particle shapes	197
Table C.1: The coefficients of curvature and uniformity as well as the mean particle sizes (D_{50}) of the grout constituents.....	215
Table C.2: The volumetric composition of the various grout mixes examined in this study. For each volumetric composition, aside from the baseline case, four samples were produced corresponding to each additive material examined.	217
Table E.1: Numerical parameters examined in the sensitivity analysis.....	227

LIST OF SYMBOLS

A	Empirical material property defining the regelation rate, see equation 2.5
AR	Aspect ratio
b	Stress sensitivity of SP
B_1, B_2	Material constants in equation 2.8
c	Specific heat capacity
c'	Cohesion
C	Volumetric heat capacity
C^*	Apparent volumetric heat capacity
d	Material constant in equation 2.11
e	Void ratio
E	Elastic modulus
F, \mathbf{F}	Particle orientation parameter, see equation B.15
g_1, g_2	Material constants in equation 2.12
G_s	Specific gravity
k	Hydraulic conductivity
l_f	Frozen fringe thickness
l_e	Element characteristic length
L	The latent heat of freezing of water
m_1, m_2	Material parameters defining the liquid water content, see equation 5.28
n	Porosity
\mathbf{n}	Unit vector defining the ice lens orientation
P	Pressure
q	Water flux
Q	Heat flux
SP	Segregation potential
SP_0	SP associated with thermal steady-state and zero overburden stress
S_r	Saturation
t	Time
T	Temperature
\dot{T}_f	Cooling rate
\dot{T}_0, \dot{T}_{nz}	Reference cooling rates used in equation 3.7
u	Displacement
v	Velocity

V	Volume
w	Water content
w_1, w_2, w_3	Material parameters defining frozen E , see equation x.6
W	Work done
X	General composite material property
\dot{x}_f	Frost front advance rate
β	Frost advance rate sensitivity on SP
γ	Unit weight
δ	Geometric distribution factor in the Halpin-Tsai Equation, Appendix B
ε	Strain
ζ	Fractional anisotropy factor of frost heave
θ	Volume fraction
λ	Thermal Conductivity
ν	Poisson's ratio
ξ	Volumetric strain distributing factor, see equation 5.21
ρ	Mass density
σ_t	Total stress
σ_b	Apparent effective stress
$\sigma_{u,f}$	Frozen, unconfined compressive strength
ϕ	Friction angle
χ	Stress portioning factor, see equation 2.3

Subscripts and Superscripts

$1,2$	Constituent phases
a	Air phase
E	Equivalent or composite property
f	Frozen fringe
H	Heave displacement
i	Ice phase
l	Liquid water phase
$lens$	Ice lens
N	Number of blows associated with the liquid limit test
s	Soil grains
U	Water uptake

PREFACE

Portions of this research were published and presented previously. The peer-reviewed publications include:

Tiedje, E. W., & Guo, P. J. (2014). Modeling the influence of particulate geometry on the thermal conductivity of composites. *Journal of Materials Science*, 49(16), 5586-5597.

Tiedje, E., & Guo, P. (2013). Thermal Conductivity of Bentonite Grout Containing Graphite or Chopped Carbon Fibers. *Journal of Materials in Civil Engineering*, 26(7).

Tiedje, E., & Guo, P. (2012, August). *Frost Heave Modeling Using a Modified Segregation Potential Approach*. Paper presented at the 15th International Conference on Cold Regions Engineering, Quebec, Canada. ASCE.

Tiedje, E. W., & Guo, P. (2011, October) *Dewatering induced by frost heave in a closed system*. Paper presented at the 14th Pan-American Conference on Soil Mechanics and Geotechnical Engineering and 64th Canadian Geotechnical Conference, Toronto, Canada.

CHAPTER 1 INTRODUCTION

1.1 BACKGROUND

Frost heave is the freezing induced expansion of soil. It composes one half of the process of frost action with the other being the corresponding thaw-weakening. Both expansion and thaw weakening are primarily attributed to segregated ice, also known as ice lenses. When segregated ice forms and grows, soils expand due to increases localized porosity. Alternatively, thaw weakening occurs when this same ice melts, which increases the local water content, induces consolidation, and leads to decreases in soil strength and stiffness. While both the heave and weakening are important engineering considerations, this research focuses on the frost heave process.

Frost heave presents a notable challenge for geotechnical engineers. It typically materializes as the upward displacement of the ground surface, though it has a diverse range of potential consequences. For example, foundations embedded in soils undergoing frost heave can be subjected to large uplift or lateral forces. Uplift occurs due to ice induced shear coupling, referred to as adfreezing, between the foundation surface and the heaving soil and lateral forces are induced by laterally oriented heaving, which can occur in heated basements during winter periods. The magnitude of these forces is noteworthy. While forming, ice lenses release enough energy to displace up to 334 MPa of overburden pressure (Henry 2000), equivalent to more than 16 km of vertically aligned soil. Other structures that are vulnerable to frost heave and frost action include roads and railways, which are relatively flexible and are susceptible to serviceability failure.

Frost heaving is a time dependent process. The slower and longer freezing occurs, the more time is available for segregated ice to form and grow. Typically soil freezing is induced naturally by seasonal weather, in which case its duration is dictated by the length of the winter. However, in some circumstances freezing is caused by human activity. These situations present a particular challenge if the activity is prolonged. A notable example is chilled gas pipelines, where the duration of freezing generally coincides with the operational life of the structure. In order to safely build and operate such structures it is critical to be able to accurately characterize the uplift forces and displacements induced by frost heave.

To date, considerable effort has been made to investigate and characterize frost heave. Extensive experimental studies have been reported and numerous numerical models have been proposed. However, despite these advancements, there is no universally accepted approach for characterizing frost heave. Existing models tend to be either highly simplified or unnecessarily complex, providing extraneous levels of detail. There is potential for improvement in these approaches. Through systematic evaluation and analysis of the frost heave process, it is possible to achieve a better balance between the physical considerations and practical utility in characterization.

1.2 OBJECTIVE

The primary objective of this work is to accurately characterize the volumetric expansion associated with frost heave under geometries and boundary conditions indicative of common practical applications. This characterization will assist in the

development of a numerical model capable of predictive analysis for the mechanical response of geotechnical structures and systems subjected to frost heave. This tool will yield improvements in the design and performance of such structures and systems. The practical concerns associated with the implementation and applications of this model will be paramount in its formulation. A theoretically comprehensive model will be of little use if it cannot be readily applied to a wide range of situations.

In order to develop a comprehensive thermodynamic-mechanical frost heave model, this research addresses the following:

1. Characterization of the thermal properties of frozen and unfrozen soil and the mass transport associated with segregated ice formation. The thermal properties will be investigated numerically and the formulated characterization will be validated through comparison with physical observations. On the other hand, mass transport will be investigated physically; observed behaviour under controlled experimental conditions will be used to both derive and validate characterizations.
2. Formulation of the frost heave model. Develop governing expressions for energy and mass transport and combine them in an appropriate manner.
3. Evaluation of the performance of the model. Simulated predictions will be compared with observations under both small-scale, highly controlled experimental conditions as well as full-scale, field conditions typical of engineering problems.

1.3 THESIS OUTLINE

This thesis contains 7 chapters including the Introduction and Conclusion. Chapter 2 presents a review of the frost heave process and the mechanical behaviour of frozen soil. The physical processes involved in segregated ice formation, the experimental explorations, and existing characterizations are featured. The mechanical properties consider the temperature and strain rate sensitivity of the shear strength and stiffness of frozen soils along with creep behaviour. This literature review provides insight and context into the characterization of frost heave.

In Chapter 3 frost heave is investigated experimentally. Firstly, the test methods are presented, including the development of an apparatus capable of inducing one-dimensional freezing using variable thermal, hydraulic, and mechanical boundary conditions. The materials examined and the sample preparation techniques are discussed in detail. Secondly, the findings are presented. The sensitivity of the frost heave response to the axial stress level and the freezing rate are examined. Of particular interest is the variation between the heave rate and the frost front advance rate. Additionally, the influence of the thermal gradient and the hydraulic boundary conditions are considered. Finally the results are analyzed and discussed. The variation in frost susceptibility is characterized through an established empirical concept, segregation potential. A modification of this concept is ultimately proposed to improve the characterization and provide better agreement with the observed frost heave behaviour.

Chapter 4 presents an investigation into the characterization of the thermal properties of frozen soil. Existing characterizations are reviewed and evaluated through

comparison with physical observations. Based on these findings, an optimal characterization is identified. The anisotropic thermal conductivity of frozen soil containing segregated ice lenses is also considered.

Chapter 5 presents the coupled, thermo-mechanical frost heave model. Governing equations of heat and mass transfer are formulated. A review of individual heat transfer mechanisms associated with frost heave is presented and the relevance of each component is considered. An anisotropic frost heave tensor defining ice lens-induced volumetric expansion is derived. The chapter includes a discussion on some of the practical implications of implementing the frost heave model into a finite element framework. The model is used to simulate the one-dimensional frost heave tests presented in Chapter 3. The results are shown to validate the conceptual approach utilized in the model derivation. The proposed modification to the segregation potential concept is explored in detail. This chapter also includes an investigation of the parametric sensitivity of the model.

Chapter 6 extends the frost heave model into two dimensions and applies it to an engineering problem: the frost heave induced deformation of a chilled natural gas pipeline. Physical observations were obtained from the reported results of a full-scale experiment. The parametric sensitivity of the model is investigated.

Chapter 7 summarizes the findings of this work and discusses potential future research activities.

CHAPTER 2 LITERATURE REVIEW

2.1 INTRODUCTION

Frost heave is the volumetric expansion of soil caused by the formation and growth of pore ice. The expansion leads to deformation and damage in geotechnical structures such as roads, pipelines and foundations. The existence of large volumes of pore ice increases the potential for thaw-induced weakening and settlements. Consequently, frost heave can be a serious design consideration where soils freeze.

Frost heave has two primary components. The first is the expansion of water upon freezing caused by its variation in density between liquid and solid phases, which is approximately 9%. The second component is the formation and growth of segregated ice, which forms as a series of discrete bands of pure ice, referred to as ice lenses. Segregated ice forms through the migration of liquid pore water throughout the soil, moving from unfrozen regions to the actively freezing interface. The magnitude of ice lens growth is limited to the availability and migration of pore water as well as the duration of freezing. For example, pingos, which are large geological landforms found in arctic regions, form in a similar process to ice lenses and over millennia can grow in excess of 70 m in thickness (Brown and Kupsch 1974). In most practical applications the second component, referred to as secondary frost heave, is generally the dominant component compared to the volumetric expansion of water upon freezing (Fowler 1989).

2.2 PHYSICAL DYNAMICS OF FROST HEAVE

There are three requirements for frost heave to take place: first the soil must be inherently frost susceptible, second freezing temperatures, and third an accessible source of pore water (Taber 1929, 1930). Furthermore, regarding temperature, there must be a thermal gradient near the bulk freezing point and $\frac{\partial T}{\partial t} < 0$. Frost heave is caused primarily by the formation of segregated ice, which is a series of discrete ice lenses containing no soil particles. As indicated by the hydrodynamic conceptualization, illustrated in Figure 2.1, ice lenses form through the migration of water from unfrozen soil to the frozen soil through a zone known as the frozen fringe (Nixon 1991). The frozen fringe is defined as a region where the temperature is slightly below the bulk freezing point of water, between approximately 0 to -2 °C, but no ice lenses are present. Adjacent to the fringe is the active ice lens, the growing ice body, and the frozen soil zone, containing inactive ice lenses. The temperature and position of the active ice lenses vary with both soil type and stress state (Taber 1929, 1930).

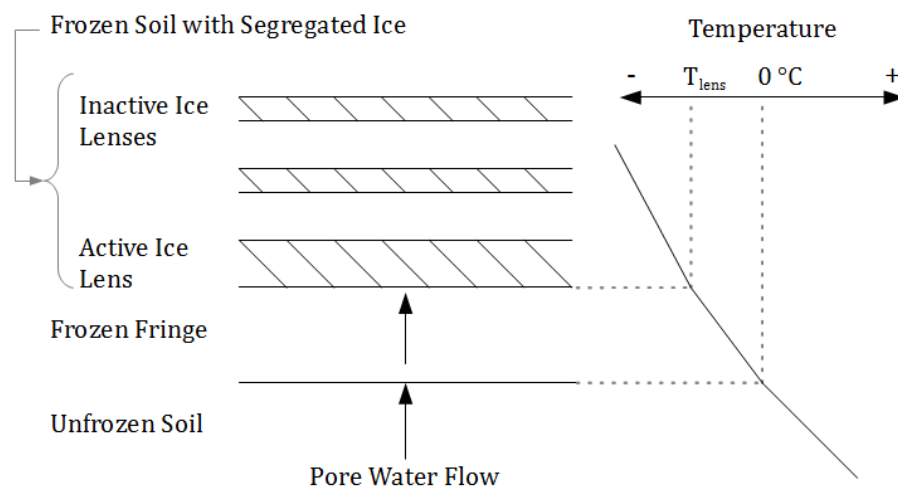


Figure 2.1: A schematic diagram of the relevant components of the frost heave process.

2.2.1 Thermodynamic Characteristics of Water

Due to its molecular structure, water has the somewhat unique property of having a lesser density in its solid phase than in its liquid phase at temperatures near the bulk freezing point. One consequence of this is that water expands upon freezing by an amount equal to the ratio between the solid and liquid densities, approximately 9%. Another consequence is that water possesses different enthalpies between solid and liquid phases at the same temperature. This difference in enthalpy is referred to as the latent heat of fusion, L , and typically manifests as heat released from water upon freezing or absorbed upon melting. The specific value of the latent heat of water is 3.34×10^5 J/kg (Andersland and Ladanyi 1994).

2.2.2 Unfrozen Water in Soil

It has been well established that a portion of pore water in a soil exists in a liquid state at temperatures below the bulk freezing point (Lovell 1957). Two mechanisms have been proposed to account for this phenomenon: the Gibbs-Thomson effect which relates the depression in the freezing temperature to the high level of curvature of the ice-liquid interface in small pores (Williams 1964); and intermolecular forces resulting in interfacial premelting between the soil grains and ice (Rempel 2007). The first mechanism is primarily dictated by the pore sizes and is responsible for the majority of the volume of unfrozen water. The second mechanism is related to the specific surface area and soil mineralogy. At -1°C , the thickness of the premelted liquid film between ice and silica is of the magnitude of nanometres and does not contribute significantly to the volumetric

unfrozen water content (Rempel et al. 2001). Generally, fine-grained soils containing smaller voids and larger surface areas are associated with more unfrozen water as compared to coarse soils at temperatures below 0°C.

One common approach for measuring the liquid water and ice content of frozen soil is the calorimetric approach (Williams 1964). The apparent specific heat capacity of the frozen soil is determined by measuring the change in temperature induced by a known quantity of heat input. When the thermal properties of the soil constituents are known, the latent heat of the pore water can be determined which indicates the change in ice content. Other techniques include nuclear magnetic resonance, which requires sophisticated equipment, and time domain reflectometry, which requires known calibration readings (Tice et al. 1978). Considering solute-free, fully saturated soils, the variation of unfrozen water content, θ_l , with temperature can be approximated empirically with the following exponential relation (Tice et al. 1976):

$$\theta_l = m_1 |T|^{m_2} \quad (2.1)$$

where T is the temperature in °C below the bulk freezing point and m_1 and m_2 are empirically derived material parameters associated with a particular soil fabric.

An alternative approach to determine unfrozen water content is proposed based on the postulation that the unique relationship between the liquid water content of a fully saturated frozen soil and temperature can be established similar to the soil water retention relation, or soil water characteristic, for unsaturated soils (Williams 1964; Koopmans and

Miller 1966; Spanns and Baker 1996). In this approach the air voids in the partially saturated soil are considered analogues to the pore ice in the frozen soil. The matric suction can be related to the freezing temperature through the generalized Clapeyron equation, see equation 2.2, using the same concepts of curvature at the phase boundaries. This implies that the unique variation of liquid water content with temperature can be directly related to the soil water characteristic. To date, conceptual approaches available for characterizing the liquid water content in a partially saturated, frozen soil are limited.

2.2.3 Cryogenic Potential

In order for frost heave to occur pore water must flow through the frozen fringe, as illustrated in Figure 2.1. Commonly this flow is in the opposite direction to the gravitational potential gradient, implying an additional potential gradient exists for this process to occur. Furthermore, as the active ice lens grows it must displace the pressure acting on the lens due to overburden soil, doing work in the process. From a thermodynamics perspective, this is possible because the system approaches a condition of greater enthalpy as the water flows upwards (Ozawa 1997). As the pore water freezes at the ice lens, some of the latent heat is released as thermal energy and some produces work in the system.

In order to characterize this thermodynamic potential the generalized form of the Clapeyron equation can be employed (O’Neil and Miller 1982; Gilpin 1980; Nishimura et al. 2009). This approach relates temperature, T , to the localized difference in pressure at the ice and liquid water phase interface.

$$P_i = \frac{\rho_i}{\rho_l} P_l - \rho_i L \ln \left(\frac{T}{273.15} \right) \quad (2.2)$$

where L is the latent heat of the water, P_l and P_i are the pressure of the liquid water and ice phases respectively, and ρ_l and ρ_i are the respective densities of liquid water and ice.

With regards to the frost heave process, the Clapeyron equation implies a gradient in the pressure variation between the solid and liquid phases in the frozen fringe. If the ice pressure is known either throughout the region or at specific locations, such as the active ice lens, the above equation yields the pressure gradient in the liquid pore water. The Clapeyron equation implies that there is enough thermodynamic potential energy in the pore water for an active ice lens to displace a stress of up to 334 MPa. The existence of this cut-off pressure is supported by experimental observations (Hoekstra 1969).

2.2.4 Frozen Hydraulic Conductivity

Frozen soils are known to possess some hydraulic conductivity at freezing temperatures, albeit substantially less than under unfrozen conditions. This conductivity is attributed to the presence of unfrozen water in the pores, which forms flow path networks, and the deformation and possible permeability of the pore ice (Horiguchi and Miller 1980). The first component is a function of the intrinsic permeability of the soil, the unfrozen water content, and the temperature, which influences pore water viscosity. As with unfrozen soils, any adsorbed pore water will not contribute to the flow path. Coarse-grained soils with large voids are associated with large unfrozen hydraulic conductivities, but due to the small volume of liquid water present at freezing temperatures, they will

have very small frozen hydraulic conductivity. Alternatively, fine-grained soils may have lower permeability but can be associated with larger frozen conductivities as compared to coarse soils due to their greater liquid water content (Horiguchi and Miller 1983). In general, the hydraulic conductivity of frozen soil decreases at lower temperatures, as illustrated in Figure 2.2. The deformation of the pore ice is dependent on both the temperature and pressure gradients. Ice deformation is difficult to characterize and is typically assumed to be immaterial (Miller 1970). If this process is of a significant magnitude, the application of Darcy's law for frozen soils may not be valid.

Due to the technical challenges associated with directly measuring the conductivity of frozen soils, there are a limited number of reported values. Two procedures have been successfully developed to allow for direct measurements. The ice-sandwich technique developed by Miller (1970) uses two pressurized ice sheets at either end of a permeameter mould to induce a controlled pressure gradient. In this case pore water flow is determined by the changes in ice sheet volume. Alternatively, Burt and Williams (1976) developed a similar technique using two pressurized reservoirs containing a water and lactose solution to suppress the bulk freezing point. The duration of the test is minimized in order to avoid a significant amount of solute from diffusing into the soil sample. In both techniques very large pressure gradients are required due to the small frozen conductivities involved, introducing the potential for significant ice deformation effects. As a result, these measured conductivities are considered to be apparent values.

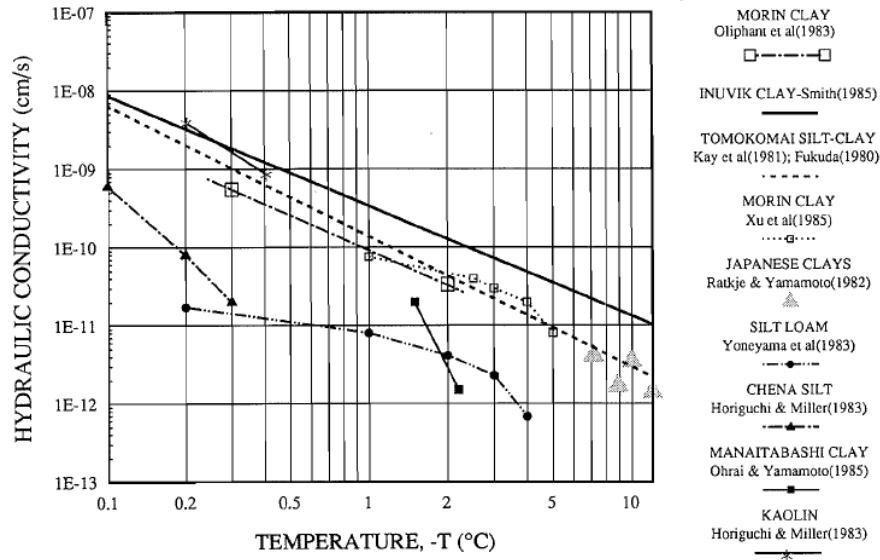


Figure 2.2: The reported hydraulic conductivities of select frozen soils (Nixon 1991).

Several models have been proposed to characterize the frozen hydraulic conductivity, ranging from empirically based (Lundin 1990; Nixon 1991), to more sophisticated physical based models derived from the concepts of unsaturated permeability, such as the capillary bundle model (Watanabe and Wake 2008; Watanabe and Flury 2008).

2.2.5 Ice lens Initiation

Although all soils possess some amount of liquid water at temperatures below the bulk freezing point, not all soils produce segregated ice lenses. Beyond the development of a liquid pore water pressure gradient, another requirement must be satisfied for ice lenses to initiate. Most common criteria used for ice lens initiation involve examining the balance between the temperature induced cryogenic stresses, the pore pressure, and the external mechanical stresses acting on soil particles, typically considered to be the

overburden stress (Gilpin 1980). Separation between the soil particles is assumed to take place when the effective soil stress approaches zero. This theoretical pressure may be a function of both the material type and the pore pressure.

In the rigid ice model proposed by Miller (1978) the balance of stresses, σ , between the soil grains, the liquid pore water pressure, P_l , and the pore ice pressure, P_i , in the frozen fringe is characterized through the use of a stress partitioning factor, such that:

$$\sigma_t = \sigma_b + (\chi P_l + (1 - \chi)P_i) \quad (2.3)$$

where σ_t is the total stress, σ_b is the apparent effective stress, and χ is the stress partitioning factor. The ice pressure is assumed to be equal to the overburden stress and the liquid water pressure can be determined through the Clapeyron equation. A new ice lens is assumed to initiate when the effective stress approaches zero.

2.2.6 Frost Heave Susceptibility

Frost heave susceptibility is typically characterized qualitatively by comparing the observed heave rate of various soils under some constant set of thermal, hydraulic, and mechanical conditions. The specific conditions vary, as there is no universally accepted protocol. Observations indicate that particle size plays an important role in the frost heave tendencies of soils and traditionally this has been the primary metric for predicting frost susceptibility. Figure 2.3 illustrates the observed frost susceptibility of various soils with respect to of particle size. Silts and clayey-silts show the greatest tendency for heave while clean sands and gravels are least susceptible. The relationship between frost

susceptibility and particle size, however, is not linear. For example, while clay soils are generally frost susceptible they typically display less heave as compared to larger grained silts.

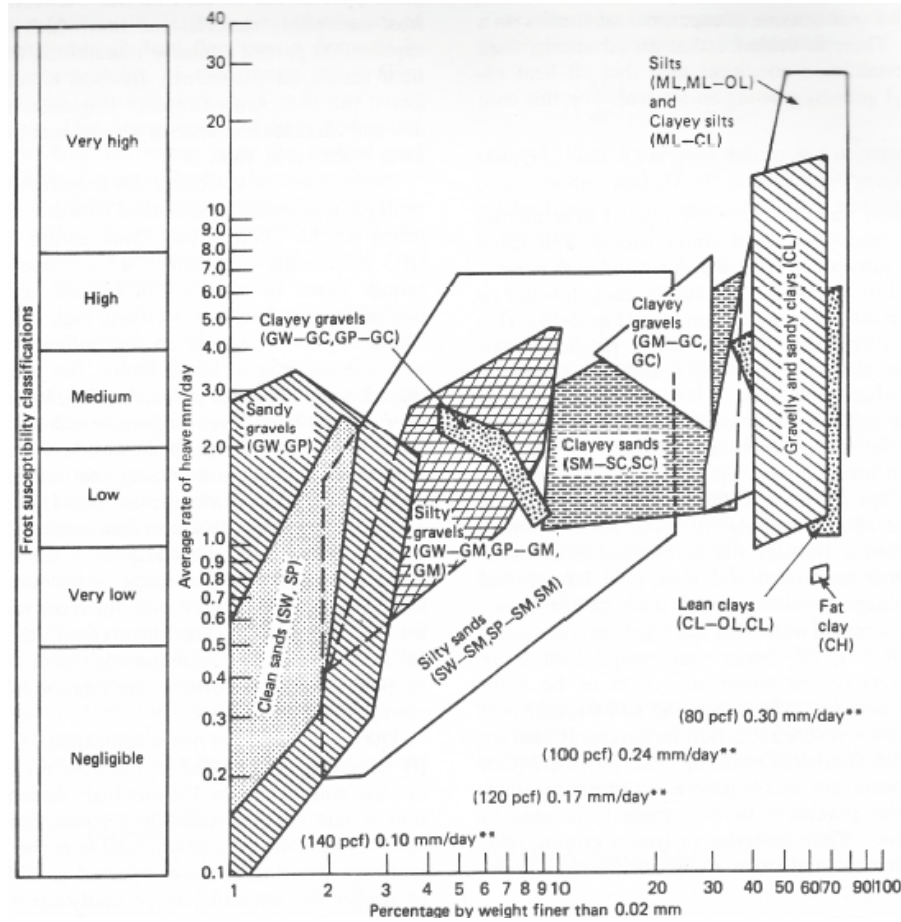


Figure 2.3: The frost susceptibility of soils based on the Unified Soil Classification System (Andersland and Ladanyi 1994).

As expressed by the Clapeyron equation, the potential gradient driving pore water flux in the frozen fringe is a function of temperature, ice pressure, and the characteristics of water. Assuming pore water flux is the dominant mass transport mechanism, the heave rate is primarily dependent on the frozen hydraulic conductivity of the soil. This implies

that frost susceptibility is essentially a reflection of the hydraulic conductivity of a soil at frozen fringe temperatures.

2.3 EXPERIMENTAL INVESTIGATIONS

Prior to the pioneering work of Miller (1972,1978), Konrad and Morgenstern (1980), and Gilpin (1982), the physical processes involved in frost heave were not well understood. Up until then engineers relied heavily on experimental and field observations to predict frost heave behaviour. While the better physical understanding has improved predictions, in many cases empirical approaches still yield practical and effective solutions.

2.3.1 Laboratory Frost Heave Experiments

Taber (1929,1930) and later Beskow (1935) published the first experimental observations of frost heave under laboratory conditions. Taber's experiments demonstrated that the formation of segregated ice through pore fluid migration was the dominant expansion process. He replaced the pore water in the soil with liquid benzene, which contracts upon freezing, and demonstrated that the soil-benzene mixture would heave and produce ice lenses when frozen.

The principle of uniaxial freezing conditions that Taber and Beskow used is still the most widely adopted approach for examining frost heave (Chamberlain 1981). In uniaxial freezing tests, a soil sample (typically cylindrical) is insulated laterally while the thermal and hydraulic conditions at either end are controlled. The mould containing the

sample is designed in such a way that the sample may expand by displacing at either end and this displacement is monitored. A force is applied axially through either a weight or a beofram piston and the corresponding stress is referred to as the overburden. Typically, circulating coolant through heat exchangers controls the temperature at the top and bottom of the cylindrical specimen. Water is usually made available at the warm end of the sample for ice lens growth and its uptake is monitored. The frost heave response is assessed as either the total surface displacement and/or the volume of water uptake per unit area for a specific time frame or as the steady state heave rate.

Ideally the boundary conditions of frost heave tests should closely reproduce natural conditions. However, the applied thermal gradient in laboratory tests often exceeds in situ values, typically 10 – 40 °C/m as compared to 1 – 5 °C/m expected in nature (Konrad 1988). Small gradients require large sample lengths and/or particularly precise temperature control systems and produce small displacement rates requiring long test durations. Typical test durations are between 1 and 10 days, though some laboratory tests have been conducted for up to 100 days (Eigenbrod et al. 1996). Sample heights range between 50 mm to 1 m while diameters range between 50 to 200 mm. The tested soils may be undisturbed or artificially prepared, such as from a consolidated slurry.

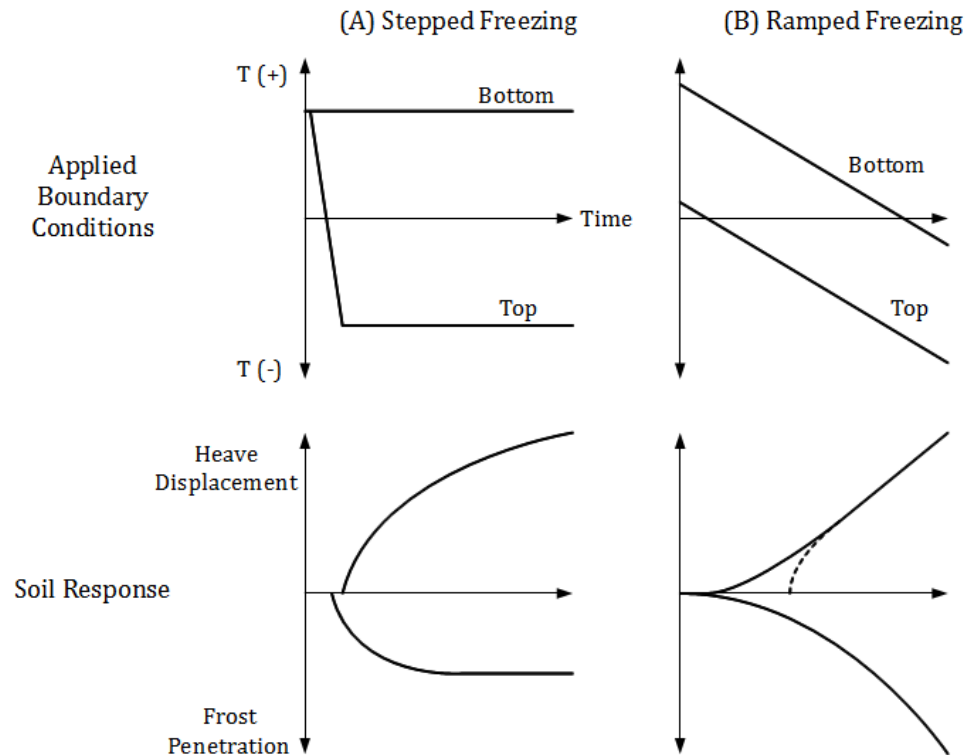


Figure 2.4: An illustration of the stepped and ramped freezing boundary conditions used in 1D laboratory frost heave tests and the typical soil response.

Two categories of thermal boundary conditions are typically employed in laboratory frost heave tests: stepped and ramped temperature variation (Konrad 1994). In a stepped freezing test, the temperatures at the top and bottom of the soil sample are first brought to the same value, often slightly above 0°C , so that the sample is at a uniform initial temperature. Then the temperature at one end is decreased quickly to some value below 0°C and maintained, as illustrated in Figure 2.4a. This results in a period of quick frost penetration through the sample followed by a period of a constant temperature profile. Ramped freezing involves varying the temperatures at the top and bottom linearly

while maintaining the same temperature gradient throughout the sample, resulting in a constant frost penetration rate, as shown in Figure 2.4b. Stepped freezing is the more common of the two methods as it requires less sophisticated temperature controllers but does not allow for precise control of the frost penetration rate (Konrad 1994). Stepped tests produce high concentrations of segregated ice around the final position of the frozen fringe while ramped test yield more evenly distributed ice lenses. An important consideration is that stepped tests are not limited in their duration, unlike ramped tests where the duration is dictated by the sample length and the frost penetration rate.

Of course it is possible to impose other thermal boundary condition types, although these are generally less common in the reported literature. Additional boundary types include multi-stepped boundaries (Seto and Konrad 1994) and those used in the Japanese Geotechnical Standard Test, JGST, which involve a constant warm boundary and a linearly decreasing cold boundary (Japanese Geotechnical Society 2003).

2.3.2 Full-Scale Frost Heave Studies

While laboratory experiments can provide insight into the frost heave behaviour of a specific soil, full scale tests and field observations are necessary to examine the effect of frost heave on geotechnical systems involving complex soil-structure interactions and multiple soil types, as well as varying geometries and boundary conditions. Frost heave often induces damage or failure of structures that may or may not have been anticipated, mainly owing to differential heave. For example, if constructed on frost susceptible soils, ice rinks can be particularly susceptible to differential heaving after prolonged

periods of operation. If excessive, the heaving can lead to serviceability failures or structural failure in the underlying concrete slab (Leonoff and Lo 1982). In cold regions, frost heave and freeze-thaw settlements are considered major factors in the differential deformation of flexible pavements and failure of concrete slabs in rigid pavements (Doré and Zubeck 2008).

Transmission line poles in cold regions have been noted to be susceptible to uplift forces induced by frost heave (Lyazgin et al. 2004). Penner (1974) examined the uplift forces caused by frost heave on circular steel, wood, and concrete piles embedded 5' in the ground over the winter in Ottawa, Canada. The results demonstrate that the presence of the piles influences the freezing of the soil. The thermal conductivity of concrete and steel is significantly greater than most soils and the piles increase the frost depth in the adjacent soil. The uplift forces are also highly sensitive to the adfreeze strengths and frictional characteristics at the pile-soil interface.

Gas pipelines present a particular challenge in cold regions containing discontinuous permafrost where both permafrost and seasonally frozen ground are present. If buried, the gas must be chilled to sub-zero temperatures to avoid melting areas containing permafrost. Melted permafrost presents considerable challenges regarding settlement, softening, and soil instability that may lead to catastrophic pipeline failures. The chilled pipeline also actively freezes the permafrost-free soils, and if the soil is frost susceptible, this can induce large heave related deformations. Consequently, frost heave is a critical design consideration in such situations. The alternative of constructing the

pipeline above ground in many cases is economically prohibitive. An illustration of this point is the Trans-Alaska Pipeline System (Godfrey 1978). Because this system carried oil that could not be transported in a chilled state much of it was constructed suspended above ground on specially designed vertical supports. The supports provided the additional role of thermal piles, continuously removing excess heat from the underlying permafrost. The design considerations for preserving permafrost contributed to the final costs of the Trans-Alaska Pipeline System exceeding initial estimates by over seven times (Williams 1986, Kim 2011).

To support the design of such large strategic infrastructure projects, several full-scale frost heave-pipeline experiments have been constructed in different countries. These include tests conducted in Calgary, Canada (Slusarchuk et al. 1978), Caen, France (Foriero and Ladanyi 1994), and Fairbanks, USA (Huang et al. 2004). The Fairbanks experiments were a joint project between the University of Alaska Fairbanks and the Hokkaido University in Japan. The common objective of these tests was to investigate the displacement and stress response of the pipelines due to freezing. At Calgary, the experimental variables were generally tailored to closely follow anticipated conditions wherever possible, and in some respects to evaluate or validate existing designs. Of particular interest was the overburden stress induced by a berm above the buried pipe. The Caen and Fairbanks tests examined differential heaving, where the pipeline would transition from frost susceptible to non-susceptible soils.

In addition frost heave in pipelines can also be examined using centrifuge modelling (Clarke and Phillips 2003). This approach involves the construction of scale models of particular pipe configurations and then placing such models into a large centrifuge to increase the g-forces acting on the soil. Stresses within the model can then be physically observed. This approach has been successfully used to both analyze frost heave induced stresses in buried gas pipelines (Piercy et al. 2011) as well as to physical evaluate potential mitigation techniques (Morgen et al. 2006).

2.4 FROST HEAVE MODELS

Since the first identification of the frost heave process, different models have been developed to predict its effects. These models vary greatly in both their level of sophistication, founding assumptions, and performance. Some are based on general soil classifications and freezing indices and at best provide rough estimates of heave displacements (Chamberlain 1981). Others involve coupled thermodynamic, mechanical, and hydraulic analyses in conjunction with a constitutive frost heave relation. The characterization relations can be categorized as one of two types: empirically or semi-empirically based expressions and physically based models. Regardless of their derivation, the practical objective of these models is typically the same, to predict the mechanical response of geotechnical systems to frost heave.

2.4.1 Empirical Frost Heave Models

One of the simplest approaches for quantifying heave effects is through empirical relations utilizing the freezing index, generally defined as the average degree-days of freezing of a particular climate (Boyd 1976). When used in conjunction with past observations of the general frost susceptibility of a specific soil, the freezing index may provide approximate estimates of uplift pressures, ground surface displacements, and pavement distress. In this approach frost susceptibility is approximated based on the Unified Soil Classification System, where silts and clayey silts are considered to be most susceptible and clean coarse materials are least, see Figure 2.3 (Andersland and Ladanyi 1994).

Konrad and Morgenstern (1980) developed the concept of segregation potential as a means of predicting expansion associated with ice lens growth. The approach relates the water flux across the frozen fringe to the temperature gradient across the same region when the frost penetration rate is at a small, constant value. This concept can be expressed mathematically as:

$$q_f = SP \left(\frac{\partial T}{\partial z} \right)_f \quad (2.4)$$

where the subscript f refers to the frozen fringe and the segregation potential (SP) is a material parameter, considered to be sensitive to other factors such as the stress level. Segregation potential combines the complex concepts of cryogenic suction, frozen hydraulic conductivity, and ice deformation into a single, empirically derived material

property, SP . This property varies with the same factors influencing general soil frost susceptibility, such as the particle size distribution and void ratio. Additionally, it is important to note that SP is not a material constant as it is known to be influenced by external factors such as stress level and the rate of cooling (Konrad and Morgenstern 1981).

The segregation potential model has the advantage of being simple to determine and implement in a thermodynamic model while at the same time producing results accurate enough for many engineering applications. However, it is not without its drawbacks, specifically its accuracy decreases when varying frost penetration rates are involved (Nixon 1991; Fukuda et al. 1997). Despite this, the segregation potential concept is reported to be one of the most widely used frost heave models in current engineering practice (Kujala 1997).

Similar to segregation potential model, the porosity rate function proposed by Michalowski (1993) estimates frost heave by correlating volumetric expansion to the thermal gradient and temperature values in a region close to the 0°C isotherm through the use of empirical material parameters. The primary conceptual difference between the two approaches is the manner in which heave is defined. More specifically, the porosity rate function considers frost heave to be a localized change in soil porosity, whereas the segregation potential describes the pore water flux entering the frozen fringe. An advantage of the porosity rate function is that it is ideally suited for implementation into

existing thermodynamic finite element models without modification, in contrast to the segregation potential concept.

2.4.2 Physical Frost Heave Models

Several models have been developed to characterize the various physical processes associated with frost heave. Although not limited to, these models include: the hydrodynamic model, the fully coupled thermo-hydro-mechanical models, the rigid ice model, and the premelting dynamics approach. The principal of each physical model is generally consistent: they provide solutions for governing equations of heat and mass transport through a series of assumptions regarding ice and water pressure. The founding assumptions regarding mass transport are primarily what differentiate each model.

The hydrodynamic model approaches the formation of segregated ice as primarily a ground water flow problem in a frozen and partially saturated soil (Hansson et al. 2004). Considering unsaturated conditions is somewhat unique with regards to frost heave modelling, however it adds substantial complexity to the problem. The pressure differential between pore ice and unfrozen pore water is defined based on temperature using the generalized Clapeyron equation. The gauge pressure of the ice is assumed to be zero and osmotic pressure is neglected. Based on the pore water pressure, water flux to the active ice lens can subsequently be defined with Darcy's law. Ice lens initiation is not considered and the position and size of the frozen fringe is assumed to be within a specific temperature range. This approach requires an accurate representative value of the frozen, partially saturated hydraulic conductivity, which explicitly quantifies frost

susceptibility. The primary purpose of this model is to describe the moisture migration associated with the frost heave process, as opposed to the mechanical deformation that can only be inferred implicitly.

More recently, fully coupled thermal-hydraulic-mechanical (THM) frost heave models have been developed which extend the conceptual approach of the hydrodynamic model to include the mechanical response (Nishimura et al. 2009). Consistent with the previous model, the THM approach defines mass transport through Darcy's law. However, unlike the hydrodynamic model this approach does not consider unsaturated soils. Hydraulic conductivity of frozen soil is inferred from unsaturated conductivity through the van Genuchten (1980) function of relative permeability; where the pore ice is considered analogous to the vapour phase. The liquid water pressure is defined relative to the temperature and ice pressure through the Clapeyron expression. Ice pressure is characterized from the total stress through a stress partitioning function, identical to the functional form used in the rigid ice model and presented in equation 2.3. The equivalent effective stress is used to define elasto-plastic deformation through a modified formulation of the Cam-Clay model, providing a constitutive mechanical representation of the frozen soil. The THM model shares the same limitations as the hydrodynamics model in that it requires an accurate characterization of frozen soil hydraulic conductivity. Furthermore, the pressure partitioning function is inherently empirical and to date this concept has not been thoroughly examined in the reported literature.

As opposed to the hydrodynamic and THM models that define heave primarily through Darcy's law, the rigid ice model relates displacement of a soil to regelation (Miller 1978). Regelation is a process of continuous melting and freezing which over time causes deformation in ice bodies. In this formulation the unfrozen soil is fixed in space and pore ice moves through regelation along the temperature gradient towards colder temperatures. The relative velocity of the ice is defined relative to the temperature gradient through the following expression (Gilpin 1980):

$$v_i - v_s = -A \frac{\partial T}{\partial z} \quad (2.5)$$

where $v_i - v_s$ is the relative ice velocity and A is an empirical material property. Furthermore, mechanical equilibrium is considered between ice and liquid water through the use of a stress partitioning function, which was presented previously in equation 2.3. This function allows for the characterization of effective soil particle stress, which can then be used to define the formation of individual ice lenses, similar to the THM model. Algebraically, the rigid ice model is similar to the segregation potential concept in that frost heave is generally linearly proportional to the temperature gradient. The coupling between ice velocity and the temperature gradient is empirically characterized. Interestingly, the thermal analysis in the rigid ice model is not directly coupled with the hydraulic process as the model assumes a constant supply of available pore water. A hydraulic analysis can be conducted concurrent to the rigid ice model if the heave rate is considered to be an effective hydraulic boundary. To date, this approach is the most

common of the physically based models and since it was first presented (O’Neil and Miller 1982, Gilpin 1980; Nixon 1991; Fowler and Krantz 1994; Noon 1996).

Similar to the rigid ice model, the premelting dynamics concept assumes that frost heave is caused primarily by the relative deformation of pore ice (Rempel et al. 2004). This approach differs from other model in regards to the mechanism responsible for freezing induced potentials. Repulsive forces between the ice and the soil grains induce a net decrease in pore pressure of the liquid water films between these two interfaces. This pressure differential is temperature sensitive and under a temperature gradient induces a corresponding pressure gradient (Rempel et al. 2001). Effectively this model offers a more comprehensive physical description of the regelation induced ice velocity, as opposed to the empirical characterization in equation 2.5. Upon implementation the premelting dynamics model is algebraically similar to that of the rigid ice model (Rempel 2007).

Regardless of how physically comprehensive a frost heave model is, its practical utility will be limited to the quality and availability of the required input parameters. It is important to acknowledge that most physical models rely on simplifying assumptions or empirical characterization of certain processes. Consequently, physically derived models as a category are not inherently superior to empirically based counterparts, rather their performance depends on the details of their formulations.

2.4.3 Thermal Analysis

With the exception of freezing indices empirical approach, all of the aforementioned frost heave models are integrated with some form of thermal analysis. This requires a governing expression for the energy balance of the system. Time-dependent, conduction dominated, heat transfer in most materials can be represented by what is often referred to as the heat transport equation, which has the following basic form:

$$C \frac{\partial T}{\partial z} = \frac{\partial}{\partial z} \left(\lambda \frac{\partial T}{\partial z} \right) + Q \quad (2.6)$$

where λ refers to the thermal conductivity, C the volumetric heat capacity, and Q the external heat source/sink. When the above equation is applied to frozen soils often an additional term is introduced to account for the latent heat effects related to phase change in the pore water. Mathematically, this effect can either be accounted for through a modification of the heat capacity term, C , or through the introduction of a term defining latent heat release/absorption (O'Neill and Miller 1982, Konrad and Shen 1996, Selvadurai et al. 1999, Hansson et al. 2004, Michalowski and Zhu 2006, Nishimura et al. 2009). One potential functional form defining the modified C is as follows:

$$C^* = C - L\rho_i \frac{\partial \theta_i}{\partial T} \quad (2.7)$$

where C^* is the effective heat capacity of the material, C would be the assumed heat capacity of the soil, L is the latent heat in water, and θ_i is the volumetric ice content. The

thermal properties λ and C are typically an expression of the composite behaviour of soils. How these properties are defined varies between models. The advective heat transport and energy sink (such as work done within the system) are typically neglected in most frost heave models, with the exception of Nishimura et al. (2009). Heat transport through diffusion is ignored across all reported models.

2.5 MECHANICAL PROPERTIES OF FROZEN SOIL

Due to the presence of ice, the mechanical properties of frozen soil are significantly different from unfrozen soil. Frozen soils are complex composite materials containing three or four phases with dramatically different mechanical properties. Physical characterization of these properties can be challenging and consequently for most practical applications empirical characterizations are relied upon. Generally, ice increases the strength and stiffness of soils while at the same time introducing substantial time, strain rate, and temperature sensitivities.

The stiffness of frozen soils is dependent on the temperature and applied strain rate. More specifically, the elastic modulus increases with decreasing temperature and increasing loading rate. Zhu and Carbee (1984) proposed the following empirically derived functional form to describe the initial tangent modulus, specifically quantified as the modulus associated with 50% of peak strength, based on temperature and the applied strain rate.

$$E_{50} = w_1 \left(\frac{\dot{\epsilon}}{\dot{\epsilon}_0} \right)^{w_2} \left(\frac{T}{T_0} \right)^{w_3} \quad (2.8)$$

where $\dot{\epsilon}_0$ and T_0 are reference strain rates and temperature, respectively and w_1 , w_2 , and w_3 , are empirically determined material constants. Figure 2.5 illustrates the comparison of this expression with observed results in log-log space. In this figure θ refers to temperature which is normalized through a reference temperature.

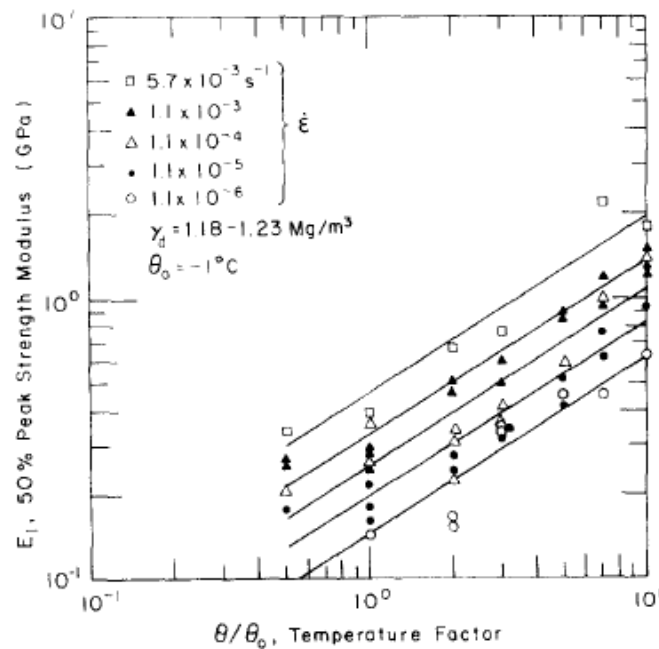


Figure 2.5: The variation of the 50% peak strength modulus with temperature and the applied strain rate for a frozen Fairbanks silt (Zhu and Carbee 1984).

Experimental observations indicate that the Poisson's ratio of frozen soils is moderately sensitive to temperature, decreasing from 0.2 – 0.4 near 0°C to 0.1 - 0.2 at -20°C (Shibata et al. 1985, Christ and Park 2009). The Poisson's ratio of polycrystalline

ice is between 0.29 – 0.32, which is generally consistent with the values of most soils (Petrovic 2003).

Frozen soils share similarities with unsaturated soils in that effective stress levels can be challenging to determine. This is due to difficulty in partitioning the pore stress between the liquid and ice phases; this partitioning is often assumed somewhat arbitrarily through empirical characterizations (see the discussion on the physical frost heave models). Consequently, the state-of-the-art analysis typically uses a total stress treatment for frozen soils (Nishimura et al. 2009).

The shear strength of frozen soils can be considered to have two components: the resistance of ice to deformation and the frictional interaction of soil grains. The first component is highly sensitive to temperature and the applied strain rate. The second component is independent of time or temperature and is primarily a function of soil fabric and the frictional characteristics of the soil grains. Considering this in the context of the Mohr-Coulomb yield criterion produces the following expression for the failure envelope.

$$\tau = c'_{(t,T)} + \sigma \tan\phi_{(t,T)} \quad (2.9)$$

Multiple functions have been proposed for both the cohesive and frictional terms in equation 2.7. For example, Vyalov and Shusherina (1970) proposed the following expression for time dependent cohesion:

$$c'_{(t)} = \frac{B_1}{\log\left(\frac{t}{B_2}\right)} \quad (2.10)$$

where B_1 and B_2 are constant material properties, which are typically empirically derived, and t is the time after loading. Alternatively, cohesion can be related to the uniaxial, unconfined compressive strength, which is a function of the soil characteristics, the volumetric composition, temperature, and the applied strain rate:

$$c'_{(t,T)} = \frac{\sigma_{uf(t,T)}}{2\sqrt{N_\phi}} \quad (2.11)$$

$$N_\phi = \frac{1 + \sin\phi}{1 - \sin\phi} \quad (2.12)$$

Multiple expressions for σ_{uf} have been developed based on experimental observations. For example, Ladanyi (1972) proposed the following function of σ_{uf} based on the applied strain rate.

$$\sigma_{uf(t,T)} = \sigma_{0(T)} \left(\frac{\dot{\epsilon}}{\dot{\epsilon}_0}\right)^{1/d} \quad (2.13)$$

where, $\sigma_{0(T)}$ is the unconfined compressive strength at a reference temperature and strain rate $\dot{\epsilon}_0$, and d is a material constant. Alternatively, a similar empirical expression relates compressive strength with temperature (Azmatch et al. 2011; Zhu and Carbee 1984; Sayles and Haines 1974):

$$\sigma_{uf(t,T)} = g_1 \left(\frac{T}{T_0} \right)^{g_2} \quad (2.14)$$

where g_1 and g_2 are empirical material parameters and T_0 is a reference temperature typically taken as -1°C . Combining both these concepts, Haines (1978) proposed a function for compressive strength for Fairbanks silt based on both temperature and strain rate:

$$\sigma_{uf(t,T)} = 7.1\dot{\epsilon}^{0.25} + 0.33T + 0.01T^2 \quad (2.15)$$

While the shear strength of frozen soils is typically expressed as a function of temperature, more accurately, the mechanical properties are dependent on the ice content, which is indirectly related to temperature. An alternate approach to describing the strength characteristics is to consider frozen soils as composite materials. Generally, confining stress has little impact on the shear strength of polycrystalline ice (Hooke et al. 1980), which indicates the internal friction angle of pure ice is approximately 0° . Therefore, as the volumetric ice content increases the long-term friction angle of a frozen soil will ultimately approach 0° . Arenson and Springman (2005) demonstrated good agreement between the following expression and the friction angle, $\phi_{(T)}$.

$$\phi_{(T)} = \phi_0(1 - \theta_i^{2.6}) \quad (2.16)$$

where ϕ_0 is the friction angle of the unfrozen soil. Figure 2.6 shows a comparison of equation 2.4 with experimental observations of a ice-rich granular permafrost.

The long-term shear strength of pure ice is influenced by both the applied strain rate and temperature. For example the unconfined compressive strength may vary between 0 and 40 MPa depending on the crystalline structure, temperature, and loading rate (Petrovic 2003). Figure 2.7 illustrates the variation of the compressive and tensile strength of ice with applied strain rate. At very low strain rates, $< 10^{-8} \text{ s}^{-1}$, ice offers very little resistance to deformation and behaves essentially as a fluid. This indicates that the cohesive strength of frozen soil will be a function of not only the ice content but also the applied strain rate and to a lesser extent the temperature.

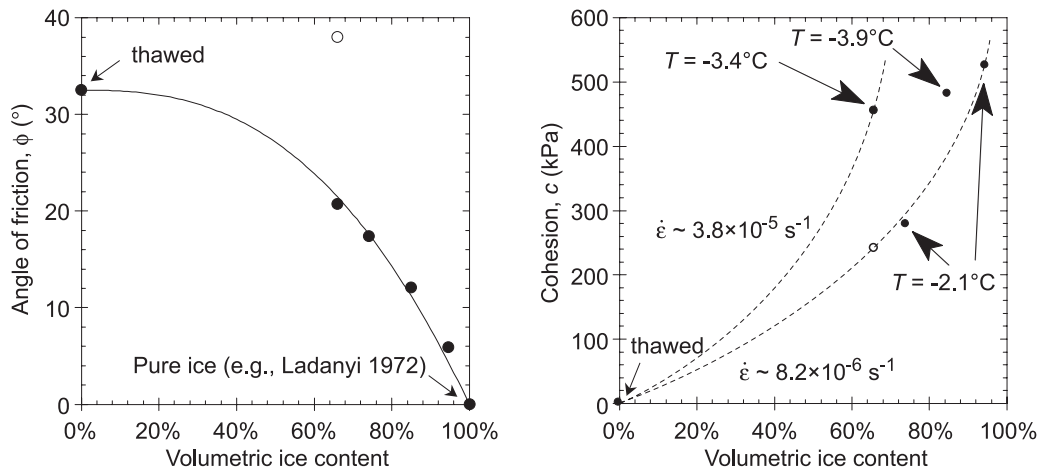


Figure 2.6: Variation in the angle of friction, ϕ , and cohesion, c , with the volumetric ice content of an ice-rich granular permafrost (Arenson and Springman 2005).

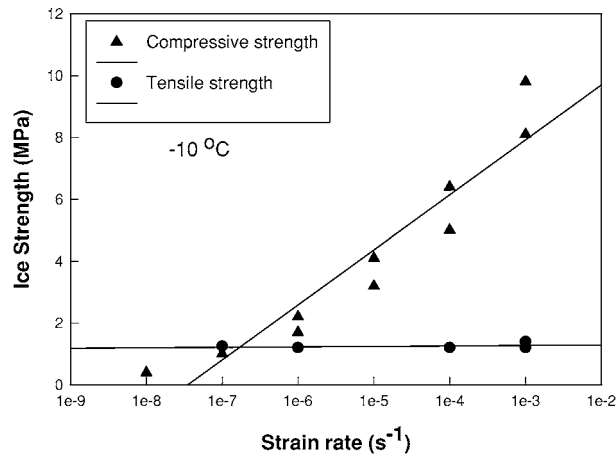


Figure 2.7: The variation in compressive and tensile strength of pure ice as a function of the applied strain rate at -10 °C (Schulson 1999).

2.6 SUMMARY AND CONCLUSIONS

Frost heave is the expansion of soil due to freezing. It is primarily caused by the formation and growth of segregated ice, also known as ice lens, with secondary contribution from the expansion of in-situ pore water upon freezing. Segregated ice forms through pore water migration caused by the development of pressure gradients, which are in turn induced by temperature gradients and the thermodynamic equilibrium requirements of ice-liquid water systems. The rate of ice lens related frost heave is influenced by both external factors and the intrinsic soil characteristics. The external factors include the temperatures, total stress, and hydraulic conditions; while the soil characteristics are primarily the frozen hydraulic conductivity and the nature of the distribution in pressure between soil grains and the pore phases. Research has shown that temperature gradients are positively correlated with the heave rate while the stress level is negatively correlated. The susceptibility of a soil to heave is influenced by the particle

size distributions, with fine grained soils, particularly silts, displaying the greatest infinity for frost heave.

Much of the physical and practical understanding of frost heave has been derived from laboratory experiments. These studies have relied on 1D thermal boundary conditions to induce heave in cylindrical soil samples. Several full-scale frost heave studies have been reported, which have typically examined the complex soil-structure interactions that cannot be examined in laboratory scale tests.

Different numerical models have been proposed to characterize the frost heave process. These models are broadly categorized as either empirically or physically derived. These models vary widely in both their level of sophistication and in their objectives. While the physical models are more comprehensive, they still rely on assumptions or empirical characterizations of sub-processes associated with frost heave.

This chapter also reviewed the mechanical properties of frozen soils. Polycrystalline ice is highly susceptible to time-dependent deformation, i.e. creep behaviour. Due to the presence of ice, the mechanical properties of frozen soils become sensitive to both temperature and the strain rate. Colder temperatures and higher strain rates are generally associated with greater stiffness and shear strength. Due to challenges and uncertainty associated with the partitioning of pore pressure between the ice and liquid water phases, total stress treatments are typically utilized over effective stress analysis in frozen soils.

CHAPTER 3 EXPERIMENTAL FROST HEAVE INVESTIGATION

3.1 INTRODUCTION

The objective of the experimental investigation is to examine the physical processes associated with frost heave and characterize them for the purposes of engineering design and analysis. Volumetric change and internal pore water migration are the principal frost action manifestations considered. Frost heave is primarily characterized in this study through the segregation potential concept, as it is conceptually simple to use and has gained wide spread acceptance.

3.2 EXPERIMENTAL METHODOLOGY

One-dimensional freezing tests were used to induce and examine the frost heave in fine grained soils. This approach allows for explicit control of the thermal, stress, and hydraulic boundary conditions.

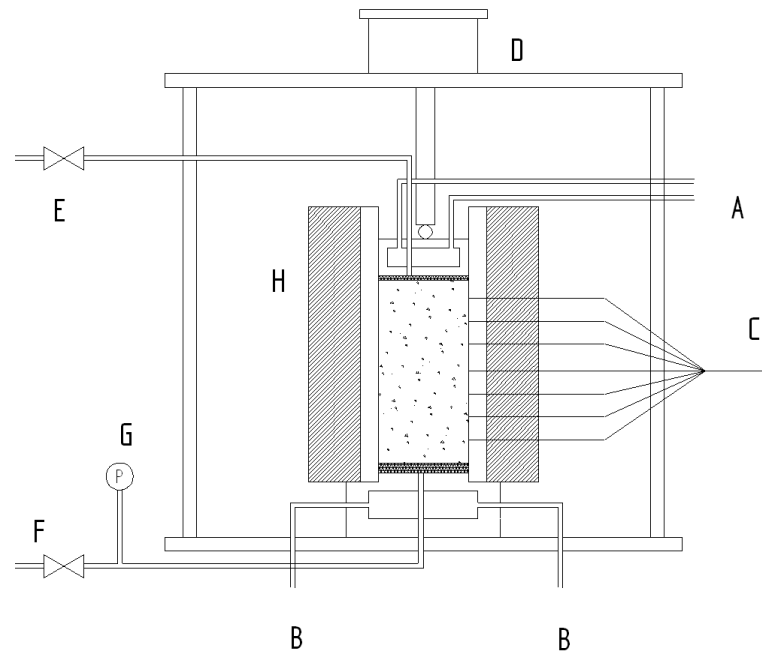
3.2.1 Description of the Experimental Apparatus

The frost heave test apparatus used in this study is illustrated schematically in Figure 3.1. Each sample is contained in a cylindrical Polyoxymethylene split-mould 25 mm thick with an inside diameter of 99.5mm and height of 300 mm. Freezing conditions are imposed through two aluminum heat exchangers one located at the top and the other at the bottom of the soil column. The temperatures in the heat exchangers are controlled through a combination of circulating an ethylene glycol-water solution. The glycol-water mixture is stored at approximately -30°C and the circulation rate for each exchanger is

controlled by thermal control units that allow for a specified temperature within $\pm 0.05^{\circ}\text{C}$. Two O-rings and silicone grease create a seal between the top heat exchanger and the inner walls of the split-mould, which allows for free axial movement similar to a piston. The bottom exchanger is fixed and sealed to the mould with silicone glue. The top plate is connected through a ball bearing and loading ram to a compressed air powered bellofram, allowing for uniaxial loading of the sample. Pore stones are positioned between the heat exchangers, and the soil sample and are connected to external water supply lines. During freezing the water supply line from the top of the sample (the cold end) is closed and the bottom line is connected to an external reservoir and a pore pressure transducer. A volume cell transducer acts as the external water supply reservoir, allowing for the continual measurement of water uptake or expulsion volumes. The bottom supply line passes through the heat exchange mechanism. When the water enters the soil it is assumed to be equal to the bottom thermal boundary condition.

In order to minimize lateral heat flow, the outside of the cell is wrapped in 57mm of flexible foam rubber insulation providing a total R -value, thickness of the insulation divided by its thermal conductivity, of approximately $1.93 \text{ m}^2 \cdot \text{K} \cdot \text{W}^{-1}$. Furthermore, the test apparatus, including the water reservoir, is located in a thermally controlled chamber with a maintained ambient air temperature between 3 and 6 $^{\circ}\text{C}$. The mould is instrumented with seven thermocouples, with a theoretical precision of $\pm 0.05^{\circ}\text{C}$, positioned vertically and spaced 25mm apart starting at 25mm from the bottom porous stone. Thermocouples are selected over more precise thermistors or RTDs due to their perceived durability. Side friction between the soil sample and the mould is minimized by

constructing the mould out of Polyoxymethylene, which has frictional properties comparable to Teflon, and by coating in the inside wall with lithium grease.



(A&B) Coolant lines to the top and bottom heat exchanges respectively; (C) Thermocouples; (D) Compressed air powered belofram; (E&F) Water and drainage lines; (G) Pressure transducer; (H) Insulation.

Figure 3.1: Frost heave test apparatus schematic.

3.3 MATERIALS AND SAMPLE PREPARATION

Two soils were examined in the frost heave tests, a lean clay referred to as FHC and a sandy silt referred to as BSM. Table 3.1 outlines the properties of the two materials and Figure 3.2 illustrates the respective particle size distributions. Based on their characterization, both soils are expected to be frost susceptible.

Table 3.1: Soil properties

	FHC	BSM
USCS Classification	CL – Lean clay with sand	ML – Sandy silt
Liquid Limit, %	29.5	18.7
Plastic Limit, %	20.0	17.5
Plasticity Index	9.5	1.2
Sand (%) (0.075-2mm)	19.5	49.5
Silt (%) (0.005-0.075mm)	60.5	34.5
Clay (%) (<0.005mm)	20.0	16.0
Specific Gravity	2.60	2.73
Initial Void Ratio	0.381 - 0.389	0.522 - 0.537

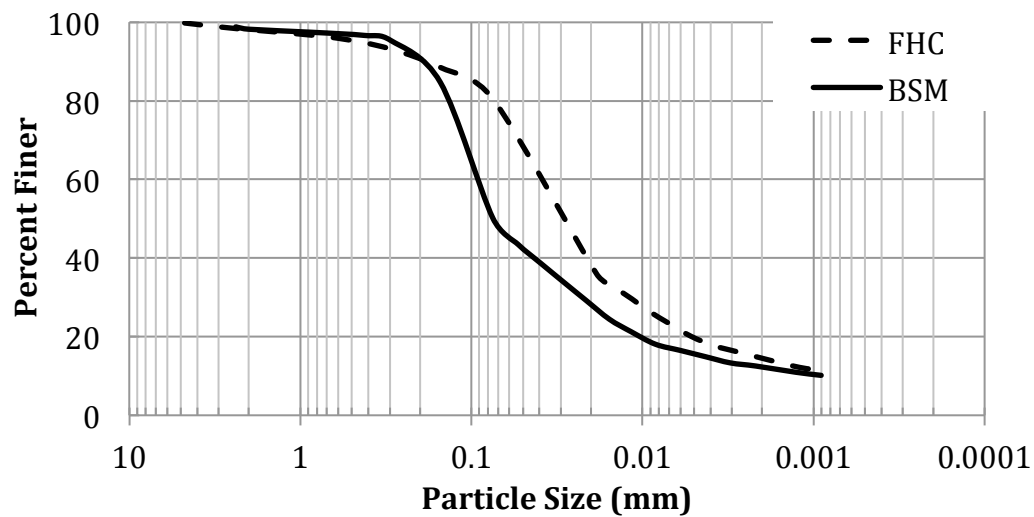


Figure 3.2: Particle size distribuion of the two examined soils.

Different sample preparation techniques were used to prepare the soil specimens.

The sandy-silt samples (BSM) were produced through the consolidation of a saturated

slurry. Dry soil was first mixed with de-aired water to produce a slurry with a water content of 35%, approximately twice the liquid limit of the soil. The slurry was put into a chamber under an 80 kPa vacuum for approximately 2 hours to minimize any trapped air. Next, the slurry was poured into the mould of the frost heave test apparatus and consolidated axially using the loading bellofram at a consolidation pressure of 100 kPa while allowing for drainage from both ends. Based on the recorded displacement of the consolidation of the sandy-silt, the soil has a coefficient of consolidation between $9.0 - 5.3 \times 10^{-3} \text{ cm}^2/\text{s}$ and required approximately 36 to 48 hours to fully consolidate. Next the samples were unloaded to the desired testing overburden pressure and allowed to rebound for 24 hours. The BSM samples prepared through this were considered fully saturated with a void ratio between 0.52 – 0.54.

The lean clay samples (FHC) were produced through moist compaction. The clay was compacted in the testing mould at 8 % moisture content with a standard proctor hammer using 5 lifts of 20 blows each. After compaction the samples were placed in the testing frame and additional pore water was introduced into the sample from the bottom. A positive 100 kPa pressure was applied to the de-aired water supply at the base and a suction of approximately 80 kPa was applied to the top. The loading ram applied an additional 100 kPa surcharge concurrently. The water supply and water pressure gradient were maintained for approximately 24 hours. Like the BSM samples, the compacted samples were consolidated to 100 kPa and then unloaded to the testing overburden pressure and allowed to rebound for 24 hours. The moist compaction and subsequent bottom-up flushing technique was necessitated by the low intrinsic permeability of the

FHC material, as consolidation of a 200 mm long sample of this material was prohibitively time consuming. Volumetric analysis of the prepared samples indicate this preparation technique yielded samples with a degree of saturation in the range of 80 - 90%. The initial void ratio was between 0.38 - 0.39.

3.4 EXPERIMENTAL PROGRAM

The testing program consisted of both step and ramped-freezing boundary conditions on FHC and BSM soils. The primary variables of interest were the overburden stress, rate of freezing, type of boundary condition, and the material influence on the frost heave response, particularly on the observed segregation potential. The testing program did not explore in detail the relationship between the thermal gradient and the heave response as this influence is well established in the reported literature (Konrad and Morgenstern 1981). Tables 3.2 and 3.3 outline the testing program for both materials.

Table 3.2: Step-freezing testing matrix.

Test Name	Material	Overburden (kPa)	Initial Temp (°C)	Top Temp (°C)	Bottom Temp (°C)	Approximate Duration (hrs)
FS-3	FHC	20	5.5	-2.0	4.2	110
FS-7	FHC	15	4.0	-2.5	3.0	120
FS-8	FHC	45	4.0	-2.5	3.0	120
FS-9	FHC	125	4.0	-2.5	3.0	120
FS-10	FHC	75	4.0	-2.5	3.0	120
BS-1	BSM	20	4.5	-3.0	3.2	212
BS-2*	BSM	20	4.5	-3.0	3.2	72
BS-3*	BSM	20	4.5	-3.0	3.2	212

*Note: BS-4 and BS-5 were conducted without an external water supply.

Table 3.3: Ramped-freezing testing matrix.

Test Name	Material	Overburden (kPa)	Temperature Gradient (°C/m)	Rate of Cooling (°C/hr)	Approximate Duration (hrs)
FR-1	FHC	20	20.0	0.018	220
FR-2	FHC	20	20.0	0.027	165
FR-3	FHC	20	20.0	0.036	110
BR-1	BSM	20	20.0	0.072	55
BR-2	BSM	20	20.0	0.036	110

Once samples were prepared and consolidated, the initial thermal boundary conditions were applied. For step-freezing tests initial temperatures were constant throughout a sample, see Table 3.2, while for ramped-freezing the testing thermal gradient was first imposed, Table 3.3. For all tests, the initial temperatures exceeded the bulk freezing point. Once steady-state was reached under the initial conditions (approximately 24 hours) the test boundary conditions were imposed. Step-freezing involved an initial uniform sample temperature followed by quickly applied, then constant boundary temperatures. Under ramped-freezing conditions a constant thermal gradient with linearly varying temperatures was utilized. Once an initial thermal gradient was established, with temperatures throughout the sample above freezing, both boundary temperatures decreased linearly at the same, constant rate. Ramp durations typically ranged between 1 to 5 days, depending on the desired freezing rate. The temperature along the length of the sample, the warm-end pore pressure, water uptake, and the displacement of the top heat exchanger were monitored and recorded every 2 minutes.

3.5 TEST RESULTS

Under the imposed thermal conditions all samples tested displayed significant volumetric expansion. This expansion was well in excess of the theoretical limit associated with the phase change of the pore water, which is therefore attributed to the formation of segregated ice owing to water migration. This conclusion was supported by visual inspection of the frozen soils upon test completion. Figure 3.3 shows the growth of an ice lens in the middle of a sample under step-freezing conditions. In the figure the imposed boundary conditions were identical between tests and the only differentiating parameter was the freezing duration. The three distinct regions during frost heave are also illustrated in the figure: frozen, unfrozen, and the fringe transition zone between the two.

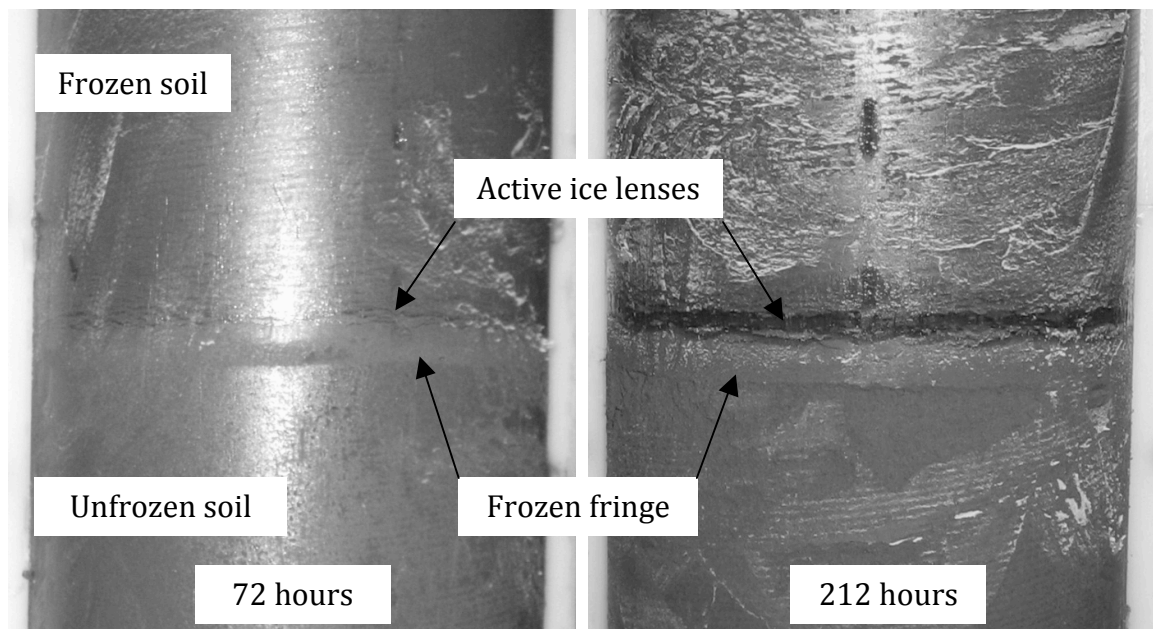


Figure 3.3: Ice lens formation at 72 and 212 hours of freezing for BS-2 and BS-3, respectively.

Comprehensive results of the testing program outlined in Tables 3.2 and 3.3 are presented in Appendix A. This chapter presents only select findings and observations relevant to the discussion and analysis contained herein.

3.5.1 Thermal Boundary Conditions

Figure 3.4 illustrates the measured thermal profile and heave response of FS-3, a step-freezing test conducted on an approximately 200 mm long FHC sample at an overburden pressure of 20 kPa. This sample displaced approximately 6.2 mm over a period of 110 hours. These results are typical of the heave response of FHC under step conditions, where initially there is a large rate of displacement, and then once the thermal gradient within the sample stabilizes, the heave rate drops substantially. Surface heave was determined through measurement of the axial displacement of the cold-end heat exchanger. It was assumed that K_0 conditions applied, i.e. without lateral deformation axial displacement is directly correlated to volumetric expansion. In addition, the volume of water uptake of the sample was also used to infer the axial displacement based on the cross sectional area. Assuming a constant saturation in the unfrozen soil, the uptake volume divided by the cross sectional area, and increased by 9%, indicates the ice lens thickness and the frost heave. Small discontinuities in the uptake-implied displacement time history are attributed to minor adjustments made to the reservoir back-pressure during testing. As illustrated in the results, the implied and directly measure heaves do not perfectly correlate. This was attributed to due to imperfect saturation of the samples.

The maximum theoretical heave possible due to in-situ pore water expansion is included in Figure 3.4. This was determined as the length of the sample below the bulk freezing point multiplied by the average sample porosity, assuming 100% saturation, and the 9% expansion associated with water freezing. The figure clearly demonstrates the contribution of segregated ice formation to the frost heave expansion. The small, short duration increase in temperature recorded by the 175 mm thermocouple is attributed to supercooling of the pore water. This will be discussed in more detail latter.

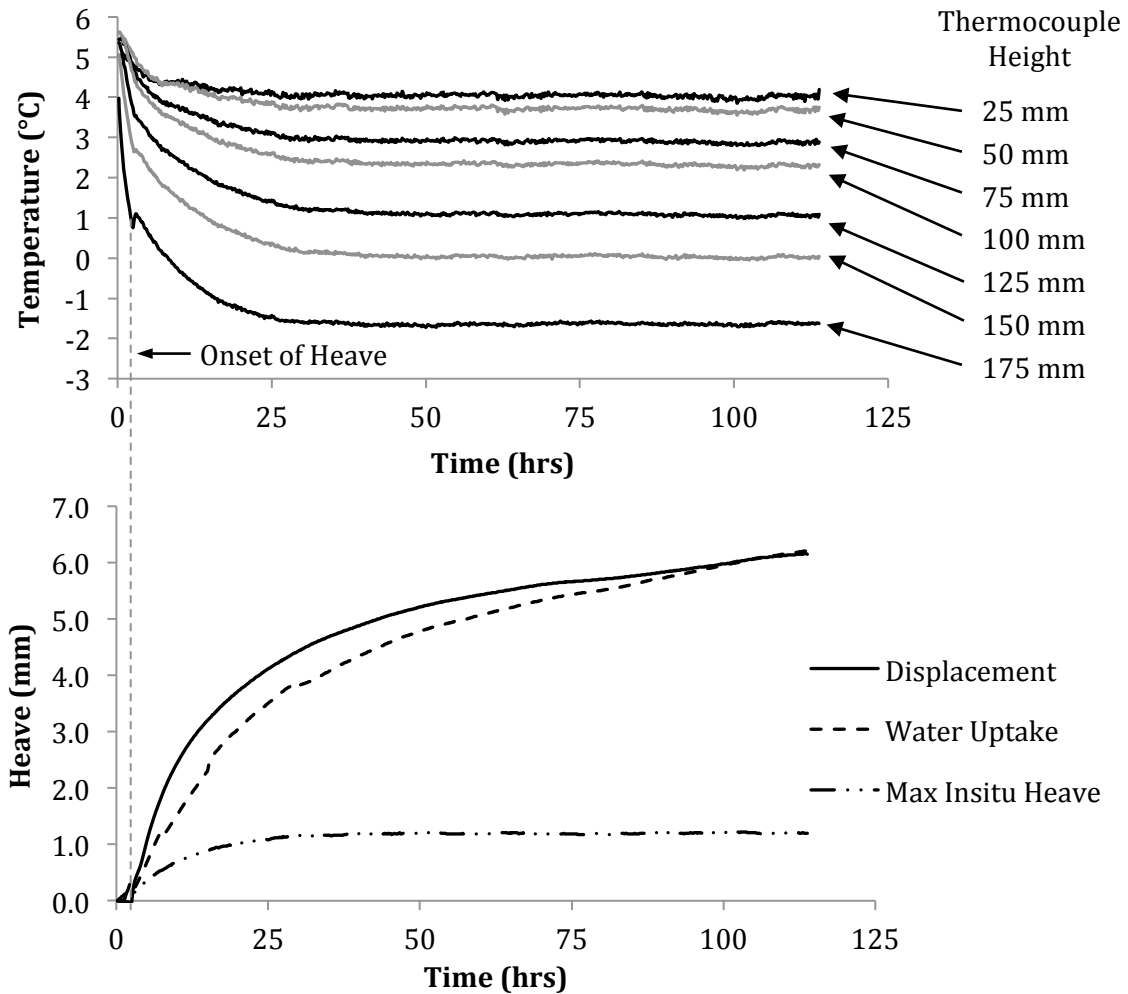


Figure 3.4: The observed temperature profile and surface heave during step freezing of FS-3, corresponding to FHC, $\sigma_0 = 20.0$ kPa, $T_{initial} = 5.5$ °C, $T_{min} = -2.9$ °C, $T_{max} = 3.8$ °C.

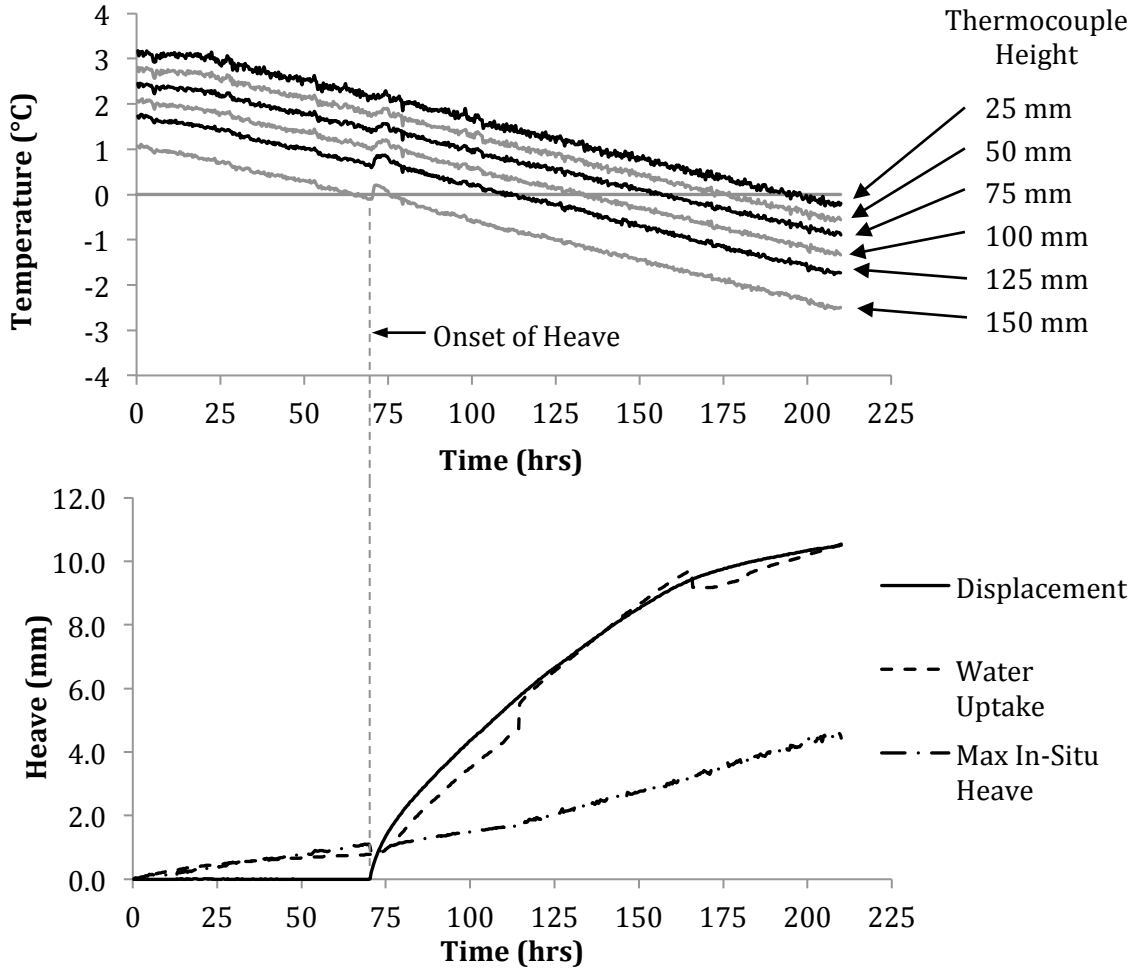


Figure 3.5: The observed temperature profile and surface heave during ramped-freezing of FR-1, corresponding to FHC, $\sigma_0 = 20.0$ kPa, $dT/dz = 20.0$ °C/m, $dT/dt = 0.018$ °C/hr.

Figure 3.5 illustrates the results of a ramped freezing test on the same materials, FR-1; both FS-3 and FR-1 were performed under the same overburden pressure of 20 kPa. The results of this particular test exclude the recorded values of one thermocouple, positioned at 175 mm, because of the damage it sustained prior to initiating the test. Similar to FS-3, the observed displacement is well in excess of the primary frost heave. It

should be noted that the cold end of the sample was below the bulk freezing point shortly after the initiation of the test which does not correspond to the onset of expansion, occurring at approximately 70 hours.

The results of FS-3 and FR-1 illustrate an interesting physical phenomenon in laboratory-scale frost heave tests, particularly in the ramped freezing tests: the supercooling of pore water and the subsequent delay in the onset of frost heave. In the illustrated results of the ramped-freezing test FR-1, the recorded temperatures show that the recorded temperature at the 150 mm position decreases below the bulk freezing point prior to any recorded volumetric expansion in the soil. The lack of volume change indicates approximately 50 mm of the sample, or ~25%, was cooled below freezing without a phase change in the pore water. The recorded temperature profiles of both tests (see Figures 3.4 and 3.5) show a single discrete and short-lived increase in soil temperature, specifically near the cold end, which correlates to the time of the onset of surface displacement. The simultaneous occurrence of these events indicates a sudden phase change of pore water at temperatures below the bulk freezing point, the temperature spike is caused by the release of latent heat. Depending on the specific soil freezing characteristic and based on the volume of the sample below the bulk freezing point, this temperature spike corresponded to a release of approximately 13.4 and 16.7 kJ for FS-3 and FR-1 respectively. A more dramatic illustration of this temperature spike can be found in the temperature profile of ramped test FR-3, presented in Figure 3.6.

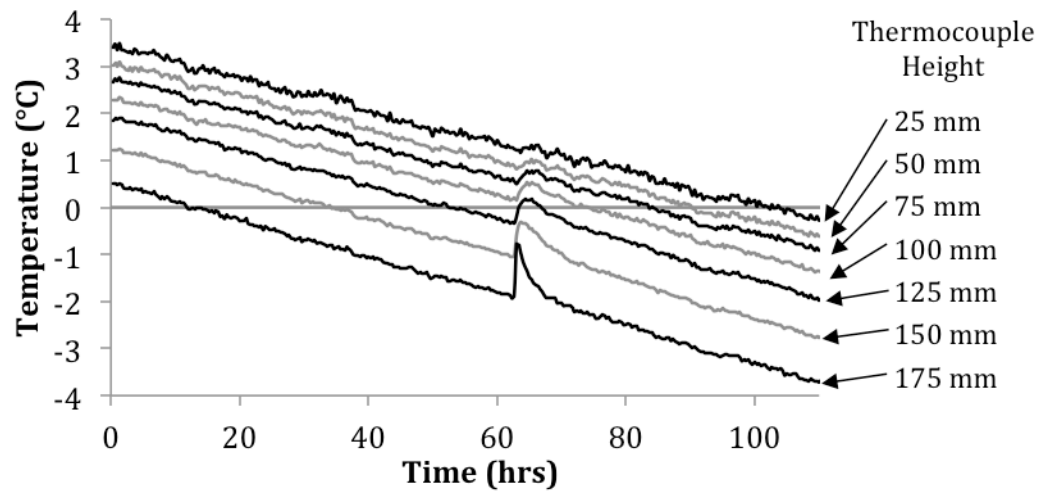


Figure 3.6: Temperature profile of FR-3, FHC tested under ramped conditions.

The existence of liquid supercooled pore water in fine-grained soils is observed at temperatures as low as $-25\text{ }^{\circ}\text{C}$ (Koopmans and Miller 1966). Ice is generally a crystalline material requiring nucleation to form and grow. In fine grained soils, water adheres to large soil-water interfacial areas or confined to small pores, that discourage the formation of seed crystals and ultimately decrease temperature required for nucleation (Kozlowski 2009). After the onset of nucleation, the volume of liquid pore water is formed to be consistent with the soil-water characteristics, the relationship between liquid water and temperature inherent to soil fabric. Unfortunately the collective test results did not provide insight into the characterization of the nucleation process as heave initiates at varying temperatures, thermal gradients, and freezing rates, resulting in varying magnitudes of observed temperature spikes.

3.5.2 Material Comparison

The frost heave responses of the two materials examined in this study (the sandy-silt BSM and the lean clay with sand FHC) are compared under consistent thermal gradients applied through step freezing and ramped freezing type boundary conditions. Figures 3.7 compares the frost heave displacement under step conditions with the same thermal gradient, but slightly different thermal boundaries. Likewise Figure 3.8 compares the frost heave response under identical ramped freezing conditions. Generally, BSM displayed significantly greater affinity for frost heave as compared to FHC under the same thermal boundary conditions. After 110 hours under the applied step conditions, total displacements were approximately 11.0 mm and 6.2 mm for BSM and FHC, respectively.

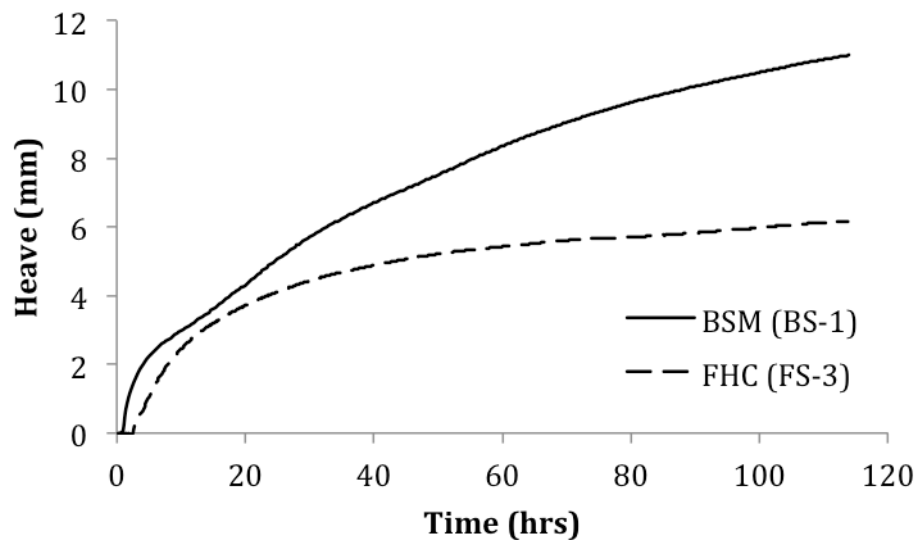


Figure 3.7: Comparison of the observed displacement between step tests on FHC (FS-3) and BSM (BS-1). For both tests $\sigma_0 = 20.0$ kPa, $T_{min} = -2.9$ °C, $T_{max} = 3.8$ °C.

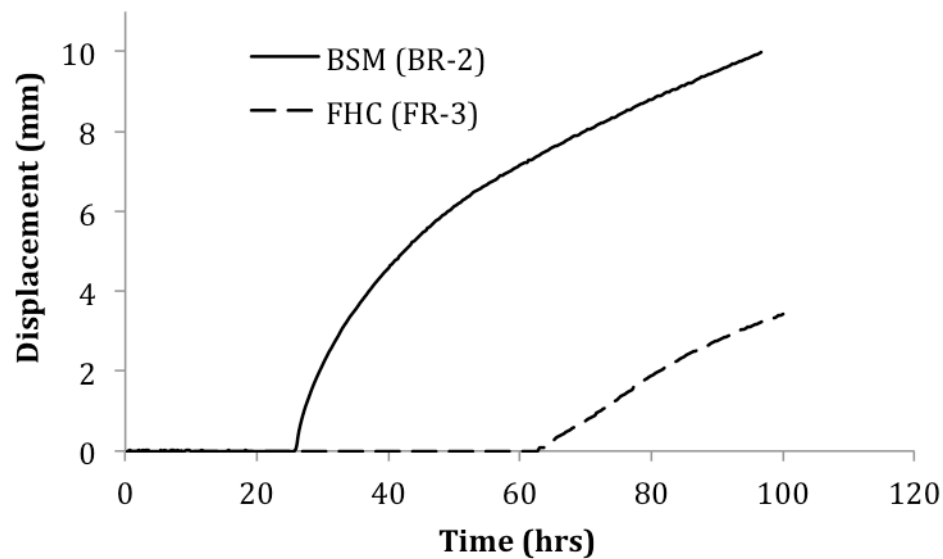


Figure 3.8: Comparison of the observed displacement between the ramped tests on FHC (FR-3) and BSM (BR-2). For both tests $\sigma_0 = 20.0$ kPa, $dT/dz = 20.0$ °C/m, $dT/dt = 0.036$ °C/hr.

It is observed in Figure 3.8 that after 100 hours under ramped conditions, the deviation in heave response between the two materials is substantial, with total heave of approximately 10.0 mm and 3.4 mm for BSM and FHC, respectively. The results of the ramped-freezing tests in Figure 3.8 demonstrate a significant difference in the time of the initiation of frost heave; heave initiated at approximately hour 25 for BSM and 63 for FHC. This difference significantly influenced the total observed sample displacement. After initiation, there was less variation in heave rates between 80 – 100 hours: 0.071 and 0.059 mm/hr for BSM and FHC respectively. It should be noted that the duration of ramped frost heave tests are dictated by the gradient and cooling rates imposed, and it is impossible to extend the test duration.

The perceived difference in frost susceptibility between BSM and FHC may be due to either the intrinsic characteristics of the materials or the prepared saturation level. The BSM samples were virtually fully saturated while the degree of saturation of the FHC samples varied between 80 – 90%. Soil saturation has been demonstrated to be positively correlated with observed frost susceptibility (Miller 1972).

3.5.3 Segregation Potential

Segregation potential (SP) is a widely employed descriptive concept of frost heave. As discussed in Chapter 2, the approach characterizes the water flux, q , supplying the active ice lens (which is proportional to the rate of frost heave) is related to the local thermal gradient, $\frac{\partial T}{\partial z}$, by:

$$q = SP \frac{\partial T}{\partial z} \quad (3.1)$$

Contrary to its conception as a constant material property, SP can in fact vary significantly during freezing. This effect was acknowledged by the original authors who carefully defined how experimental data should be interpreted so as to allow for universal comparisons of values (Konrad 1987). Specifically, SP should be calculated from step-freezing tests when the rate of cooling approaches zero, $\frac{\partial T}{\partial t} \rightarrow 0$. However, to further explore this concept the apparent SP was determined continually throughout the tests.

Segregation potential was calculated based on two different soil responses: surface displacement and water uptake. While strictly SP is defined in terms of water flux through the frozen fringe, this value cannot be measured directly and must be inferred

from either the recorded water flux entering the warm end of the sample (Equations 3.2 - 3.3) or the surface displacement (Equations 3.4 - 3.5).

$$v_{(t)}^U = \frac{V_{(t-\Delta t)} - V_{(t)}}{A\Delta t} \quad (3.2)$$

$$SP^U = \frac{v_{(t)}^U}{\nabla T_{(t)}^f} \quad (3.3)$$

$$v_{(t)}^H = \frac{h_{(t)} - h_{(t-\Delta t)}}{1.09\Delta t} \quad (3.4)$$

$$SP^H = \frac{v_{(t)}^H}{\nabla T_{(t)}^f} \quad (3.5)$$

where in the above equations v refers to the water flux, h the sample height, V the water reservoir volume, A the cross-sectional area of the testing specimen, and $\nabla T_{(t)}^f$ the thermal gradient of the frozen fringe, which is computed from the recorded temperature profile. The superscripts H and U refer to the surface heave and water uptake, respectively. In addition, the frozen fringe is assumed to be located at the 0 °C isotherm. Data was recorded on 2-minute intervals; due to measurement noise associated with the thermocouples, the thermal gradient was determined using a 20-minute moving average.

Figure 3.9 illustrates the variation in the calculated SP during a step-freezing and ramped-freezing test conducted on FHC. Under step freezing conditions, at the onset of heaving SP is the largest and then decreases exponentially, eventually reaching roughly constant values. From start to steady state, SP varies 2 orders of magnitude from

approximately 200×10^{-5} to 3×10^{-5} $\text{mm}^2/\text{°C}\cdot\text{s}$ under step conditions. Alternatively under ramped conditions the same material displayed significantly less variation in SP once heave initiates, varying from approximately 200×10^{-5} to 100×10^{-5} $\text{mm}^2/\text{°C}\cdot\text{s}$. Under both types of boundary conditions there is generally close agreement between the SP calculated from surface displacement and the water uptake. The results demonstrate that the apparent SP is not constant and instead is influenced by some additional factors, which will be discussed later in this section.

A comparison of the apparent SP values calculated from the displacement response of FHC and BSM under identical boundary conditions is presented in Figures 3.10 for step and 3.11 for ramped conditions. BSM tends to have greater apparent segregation potential when compared with FHC. If SP is considered a constant value, as defined by Konrad (1987), BSM and FHC have a SP of approximately 50 and 20×10^{-5} $\text{mm}^2/\text{°C}\cdot\text{s}$, respectively, at an overburden of 20 kPa.

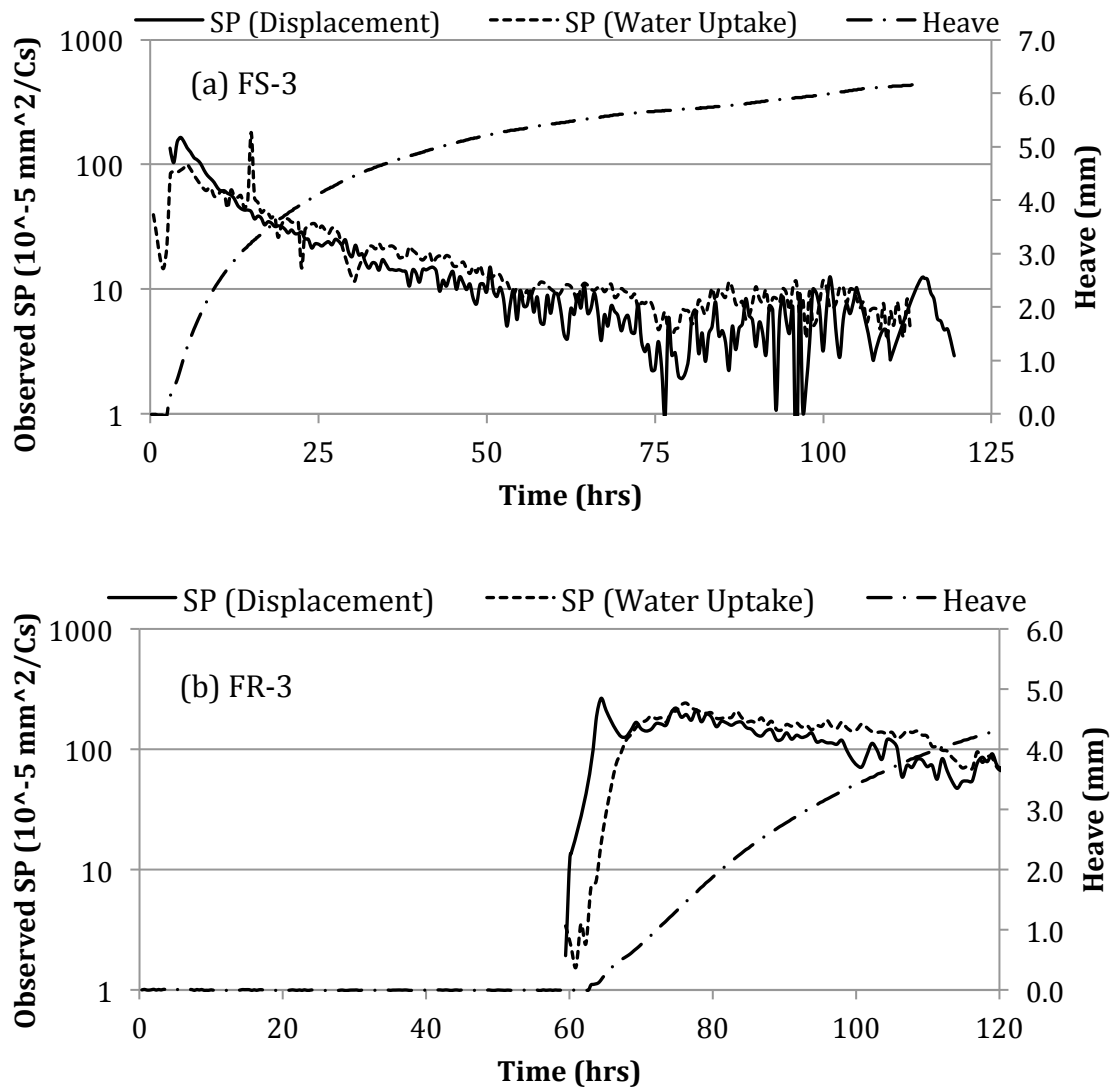


Figure 3.9: The observed SP of FHC under a step test FS-3 (a) and a ramped test FR-3 (b).

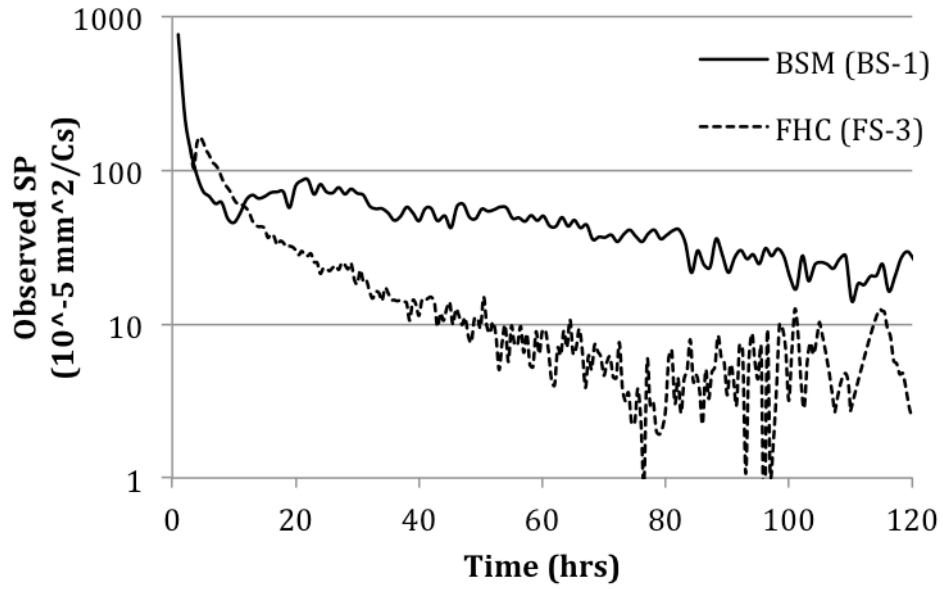


Figure 3.10: Comparison of the observed *SP* under step conditions between FHC (FS-3) and BSM (BS-1).

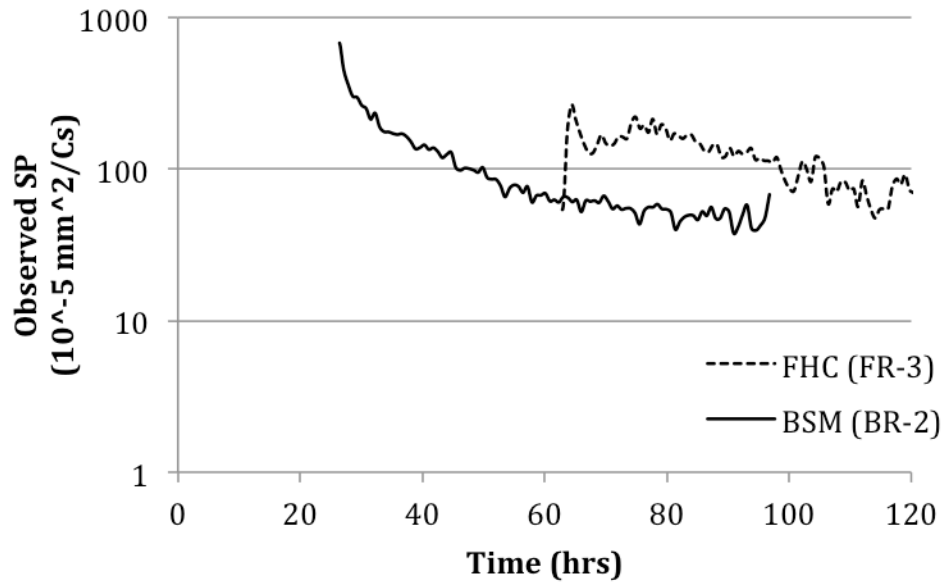


Figure 3.11: Comparison of the observed *SP* under ramped conditions between FHC (FR-3) and BSM (BR-3).

The influence of overburden stress, σ_0 , on SP is also examined for FHC under step freezing conditions. Referring to Figure 3.12 we see that SP is negatively correlated with the stress level, although the error bars are quite large. These findings are consistent with reported observations of SP behaviour (Konrad and Morgenstern 1982, Konrad and Morgenstern 1983), see Figure 6.4. An established characterization of the relationship between segregation potential and overburden stress is presented in equation 3.6 (Konrad and Morgenstern 1982).

$$SP = SP_0 e^{-b\sigma} \quad (3.6)$$

where SP is the effective segregation potential, σ corresponds to the overburden stress, and SP_0 and b are empirically determined material parameters. The units of b and σ are such that the product of the two terms is unit-less. Following this characterization, FHC is observed to have SP_0 and b values of $28.9 \times 10^{-5} \text{ mm}^2/\text{C}^*\text{s}$ and 4.95 MPa^{-1} , respectively.

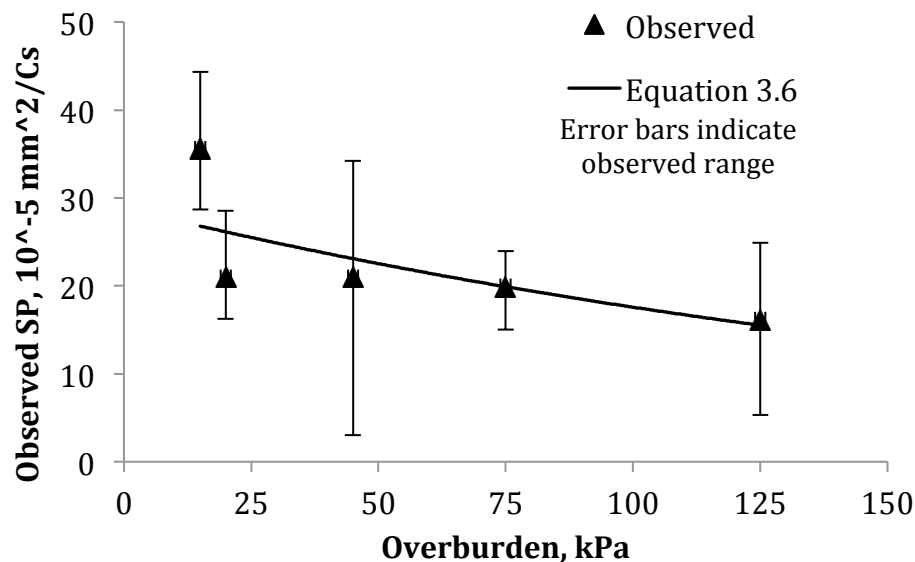


Figure 3.12: The variation in observed SP with the overburden stress for the FHC step-freezing tests.

An analysis of the variation in observed SP values indicates that SP is affected by the frost penetration rate, $\frac{\partial z_f}{\partial t}$, in addition to the overburden stress level. The frost penetration rate is defined as the velocity of the 0 °C isotherm, which is positioned at z_f in the soil while the sample is actively freezing, with $\frac{\partial T}{\partial t} < 0$. Stepped boundary conditions naturally induce a range of frost penetrations rates; initially the change in temperature is highly transient with a high penetration rate, after which it slowly stabilizes to a value close to zero. Figure 3.13 presents the variation of SP with the penetration rate for step-freezing tests conducted on FHC at four different overburden stress levels. The figure shows SP values determined from the displacement response of step-freezing tests, which induce a broad range of penetration rates and, as a result, better illustrate this effect. The results show a clear positive correlation between the penetration rate and the observed SP , which can be approximated as a linear function of the frost penetration rate. Moreover, the slope of this relation is influenced by the overburden pressure, as shown in Figure 3.14 that demonstrates that SP/\dot{z}_f varies exponentially with respect to the overburden stress.

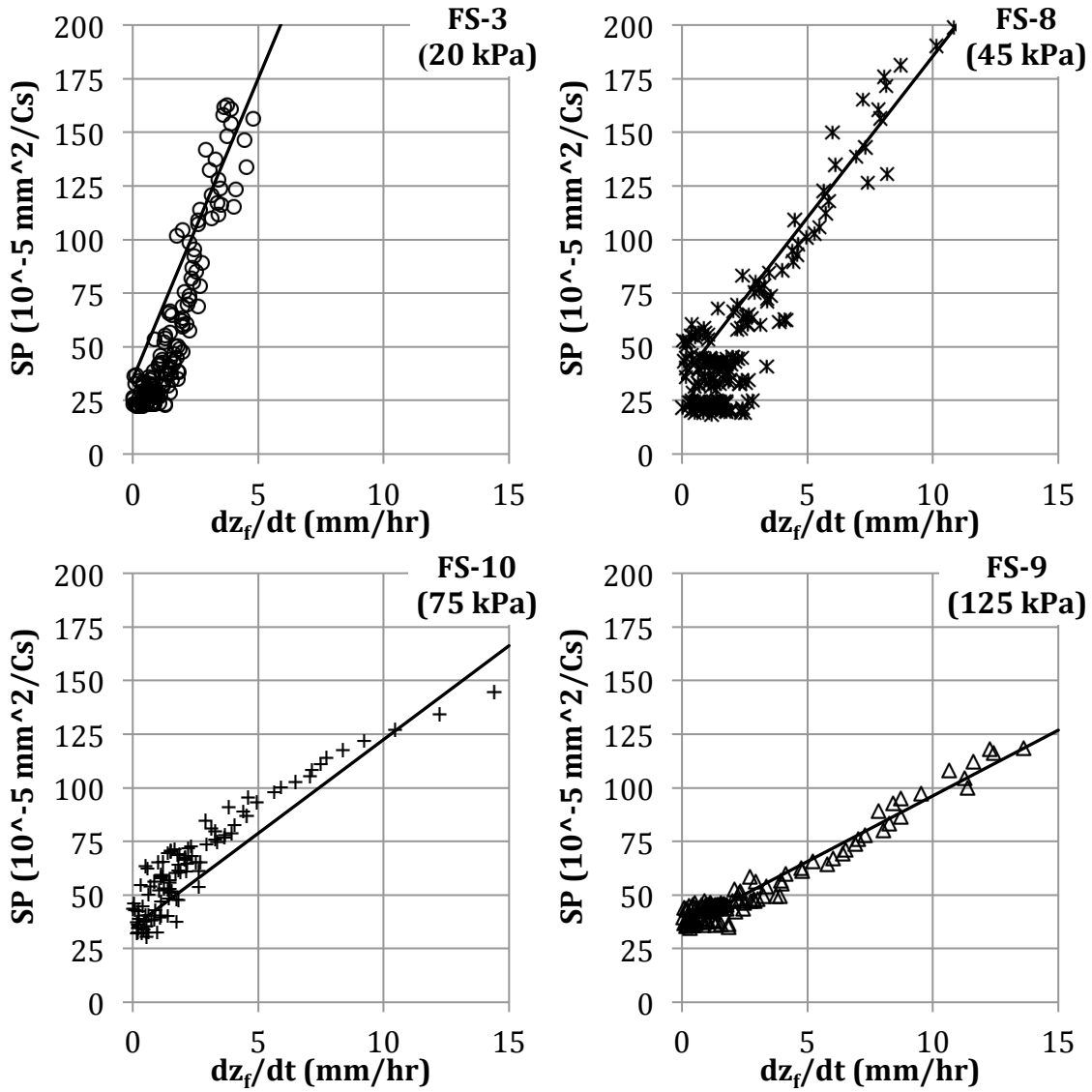


Figure 3.13: The variation of SP with the frost penetration rate for FHC under step freezing. The solid lines indicate the general observed trends.

Figure 3.15 compares the variation of the apparent SP with the frost penetration rate for FHC and BSM under step-freezing. As noted in Table 3.2, the applied temperature boundaries and overburden were constant between tests FS-3 and BS-1. Similar to FHC, a linear variation of SP with the frost penetration rate is observed for

BSM. However, the *SP* of BSM is greater than that of FHC and it is observed to be less sensitive to the penetration rate, i.e. a smaller slope in $SP - \frac{\partial z_f}{\partial t}$ space.

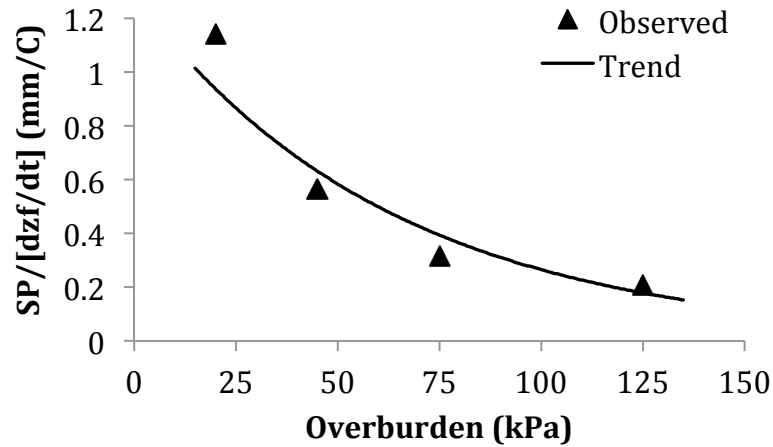


Figure 3.14: The variation of the slope of the $SP - \frac{\partial z_f}{\partial t}$ relationship of FHC with the overburden stress level, obtained from Figure 3.12.

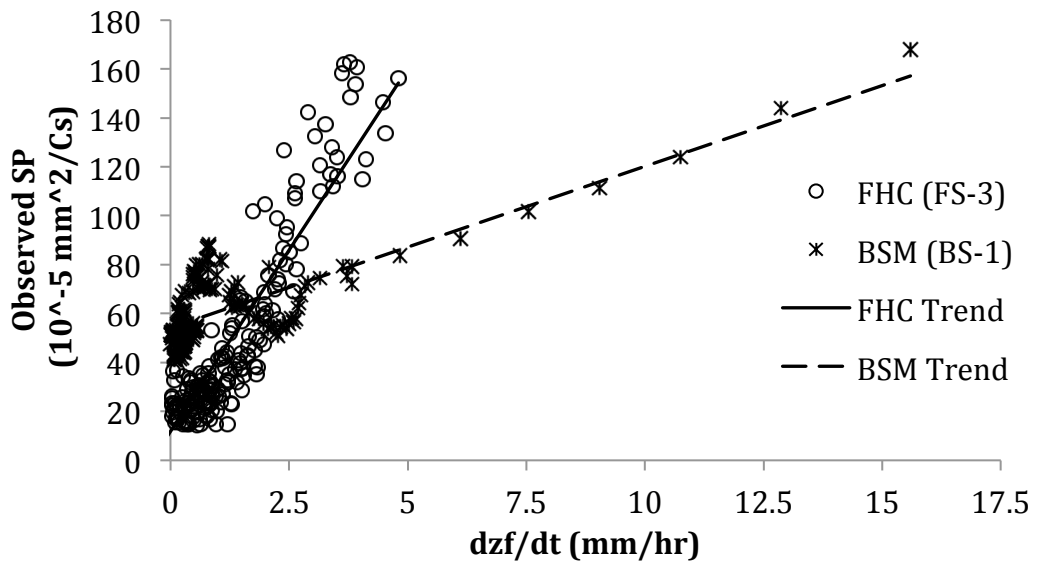


Figure 3.15: The variation of SP with the frost penetration rate of FS-3 and BS-1, which correspond to FHC and BSM.

The practical implication of these experimental findings is that the apparent segregation potential is influenced by the frost penetration rate. More specifically, at greater penetration rates, soils will exhibit a greater apparent degree of frost susceptibility. Accounting for this influence would improve frost heave predictions when using the segregation potential concept in cases of highly transient freezing conditions.

While it was previously noted that the variation in SP has been recognized in the reported literature, there has been a limited effort to characterize it. One approach, however, has been proposed by Kim (2011) to characterize the variation in SP based on the rate of cooling, which is similar to the frost penetration rate and defined as the rate of temperature change of the frozen fringe (Konrad and Morgenstern 1982). Practically, this influence is partially accounted for through defining SP at a specific cooling rate (Konrad 1989a; Konrad 1987). Kim (2011) proposes the following expression to characterize SP relative to the rate of cooling of the frozen fringe:

$$SP = SP_m \left(\frac{\dot{T}_f + \dot{T}_0}{\dot{T}_m + \dot{T}_0} \right)^2 \exp \left(1 - \left(\frac{\dot{T}_f + \dot{T}_0}{\dot{T}_m + \dot{T}_0} \right)^2 \right) \quad (3.7)$$

where SP_m is the maximum observed SP , \dot{T}_f is the cooling rate, \dot{T}_0 and \dot{T}_m are a series of reference cooling rates. Kim's empirical expression is derived from observed SP , which differs somewhat with the observations reported herein. Although Kim observed a variable SP , he reported a larger delay in the onset of heaving and lower initial SP values under step freezing conditions.

Based on the observed behaviour presented herein, the following expression is proposed to characterize SP relative to the frost penetration rate:

$$SP = SP^* \left(1 + \beta \frac{\partial z_f}{\partial t} \right) = SP^* \left(1 + \beta \left(\frac{\partial T}{\partial t} \right)_f \left(\frac{\partial z}{\partial T} \right)_f \right) \quad (3.8)$$

where SP^* is the segregation potential at a zero frost penetration rate associated with a particular overburden stress. The parameter β is the slope of the relation between apparent SP and the frost front advance rate, $\frac{\partial z_f}{\partial t}$, as illustrated in Figures 3.10 and 3.13. As noted above, the frost front advance rate can alternatively be defined as the cooling rate of the frozen fringe divided by the local temperature gradient. Figure 3.14 indicates that β varies with the stress level exponentially, similar to the variation of SP with overburden. Consequently, both the frost penetration rate and stress sensitivities can be described by a single expression.

$$SP = SP_0 \left(1 + \beta \frac{\partial z_f}{\partial t} \right) e^{-b\sigma} \quad (3.9)$$

here SP_0 is the apparent SP associated with a constant frost front position and no overburden stress. Table 3.4 summarizes the frost heave characterizing parameters observed for the two materials examined. Ultimately, the proposed modifications to the SP concept extend this observational approach to better account for the many factors influencing the very complex thermodynamic and hydraulic processes during ice lens growth.

Table 3.4: The frost heave characterizing parameters from equation 3.8 observed for FHC and BSM.

Material	SP_0 (10^{-5} mm ² /°C*s)	β (10^3 s/mm)	b (1/MPa)
FHC	22.0	3.64	4.95
BSM	26.5	5.95	N/A

Note: The b was not determined for BSM in this study.

3.5.4 Influence of the Hydraulic Boundary Conditions

The effect of the hydraulic boundary conditions on the frost heave response was briefly explored in this work. In the frost heave process, internal suction forms near the frost fringe that results in pore water flow in the adjacent unfrozen soil, supplying the water for the growth of the active ice lens. The suction is induced by both the increased surface tension due to the temperature, and the equilibrium requirement according to the Clapeyron equation. The magnitude of this flow, or flux, ultimately dictates the frost heave rate. In addition to the suction at the ice lens, the pore pressure in the unfrozen soil will influence this hydraulic gradient. The implication of this with respect to the experimental frost heave tests is the greater the pore pressure at the warm end, which supplies water to the system, the greater the rate of frost heave. Previously reported laboratory studies (Konrad 1994; Eigenbrod et al. 1996) have demonstrated this influence in step-freezing tests.

The influence of hydraulic boundary conditions on frost heave is investigated in two step-freezing frost heave tests on BSM, BS-2 and BS-3, were conducted under the same thermal and mechanical boundary conditions as BS-1. Unlike BS-1, both BS-2 and

BS-3 were conducted without an external pore water supply, which was achieved by closing the valve for the water supply during testing. The duration of freezing for BS-2 and BS-3 was 72 and 212 hours, respectively. Without an external water supply, ice lens growth is only possible through the extraction of pore water from the adjacent unfrozen soil. The pore pressure at the warm sample end was continuously monitored throughout the tests using a pressure transducer on the water supply line. Upon completion the moisture content in the unfrozen zone was measured.

Figure 3.16 presents the displacement response of BS-1 (with an external water supply), BS-2, and BS-3 (without a supply). Samples without an external water supply displayed less total heave than with a supply. At hour 212, the total displacements of BS-1 and BS-3 were 13.2 and 10.7 mm respectively. After 50 hours, however, the rate of heave was very close in all three tests as shown in the figure. Likewise the apparent SP of the three tests converged after approximately 50 hours, as illustrated in Figure 3.17. Up to hour 72 the displacement response is notably consistent between BS-2 and BS-3, which indicates an adequate degree repeatability of the step freezing tests in general. The results show that even without an external water supply ice lenses can still form and grow through the redistribution of pore water from adjacent unfrozen soil.

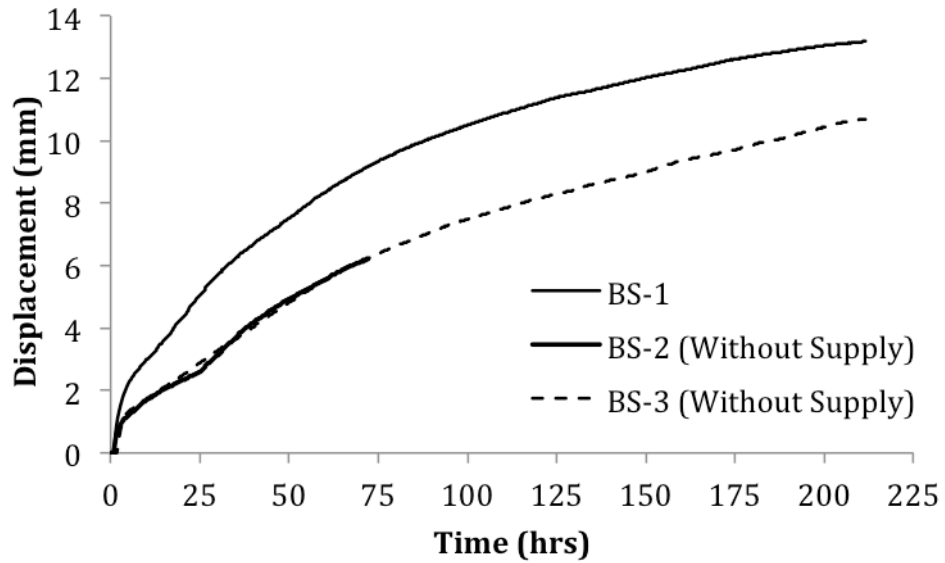


Figure 3.16: The displacement response of BSM under step freezing with an external water supply (BS-1) and without an external water supply (BS-2 and BS-3).

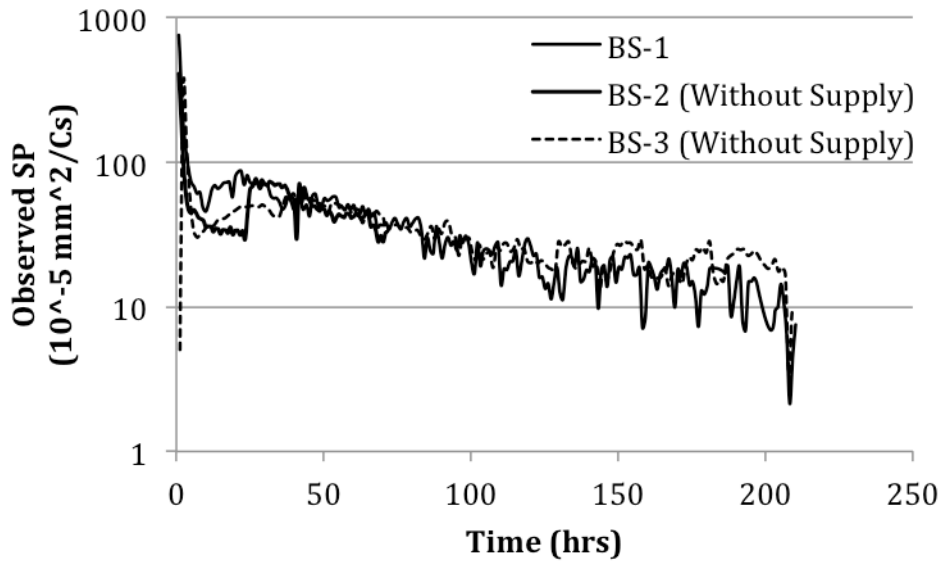


Figure 3.17: The observed *SP* of BSM with an external water supply (BS-1) and without an external water supply (BS-2 and BS-3).

Upon the completion of the closed step-freezing tests, the water content in the unfrozen zone of the samples was measured at specified intervals from the warm-end boundary. Figure 3.18 presents the distribution of water content for the three tests, in which the 0 °C isotherm was located between 99.2 and 100.8 mm upon test completion, while 0 mm corresponds to the sample base. The water content prior to testing was calculated based on the initial average sample void ratio and a 100% degree of saturation. The measured water contents in tests BS-2 (conducted for 72 hours) and BS-3 (212 hours) demonstrate the development of dewatering within the unfrozen soil, particularly in BS-3. The unfrozen soil after testing is clearly no longer fully saturated. As ice lenses form and grow they extract available pore water from the adjacent unfrozen soil. Referring to the Figure 3.3, the presence of ice lenses is confirmed by both the measured sample displacement and visual inspection upon test completion.

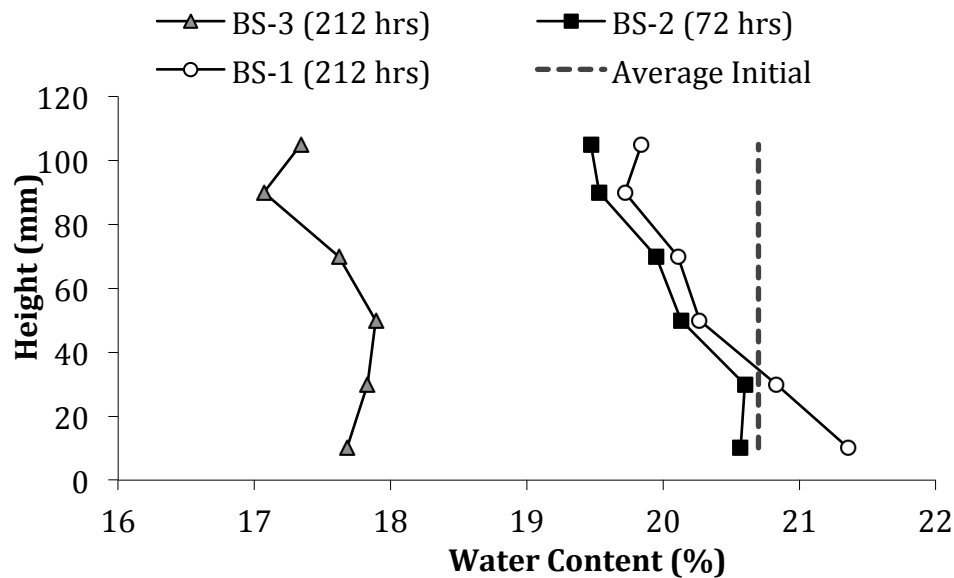


Figure 3.18: The variation in the water content in the unfrozen soil post testing of BS-1, BS-2, and BS-3.

The recorded pore pressure at the base of the sample in tests BS-2 and BS-3 is presented in Figure 3.19. For both tests, heaving initiates shortly after freezing is imposed, 1 – 2 hours after test initiation. The initial pore pressure was hydrostatic, corresponding to 2.0 kPa at the base. At the start of freezing the basal pore pressure increased to approximately 10 kPa in both tests. Upon onset of frost heave, there was a sharp drop in gauge pressure to approximately -45 kPa (gauge pressure) followed a series of oscillations ranging between -5 kPa and -65 kPa. The sharp drop in pore pressure is attributed to the suction associated with the frost heave process. Without an external water source, the unfrozen zone is effectively sealed and confined. The subsequent increase and oscillation in pressure may be indicative of two processes: the boiling of pore water at very low pressures or a leak in the sample mould introducing air into the soil. At approximately 0.81 kPa absolute pressure, nearly -100 kPa gauge pressure, water will boil at 4 °C, the warmest soil temperature in either test. Although the recorded pore pressure did not decrease below approximately 40 kPa absolute, this does not necessarily preclude the occurrence of boiling or cavitation. The initial rate of change in pressure was high and the pressure transducer was located on a supply line, which possibly introduced some time-delay into the pressure readings. Consequently, it is possible the local pore pressure did decrease sufficiently for pore water boiling in the soil. It was however not possible to definitively verify this. The oscillations in the basal pressure may have reflected the redistribution of trapped volumes of vapour phase in the pore structure.

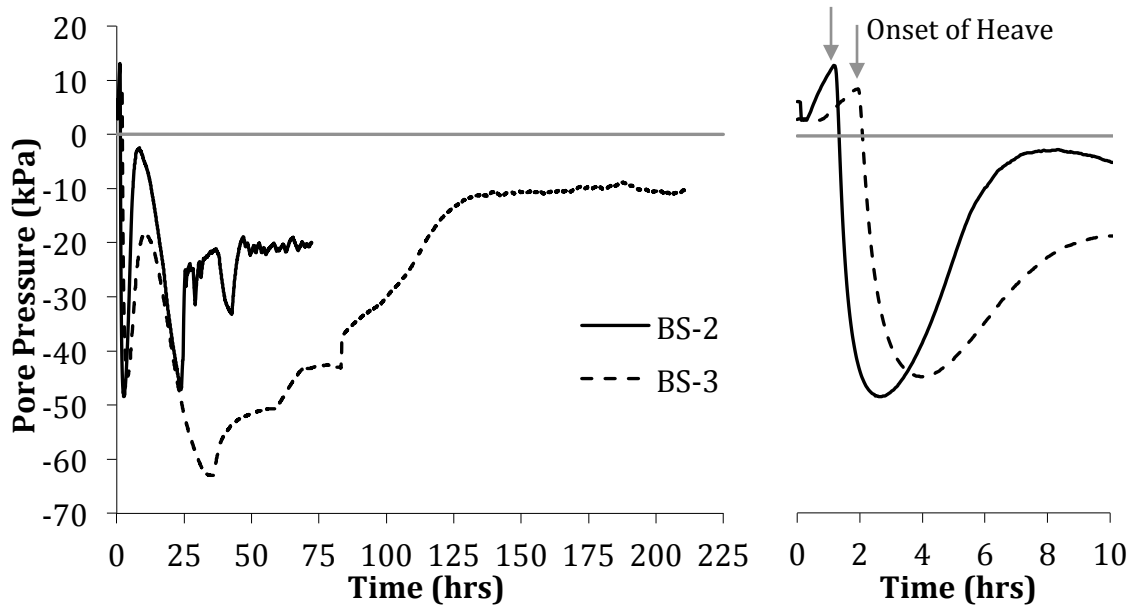


Figure 3.19: The temporal variation in the basal pore pressure of step freezing tests BS-2 and BS-3 (without a water supply).

The change in pore pressure, particularly the sharp drop upon heaving initiation, increased the effective stress in the unfrozen soil, potentially inducing consolidation in this zone. Settlement in the unfrozen soil would be expected to decrease the measured heave displacement of the sample. The influence of unfrozen zone consolidation was minimized for all tests by preparing samples at a high overconsolidation ratio of 5. Figure 3.20 presents the consolidation curve of the prepared BSM specimen. Based on the consolidation behaviour, the maximum observed change in pore pressure of approximately 70 kPa could have been responsible for as much as 3.0 mm of settlement in the 100 mm unfrozen zone under fully saturated conditions. No consolidation was expected in the frozen soil. This potential settlement exceeds the difference in final heave between the BS-1 and BS-3 (with and without an external water supply respectively)

which was approximately 2.5 mm. However, as previously noted, the unfrozen soil was observed to be not fully saturated after testing. Since the relation between matric suction and saturation (soil-water characteristic) is not known, it was impossible to precisely determine the actual change in effective stress. Based on the total volume of pore water in the unfrozen soil, the maximum aggregated thickness of ice lenses cannot exceed 38.0 mm.

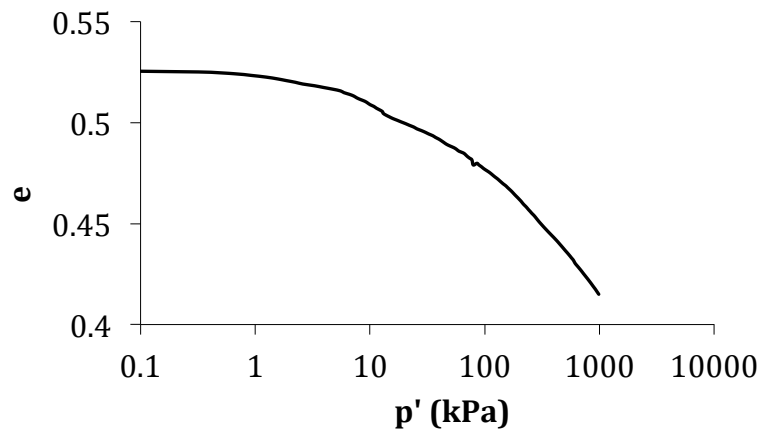


Figure 3.20: The consolidation curve of the prepared BSM samples.

3.6 DISCUSSION

The experimental results reveal the influence of two factors on the frost susceptibility of soils as characterized by segregation potential. First of all, the results indicate that the overburden stress affects the frost heave rate, which is consistent with previously established observations (Konrad and Morgenstern 1982). Secondly, the apparent segregation potential tends to increase linearly with the frost penetration rate for

a given overburden stress. Unlike the influence of overburden, the second phenomenon has not been as thoroughly examined in the literature.

To understand the influence of the freezing rate on the frost heave rate, we can consider frost heave relative to the hydraulic transport process. As illustrated in Figure 3.21, ice lens growth coincides with the development of a pore pressure profile in the unfrozen zone and frozen fringe. This pore pressure profile dictates the flux supplying water for the active ice lens, which is directly proportional to the heave rate. The far-field pore pressure, P_l , is constant throughout the process. In the case of laboratory frost heave tests, this pressure is the water supply pressure; in the case of in-situ freezing this would correspond to some distant hydraulic boundary condition. The pore pressure on the warm side of the active ice lens, P_3 , can be defined relative to the lens temperature, T_3 , and ice pressure, P_i , using the modified Clapeyron equation.

$$P_3 = P_i - \frac{\rho_w L}{T_m} (T_m - T_3) \quad (3.10)$$

where T_m is the bulk freezing temperature of water and the ice lens pressure, P_i , being equal to the overburden. If the overburden increases, P_3 will increase proportionally. Higher P_3 values imply lower pore pressure gradients across the frozen fringe and consequently lower fluxes, because hydraulic conductivity of the region is not affected. This is consistent with the observed relationship between heave rate and overburden.

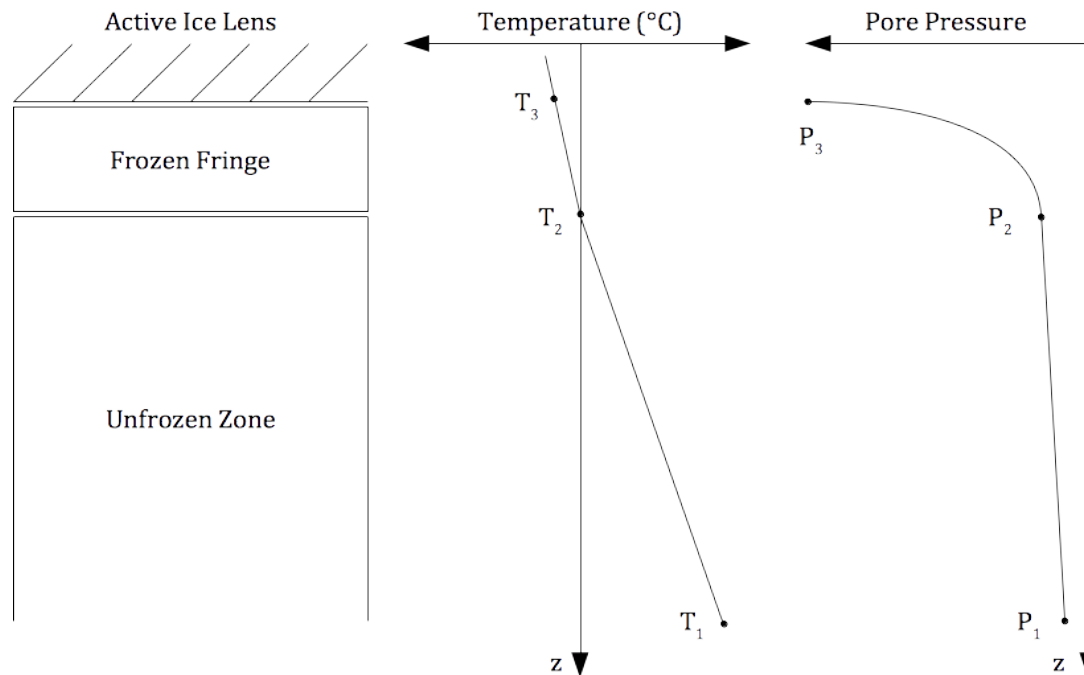


Figure 3.21: Illustration of the pore pressure profile during frost heave.

The value of the pore pressure at the fringe-unfrozen zone interface, P_2 , is less clear. The pore pressure must be continuous throughout and between the two regions, which implies P_2 cannot be defined with the Clapeyron equation alone. Physically, the inconsistency with the Clapeyron relation can be attributed to non-equilibrium hydrodynamic and possibly thermodynamic conditions at the frost front.

Figure 3.22 illustrates the hypothetical pore pressure profiles of a soil with a change in the position of the frost front. By their nature, fine-grained soils require significant amounts of time to effectively dissipate excess pore pressure and consequently P_2 will be influenced to some degree by the previous pore pressure profile. The implication of this is that the unfrozen soil will dissipate less excess pore pressure under a relatively fast frost front penetration rate, implying higher values of P_2 . Higher values of

P_2 will increase the pore pressure gradient across the frozen fringe, ultimately leading to greater migration and heave rates. This increase in the interface pore pressure is temporary and dissipates with time. The influence of the rate of change in frost front position on P_2 would however be dictated by the ability of the unfrozen soil to dissipate pore pressure, i.e. its hydraulic conductivity. In particular, the *SP* of soils with greater permeability will be less sensitive to the frost penetration rates than soils with less permeability.

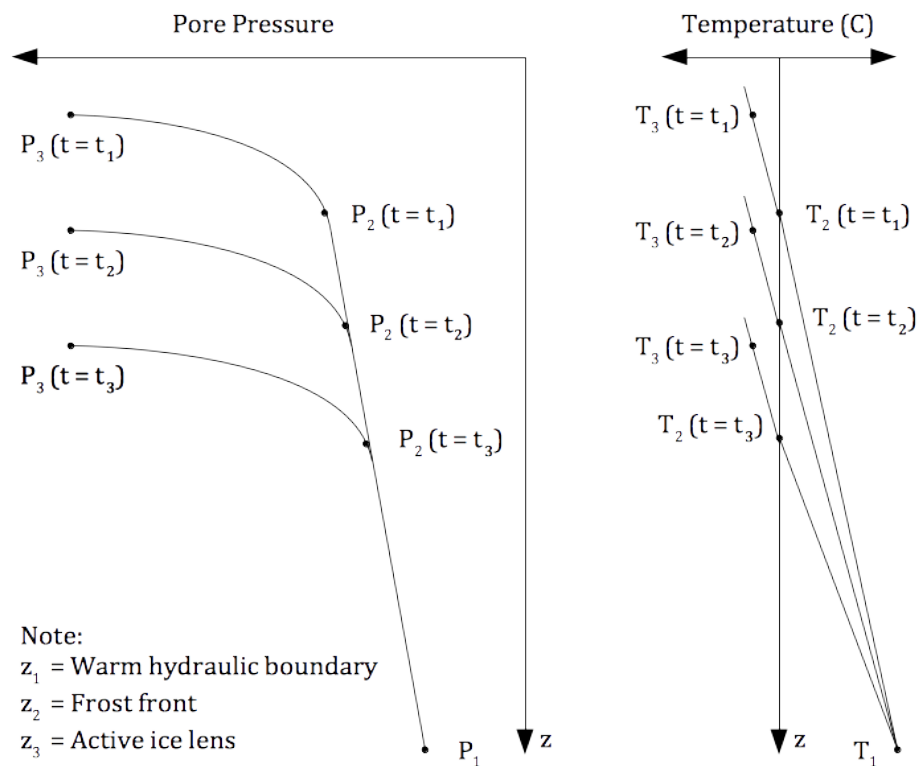


Figure 3.22: The variation in the pore pressure profile as the frost front advances.

Following this logic, changes in the far field pore pressure, P_1 , will similarly affect the pore pressure gradients driving frost heave. In particular, if the water supply

pressure (backpressure) is increased, pore pressure gradients in both the unfrozen soil and the frozen fringe increase, which in turn increases water flux supplying ice lens growth and ultimately increasing the heave rate. Experimental observations in the literature support this conclusion (Konrad 1989b; Konrad and Seto 1994). Interestingly, these findings also show that if the back pressure is increased at the same rate as the overburden stress, the heave rate remains constant.

3.7 SUMMARY AND CONCLUSIONS

This chapter presented the findings from the experimental frost heave investigation. A series of one-dimensional frost heave tests were conducted to examine the influence of the thermal, mechanical, and hydraulic on the frost heave response of two different soils (a sandy-silt and a lean clay with sand).

The segregation potential concept was used to analyze and interpret the experimental results. Instead of a constant material parameter, as is often assumed, SP varies substantially with stress level, the rate of freezing, and potentially the hydraulic boundary conditions. In particular, the observed SP is positively correlated with the advance rate of the 0 °C isotherm and negatively correlated with the overburden stress level. The latter relation agrees well with similarly reported findings. Of significance is the fact that the former relation is generally unaccounted for in current SP modelling techniques, which can contribute to underestimating frost heave effects in practical applications. Although the relation between the heave rate and the rate of cooling of the frozen fringe has been reported (Konrad and Morgenstern 1982), the variation of SP with

the frost penetration rate has not been considered to date. A novel expression (equation 3.9) has been proposed to characterize this influence based on the experimental findings. This expression is most important in situations where there is rapid freezing. Physically, this influence is attributed to non-steady state conditions during highly transient freezing. It is postulated that the sensitivity of SP to the frost penetration is impacted by the permeability characteristics of the soil.

The presence of an external water supply impacted the total heave displacement of the sandy-silt samples under step-freezing. Less total heave was observed when the supply was not present as compared to when it was present under identical imposed thermal and mechanical boundary conditions. However, due to the potential for consolidation in the unfrozen soil associated with the drop in water pressure, it is not clear how much of the observed difference in total expansion is due to a reduction in segregated ice lens growth and how much is due to consolidation.

This study explored the qualitative differences between the step and ramped freezing boundary conditions in general frost heave tests. Step conditions are noted for inducing rapid changes in temperature. These highly transient conditions are well suited for analyzing the effect of the frost penetration rate via SP and allow for good quantitative comparisons of frost heave behaviour of different materials and under varying stress levels. Alternatively, tests under the ramped-freezing conditions were shown to be highly impacted by delays in the initiation of frost heave. Under these conditions the initiation in heave displacement occurred well after the soil reached the bulk freezing point of water.

The time between when freezing temperatures were reached and onset of heave has a significant influence on the total observed displacements. The experimental findings provided little insight into characterizing this delay, as a relation could not be established between the point of heave initiation and the temperature, rate of change in temperature, or any other measured variable. However this effect is unlikely to have a material influence on in-situ frost heave situations. The observed time delay varied between approximately 10 – 70 hours, a significant length under laboratory conditions but insignificant for practical in-situ situations. Consequently ramped-freezing tests are poorly suited for quantitative comparative analysis of frost heave. Step freezing tests displayed minimal sensitivity to the timing of heave initiation.

CHAPTER 4 THERMAL PROPERTIES OF FROZEN SOIL

4.1 INTRODUCTION

This chapter examines the thermal properties of frozen soil, specifically heat capacity and thermal conductivity. The objective is to determine a suitable approach for characterizing these properties for the purpose of modelling frost heave and other thermodynamic soil processes. The chapter provides a review of several relevant thermal conductivity models and proposes a multi-level homogenization scheme to apply them to frozen soils. The proposed schemes are evaluated through comparison with measured values of frozen and partially saturated soils, obtained from the reported literature. The potential anisotropy of thermal conductivity in soils containing segregated ice will also be considered in detail. The findings presented in this chapter will be utilized in the coupled thermal-mechanical frost heave model, presented in Chapter 5.

Frozen soil is a composite of multiple phases, such as mineral particles, water, air, and ice. These phases may have drastically different physical properties which when combined yield a macro-scale homogenized, or composite, property. In order to develop a comprehensive thermodynamic frost heave model it is necessary to accurately characterize the thermal properties.

4.2 HEAT CAPACITY OF FROZEN SOIL

Heat capacity is a physical property that defines the energy required to raise the temperature of a material by some prescribed amount. Unlike thermal conductivity, heat

capacity is a scalar quantity and therefore is not influenced by the spatial distribution of different phases. For a soil, it can be defined based on the heat capacity and relative proportion of the constituent phases through a simple volumetric weighting (Andersland and Ladanyi 1994):

$$C = \sum_{j=1}^n C_j \theta_j = \sum_{j=1}^n c_j \rho_j \theta_j \quad (4.1)$$

where C and c refer to the volumetric and specific heat capacity, respectively, θ is the volume fraction, and j refers to the n soil phases.

The presence of water in soils introduces an additional consideration when characterizing heat capacity. As noted in Chapter 2, due to its physical nature, water releases or absorbs energy when undergoing a phase transition. While this process is physically different from the heat capacity concept, in practice it leads to soils displaying a larger apparent heat capacity when the internal water changes phases. Chapter 5 will discuss how this effect is accounted for.

4.3 THERMAL CONDUCTIVITY OF FROZEN SOIL

4.3.1 Review of Isotropic Thermal Conductivity Models

In addition to the relative volume and properties of the constituent phases, the thermal conductivity of composite materials, λ , is significantly affected by the geometric distribution of the phases. This presents a notable challenge when characterizing soils, as the constituent phase geometries are complex. For any heterogeneous material, there

exists both an upper and lower theoretical bound for the homogenized conductivity. The Voigt (1889), or parallel model, and the Reuss (1929), or series model, provide these respective bounds:

$$\text{Voigt upper bound:} \quad \lambda = \sum_{j=1}^n \lambda_j \theta_j \quad (4.2)$$

$$\text{Reuss lower bound:} \quad \frac{1}{\lambda} = \sum_{j=1}^n \frac{\theta_j}{\lambda_j} \quad (4.3)$$

where λ refers to the thermal conductivity, θ the volumetric fraction, and the subscript j refers to each of the n constituent phases.

Hashin and Shtrikman (1962, 1968) further refined the theoretical bounds for multiple composite properties. For the thermal conductivity of a two-phase composite where $\lambda_2 > \lambda_1$, these bounds have the following functional forms:

$$\text{HS upper bound:} \quad \lambda = \lambda_2 + \frac{\theta_1}{\frac{1}{\lambda_1 - \lambda_2} + \frac{\theta_2}{3\lambda_2}} \quad (4.4)$$

$$\text{HS lower bound:} \quad \lambda = \lambda_1 + \frac{\theta_2}{\frac{1}{\lambda_2 - \lambda_1} + \frac{\theta_1}{3\lambda_1}} \quad (4.5)$$

It is important to recognize that both the Voigt-Reuss and Hashin-Shtrikman bounds differ by as much as an order of magnitude for most soils, an unacceptable variation for typical modelling applications.

Maxwell (1881) proposed a model for the thermal and electrical conductivities of two-phase composite materials composed of a series of well dispersed homogeneous spheres suspended in a homogeneous medium or matrix. In this case the continuous medium is referred to as phase 1 and the discrete particles as phase 2. The model was developed through a solution to the partial-differential heat transfer problem of a composite containing a single spherical particle.

$$\lambda = \lambda_1 \frac{2\theta_1\lambda_1 + (3 - 2\theta_1)\lambda_2}{(3 - \theta_1)\lambda_1 + \theta_1\lambda_2} \quad (4.3)$$

the subscripts *1* and *2* refer to the matrix and particulate phases, respectively.

The geometric distribution of phases in Maxwell's model is broadly consistent with how soils are often represented (Woodside 1958). It is important to consider that this formulation assumes there is no interaction in the temperature field between the spheres. Particle interaction will only provide additional flow paths for heat transfer, so Maxwell's model essentially provides a lower bound associated with a spherical particle shape, which can be referred to as the far-field boundary. Mathematically the model is valid as the particle phase fraction approaches 100%, $\theta_1 \rightarrow 0$. Conceptually, however, it is clear there will be substantial inter-particle heat flow at high particle volumes, contrary to the model's fundamental assumption. Consequently, at the porosities typically encountered in soils it is expected that Maxwell's model will systematically under-predict true conductivity.

Expanding on the concept used by Maxwell, Rayleigh (1892) (including contributions from Meredith and Tobias (1960)) developed a thermal conductivity model of homogeneous sphere-medium composites with significant inter-sphere heat flow. The model formulation accounted for the heat transport between closely spaced particles with an assumed periodic distribution, specifically either simple, body centered, or face centered cubic. For a simple cubic distribution the Rayleigh's model has the following functional form:

$$\lambda = \lambda_1 \frac{[(2 + \kappa)/(1 - \kappa)] - 2\theta_2 - 0.525[(3 - 3\kappa)/(4 + 3\kappa)]\theta_2^{10/3}}{[(2 + \kappa)/(1 - \kappa)] + 2\theta_2 - 0.525[(3 - 3\kappa)/(4 + 3\kappa)]\theta_2^{10/3}} \quad (4.4)$$

where $\kappa = \lambda_2/\lambda_1$ for simplification. The model appears to be a conceptual improvement over the Maxwell model as it explicitly accounts for the interaction between particles that occurs in soils. The principal drawback of this approach is that it is indeterminate when the particulate fraction exceeds the volume associated with sphere contact. For the simple cubic configurations this corresponds to porosities below approximately 0.537. Unfortunately this is a severe practical limitation as many natural soils may have porosities well below this threshold.

An alternative concept for modelling composite conductivity is the effective medium theorem (EMT) based on the self-consistency assumption (Bruggeman 1935, Milton 2002). This approach is based on an assumption of a perfectly random distribution between two continuous phases, which results in the following relation:

$$\theta_1 \frac{\lambda_1 - \lambda}{\lambda_1 - 2\lambda} + \theta_2 \frac{\lambda_2 - \lambda}{\lambda_2 - 2\lambda} = 0 \quad (4.5)$$

It follows that:

$$\lambda = \frac{1}{4} \left[(3\theta_2 - 1)\lambda_2 + (3(1 - \lambda_2) - 1)\lambda_1 + \sqrt{[(3\theta_2 - 1)\lambda_2 + (3(1 - \theta_2) - 1)\lambda_1]^2 + 8\lambda_1\lambda_2} \right] \quad (4.6)$$

The assumed geometric distribution of phases for the three models discussed above is illustrated in Figure 4.1. Typically, the thermal conductivity of the soil grain is higher than the pore phases. Consequently the discrete phase in the Maxwell and Rayleigh models is assumed to be greater than the medium, $\lambda_2/\lambda_1 > 1$.

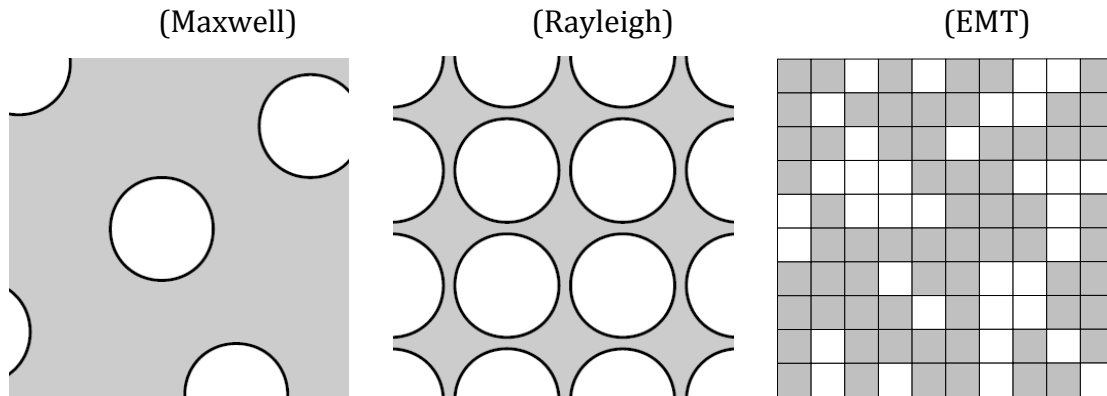


Figure 4.1: An illustration of assumptions made regarding geometric distribution of phases.

A commonly used model for the composite thermal conductivity of frozen soils is the geometric mean approximation, equation 4.7 (Michalowski 1993, Coté and Konrad 2005, Nishimura et al. 2009). While there is no theoretical justification for this particular functional form and it involves no specific assumptions regarding geometric distribution,

it can yield acceptable approximations for many soils. The advantages of this approach are that it has a simple functional form and is determinate for all volume fractions.

$$\lambda = \prod_{j=1}^n \lambda_j^{\theta_j} \quad (4.7)$$

Figure 4.2 compares the four models discussed along with the theoretical bounds for a two-phase composite material. The Maxwell and Rayleigh models closely follow each other at low volume fractions, where at low volume fractions the discrete phase is similarly well dispersed in both formulations. Unlike the Maxwell or Rayleigh models, the EMT model considers the high conductivity phase to be continuous and consequently yields conductivities closer to the upper bound. Interestingly, Maxwell's model is virtually identical to the Hashin-Shtrikman lower bound.

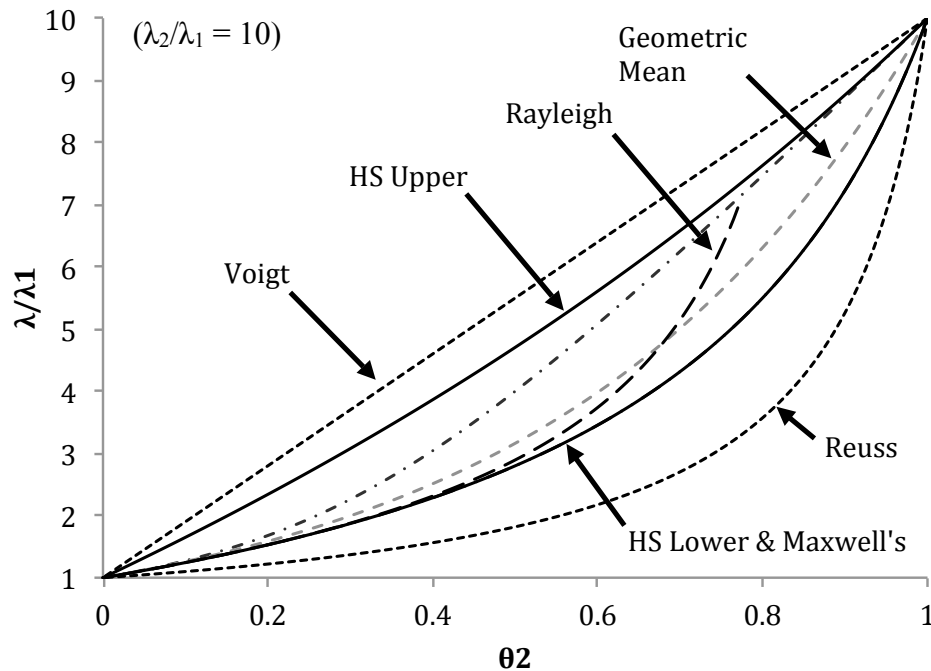


Figure 4.2: Comparison of the thermal conductivity models discussed for a two-phase composite material.

4.3.2 Multi-Level Homogenization

It should be recognized that the four thermal conductivity models previously discussed were formulated for two-phase composites (with the exception of the geometric mean approximation), while frozen soils generally contain four phases. Consequently, in their original form none of these models are adequately suited for frozen soils. Regarding Maxwell's model, the concept has been extended to n unique phases suspended in a single homogeneous medium (McCartney and Kelly 2008). However, it is not clear if this offers a relevant representation of soil.

In an inhomogeneous material like soil, geometry dictates that conductive heat transport will be dominated by the continuous phases as opposed to the discrete phases. In other words, the continuous phase conductivity will have a greater influence relative to volume content than the discrete phase, as demonstrated by Maxwell's model. For frozen soils, however, it is not always clear which phases can be considered continuous or discrete, as this can change with saturation or temperature. When fully saturated, the water phase is clearly continuous and when fully dry the air phase is continuous, but it is far less clear when soils are partially saturated. The presence of ice will further complicate the matter.

A multi-level homogenization simplifies the problem with identifying the continuous or discrete phases. In such an approach, different phases can be represented separately and then combined together through multiple composite models. For example, illustrated in Figure 4.3 in frozen soils the liquid water, ice, and air phases can be

combined into a single representative pore phase, which could then be applied to the Maxwell model, for instance. While there is little physical justification for such an approach, it has been proposed in previous modelling schemes (Wang et al. 2006, Wang et al. 2008). A double homogenization will be examined in this work, where the pore phase representation is considered the first level and then a second level model is introduced to combine the pore phase with the soil grain phase.

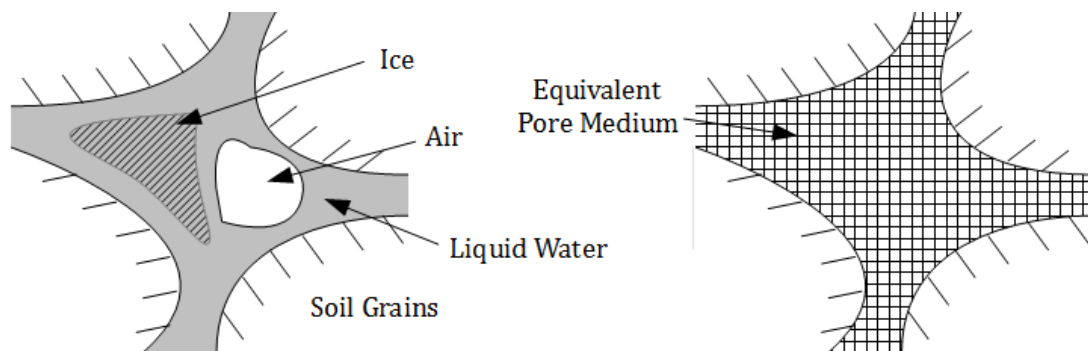


Figure 4.3: Illustration of the composite pore phase medium.

It is not initially apparent which models are best suited to describe the equivalent pore phase conductivity. If liquid water is assumed to maintain contact to the soil grain surface and form inter-pore connections, conductive heat transport will occur within this phase. This indicates the pore phase conductivity would be in excess of the lower Reuss bound. If geometry compelled conduction through low conductivity phases the lower bound would be more appropriate. The geometric mean offers a pseudo-empirical compromise between the two bounds and, consequently, it will be considered along with the Voigt upper bound in this evaluation.

Voigt pore phase:
$$\lambda_v \theta_v = \lambda_l \theta_l + \lambda_a \theta_a + \lambda_i \theta_i \quad (4.8)$$

Geometric mean pore phase:
$$\lambda_v^{\theta_v} = \lambda_l^{\theta_l} \lambda_a^{\theta_a} \lambda_i^{\theta_i} \quad (4.9)$$

where:
$$\theta_v = 1 - \theta_s = \theta_l + \theta_a + \theta_i \quad (4.10)$$

the subscripts l , a , i , s , and v refer to the liquid water, air, ice soil grains, and pore voids, respectively.

In addition, a third pore phase representation will be examined using the mean of the upper and lower Hashin-Shtrikman bounds. This expression is only applicable for two-phase pores, i.e. water-ice or water-air.

$$\lambda_v = \frac{1}{2} \left(\lambda_1 + \frac{\theta_2/\theta_v}{\frac{1}{\lambda_2 - \lambda_1} + \frac{\theta_1/\theta_v}{3\lambda_1}} + \lambda_2 + \frac{\theta_1/\theta_v}{\frac{1}{\lambda_1 - \lambda_2} + \frac{\theta_2/\theta_v}{3\lambda_2}} \right) \quad (4.11)$$

in the above expression the subscripts 1 and 2 refer to the two pore phases.

The next consideration is the second model in this two-level homogenization, combining the pore phase with the soil grains. Five models are examined: Maxwell's, Rayleigh's, EMT, geometric mean, and the mean of the Hashin-Shtrikman bounds. The first two of these models conceptually distinguish between continuous and discrete phases; while the EMT assumes a perfectly random phase distribution and the final two are mathematical formulations without physical representation. The geometric mean representation did not use a multi-level representation. Similar to equation 4.11, the Hashin-Shtrikman bound mean has the following form:

$$\lambda = \frac{1}{2} \left(\lambda_1 + \frac{\theta_2}{\frac{1}{\lambda_2 - \lambda_1} + \frac{\theta_1}{3\lambda_1}} + \lambda_2 + \frac{\theta_1}{\frac{1}{\lambda_1 - \lambda_2} + \frac{\theta_2}{3\lambda_2}} \right) \quad (4.12)$$

4.3.3 Model Evaluation

In order to evaluate the four models discussed, predicted conductivities are compared to measured physical values obtained from the literature. Two sources of data are examined: an unfrozen soil under various degrees of saturation (Coté and Konrad 2005) and a frozen, fully saturated soil under various temperatures (Penner 1970). Coté and Konrad (2005) measured the thermal conductivity of a gravel material prepared at two different dry densities, each varying in saturation from completely dry to fully saturated. Penner (1970) reported the thermal conductivity and volumetric composition of a silty-clay with a void ratio of approximately 0.8 at temperatures ranging between -0.3 to -22.0 °C, refer to Figure 4.4. The thermal conductivities of the individual phases can be determined from commonly available results (Michalowski 1993); the specific values used in the prediction are outlined in Table 4.1.

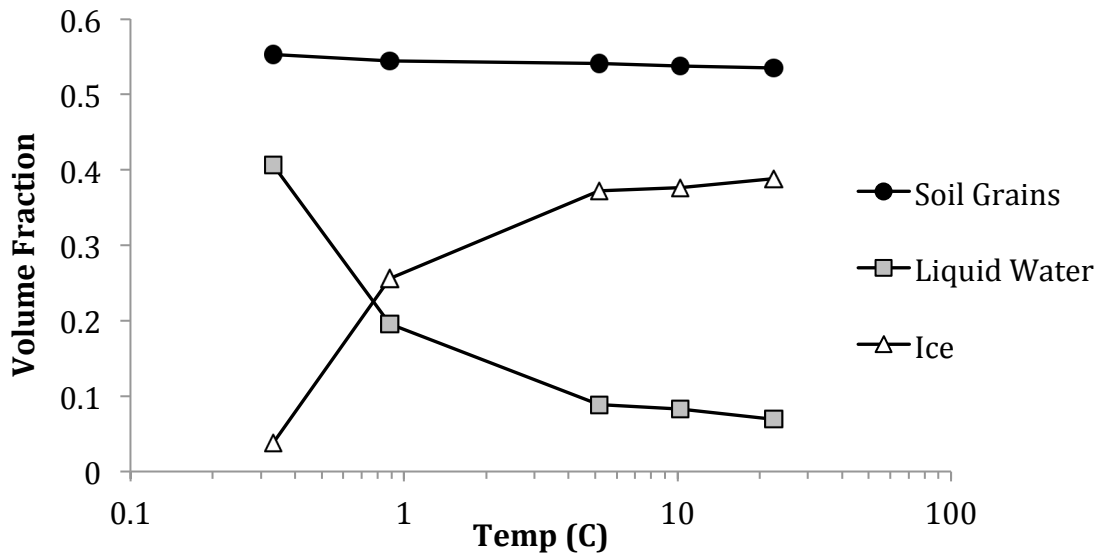


Figure 4.4: Variation of reported volumetric composition of the silty-clay referred to in Figure 4.6 (Penner 1970).

Table 4.1: Assumed thermal conductivity values of the constituent soil phases.

Phase	λ (W/mC)
Soil Grains	5.00
Liquid Water	0.60
Ice	2.24
Air	0.024

First, Figures 4.4 and 4.5 compare the different modelling approaches to the unfrozen, variably saturated soil. Of the three pore phase representations the Voigt approximation appears to best capture observed behaviour followed by the HS mean approximation, particularly at saturations around 50%. This can be attributed to liquid water wetting against the soil grain surface, while the air phase forms discrete bodies within the pores. Regarding the second level representation, the EMT model is observed

to be the least effective as it greatly over estimates the thermal conductivity of dry soils, when the difference in conductivity between the soil grains and the pore phases is greatest. At a porosity of 0.30, Rayleigh's model yield's adequate results, but at the lower porosity it is no longer mathematically applicable. Maxwell's model provides reasonable results, though with a systematic tendency to under represent conductivity. This can be attributed to its formulation as a far-field boundary. The model assumes non-interacting, dispersed particles while in the physical soil there is clearly interaction between particles resulting in greater potential for conduction. The Hashin-Shtrikman bound mean and the geometric mean approximation both yield the best predictions of observed values.

For the frozen, saturated soil, all modelling approaches yielded good agreement with the observed values when the ice content was large. This is due to the ice and soil grain phases having similar thermal conductivities; more variation was seen in the models at lower temperatures. In this case the model used in the second level homogenization had a smaller influence on the predictions as the pore phase representation. Of the three pore phase models the Hashin-Shtrikman bound mean appears most effective. Overall, the geometric mean approximation was observed to yield the best results for the frozen soil.

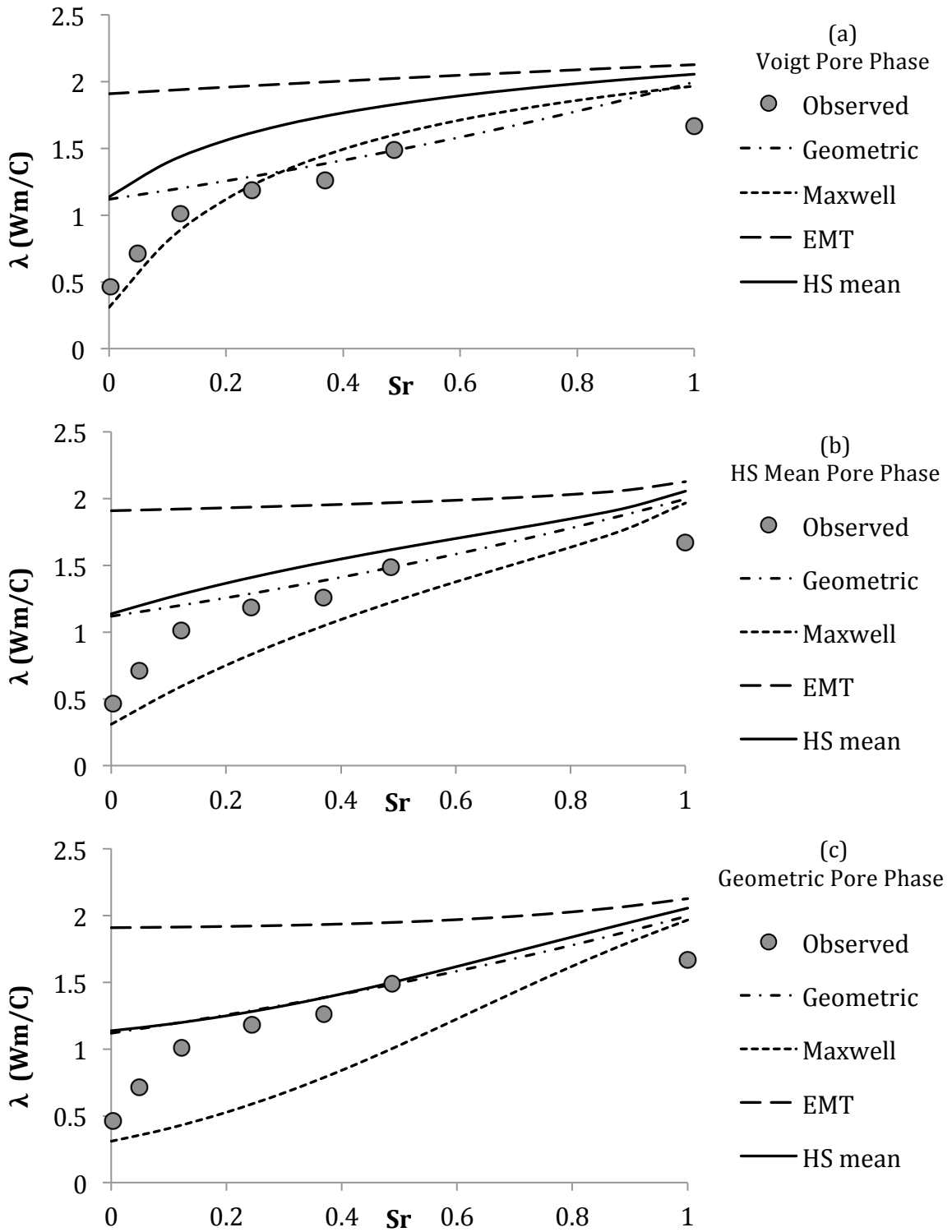


Figure 4.5: Comparison of the reported thermal conductivities of a gravel material at a porosity of 0.18 (Coté and Konrad 2005), with modeled values

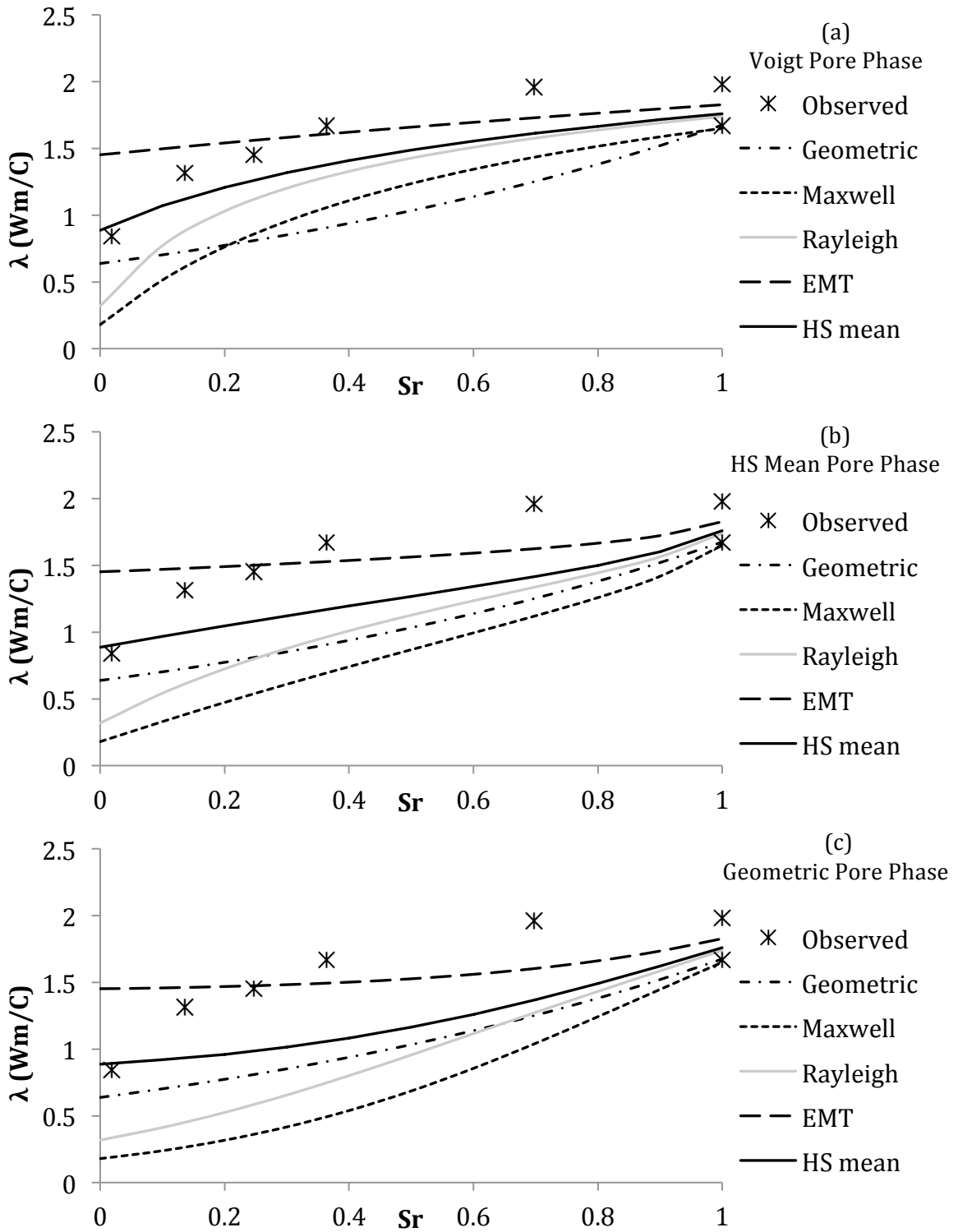


Figure 4.6: Comparison of the reported thermal conductivities of a gravel material at a porosity of 0.30 (Coté and Konrad 2005), with modeled values.

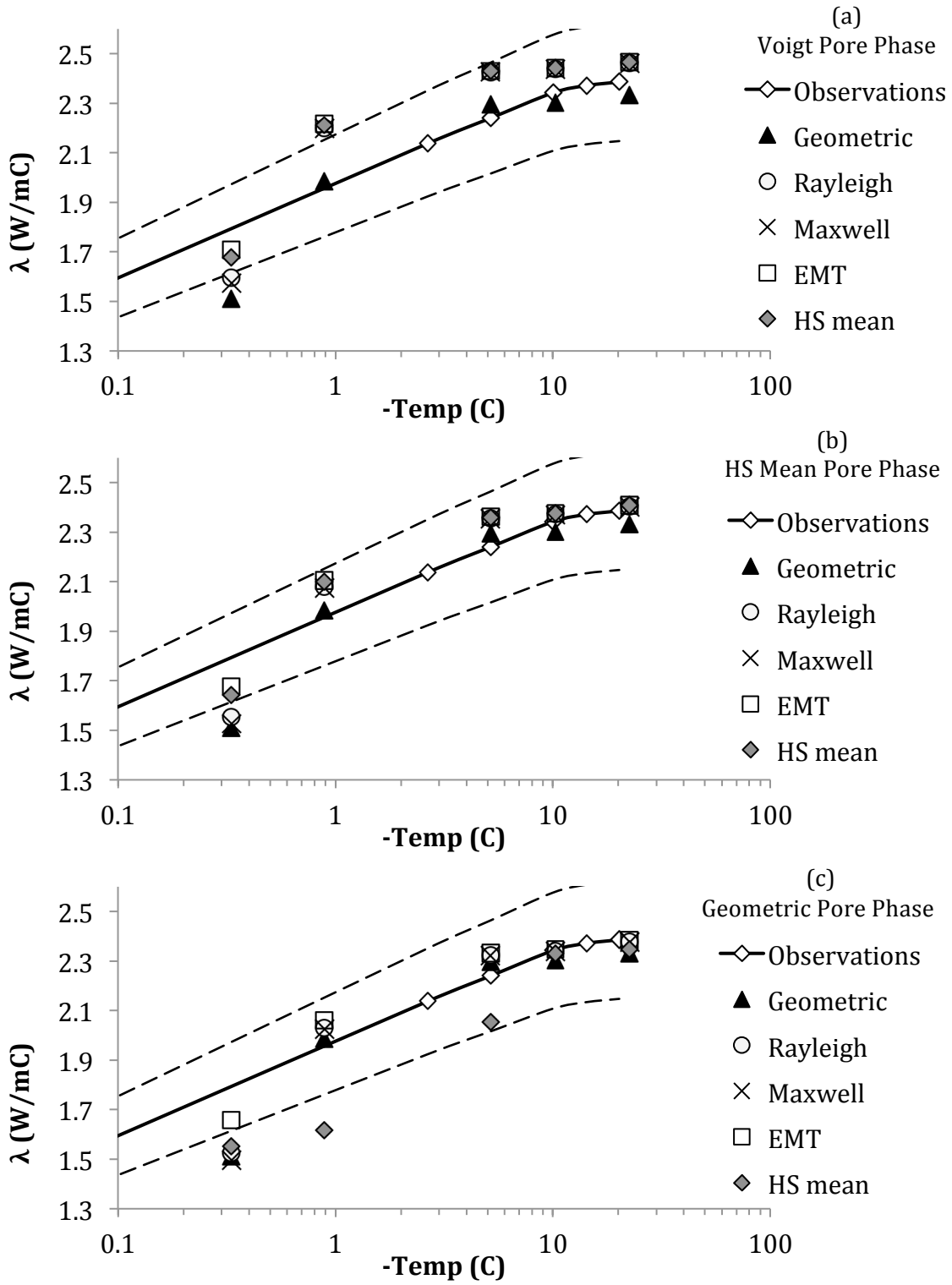


Figure 4.7: Comparison of the reported thermal conductivities of a frozen, saturated silty-clay (Penner 1970), with modeled values.

Although it best reflects the geometric characteristics of soils, Rayleigh's model is not well suited for practical applications. This is due to the inherent constraints regarding the medium phase volumes. When the particulate volume exceeds the threshold of inter-particle contact the Rayleigh model becomes indeterminate, all but very loose soils possess porosities below this threshold.

The EMT model is generally a poor reflection of the physical phase distributions as it assumes the highly conductive soil grains to be a continuous phase. While geometry indicates there will be some soil particle contact and interaction, it is also clear that this phase is far less continuous than the pore voids. Consequently, it is expected EMT will systematically over-estimate conductivities when the void phase conductivity is significantly less than the soil grains, such as in dry soils.

The Hashin-Shtrikman bound mean model with the Voigt pore phase assumption and the geometric mean approximation appear to be the most suitable approaches. While there is little physical evidence to support its application, the geometric mean approximation does offer a simpler functional form.

4.3.4 Anisotropic Thermal Conductivity

The thermal conductivity of soils that have undergone frost heave can be considered separately from conventional frozen soils. Ice lenses, which are responsible for frost heaving, are discrete bands of ice that form in a predictable manner. As discussed in Chapter 2, they exist as continuous bands or planes of ice, which form normal to the thermal gradient in the frozen fringe. As a result, such soils are inherently

anisotropic. Conceptually, these soils can be discretized into two components and the thermal conductivity can be characterized using a multi-level homogenization. The first is the frozen soil, which contains soil grains, liquid water, ice and air. The volume fractions of the pore constituents are governed by both temperature and the soil freezing characteristic, which is itself governed by mineralogy and soil fabric. The thermal conductivity of this phase can be determined based on the volumetric composition using the models discussed previously. The second component is the ice lenses. Since lenses are homogenous ice bodies, whose volumes and properties are generally independent of temperature, thermal conductivity can be readily defined. Figure 4.8 illustrates this multi-level homogenization, where phase 1 refers to the isotropic frozen soil and phase 2 to the ice lenses.

Assuming that the frozen soil, the region not containing ice lenses, is isotropic in nature, the thermal conductivity of the entire soil can be defined relative to the orientation of the ice lenses. Figure 4.9 illustrates this concept, with the unit normal vector \mathbf{n} characterizing the orientation of the local ice lens fraction. The angles η and δ define the orientation of the ice plane to the thermal gradient and the thermal gradient to a reference orientation, respectively.

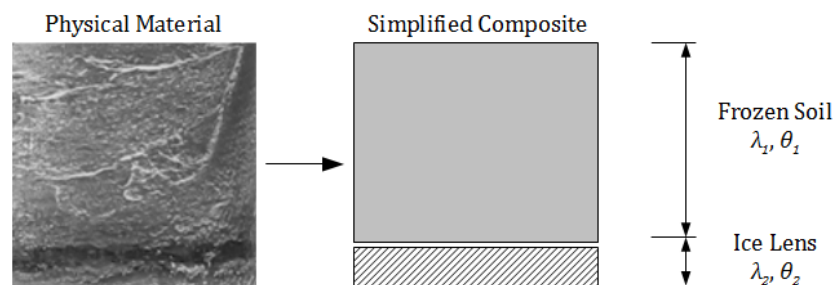


Figure 4.8: Conceptual representation of the multi-level homogenization of frozen soil containing segregated ice lenses.

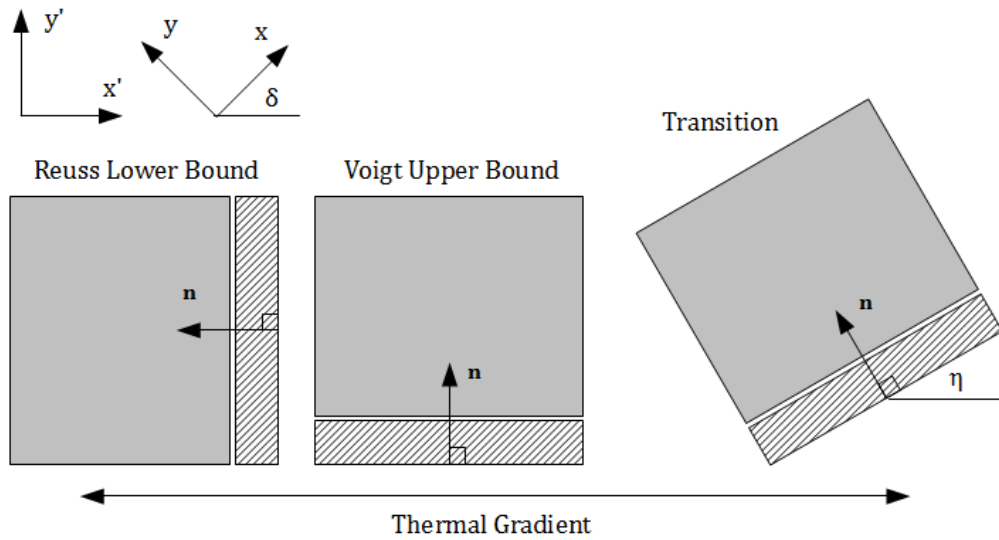


Figure 4.9: The orientation of the ice lens plane to the thermal gradient.

When the ice lens plane is oriented parallel to the thermal gradient, $\eta = 0$, the composite is best represented by the Voigt upper bound. This will be referred to as the strong orientation. Likewise, when ice lenses are oriented perpendicular to the thermal gradient, $\eta = \pi/2$, the Reuss lower bound is adopted; this is referred to as the weak orientation.

$$\lambda_S = \lambda_1 \theta_1 + \lambda_2 \theta_2 \quad (4.13)$$

$$\lambda_W = \frac{1}{\frac{\theta_1}{\lambda_1} + \frac{\theta_2}{\lambda_2}} \quad (4.14)$$

$$\lambda_i^* = \begin{cases} \lambda_S \\ \lambda_W \end{cases} \quad (4.15)$$

where λ_i and θ_i refer to the thermal conductivity and volume fraction, respectively of the ice lens-free frozen soil and λ_2 and θ_2 refer to the ice lens volume fraction, see Figure 4.8.

For orientations in between, $0 < \eta < \pi/2$, the following rotational transformation matrix can be used:

$$R_{ij} = \begin{vmatrix} \cos \eta & -\sin \eta \\ \sin \eta & \cos \eta \end{vmatrix} \quad (4.17)$$

such that:

$$\lambda'_i = R_{ip} \lambda_i^* R_{qj} \quad (4.18)$$

where,

$$\lambda'_i = \begin{Bmatrix} \lambda'_x \\ \lambda'_y \end{Bmatrix} \quad (4.19)$$

The thermal conductivity can be further transformed from the local to the global coordinate orientation through an additional rotational transformation containing δ .

$$\lambda_i = \begin{Bmatrix} \lambda_x \\ \lambda_y \end{Bmatrix} = Q_{ij} \lambda'_i \quad (4.20)$$

where,

$$Q_{ij} = \begin{vmatrix} \cos \delta & -\sin \delta \\ \sin \delta & \cos \delta \end{vmatrix} \quad (4.21)$$

It is also important to examine the rationale for utilizing an anisotropic thermal conductivity formulation. Frozen soils without ice lenses generally have a thermal conductivity between 1.5 and 3.0 W/m°C, depending on factors such as the dry density, water content, particle size, and temperature (Andersland and Anderson 1978). The thermal conductivity of pure ice is in the midpoint of this range, approximately 2.24 W/m°C as noted in Table 4.1. If the thermal conductivity of phases 1 and 2 in the multi-

level composite model are similar there is little variation between the strong and weak thermal conductivity orientations. Table 4.2 illustrates this point for an assumed ice lens volume fraction, θ_I , of 10%. Consequently, this implies that there is little advantage of utilizing an anisotropic formulation of thermal conductivity for these soils.

Table 4.2: Difference between thermal conductivity of the strong, λ_S , and weak, λ_W , orientation for a soil with a 10% ice lens volume fraction.

λ_I (W/m°C)	λ_S (W/m°C)	λ_W (W/m°C)	Δ (%)
1.5	1.57	1.55	1.3
3.0	2.92	2.90	0.7

4.3.5 Further Composite Thermal Conductivity

In addition to examining the composite thermal conductivity of frozen soils, this work was extended to two-phase composite materials containing a continuous matrix embedded with discrete particles, also referred to as discrete particle composites. Using two-dimensional finite element method simulations, with a Monte-Carlo scheme, an expression was proposed to characterize the composite thermal conductivity of such materials based on the particle shape and orientation. The expression explicitly characterizes the influence of particle elongation on the composite conductivity and allows for a comprehensive description of anisotropic behaviour of such materials. This work utilized the finite element method to solve for the temperature field of complex composite geometries and then formulating characterizations based on these approximate solutions. Although only one type of material was explored, discrete particle composites,

this approach is likely valid for a wide variety of composite materials. This study is included in this thesis as Appendix B (Tiedje and Guo, 2014).

The relationship between particle elongation and composite conductivity which was observed in the numerical simulations was utilized in a practical application, included in this thesis in Appendix C (Tiedje and Guo, 2013). Physical observations of bentonite-sand mixtures containing chopped carbon fibres of varying aspect ratios confirmed the influence of particle elongation on composite thermal conductivity. These observations demonstrate the advantage of utilizing highly thermally conductive particles with a large degree of elongation when developing high-conductivity composite materials, in this case bentonite grout used in geothermal heat pumps.

4.4 SUMMARY AND CONCLUSIONS

This chapter explored the characterization of the thermal properties, particularly thermal conductivity, of frozen soils containing segregated ice lenses. First, an expression for the heat capacity of frozen soils was presented based on a volumetric weighting of the soil components or phases.

For thermal conductivity, isotropic behaviour was first considered. Four existing models characterising thermal conductivity relevant to frozen soils were reviewed; specifically, Maxwell's model, Rayleigh's model, the effective medium technique, and the geometric mean approximation. A multi-level homogenization approach was proposed to account for the multi-phase pore voids phase as a single continuous medium for implementation into the Maxwell and Rayleigh models. The considered models were

evaluated through a comparison with measured values of an unsaturated, unfrozen soil and a fully saturated, frozen soil, which were obtained from the literature. This evaluation indicates the geometric mean approximation and the double homogenization using Hashin-Shtrikman bound mean with a Voigt pore phase representation best predicted physical observations.

In addition, anisotropic thermal conductivity was considered in frozen soils containing ice lenses. An expression was formulated characterizing the conductivity based on the orientation of the ice lens plane relative to the thermal gradient. This approach also uses a multi-level homogenization of the soil, where the ice lens volume was considered separate from the frozen soil. This investigation concluded that there is no significant quantitative advantage to accounting for anisotropic conductivity in soils containing ice lenses.

CHAPTER 5 FROST HEAVE MODEL

5.1 INTRODUCTION

Frost heave is a challenging phenomenon to characterize. Interrelated thermodynamic, hydraulic, and mechanical processes occur simultaneously during the formation of segregated ice. This chapter presents a model that characterizes the thermodynamic and mechanical processes associated with frost heave. The primary purpose is to describe the mechanical response, particularly the deformation, due to a prescribed set of thermal boundary conditions. A secondary challenge is to characterize the change in soil porosity and volumetric composition due to ice formation. The objective of this work is to develop a practical engineering tool capable of providing useful insight and predictions of the frost heave process under a complex set of boundary conditions and geometries.

The finite element method (FEM) provides a practical tool for solving continuum problems involving complex physical processes, including geometric, boundary conditions, and material property considerations. Consequently, it is an ideal framework for modelling frost heave, and the numerical model proposed in this chapter is derived specifically for implementation into FEM to solve boundary-valued problems.

In this chapter, the governing equations of the physical processes of frost heave are discussed first, followed by a continuum mechanics description for the associated soil deformation. Next, practical considerations of implementing the model into a finite

element scheme are considered and discussed. The model is applied into a FEM program to simulate one-dimensional frost heave experimental test previously presented in Chapter 3. The objective is to validate the conceptual modelling approach and examine the model performance. Chapter 6 extends the model implementation to a two-dimensional engineering problem involving natural gas pipelines undergoing large frost heave deformations.

5.2 MODEL FORMULATION

5.2.1 Physical Governing Equations

This model was developed based on the following fundamental assumptions:

- Soils are fully saturated
- The volumetric composition of the unfrozen soil is constant

5.2.1.1 Energy Conservation

The energy balance within a soil under going frost heave can be attributed to six physical components. Specifically these are: the rate of temperature change, the thermal conduction, advection due to pore water migration, energy released/absorbed due to the phase change of water, external energy flow, and the internal energy sink (i.e. the work done within the system). Combining all six components yields a governing expression of heat transport:

$$-\frac{\partial}{\partial z} \left(\lambda \frac{\partial T}{\partial z} \right) + c\rho \frac{\partial T}{\partial t} + L\rho_i \frac{\partial \theta_i}{\partial t} - q(c\rho)_i \frac{\partial T}{\partial z} - \frac{1}{V} \frac{dW}{dt} = Q \quad (5.1)$$

where λ is the thermal conductivity, c is the specific heat capacity, L is the latent heat of fusion, θ is the volumetric fraction, q is the pore water flux, V is a element volume, and W refers to the work done. The subscripts l and i refer to the material properties of the liquid and solid water phases respectively. From left to right the energy components are: conduction, heat released or absorbed due to temperature change, heat released or absorbed due to latent heat of thawing/freezing pore water, advection due to pore water migration, and the rate of work done by the system. The term Q accounts for the external heat flux on the system, which is typically introduced through the thermal boundary conditions.

The work done by the system is the expansion of the ice lens against the overburden stress acting on it, σ_0 . The rate of work done can then be related to the volumetric strain rate of the active ice lens, $\dot{\epsilon}_{lens}^v$, illustrated as follows:

$$\frac{1}{V} \frac{dW}{dt} = \frac{P}{V} \frac{dV}{dt} = \sigma_0 \dot{\epsilon}_{lens}^v \quad (5.2)$$

Where P refers to the pressure acting on the reference ice body with volume V and σ_0 is the overburden stress.

Since ice lens formation is a discrete process, occurring at a specific location within the soil at the cold edge of the frozen fringe, a characteristic length must be introduced to determine the average strain in a representative element volume (REV). In

this study, the thickness of the frozen fringe is selected for the characteristic length. As a result, the volume change of the REV induced by ice lens growth is defined as:

$$\varepsilon_{lens}^v = \frac{\dot{u}_{lens}}{l_f} \quad (5.3)$$

where u is the localized displacement of the system, \dot{u}_{lens} is approximately the frost heave rate, and l_f is the thickness of the frozen fringe. Assuming the temperatures on the boundaries of the frozen fringe, the thickness, l_f , can be expressed as:

$$l_f = \frac{T_{f1} - T_{f2}}{\left(\frac{\partial T}{\partial z}\right)_f} \quad (5.4)$$

where T_{f1} and T_{f2} are temperatures on the boundaries of the fringe, for example -1.0 and 0.0 °C respectively. Generally, the l_f is sufficiently small so that the thermal gradient, $\left(\frac{\partial T}{\partial z}\right)_f$, is assumed to be constant across its depth.

The total rate of the change in the ice volume fraction includes the phase change of the in-situ pore water and the segregated ice lens growth, such that:

$$\frac{\partial \theta_i}{\partial t} = \frac{\partial \theta_i}{\partial T} \frac{\partial T}{\partial t} + \frac{\varepsilon_{lens}^v}{1.09} \quad (5.5)$$

While there is some heat transport due to radiation, this amount is assumed to be negligible for this study. Similarly, it is important to recognize that not all of the presented mechanisms may be materials due to their relative magnitudes. Table 5.1

presents the expected range of values for each of the parameters in equation 5.1, while Table 5.2 contains subsequent implied magnitude of each heat transport mechanism.

Table 5.1: The range in parameter values in equation 5.1 that may be expected under natural conditions (Andersland and Ladanyi 1994).

Parameter	Expected Range of values
λ	1.0 – 3.0 (W/mC)
$\frac{\partial T}{\partial z}$	1.0 – 50.0 (C/m)
$c\rho$	$1.0 \times 10^6 - 3.0 \times 10^6$ (J/m ³ C)
$\frac{\partial T}{\partial t}$	0.0 – 1.0×10^{-3} (C/s)
$(L\rho)_l$	3.34×10^8 (J/m ³)
$\frac{\partial \theta_i}{\partial T}$	0.0-0.25 (1/C)
\dot{u}_{lens}	0.0 – 1.0×10^{-8} (m/s)
l_f	0.05 – 0.5 (m)
$q(c\rho)_l$	0.0 – 3.8×10^{-2} (J/m ² Cs)
σ_0	0 – 100×10^3 (Pa)

Scrutiny of the magnitudes in Table 5.2 indicates the advective heat transport will not exceed 4% of the conductive heat transport for any thermal gradient. From a practical consideration, it is unlikely the thermal conductivity can be reliably defined to an accuracy of less than 4%. Therefore due to its relative magnitude, advection is not considered to be material to the heat transport process. Similarly, the energy consumed in the work done by the ice lens growth will be three orders of magnitude less than the latent

heat released due to the formation of the same ice; consequently this heat is neglected in the energy balance of the system.

Table 5.2: The range in heat transfer mechanisms implied by the parameter values in Table 5.1.

Mechanism	Expression	Minimum - Maximum (J/m³s)
Conduction	$\lambda \frac{\partial T}{\partial z}$	1.0 - 150.0
Heat Capacity	$c\rho \frac{\partial T}{\partial t}$	0.0 - 3.0x10 ³
Latent Heat – Pore Ice	$(L\rho)_i \frac{\partial \theta_i}{\partial T} \frac{\partial T}{\partial t}$	0.0 - 8.4x10 ⁴
Latent Heat – Ice Lenses	$\frac{(L\rho)_i}{1.09} \dot{\epsilon}_{lens}^v$	0.0 - 61.2
Advection	$q(c\rho)_i \frac{\partial T}{\partial z}$	0.0 - 1.9
External Work	$\sigma_0 \dot{\epsilon}_{lens}^v$	0.0 - 2x10 ⁻²

Accounting for the relative magnitude of each transport mechanism, the heat transfer equation can be simplified to:

$$-\frac{\partial}{\partial z} \left(\lambda \frac{\partial T}{\partial z} \right) + c\rho \frac{\partial T}{\partial t} + (L\rho)_i \left(\frac{\partial \theta_i}{\partial T} \frac{\partial T}{\partial t} + \frac{\dot{\epsilon}_{lens}^v}{1.09} \right) = Q \quad (5.6)$$

For the sake of numerical simplification, the equation can be further modified through the use of an apparent volumetric heat capacity term, C^* :

$$-\frac{\partial}{\partial z} \left(\lambda \frac{\partial T}{\partial z} \right) + C^* \frac{\partial T}{\partial t} = Q \quad (5.7)$$

$$C^* = c\rho + (L\rho)_i \left(\frac{\partial \theta_i}{\partial T} + \frac{d\varepsilon_{lens}^v}{1.09dT} \right) \quad (5.8)$$

The values of λ and $c\rho$ are generally not constant and vary by the volumetric composition of the soil, which was discussed in Chapter 4. The inclusion of the heat released due to ice lens formation, and therefore the localized volumetric strain, explicitly couples the governing equation of heat transfer with the description of ice lens growth.

5.2.1.2 Mass Conservation

The mass transport associated with the frost heave process can be attributed exclusively to the pore water migration. There are two transport mechanisms relevant to frozen soils: liquid water movement, as well as ice deformation and migration. Since the model considers saturated or nearly saturated soils, water vapor transport, namely bulk and diffusive flow, is neglected based on their small relative magnitudes.

Liquid water transport in soils is typically characterized through Darcy's law:

$$q_l = -\frac{k}{\gamma_l} \left(\frac{\partial P_l}{\partial z} + \gamma_l \right) \quad (5.9)$$

where P_l is the liquid water pressure and k is the hydraulic conductivity. For frozen soils, both the hydraulic conductivity and water pressure are particularly sensitive to the ice content and temperature. While the water pressure can be defined relative to the ice pressure through the Clapeyron expression (please see equation 2.2), frozen hydraulic conductivity is more difficult to characterize. As noted in Chapter 2, hydraulic

conductivity may vary in excess of an order of magnitude with less than a 1 °C change in temperature in a frozen soil. Furthermore, this material property is notably difficult to measure directly and to date there are a limited number of reported values available. It is apparent that Darcy's law is poorly suited to describe the liquid water migration in the frozen zone and frozen fringe if an accurate relation between k and temperature is not readily available.

Ice deformation during frost heave can be physically attributed to thermal regelation, a process of continual melting and refreezing of ice due to pressure or temperature differentials. Consider an ice body in the pores of a frozen soil, which is surrounded by a thin film of liquid water. Changes in pressure or temperature drive phase change at the ice-water interface, as characterized in the Clapeyron expression. Under a thermal gradient, the liquid film around the ice body experiences an associated pressure gradient. Depending on the geometric arrangement, this pressure gradient may induce a process of melting, liquid water migration, and refreezing. In frozen soils this results in two possible behaviors: either pore ice within the soil structure migrates parallel to the thermal gradient and towards the cold direction, or soil particles in ice rich areas migrate through the ice, along the gradient, towards the warm direction. The second behavior is the founding assumption of the rigid ice model (O'Neill and Miller 1982).

Characterizing regelation is challenging. For example, the rate of regelation depends on the rate at which the latent heat of refreezing is dissipated, which is related to micro scale thermal conduction (Gilpin 1980). To comprehensively characterize this

process the soil would need to be analyzed at the particulate level. Further complicating the situation is that thermal induced regelation can occur concurrently with liquid pore water migration driven by global pressure gradients.

Characterizing the mass transport presents significant practical challenges; physically comprehensive models require accurate values of parameters that are prohibitively difficult to measure and complex geometric representations. A robust numerical model requires only inputs that are either readily available or straightforward to determine.

The segregation potential concept offers an adequate overall approximation of the mass transport process, regardless of its empirical derivation. Segregation potential characterizes the ice lens growth rate using a simple relation to the thermal gradient, presented in equation 5.10. This is somewhat consistent with the underlying physical processes of both the liquid pore water migration and ice regelation, which are both driven by the thermal gradient. The form of the Clapeyron expression (equation 2.2) indicates that the pore pressure is proportional to temperature, which partially supports the assumed linear relation:

$$q_l = SP \frac{\partial T}{\partial z} \quad (5.10)$$

where q_l is the liquid water flux in the frozen fringe and SP is the segregation potential of the soil. The SP parameter encompasses multiple physical properties, including frozen

hydraulic conductivity and ice regelation behavior. In practice, SP varies with a large number of soil characteristics and must be determined experimentally.

While segregation potential provides a characterization of the mass transport in the frozen fringe, it is by itself not a governing expression of mass transport throughout the soil. The approach can readily be integrated into a separate hydraulic analysis, thereby producing a fully coupled thermal-mechanical-hydraulic frost heave model. More specifically, the pore water flux (indicated by the segregation potential) could provide a flux boundary for the hydraulic analysis of the unfrozen zone; if mass transport in the frozen zone is considered to be negligible, then only an analysis of the unfrozen soil is required. While incorporating a hydro analysis into the model would be more physically comprehensive, it is not clear if it would provide a practical benefit for a frost heave expansion problem.

As noted in previous discussion, the advective heat transport term is relatively small under anticipated conditions. Consequently, the full hydraulic consideration is not necessary to effectively analyze the soil thermally. Analyzing the pore pressure in the unfrozen soil would provide for an effective stress analysis, which would allow the model to account for consolidation due to ice lens growth. But qualitative consideration of the frost heave process indicates that consolidation deformation will be significantly smaller than the large deformations caused by frost heave. It was ultimately determined in the formulation of this model to not include an explicit and comprehensive analysis of the pore water transport in the unfrozen soil.

5.2.2 Deformation

The deformation of the soil during the freezing process consists of two components: the volumetric expansion associated with the phase change of water and ice, and the deformation induced by the mechanical processes, including the stress-induced deformation.

5.2.2.1 Mechanical Deformation

The mechanical response of the soil was determined concurrently with, and independently from, the deformation response due to ice lens growth. A linear elastic-perfectly plastic stress-strain response using Mohr-Coulomb failure criterion and total stress analysis was adopted for this model. The magnitude of displacement associated with ice lens growth is typically significantly larger than the internal mechanical deformation response of the soil. However, the mechanical analysis is a critical component of the model due to the redistribution in stress it facilitates and ice lens growth is sensitive to the stress level.

In frozen soils the mechanical material properties of the soil (specifically: E , ν , ϕ , and c) may vary with temperature, volumetric composition, and the strain rate. These properties are defined as deemed prudent for a particular problem. Typical values of E , c , and ϕ in frozen soils have been discussed in Chapter 2.

5.2.2.2 Anisotropic Ice Lens Growth

The volumetric expansion of freezing soils due to ice formation is attributed to two components; the formation of ice owing to the phase change of pore water, and the formation of discrete ice lenses. Consequently, the incremental volumetric strain can be considered the sum of the two components.

$$d\varepsilon_v = d\varepsilon_v^{insitu} + d\varepsilon_v^{lens} \quad (5.11)$$

The rate of volumetric strain due to in-situ pore ice is assumed to be isotropic and can be expressed as follows:

$$\frac{\partial \varepsilon_v^{insitu}}{\partial t} = \frac{\rho_l}{\rho_i} \frac{\partial \theta_i}{\partial T} \frac{\partial T}{\partial t} \quad (5.12)$$

where $\frac{\partial \theta_i}{\partial T}$ was defined previously as the change in the ice fraction in the in-situ pore water and excludes the ice lens volume. This expansion can be considered the primary frost heave of the soil

The volumetric strain due to ice lens formation, or secondary frost heave, is expressed through the use of the segregation potential, SP :

$$d\varepsilon_v^{lens} = \frac{\rho_l}{l_f \rho_i} SP_{(\sigma_l, \dot{z}_f)} \left(\frac{\partial T}{\partial z} \right)_f dt \quad (5.13)$$

where $d\varepsilon_v^{lens}$ is volumetric strain increment of the entire frozen fringe, which has a thickness l_f .

As illustrated in the experimental investigation discussed in Chapter 3, the heave response of a soil, as described by the segregation potential, is dependent on both the stress level and the frost penetration rate. A modified expression of SP was previously proposed in equation 3.9 in Chapter 3 and is presented again here:

$$SP = SP_0(1 + \beta \dot{z}_f)e^{-b\sigma_l} \quad (5.14)$$

where SP_0 , b , and β are empirically determined material constants. The stress acting normal to the active ice lens, σ_l , can be determined from the orientation of frozen fringe.

$$\sigma_l = \sigma_{ij}n_in_j \quad (5.15)$$

where \mathbf{n} is the unit vector defining the normal of the ice lens plane, illustrated in Figure 5.1. The frost penetration rate, \dot{z}_f , can be defined as:

$$\dot{z}_f = \frac{dT}{dt} \left(\frac{\partial T}{\partial z} \right)_f^{-1} \quad (5.16)$$

Due to the nature of ice lenses, most of the displacement associated with lens formation occurs in the direction of the thermal gradient across the frozen fringe. Consequently the deformation induced by lens formation is at least partially anisotropic. This behavior is characterized by an ice lens growth tensor. The second rank tensor accounts for the anisotropy of the ice lens growth through a fractional anisotropy factor ζ and includes a tensor transform about the z-axis to orient the expansion relative to the frozen fringe (Michalowski and Zhu 2006).

$$\varepsilon_{ij}^{lens} = Q_{ip}Q_{jq}\varepsilon^{lens}a_{pq} \quad (5.17)$$

where \mathbf{Q} and \mathbf{a} are the transform based on \mathbf{n} and the unit growth tensor respectively, defined as follows:

$$Q_{ij} = \begin{vmatrix} \cos \theta & -\sin \theta & 0 \\ \sin \theta & \cos \theta & 0 \\ 0 & 0 & 1 \end{vmatrix} \quad (5.18)$$

$$a_{ij} = \begin{vmatrix} \zeta & 0 & 0 \\ 0 & (1-\zeta)/2 & 0 \\ 0 & 0 & (1-\zeta)/2 \end{vmatrix} \quad (5.19)$$

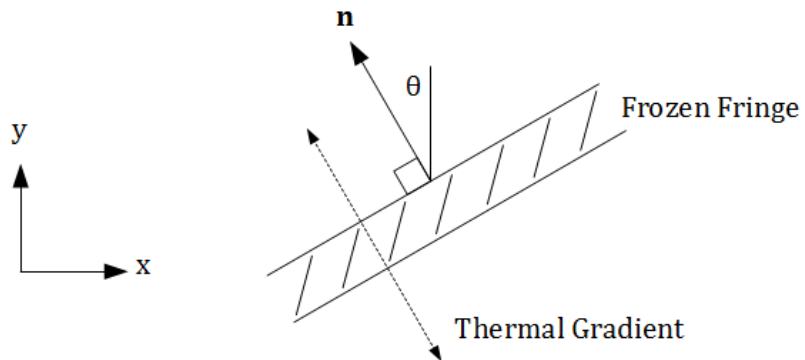


Figure 5.1: Illustration of frozen fringe and heave orientation.

The parameter ζ can vary between 1 and 1/3. When ζ is 1, all of the volumetric strain due to frost heave occurs parallel to the thermal gradient of the frozen fringe. When ζ is 1/3 the volumetric strain is isotropic. The value of ζ has not been extensively investigated in the reported literature. Experimental observations generally indicate a value closer to 1 and similar studies have typically assumed a value between 0.75 – 1.0 (Michalowski 1993; Konrad and Shen 1996; Kim 2011). In this work ζ is generally

assumed to be 0.9 and its influence is explored in more detail in Appendix E and Chapter 6.

5.2.3 Numerical Considerations

5.2.3.1 Model Implementation

Ice lenses form in discrete locations within the soil and their growth rate is independent of the ice lens volume. More specifically, the active ice lenses are located along isotherms associated with the cold end boundary of the frozen fringe. Finite elements are poorly suited to characterize such discrete internal process; assigning large volumetric strains to single integration points within elements introduces unnecessary numerical instability and computation error. This presents a challenge when representing frost heave deformation in a finite element scheme.

In the interest of numerical stability, it is advantageous to distribute the volumetric strain across multiple integration points. While this deviates from the understanding of the physical process, as long as the number of integration points is kept to a moderate number, it should not significantly affect the numerical solution. A smearing function is introduced using a proportionality parameter, ξ , to distribute the ice lens induced strain based on temperature. The parameter ξ varies between 0 and 1 with temperature as illustrated in Figure 5.2. As a result, the volumetric strain induced by ice lens growth in an element is determined as:

$$\varepsilon_{(T)}^{lens} = \xi_{(T)} \varepsilon^{lens} \quad (5.20)$$

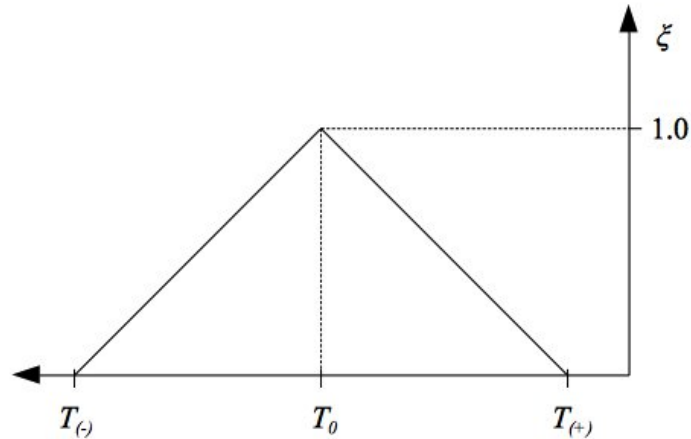


Figure 5.2: Illustration of the definition of the proportionality parameter, ξ , used to distribute volumetric strains due to ice lens growth within a FEM element.

$$T_{(-)} = T_0 - \left(\frac{\partial T}{\partial z} \right)_f l_e \quad (5.21)$$

$$T_{(+)} = T_0 + \left(\frac{\partial T}{\partial z} \right)_f l_e \quad (5.22)$$

where l_e is the element characteristic length. The term T_0 can be considered as the expected temperature of the active ice lens and is defined as the cold end temperature of the frozen fringe. This formulation distributes the heave strains across roughly two elements in the direction of heat flux in the frozen fringe, i.e. parallel to the fringe thermal gradient. This approach assumes equally sized, square elements. Any deviation in either of these assumptions in the actual mesh will introduce numerical error. The mesh sensitivity is examined and discussed in Appendix E and Chapter 6.

5.2.3.2 Solution Framework

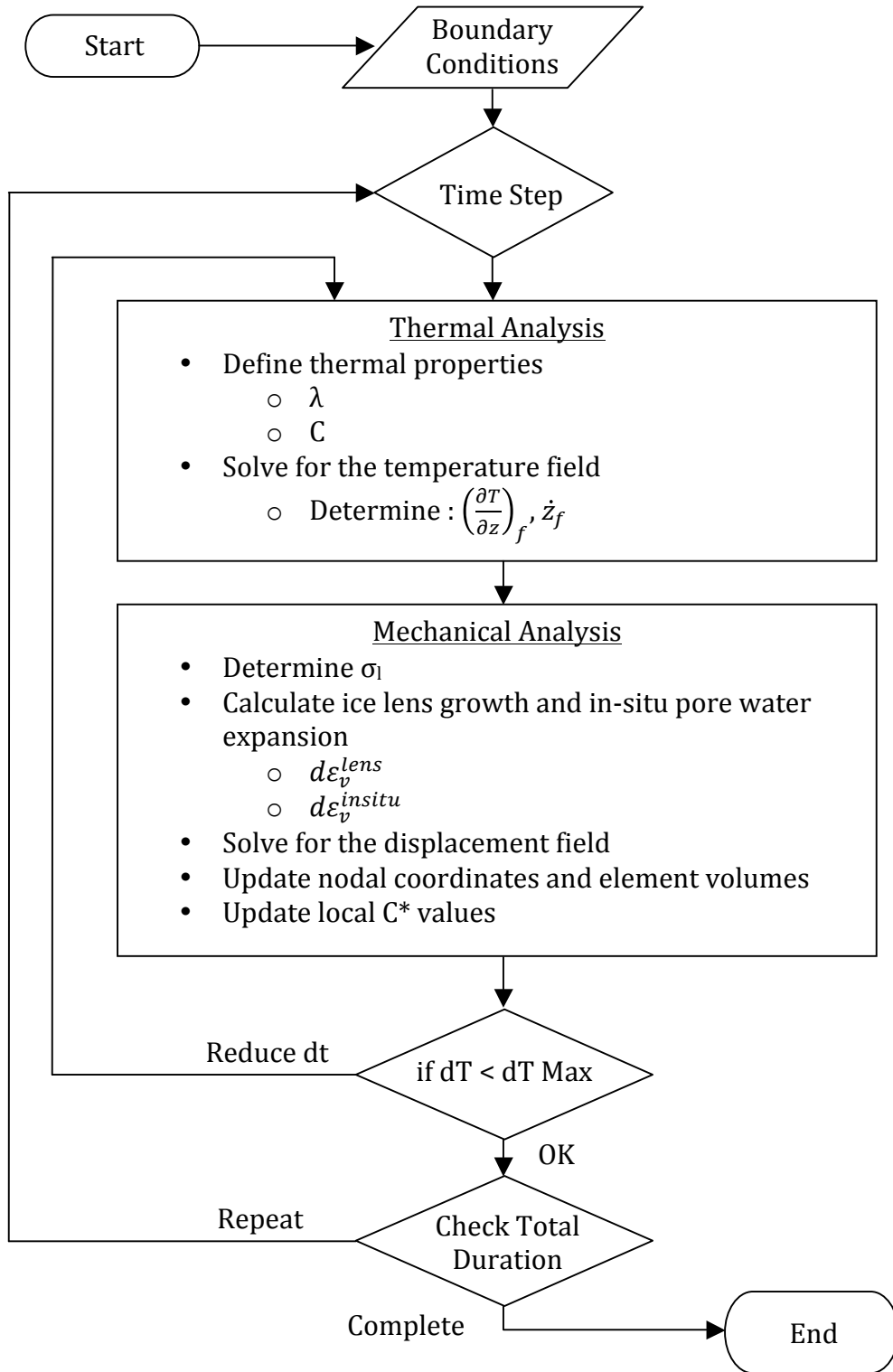


Figure 5.3: Flowchart of the model procedure.

The solutions to the governing equations outlined above are approximate in this approach through an implicit, iterative scheme. Figure 5.3 illustrates the solution procedure implemented into the FEM simulations.

5.3 SIMULATIONS OF LABORATORY TEST

The laboratory frost heave tests presented in Chapter 3 are used to evaluate the performance of the frost heave model under one-dimensional conditions. Simulations conducted under the same thermal and mechanical boundary conditions as the experimental test are compared to the observed results.

The thermal-mechanical frost heave model is implemented into and solved using the finite element method in the commercial software ABAQUS/Standard and analyzed with ABAQUS/CAE. User defined subroutines (specifically ‘USDFLD’, ‘UEXPAN’, and ‘UVARM’) are used to define the frost heave model with the ABAQUS framework. These subroutines can be found in Appendix D. Although the experimental tests are one dimensional, the FEM model was developed for two dimensional plane strain conditions. The system was discretized with 8-node elements, referred to as CPE8RT in ABAQUS/Standard, which were approximately square and 0.02 m in size. Reduced integration, with 4 integration points per element is utilized. In CPE8RT elements, the displacement is interpolated using a quadratic shape function, while temperature is interpolated linearly. Figure 5.4 illustrates the geometry and boundary conditions of the simulations and the corresponding FEM mesh utilized. The height of the simulated body was approximately 200 mm, but varied slightly between specific tests. The sample width,

while generally assumed to be immaterial, was nonetheless maintained at a constant 100 mm.

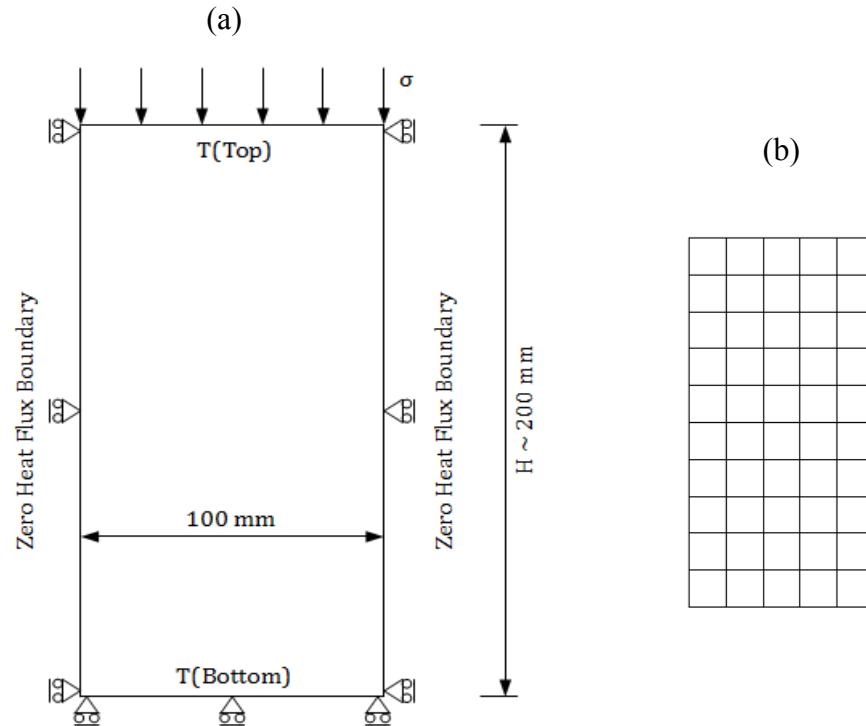


Figure 5.4: Schematic and boundary conditions of the 1D simulations (a) and the corresponding FEM mesh utilized (b).

5.3.1 Material Properties

Due to the specific mechanical boundary conditions of the one-dimensional frost heave tests, the volumetric expansion associated with ice lens growth does not induce significant changes in the stress level within the soil. Furthermore, the surcharge applied in these tests is well within the elastic limit of the soil. Consequently, the mechanical constitutive relation was simplified as linear elastic in these simulations. The elastic modulus and Poisson's ratio of the two materials were assumed to be 11.2 MPa and 0.30 respectively for both frozen and unfrozen conditions; please refer to sections 2.4 and 6.2.2.1 in Chapters 2 and 6 respectively for a more detailed discussion on the mechanical

properties of frozen soil. As the material stiffness does not have significant influence on the simulation, it was not considered in detail in the analysis.

The thermal conductivity and heat capacity of the two materials, FHC and BSM in Chapter 3, were characterized from the constituent volumetric fractions using the geometric mean approximation and simple volumetric weighting approximation respectively (as discussed in Chapter 4) such that.

$$\lambda = \prod_{i=1}^4 \lambda_i^{\theta_i} \quad (5.23)$$

$$C = \sum_{i=1}^4 C_i \theta_i \quad (5.24)$$

This approach requires the relationship between the liquid water content and temperature, also referred to as the soil-freezing characteristic, which was not directly measured for either material. Following the empirical approach proposed by Tice et al. (1976), the soil-freezing characteristic was approximated from the liquid-limit, as.

$$w_{u,T=-1} = 0.364w_{N=25} - 3.01 \quad (5.25)$$

$$w_{u,T=-2} = 0.338w_{N=100} - 3.72 \quad (5.26)$$

$$w_u = m_1 |T|^{m_2} \quad (5.27)$$

where w_u is the unfrozen or liquid water content in %, T is the temperature in °C, and $w_{N=25}$ and $w_{N=100}$ are the water contents in % corresponding to 25 and 100 blows respectively in the liquid limit test. The material parameters m_1 and m_2 are determined through regression analysis from equations 5.1 and 5.2. Equation 5.25 – 5.27 are only valid for $T < 0$ °C. The soil-freezing characteristic is also used to determine the in primary frost heave caused by in situ pore water expansion and the corresponding latent heat released. The parameters used to define the thermal properties of both soils are summarized in Table 5.3.

Table 5.3: Material properties defining the thermal conductivity of FHC and BSM.

Property	FHC	BSM
m_1	7.18	3.46
m_2	-2.19	-6.84
n	0.278	0.346
Sr (%)	85	99
Gs	2.60	2.73
λ_s (W/m°C)	2.92	2.92
λ_l (W/m°C)	0.56	0.56
λ_i (W/m°C)	2.24	2.24
λ_a (W/m°C)	0.024	0.024
$C_s 10^6$ (J/m ³ °C)	2.36	2.36
$C_l 10^6$ (J/m ³ °C)	4.18	4.18
$C_i 10^6$ (J/m ³ °C)	1.94	1.94
$C_a 10^6$ (J/m ³ °C)	0.001	0.001

Figure 5.5 illustrates the calculated effective thermal conductivity of the two materials using the approximated soil-freezing characteristic and the geometric mean. The prepared BSM samples have a higher frozen conductivity due to its higher void ratio and the degree of saturation.

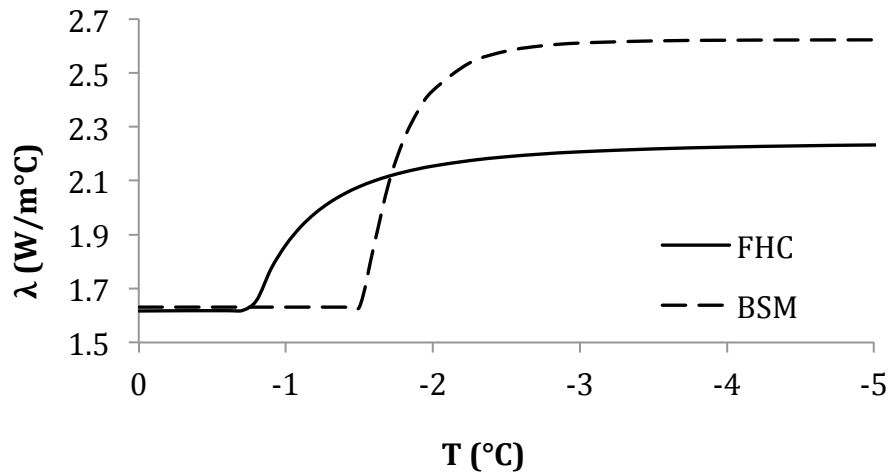


Figure 5.5: The modeled variation in soil thermal conductivity with temperature.

Frost susceptibility in this model is characterized through equation 3.9 in Chapter 3. This expression contains the following parameters: the baseline segregation potential, SP_0 , the freezing rate sensitivity, β , and the stress level sensitivity, b . These parameters for both FHC and BSM were determined based on the experimental results, discussed in Chapter 3; Table 5.4 summarizes these values.

Table 5.4: Frost heave characterizing parameters.

Property	FHC	BSM
$SP_0 \times 10^5$ (mm ² /s°C)	22.00	26.50
$\beta \times 10^6$ (s/m)	3.64	5.95
b (1/MPa)	4.95	5.00

5.3.2 Boundary Conditions

Two types of thermal boundary conditions were applied in the laboratory tests: step and ramped freezing, which are discussed in details in Chapter 3. Under step freezing conditions, there is an initial and dramatic decrease in the temperature at the top, or cold-end, boundary of the specimen. Due to the capacity limitations of the heat exchanger, in practice it requires a certain amount of time to reach the prescribed temperature. Ignoring this effect would lead excessive and fictitious thermal fluxes through the soil during the initial freezing period. In addition to being a poor physical representation of the experimental system, the extreme thermal gradients induce unnecessary additional potential for numerical error during the transient analysis. To address these concerns, the thermal boundaries were ramped linearly from the initial body temperature to the imposed boundary temperature over a period of approximately, 2.5 to 5.0 hours, depending on the difference between the temperatures. The small ramp time was significantly less than the test duration. Alternatively, the ramped thermal boundary conditions did not induce the same rate of temperature change or large thermal fluxes, and consequently were applied without adjustment. A superior representation of the system would be to define the top and bottom boundaries using thermal flux as opposed to temperature. However, since the flux was not measured in the experiments temperature boundaries were employed.

The pressure at the top of the simulated body was constant throughout the simulations and equal to the applied surcharge associated with a particular test. Additionally, body forces due to the material self-weight were included in the simulation,

but due to the relatively small heights of the samples, self-weight has little impact on the results. Other mechanical boundary conditions are illustrated in Figure 5.4.

5.3.3 Evaluation of Model Performance

The simulated frost heave response of test BS-1 is presented and compared with the experimental observations in Figure 5.6. The metrics used to evaluate the model performance are the heave or the surface displacement, the vertical position of the frost front, and the variation of the segregation potential. For all three considerations the model achieved good agreement with the observed behavior. More specifically, the frost heave profile closely reproduces the total heave values, 13.8 mm predicted versus 13.1 mm observed, though under-predicting the terminal heave rate. Similarly, the final frost front position in the simulation agrees well the laboratory test observations, 94.1 mm predicted versus 101.3 mm observed. Regarding the segregation potential, the model does appear to yield higher values than observed during both the initial freezing stage and the final 50 hours of the test. This deviation is an indication that the characterization function of SP, equation 3.9 in Chapter 3, does not perfectly capture this complex physical process. However, it is clear that a constant segregation potential poorly represents these frost heave experiments.

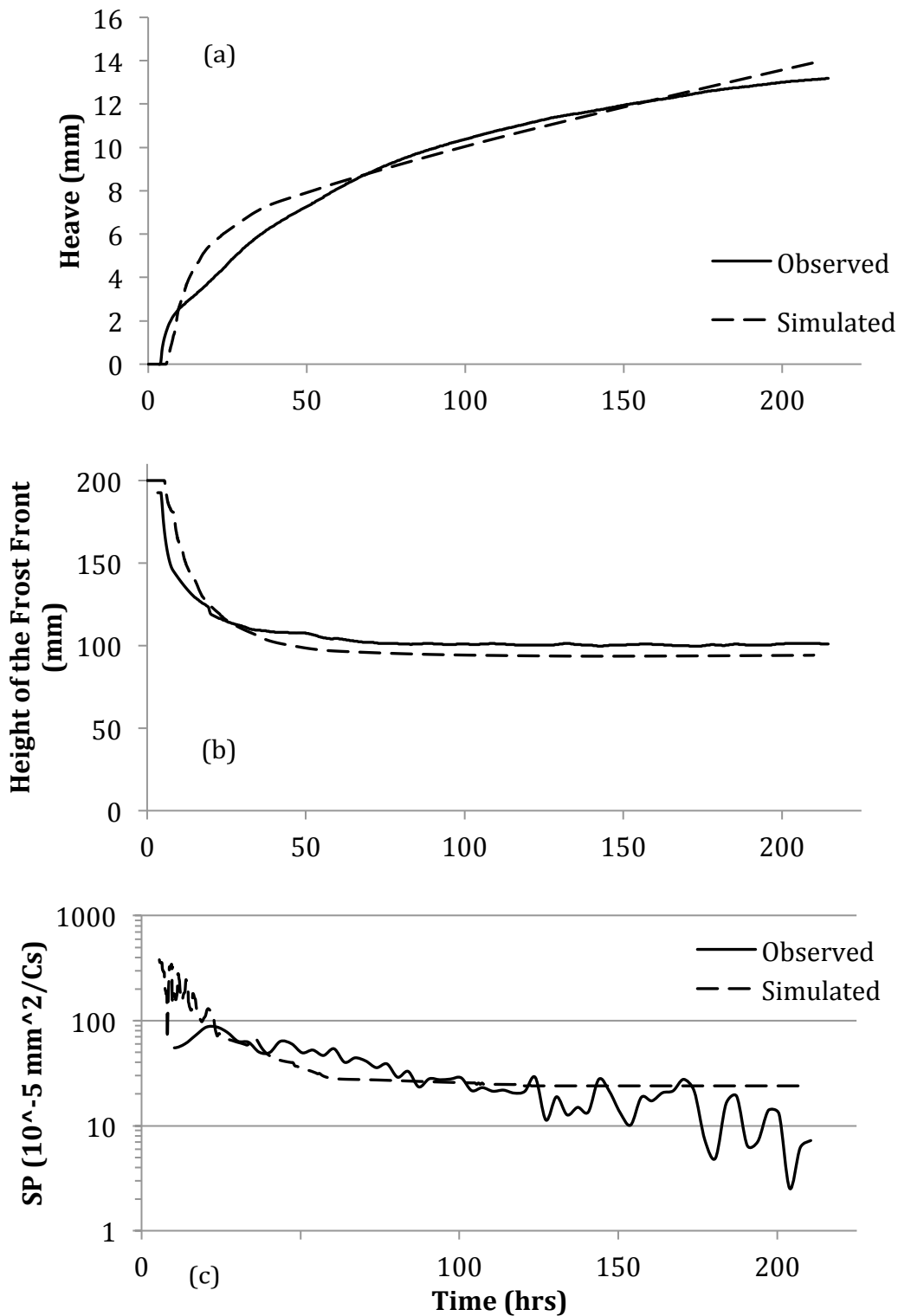


Figure 5.6: The simulated and observed heave, (a), frost penetration, (b), and segregation potential (c) of test BS-1.

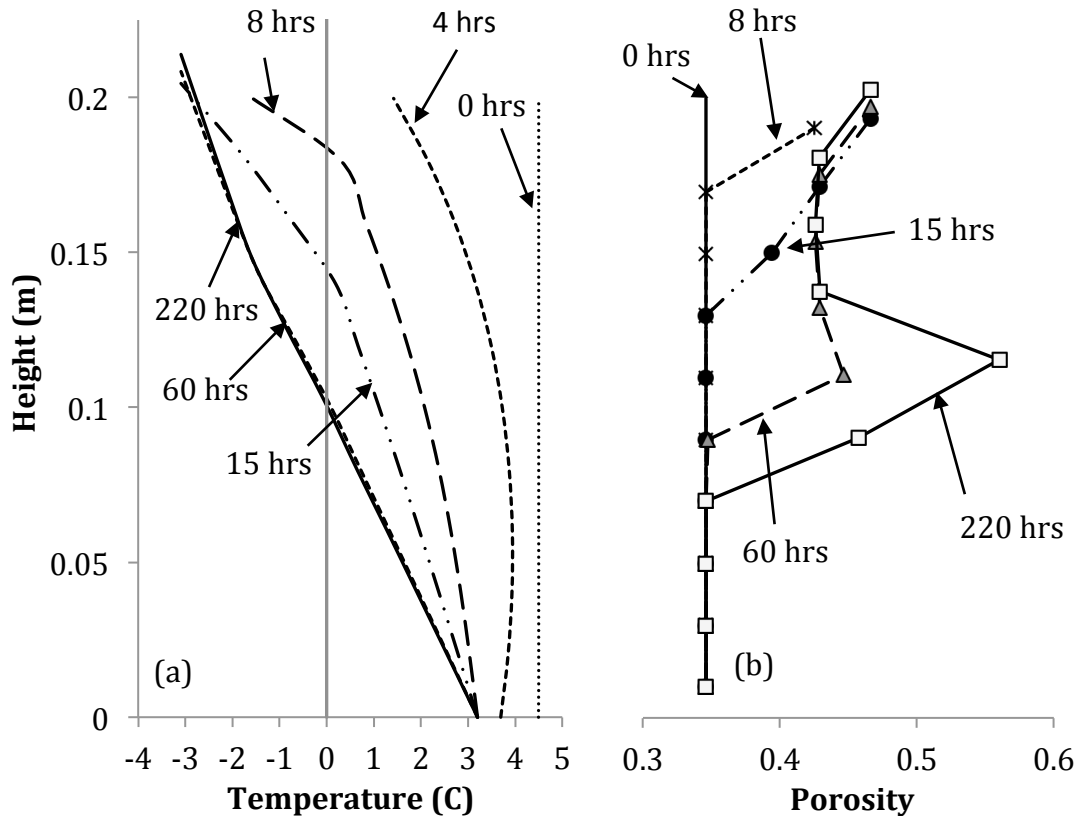


Figure 5.7: The simulated temperature (a) and porosity (b) profiles corresponding to select time points in test BS-1.

Figure 5.7 illustrates the vertical profiles of temperature and porosity at select times during the simulation of test BS1. A large change in porosity develops adjacent to the final position of the frost front, corresponding to the formation of substantial ice lenses. The values represent the average porosity associated with the particular integration element and consequently will be affected by the degree of discretization associated with the model. Please refer to Appendix E for a mesh sensitivity analysis.

The simulations utilized a set of material parameters including several properties that were inherently empirical, specifically the frost heave characteristics SP_0 , β , and b .

The quality of the simulated results is subject to the quality of the reliability of these quantities. Figures 5.8 and 5.9 present the variation in the simulated heave development with the input values characterizing frost susceptibility: SP_0 and β . For BSM, $SP_0 = 26.5 \times 10^{-5} \text{ mm}^2/\text{Cs}$, $\beta = 5.95 \times 10^6 \text{ s/mm}$, and $b = 5.0 \text{ 1/MPa}$, which yields a simulated heave of 13.8 mm at hour 200. When SP_0 is varied by $26.5 \pm 2.5 \times 10^{-5} \text{ mm}^2/\text{Cs}$, or 9.4%, the predicted frost heave varies between 12.5 and 15.0 mm at hour 200, as illustrated in Figure 5.8. Similarly, when β is varied by $5.95 \pm 0.6 \times 10^6 \text{ s/mm}$, 10.1%, predicted heave ranges from 13.3 to 14.4 mm at hour 200, see Figure 5.9. This indicates the model is generally more sensitive to SP_0 than β over the first 200 hours of this particular test.

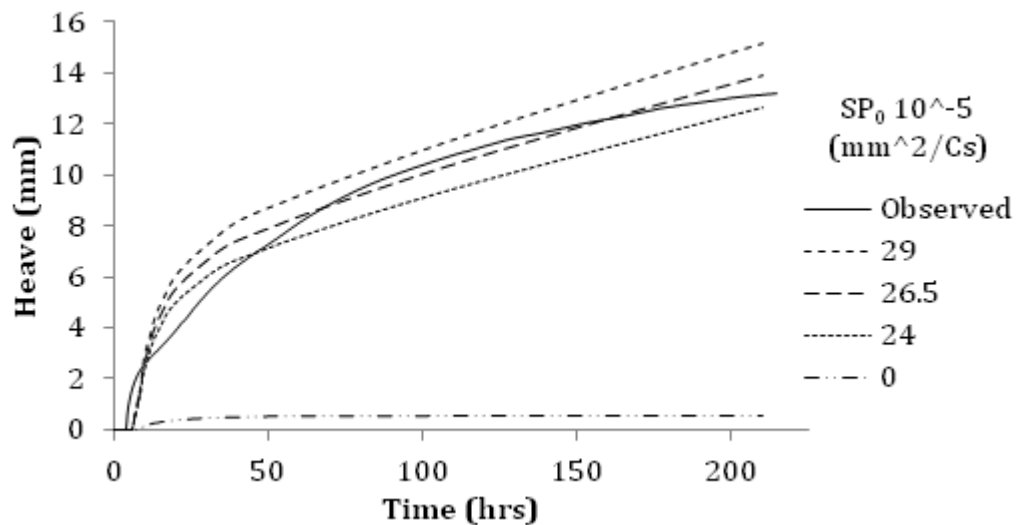


Figure 5.8: The observed and simulated frost heave profiles of BS-1 at varying SP_0 by 9.4% ($\beta = 5.95 \times 10^6 \text{ s/mm}$).

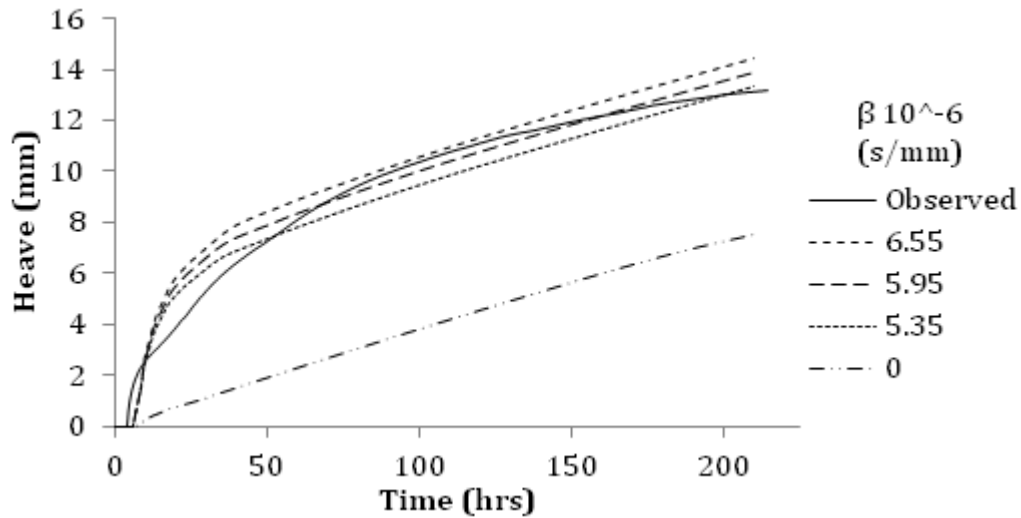


Figure 5.9: The observed and simulated frost heave development with time of BS-1 when β varies by 10.1% ($SP_0 = 26.5 \times 10^5 \text{ mm}^2/\text{s}^\circ\text{C}$).

Also included in Figures 5.8 and 5.9 is an evaluation of simulated heave when $SP_0 = 0$ and $\beta = 0$, respectively. While it is unsurprising that without a segregation potential term the simulations under predict frost heave, the results quantify the contribution of in-situ pore water expansion on the frost heave. Alternatively, with $\beta = 0$ the predicted time history of the heave fails to adequately capture the observed behavior; without β the simulations under-predict the initial heave rate, though provide reasonable agreement with the final heave rate.

As discussed in the model formulation in Chapter 5, the soil heat capacity is made a function of the volumetric composition of the constituent phases while simultaneously accounting for the latent heat released in the phase change of the pore water. For comparison purposes, the simulations were also conducted using a constant approximation of the heat capacity, $C = 3.10 \times 10^6 \text{ J/m}^3\text{C}$, approximately the average heat capacity of the frozen and unfrozen soil. As presented in Figure 5.10, using a

constant C value the gradual development of frost heave is not adequately captured. The amount of frost heave is significantly underestimated while the depth of frost penetration is slightly overestimated. While it may seem counterintuitive for heat capacity to affect the long term temperature profile, the latent heat released from ice lens formation was accounted for through C and this heat is released at a rate proportional to the heave rate. Neglecting latent heat effects during freezing has a similar effect to underestimating the unfrozen thermal conductivity. The results provide anecdotal evidence supporting the importance of a physically comprehensive thermodynamic frost heave model.

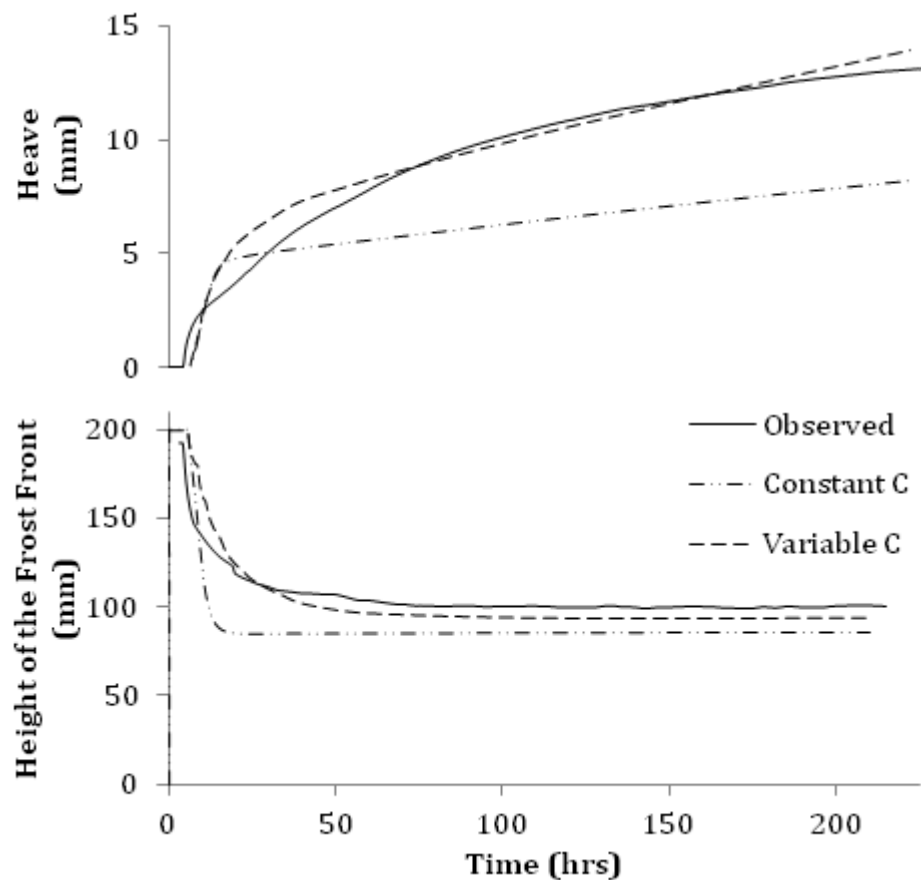


Figure 5.10: The variation in the simulated results of BS-1 with constant soil volumetric heat capacity and the base-line variable case.

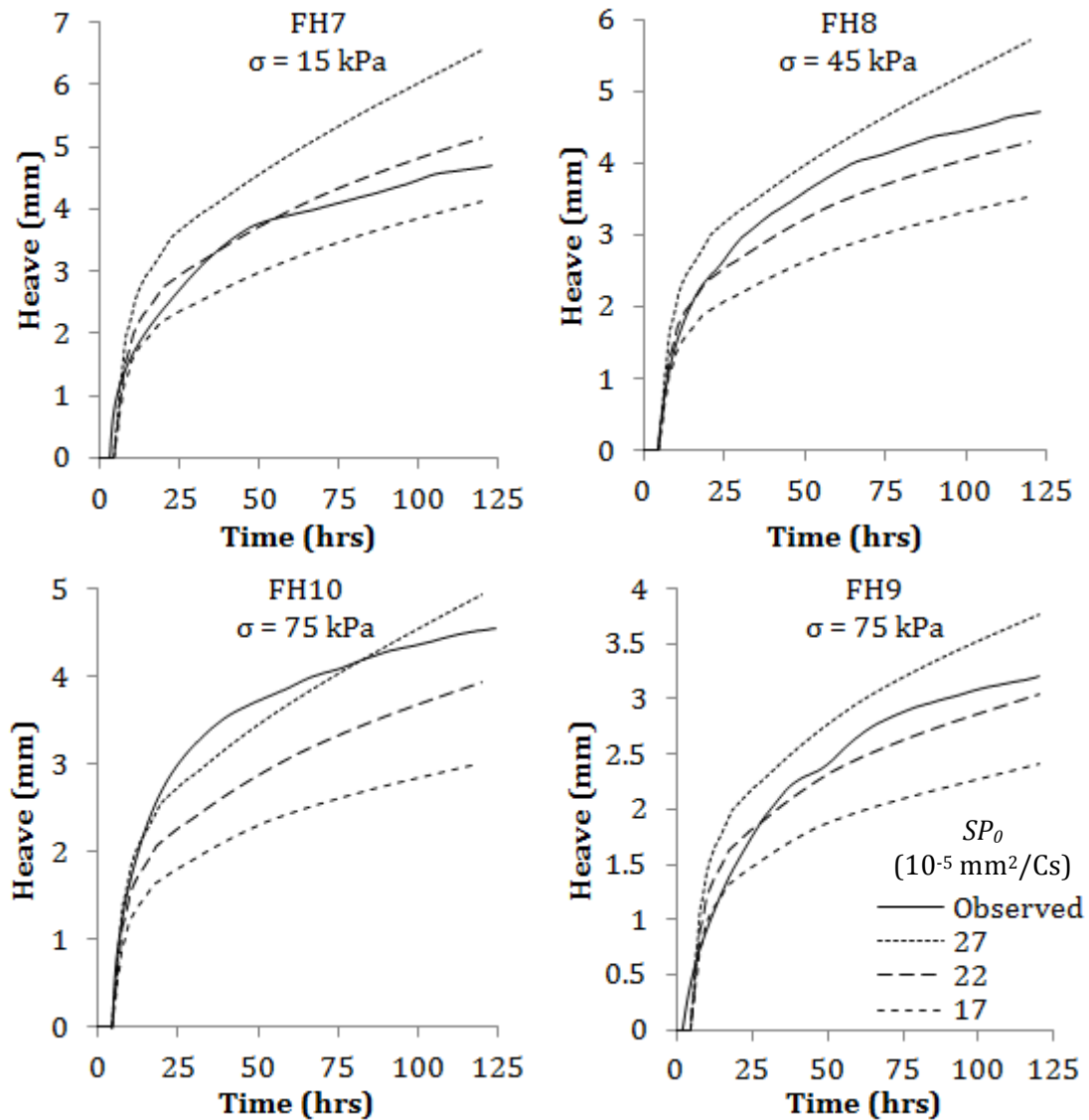


Figure 5.11: The observed and simulated frost heave evolution of FHC under overburden stress levels of: 15 kPa, 45 kPa, 75 kPa, and 125 kPa. The simulations include three values of SP_0 .

The influence of overburden stress level on the frost heave response is next examined. The evolution of frost heave with time in four tests of step freezing conducted on the lean clay with sand, FHC, at various overburden stress levels, but with identical thermal boundary conditions is presented in Figure 5.11. The simulations were conducted

with three values of SP_0 , with constant values of $\beta = 3.64 \times 10^6$ s/m and $b = 4.95$ 1/MPa. The results show that there is generally good agreement between the observed and the simulated results with regards to stress level. However, the simulations of test FH10 under-predicts total heave values. This is attributed to the general error and variability of both the frost heave tests and the interpretation of the SP_0 parameter. These results also provide a general indication of the robustness of the model and conceptual approach, as the model parameters determined from one set of boundary conditions provide reasonable predictions of the heave response under different boundary conditions.

Simulations were also performed to reproduce results of the frost heave tests under ramped freezing boundary. As previously mentioned, the model parameters characterizing frost heave of BSM and FHC were obtained from results of step freezing tests. Figure 5.12 compares the simulated heave response in tests BR-2 and FR-3, which were conducted under identical thermal boundary conditions, with the experimental observations. For comparison purposes, the simulation results with an approximate $\pm 10\%$ variation in the SP_0 are also included in Figure 5.12. The model does not fully capture the time history of heave of either material under ramped thermal boundary conditions. The terminal heave rate of both simulations agrees well with the test results; however the model fails to capture both the delay in the onset of heaving and the large initial apparent segregation potential that was observed in the tests. Simulations of the heave time histories of the remaining ramped tests BR-1, FR-1, and FR-2 can be found in Appendix F. Altogether, the results display consistent behavior as the model appears to under-predict total heave while providing a good presentation of the terminal heave rate.

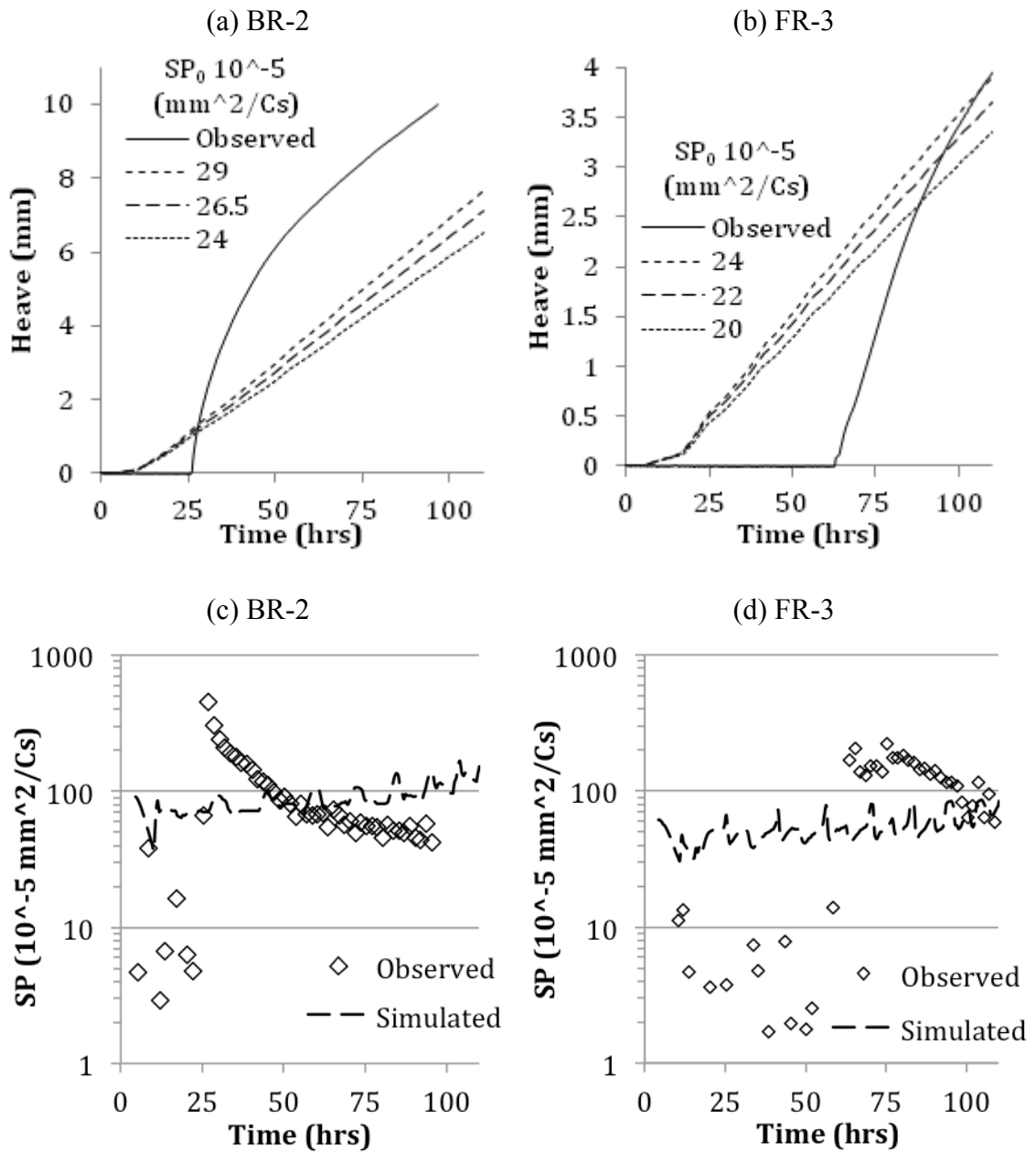


Figure 5.12: The simulated and observed heave evaluations of tests BR-2 (a) and FR-3 (b) and the simulated and observed apparent SP values of the same materials (c) and (d).

The deviation in the simulated heave from the observed values under ramped conditions is attributed to the characterization of SP , equation 3.9 in Chapter 3. As noted

previously, this characterization does not adequately capture the delay in the onset of heaving or the corresponding large heave rates. While the delay in heave onset is a tangible physical process, consistently observed across all frost heave tests, it is not necessarily relevant in practical applications. The maximum observed time delay in the heave onset is approximately 80 hours, a significant period of time for the laboratory scale tests. However, in practical frost heave problem freezing will likely be on the order of months to years. Therefore not accounting for the delay in heave onset should have a minimal impact on variation between the model's prediction and the real displacement in a full-scale engineering problem.

In addition, the sensitivity of the simulations to various numerical parameters was explored. More specifically, the time step and the element geometry were considered. It was found that a fixed time step yields unsatisfactory results when exceeding 1000 s; at time steps smaller than this the computational time became excessive. Alternatively the variable, temperature controlled time step scheme was far more efficient and the results were found to be generally insensitive to the prescribed temperature increment. This was the time stepping scheme used in this transient analysis. Regarding element geometry, the results showed limited sensitivity to the element size, but significant sensitivity to the element aspect ratio. Variations in the simulated results were minimal when the aspect ratio did not exceed 2.0. This investigation is included in Appendix E.

5.5 SUMMARY AND CONCLUSIONS

This chapter presents a fully coupled thermodynamic-mechanical model of the frost heave process. A comprehensive governing equation of heat transport was presented and its components were explored in detail. Mass transport is characterized through the segregation potential concept. Segregation potential is used to explicitly characterize ice and liquid water transport in the frozen fringe, while implicitly describing the pore water transport in the unfrozen soil. Ultimately volumetric expansion associated with ice lens growth is characterized through this concept. A tensor is proposed to describe the two dimensional volumetric expansion associated with ice lens growth in a plane-strain context. This tensor utilizes a fractional anisotropy parameter, ζ , to define the anisotropic strain. A further summary of the relevant fundamental assumptions in the model derivation is as follows:

- The soil is fully saturated.
- The frozen and unfrozen soil is isotropic and can be locally homogenized using appropriate composite models based on volumetric composition.
- The frozen fringe can be defined using assumed thermal boundaries
- Mass transport in the frozen soil is negligible.
- Mass transport in the frozen fringe can be fully represented with the segregation potential concept.
- The magnitude of consolidation in the unfrozen soil due to effective stress changes induced by frost heave is not material.

- Advective heat transport and work associated with ice lens expansion is negligible with respect to the energy balance.
- The mechanical response of both the frozen and unfrozen soil can be represented with Mohr-Coulomb failure criteria and total stress analysis.

The model was derived specifically for implementation into a finite element method scheme. This chapter discussed some of the practical consideration involved in this implementation, such as the distribution of volumetric strain across multiple elements and integration points was examined.

In addition, the frost heave model was implemented to simulate the frost heave response of the 1D frost heave tests, presented in Chapter 3. The model adequately captured both the displacement and thermal responses under stepped thermal boundary conditions. Under ramped boundary conditions the model failed to simulate the delay in the onset of heaving or the initial large apparent SP observed in these tests. As a result, the simulations tend to under-predict total heave under ramped conditions. Regardless, the model provides good agreement with the observed terminal heave rate, indicating that for sufficiently long durations the model may be effective under such boundary conditions.

The expression proposed in Chapter 3, equation 3.9, to characterize the variation in the apparent SP improves the agreement between the modeled and observed heave response. However, some deviation is observed between the characterized SP and the observed values, particularly during the initial, highly transient freezing under step

conditions. This deviation is ultimately attributed to the empirical nature of the proposed expression; while it is derived from observed physical behavior it may not fully capture the complex hydrodynamic process associated with segregated ice growth.

The frost heave model is validated using the experimental results, albeit with some notable conditions. The developed model has some limitations, specifically, it is poorly suited for short duration problems involving thermal delays in the onset of freezing associated with super-cooling of pore water. This behavior is not characterized by this approach.

CHAPTER 6 MODELLING OF THE CALGARY PIPELINE TEST

6.1 INTRODUCTION

The frost heave model that was formulated, implemented, and evaluated within a one-dimensional context in Chapter 5 is applied to a two-dimensional field problem in this chapter. The objective of this chapter is to verify the capability of the proposed model to predict, within a reasonable degree of accuracy, the displacement response of a geotechnical structure during the frost heave process under two-dimensional conditions.

6.1.1 Description of the Calgary Pipeline Tests

The Calgary pipeline experiments were originally conducted to support the design of a 1200 km natural gas pipeline connecting the Mackenzie River delta with existing gas transportation infrastructure in northern Alberta. Known as the Mackenzie valley pipeline, it was to carry chilled gas at around -10 °C and be buried in a region of discontinuous permafrost where it was expected to be actively freezing frost susceptible soils during its operations. Consequently, from its inception it was apparent that frost heave would be a critical design consideration. At the time, the conceptual understanding of the frost heave process was modest and there were limited tools available for engineers to predict the displacement response. A series of full-scale experiments examining different pipe burial configurations and designs were conducted to provide the much-needed empirical design data. A detailed description of the experiments and the test

facility can be found in the work published by Slusarchuk et al. (1978) and Carlson et al. (1982).

Conducted at the University of Calgary starting in 1974, several full-scale experiments examined the frost heaving of buried pipelines over approximately 10 years. Initially four separate pipe burial configurations were examined; each pipe section was 12.2 m long and 1.2 m in outer diameter. Three of these pipe configurations are examined herein. They are referred to as: control, deep burial, and gravel sections. The control section was buried in a 2.0 m deep trench and the deep burial section was located 2.9 m deep. For the gravel configuration, the trench was dug to 3.0 m then a 1.0 m layer of gravel was added followed by the pipe. The three configurations are illustrated in Figure 6.1. The excess spoil for all sections was mounded over the pipelines after burial. Assuming the trenches were dug 2.0 m wide and the berm was approximately 3.0 m wide, the implied berm height of the control and the deep burial sections was approximately 0.3 m and the gravel section was 1.0 m. On day 400, the berms on the control and deep burial sections were increased to 1.5m (Slusarchuk et al. 1978).

Sampling of the upper 8.0 m of soil at the facility indicated the soil consisted of 13% sand, 64% silt, and 23% clay, with a plastic and liquid limit of between 18-24% and 24-31%, respectively. The soil is classified as an overconsolidated inorganic clayey silt with a low to medium plasticity, referred to here as Calgary silt or CS. The depth of the water table at the test facility was observed to be between 2.3 and 2.6 m below the ground surface. Accounting for the height of the capillary fringe, the top 1.4 m of soil was

assumed to have insufficient moisture to support ice lens growth and was considered to be non-frost susceptible (Slusarchuk et al. 1978).

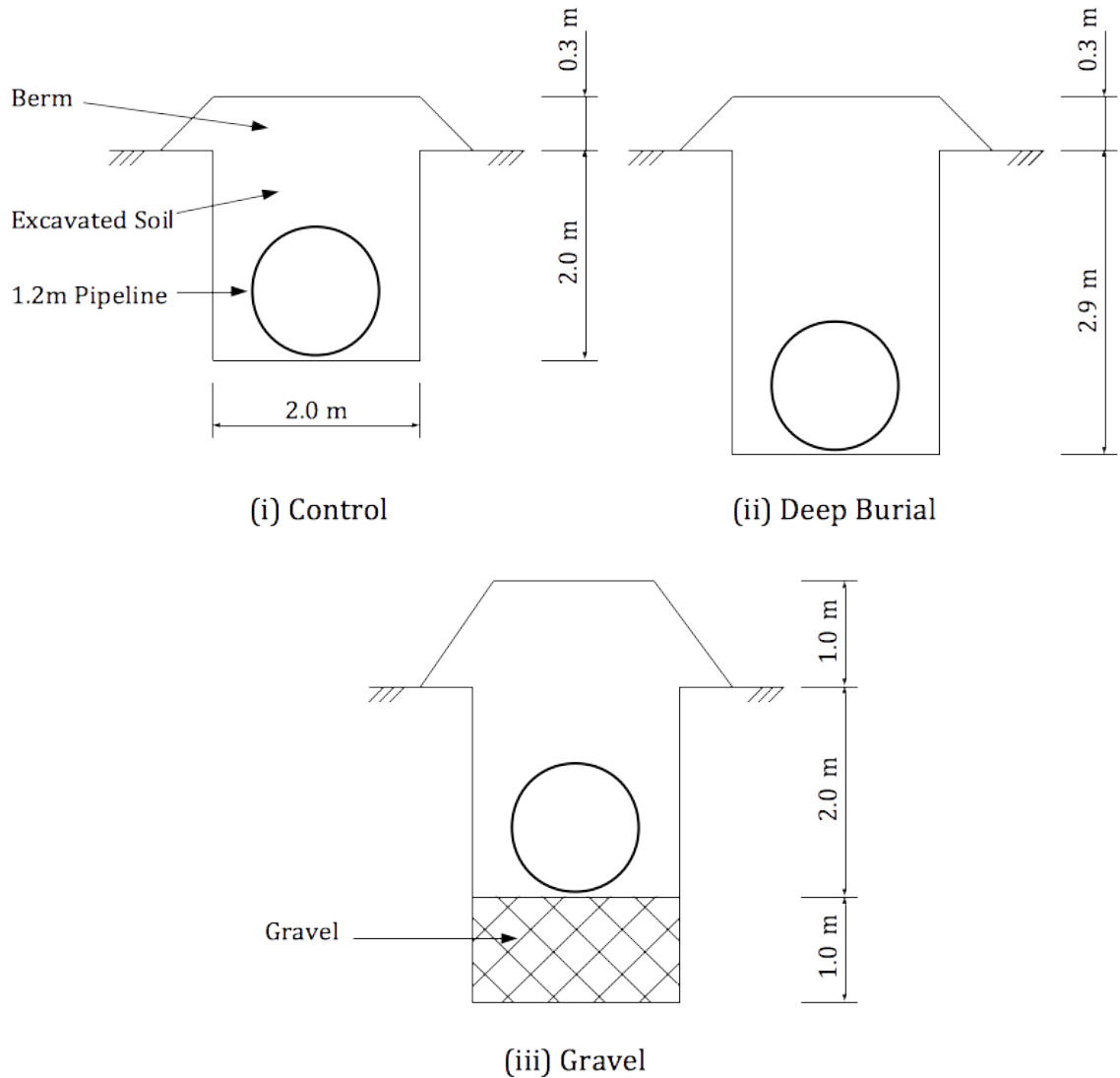


Figure 6.1: Schematic of the three examined pipe configurations (Slusarchuk et al. 1978).

Circulating chilled air was used to maintain a target pipe temperature of $-10\text{ }^{\circ}\text{C}$ for all sections. A nearby refrigeration system provided cooling for the facility. The specific

capacity of the system was not disclosed though it was observed to take several months for the pipelines to reach the target temperature.

6.2 MODEL FORMULATION

The frost heave model developed in this study was implemented into a two-dimensional finite element model to simulate select field tests in the Calgary pipeline experimental study. The software packaged used in the analysis was *ABAQUS/Standard*. The soil and pipe were simplified as a plane-strain system, discretized with eight-node continuum elements with reduced integration, referred to as CPE8RT. No sliding was assumed between either the different soil layers or the pipe-soil interface. The duration of the analysis was 9×10^7 s or the first 1042 days of testing.

6.2.1 Geometry and Boundary Conditions

The geometric representation of the control configuration is illustrated in Figure 6.2. The geometric details, mechanical boundary conditions, and the finite elements meshes used in the model for the other two configurations can be found in Appendix F. The meshes representing the control, deep burial, and gravel configurations consists of 391, 376, and 373 elements, respectively, with the differences due to the variations in geometry. A 15 m square domain, which was large enough to avoid mechanical and thermal boundary effects, represented all three configurations. Figure 6.2 illustrates the geometry and boundary conditions of the simulated control configuration, for the deep burial and gravel configurations, please refer to the appendix. Minor geometric

simplifications were made to the deep burial and gravel configurations in order to ensure minimal element distortion; more specifically, a section of soil above the deep burial pipeline was defined as non-susceptible and the bottom of the trench was rounded slightly in the gravel section. Further details regarding the geometric representation can be found in Appendix F.

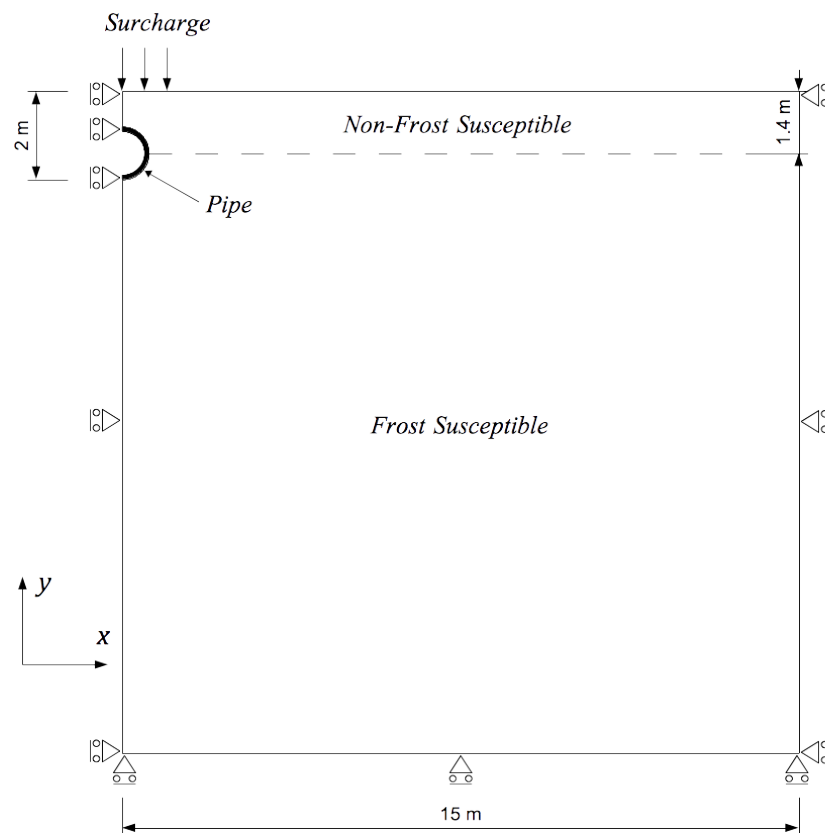


Figure 6.2: Geometry and mechanical boundary conditions used to represent the control configuration.

Ground surface temperatures were assumed to be equal to the monthly mean air temperature for Calgary, as illustrated in Figure 6.3. Temperatures were initialized by

applying a small vertical thermal gradient across the domain under steady-state conditions; the top edge was initialized at 4.0 °C and the bottom at 5.5 °C, which approximately corresponds to the long-term mean air temperature for the site (Environment Canada 2013). During the primary transient analysis, the bottom edge of the model was maintained as a zero heat flux boundary. The pipe temperature was assumed to decrease exponentially from the initial ground temperature to -10.0 °C over a period of 46 days for the control and gravel configurations and 174 days for the deep burial. The longer chill-time for the deep burial section was deemed prudent due to the warmer than expected initial soil temperature at the deeper burial depth; i.e. if the rate of heat extraction of the cooling system is constant between sections, the deeper pipe will take longer to cool.

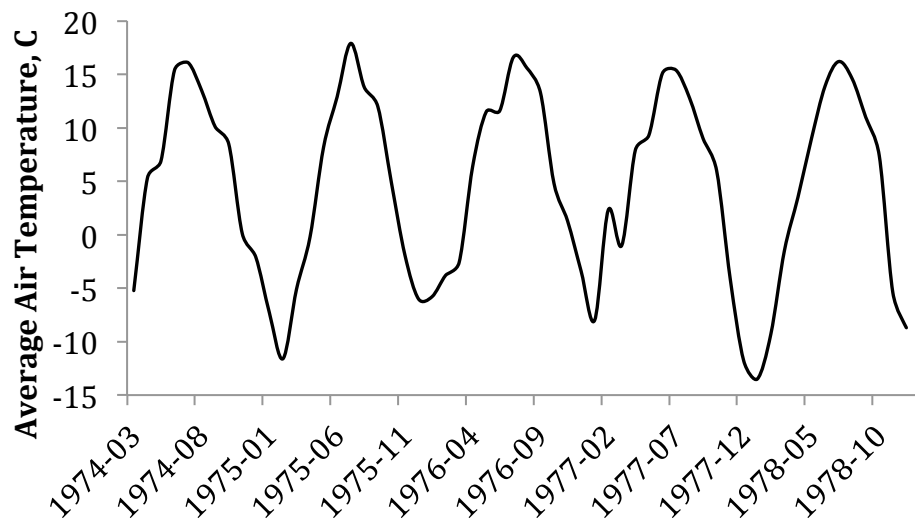


Figure 6.3: Monthly mean air temperature in Calgary, Alberta during the first 5 years of the pipeline experiment (Environment Canada 2013).

6.2.2 Material Properties

6.2.2.1 Frost Susceptibility

Extensive laboratory tests conducted on both undisturbed and remolded soil specimens indicate the Calgary silt (CS) has a segregation potential, SP_0 , of between $18.0 - 30.0 \times 10^{-5} \text{ mm}^2/^\circ\text{Cs}$, with $23.0 \times 10^{-5} \text{ mm}^2/^\circ\text{Cs}$ typically considered to be the best representative value (Hardy Associates 1978, Penner and Ueda 1977; Konrad and Morgenstern 1984; Konrad and Shen 1996). Regarding stress sensitivity, the same studies indicate the material has a b value of 9.5 MPa^{-1} , see Figure 6.4.

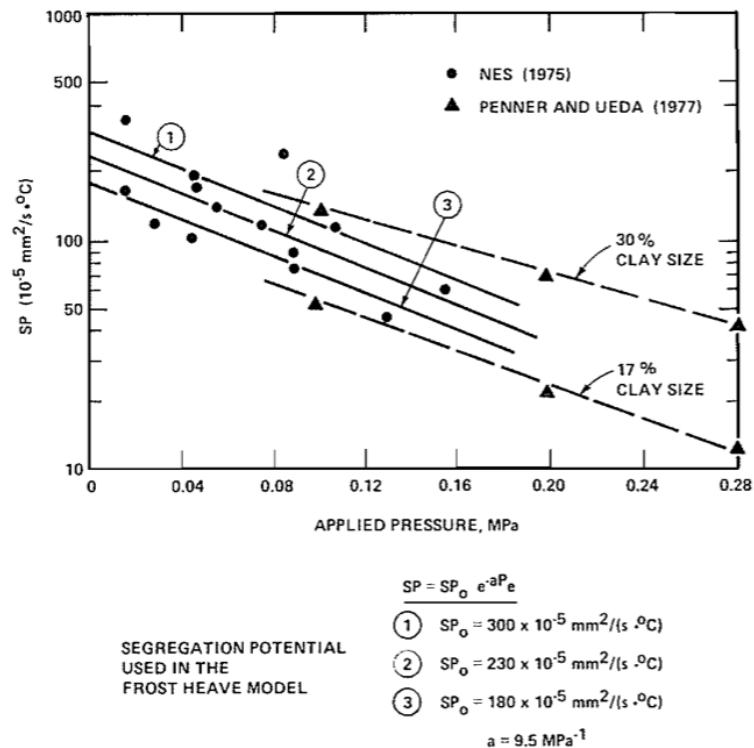


Figure 6.4: The variation of SP with applied surcharge for Calgary silt obtained from laboratory frost heave tests conducted under step-freezing conditions (Konrad and Morgenstern 1984).

The influence of the frost front advance rate on SP was not accounted for in the previous investigations of CS. In order to quantify this influence, β (defined in equation 3.9 in Chapter 3) was characterized through one-dimensional numerical simulations. The time history of the frost heave in a series of step-freezing frost heave tests on undisturbed CS samples conducted by Hardy Associates (1978) was reproduced numerically to back-calculate β . The value of β was found to vary between 1.7 and 2.3 x 10⁶ s/m with a mean of 1.95 x 10⁶ s/m.

6.2.2.2 Mechanical Properties

The mechanical constitutive relationship of the soil was considered to be elastic perfectly plastic using a Mohr-Coulomb failure criterion. The cohesive and frictional strength parameters were constant with respect to both stress and strain level. As discussed in Chapter 2, the mechanical properties of soils change upon freezing. With decreasing temperature, strength and stiffness are typically considered to increase along with the propensity for creep behavior. However, these properties are sensitive to the strain rate; specifically the strength and stiffness decrease with decreasing strain rates. Based on a preliminary analysis of the reported results, and later confirmed in the numerical simulations, the frost heave rate induces a strain rate in the soil around the pipeline sections with the order of magnitude of no more than 10⁻⁹ s⁻¹. At such a slow rate ice offers little resistance to deformation and is effectively a fluid (Arenson and Springman 2005, Arenson et al. 2004). This can be considered as an analogy with the shearing of a saturated fine-grained soil, if the shear strain rate is small compared to the

rate of dissipation of excess pore pressure, the soil exhibits drained behavior. It should also be noted that a lower assumed shear strength is conservative assumption with respect to pipe displacement, as discussed in the preceding sections.

Consequently, the elastic modulus and cohesion of the frozen soil were assumed to be equal to the corresponding unfrozen soil properties (Schulson 1999). In other words, both the stiffness and cohesion were considered to be constant with respect to ice content and temperature, see Figures 2.5 and 2.7. It is assumed that the pore ice does not resist deformation, the frozen soil will not be susceptible to creep deformation, and, consequently, the rate effects can be neglected. Alternatively, the friction angle was assumed to be sensitive to the ice content. If it is assumed that ice behaves as a fluid at low strain rates, then increasing the ice volume would lead to shear strength decreasing. The internal friction angle is assumed to vary with the ice content by the following expression, proposed by Arenson and Springman (2005) and discussed in Chapter 2:

$$\phi_{(T)} = \phi_0(1 - \theta_i^{2.6}) \quad (6.1)$$

where θ_i refers to the volume fraction of ice and ϕ_0 is the unfrozen friction angle. The inclusion of this expression was deemed prudent due to the existence of localized ice-rich regions within the soil where ice lenses form. The intrinsic friction angle, ϕ_0 , was assumed to be 30° for both the frost susceptible and non-susceptible soil regions, which was based on the general material type. The sensitivity of the model to ϕ_0 is discussed in Section 6.3.2. The friction angle of the gravel was assumed to be 35°, independent of both temperature and ice content.

Consistent with other published results on the Calgary pipeline experiments, the unfrozen elastic modulus of CS was selected as 11.2 MPa and the Poisson's ratio as 0.3 (Konrad and Shen 1996, Nishimura et al. 2009). Since CS is slightly over-consolidated, moderate dilative behavior was expected and the dilation angle of the material was assumed to be a constant 5° . The steel pipe section was assumed to be linear elastic with an elastic modulus of 200 GPa and a Poisson's ratio of 0.25. The stress level in the steel was assumed to not exceed the yield limit. The gravel, if present, had an elastic modulus of 50 MPa and Poisson's ratio of 0.25.

The cohesion (c') of the CS is not reported in the literature. Based on its general classification as a clayey-silt, CS has an expected cohesion of between 5 to 20 kPa (Mitchell and Soga 2005). In addition, it has been established from field observations that cohesion increases significantly with soil depth (Bishop 1966, Lamb 1966). Consequently, an assumed profile of cohesion and depth was adopted, see Figure 6.5. In the interest of numerical stability and computational efficiency, it was necessary to utilize a single cohesion value for each soil zone. This value was determined through averaging the values across the depth of the active zone, which was considered to be the observed frost penetration depth. Consequently, c' was assumed for each soil layer and higher values were used for the deep burial configuration. The cohesion of the unsaturated, non-frost susceptible top zone was assumed to be 7.5 kPa and constant with depth. Furthermore, it was necessary to assume a small amount of cohesion for the gravel material as *ABAQUS* requires non-zero values for numerical stability. Table 6.1 presents the c' values for all soil zones.

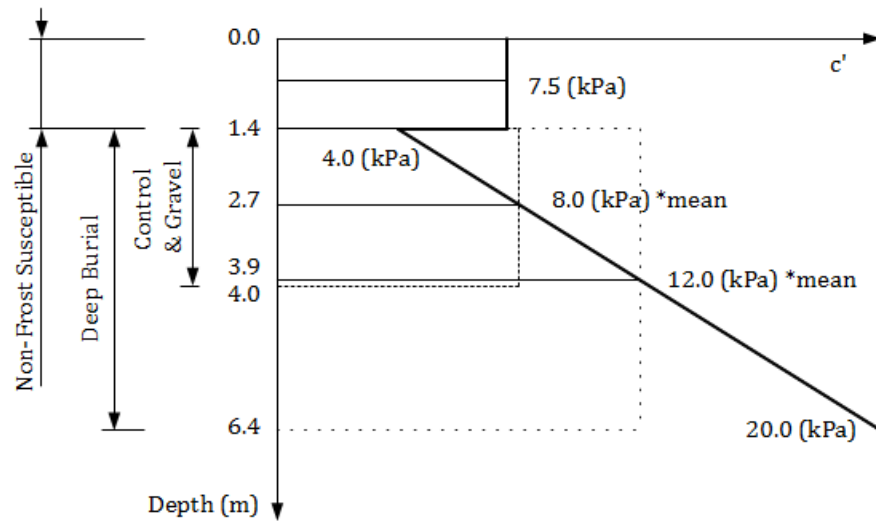


Figure 6.5: Assumed variation in cohesion at the Calgary pipeline test site. The active zones of the three configurations are noted on the left.

Table 6.1: The assumed cohesion, c' , and friction angle, ϕ_0 , of each soil region.

Material	c' (kPa)	ϕ_0 (°)
Non-Frost Susceptible	7.5	30
Frost Susceptible (Control & Gravel)	8.0	30
Frost Susceptible (Deep Burial)	12.0	30
Gravel	3.0	35 (constant)

The soil freezing characteristic of CS was measured by Patterson and Smith (1981), which is expressed as:

$$\theta_l = 0.096|T|^{-0.364} \quad (6.2)$$

where T refers to temperature in °C specifically below the bulk freezing point and θ_l is the liquid water volumetric fraction. The thermal conductivity, λ , of soil was assumed to vary with volume fraction following the geometric mean approximation and the

volumetric heat capacity, C , was assumed to follow the parallel or proportionate model, both of which are expressed as follows.

$$\lambda = \prod_{j=1}^4 \lambda_j^{\theta_j} \quad (6.3)$$

$$C = \sum_{j=1}^4 C_j \theta_j \quad (6.4)$$

where the subscript $j = 1$ to 4 refers to the conductivity, heat capacity, or volume fraction associated with the four soil phases: soil grains, water, air, and ice. The assumed values of the thermal properties of these phases are listed in Table 6.2. The frost susceptible soil and the gravel were assumed to be fully saturated while the non-susceptible soil had an assumed saturation of 50% for the purpose of the thermal property calculations. The thermal boundary of the pipe was defined at the outer pipe edge and therefore the thermal properties of steel were not relevant in the analysis.

Table 6.2: The assumed thermal properties of each soil constituent phase (Michalowski 1993).

Phase	Thermal Conductivity (W/m°C)	Volumetric Heat Capacity (J/m³°C)	Density (kg/m³)
Soil Grains	2.92	2.39 x 10 ⁶	2650
Liquid Water	0.56	4.18 x 10 ⁶	1000
Ice	2.24	1.93 x 10 ⁶	917
Air	0.024	1.21 x 10 ³	1.29

6.3 RESULTS

6.3.1 Base Analysis

The simulated vertical pipeline displacements, for the three configurations shown in Figure 6.1, over time are compared with the reported measurements of the Calgary pipeline tests in Figure 6.6. The results show good agreement between the simulations and observed frost heave time histories for all three pipe configurations in the first three years of testing. Some deviation is noted in the first 200 days for the gravel configuration, which is attributed to the minor modification to the model geometry. As illustrated in Appendix F, the simulated geometry neglected any frost susceptible soil between the pipe and the gravel bed, whereas the section schematic indicates the presence of a thin layer of CS. The measured data indicates larger displacements associated with the berm expansion than that obtained from the simulations. The deviation may be due to disturbances in the displacement measurements during the test owing to activity around the pipe during the berm construction. In the simulation, the berm was accounted for as an instantaneous increase in the applied surcharge.

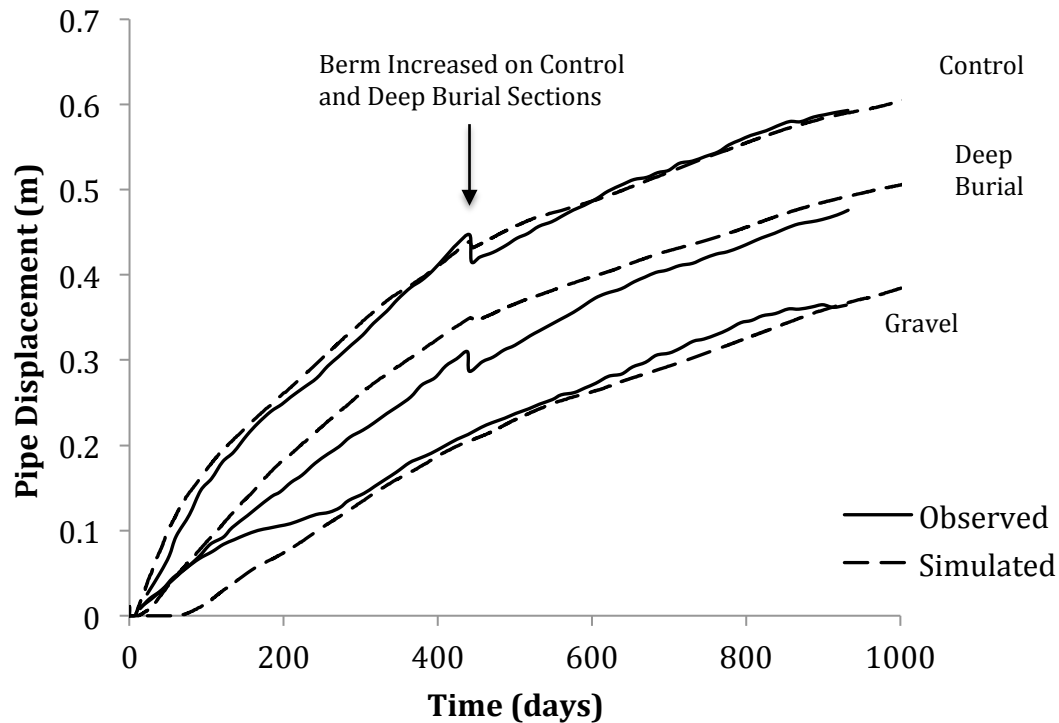


Figure 6.6: The simulated and observed (Slusarchuk et al. 1978) vertical pipe displacements due to frost heave.

Figure 6.7 compares the thermal output from the simulations with the observed behavior. The vertical distance between the bottom of the pipe and the 0 °C isotherm provides an approximate evaluation of the thermal analysis, though it is important to note that the mechanical and hydraulic response of the system is highly coupled to the thermal analysis. Regardless, the results demonstrate that the thermal properties used in the simulations provide a reasonable representation of the physical behavior of CS. For the three configurations the closest agreement between the predicted results and the observations is seen with the control configuration, followed by deep burial and then gravel configurations.

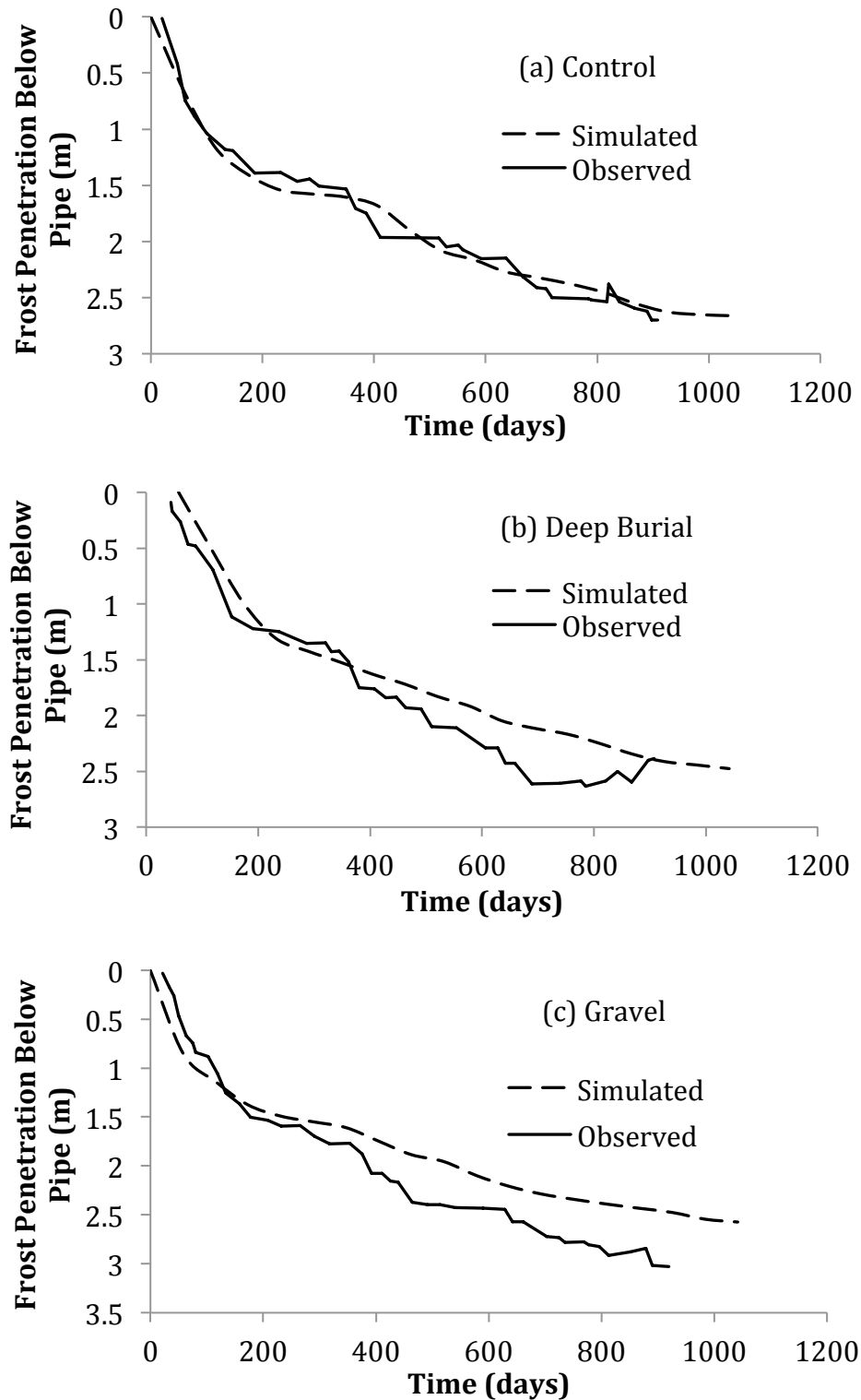


Figure 6.7: The simulated and observed (Slusarchuk et al. 1978) frost penetration below pipeline, defined as the distance between the bottom of the pipe and the 0°C isotherm.

Figure 6.8 shows the development of plastic deformation in the soil around the pipe section due to frost action in the control section. As ice lenses grow, the pipeline along with the frost bulb, the frozen area surrounding the pipe, and some adjacent soil displace upward. Owing to the large magnitude of frost heave displacements the strain is well in excess of the elastic limit of the soil and a large plastic zone is mobilized in the adjacent soil, both frozen and unfrozen. The simulated results illustrate particularly high plastic strain levels at the interface of the frost susceptible and non-susceptible soil regions, which is attributed to the smaller cohesive strength of the non-susceptible soil compared to frost susceptible one. Refer to Appendix F for the plastic strain and temperature profiles of the deep burial and gravel configurations.

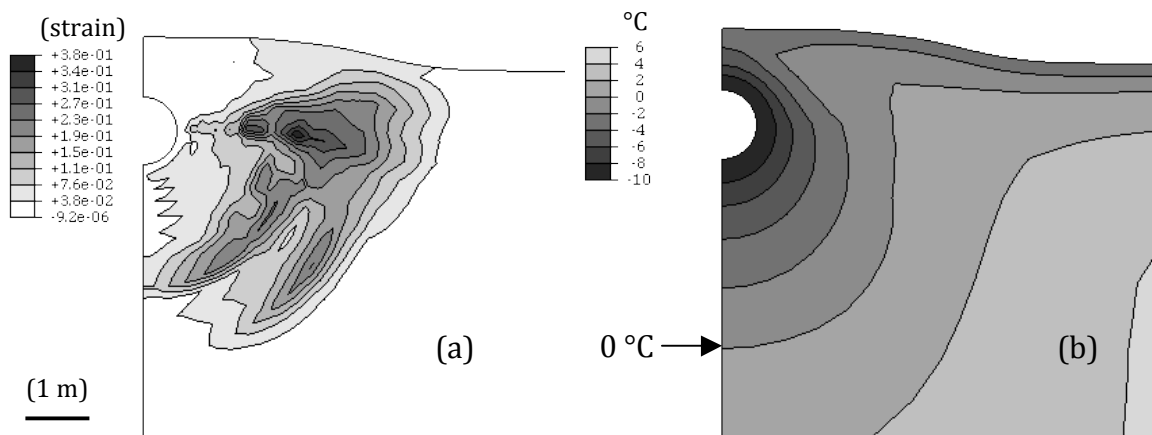


Figure 6.8: The simulated maximum in-plane plastic strain (a) developed by day 1042 and the corresponding temperature profile (b) of the control section.

A noteworthy feature of the frost heave model is that it takes into account the change in soil porosity due to the formation of segregated ice. Although not a primary

objective of the model, knowing the change in ice content provides valuable insight with regard to thaw weakening. As illustrated in Figure 6.9, the simulations indicated a significant increase in porosity in the frost susceptible soil around the pipeline, which corresponds to the observed frost bulb. Since the frost susceptible soil was assumed to be fully saturated throughout the analysis, the change in porosity is attributed to a direct change in the local ice fraction. The model did not account for soil consolidation, and all changes in predicted porosity were due to ice lens formation. Consequently the model did not consider any porosity change in either the partially saturated, non-susceptible soil or the gravel. The magnitude of the simulated change in porosity should be noted, varying from 0.341 initially to as much as 0.74 in certain locations, indicating the presence of very ice-rich regions. The change in porosity was significantly greater than any potential change due to consolidation or dilation. The porosity profile of the deep burial and gravel sections please can be found in Appendix F.

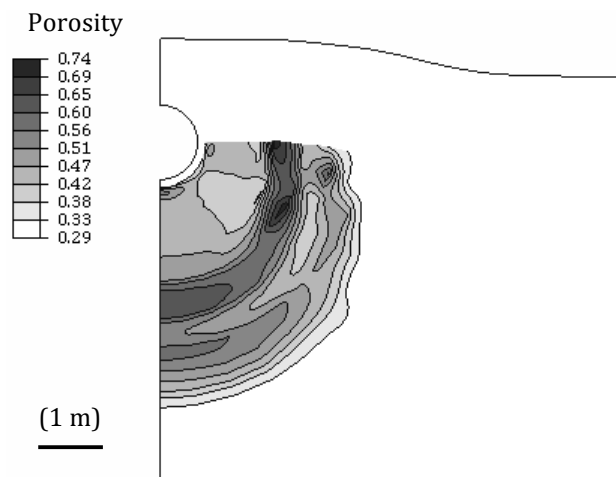


Figure 6.9: The simulated porosity on day 1042 for the control configuration. Initial porosity in the frost susceptible and non-susceptible soil was 0.341.

6.3.2 Parametric Sensitivity

The sensitivity of the numerical simulation results to the selected parametric inputs was also considered. Since the primary objective of this work was to predict pipeline displacement due to frost heave, the displacement on day 1000 was used to evaluate and compare the influences of different parameters. In the preceding discussion, unless it is explicitly stated otherwise, all input parameters are consistent with those of the base analysis, which is outlined in Table 6.3.

Table 6.3: Input parameters for the base case simulations.

Parameter	Value
SP_0 ($\times 10^5 \text{ mm}^2\text{C}^{-1}\text{s}^{-1}$)	23.0
β ($\times 10^6 \text{ sm}^{-1}$)	1.95
ζ	0.9
ϕ_0 ($^\circ$)	30.0 <i>see Table 6.1</i>
c' (kPa)	<i>see Table 6.1</i>
E (MPa)	11.2
ψ ($^\circ$)	5.0

First, the sensitivity of the simulations to the variation in segregation potential was examined and the results are presented in Figure 6.10. Previous experimental investigations show that segregation potential value of Calgary silt varies between 18.0 and $30.0 \times 10^{-5} \text{ mm}^2\text{s}^{-1}\text{C}^{-1}$ (Konrad and Morgenstern 1984). With SP_0 values in this range yields a dramatic variation in predicted pipe displacements, varying by as much as 100%, with all three configurations showing a similar amount of SP_0 sensitivity. The cause of

this sensitivity is clear, as segregation potential is the primary driver of displacement associated with frost heave.

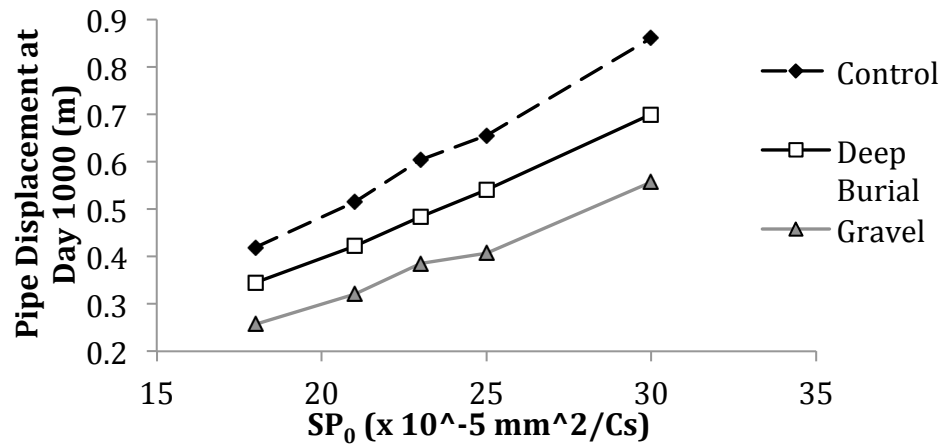


Figure 6.10: The variation in the simulated pipe displacement with SP_0 .

The pipe displacement shown in Figure 6.11 is seen to be less sensitive to the rate of freezing, which is quantified by β . Based on the results of one-dimensional simulations, the value of β was observed to lie in the range of 1.7 and $2.3 \times 10^6 \text{ sm}^{-1}$ for CS. The variation of β in this range had little impact on the predicted displacement response. Neglecting β results in an approximate 10% reduction in predicted pipe displacement. These results contrast the one-dimensional simulations, which were more sensitive to β . This may be attributed to the long-term nature and generally lower frost penetration rates associated with this pipeline problem.

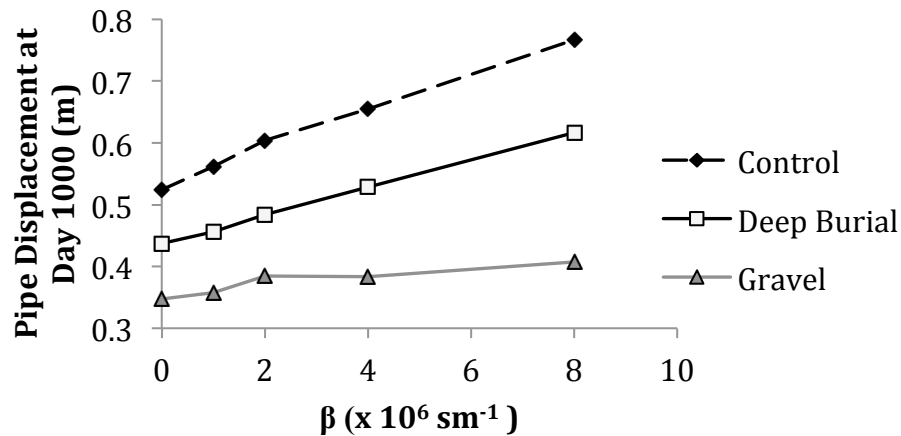


Figure 6.11: The variation in the simulated pipe displacement with β , the parameter expressing heave rate sensitivity to the freezing rate.

The fractional anisotropy parameter, ζ , contained in the frost heave growth tensor was assumed to be 0.9 for the base case, which represents near unidirectional volumetric expansion. The sensitivity of this parameter to the displacement response of the model was explored. Figure 6.12 illustrates a strong negative correlation between ζ and the pipe displacement for all configurations. This is in contrast to the simulated results for the one-dimensional implementation of the model, illustrated in the model sensitivity presented in Appendix E. In that case the magnitude of heave showed a slight positive correlation with ζ . The difference in the ζ sensitivity of the pipeline simulations is attributed to the non-uniform development of the frost bulb surrounding the pipe section. Referring to Figure 6.8(b) the temperature gradient near the top of the soil is mostly aligned with the x -axis and larger than the gradient at the bottom, aligned with the y -axis. In this case the more volumetric growth tangential to the frost front, the greater the overall vertical displacement of the system.

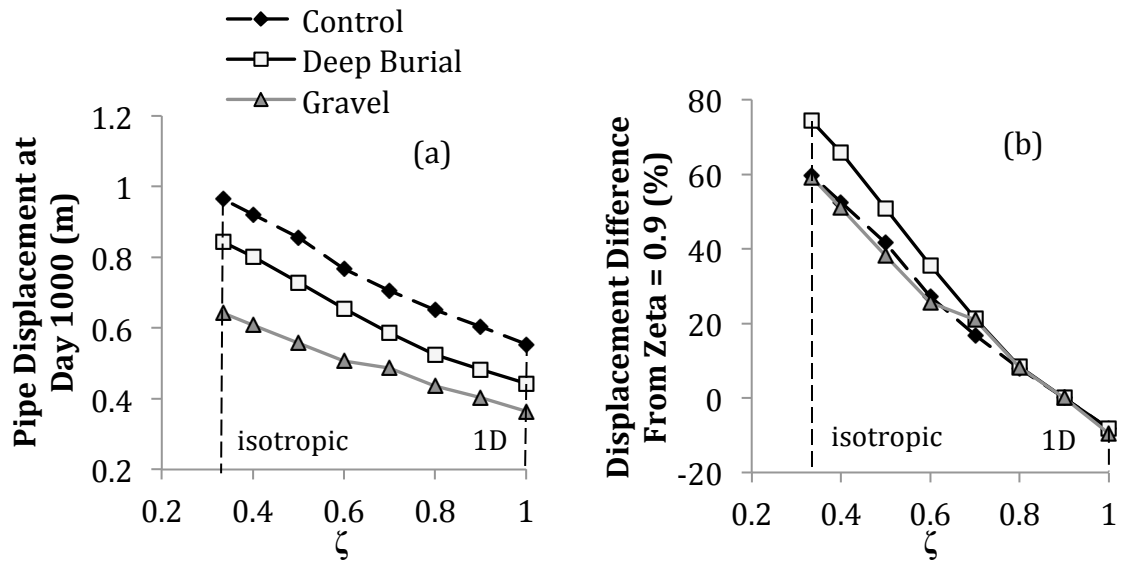


Figure 6.12: The absolute, (a), and relative, (b), variation in the simulated pipe displacement with fractional anisotropy parameter, ζ .

The shear strength of the soil has a significant impact on the displacement response of the pipe. Increasing the values of the Mohr-Coulomb shear strength parameters greatly reduces the pipe displacement, as shown in Figure 6.13. The values of the cohesion and frictional angle were applied to both the frost susceptible and non-susceptible regions, while the strength parameters of the gravel region remained constant. The greater the soil shear strength, the more soil resistance there is to upward pipe displacement, and therefore the greater the stress level at the frost front, particularly directly below the pipe section. This increased stress reduces the heave rate of the soil due to the stress level dependency of the frost heave process as explicitly accounted for in the segregation potential formulation. The results also demonstrated the importance of taking into account the plastic deformation behavior of soil in frost heave simulations, as

assuming elastic conditions in the soil would clearly cause the model to under-predict the heave response.

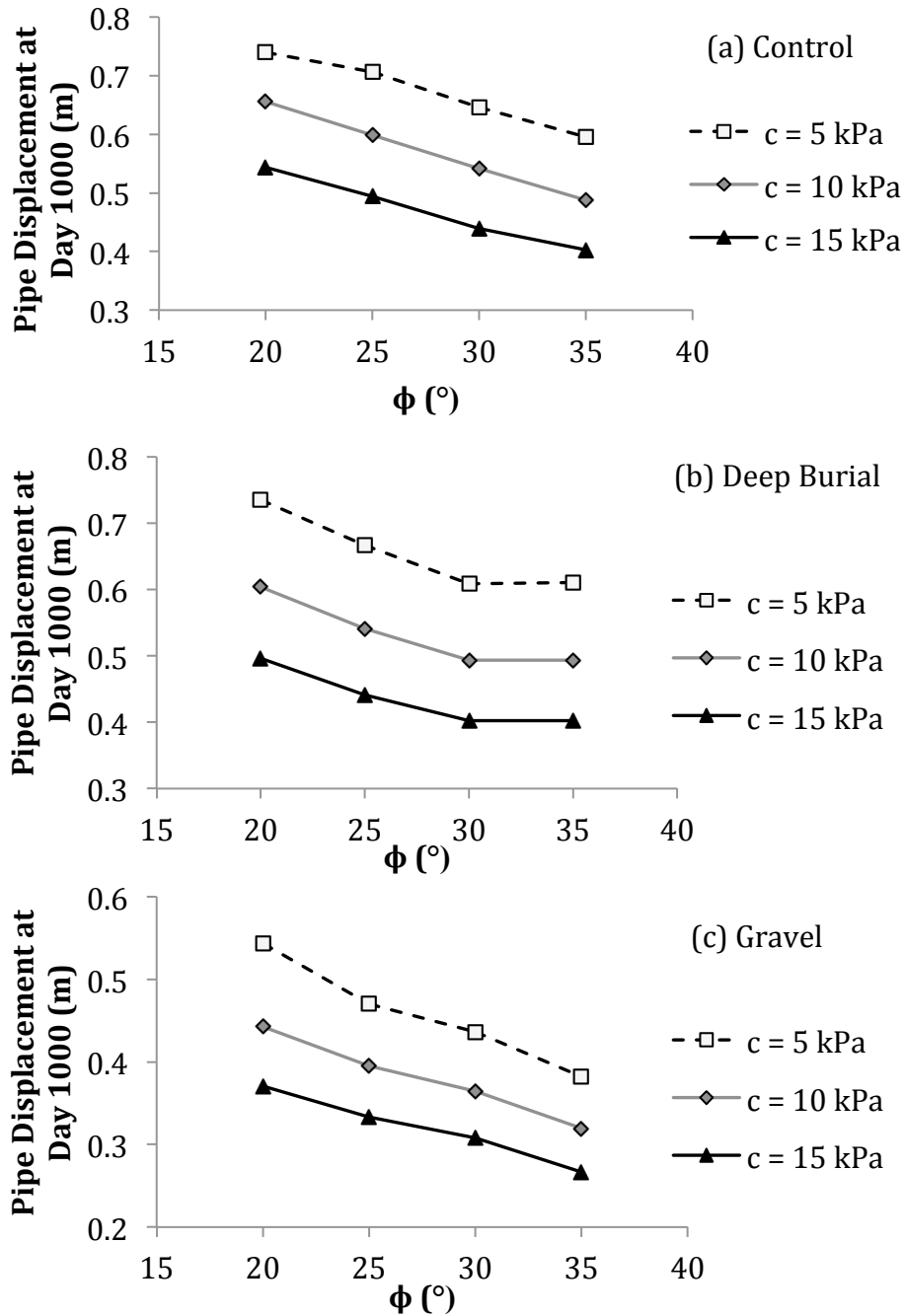


Figure 6.13: The variation in the simulated pipe displacement with the Mohr-Coulomb failure parameters of the soil for the three sections.

When taking into account the plastic deformation of soil, the elastic modulus did not have a significant impact on the heave response of the pipe. Figure 6.14 shows the development of pipe displacement with time at two different orders of magnitude of E . Pipe displacement is generally consistent with E , showing a slight tendency for larger displacements with greater stiffness. The frost heave induced strains will exceed the plastic strain limit in the soil above the pipe section regardless of the soil stiffness, while at the same time, the strain level below the frost bulb does not exceed the elastic range. Consequently, the net effect of a decrease in overall soil stiffness is a decrease in pipe displacement.

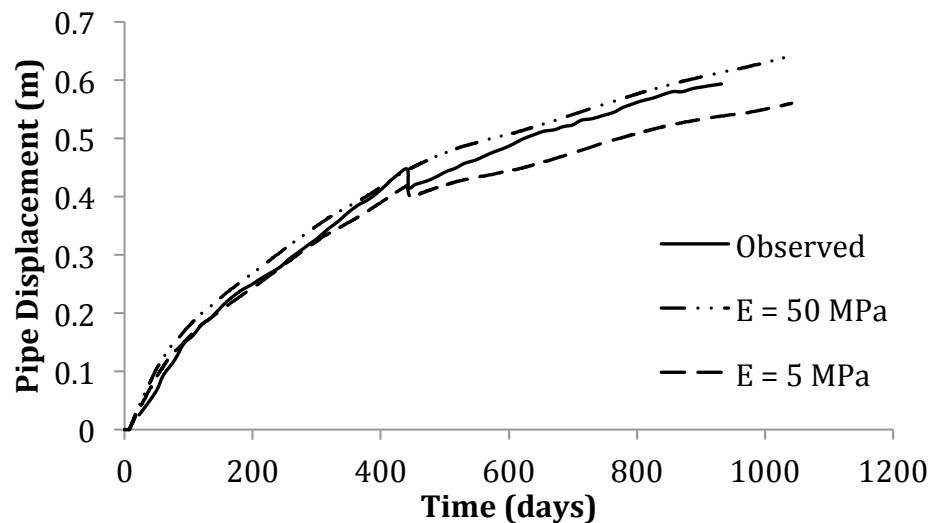


Figure 6.14: The variation in the pipe displacement with elastic modulus of the soil for the control configuration.

In terms of the effect of soil dilatancy characteristics, the simulated pipe displacement was positively correlated with the soil dilation angle, as illustrated in Figure 6.15. During a plastic deformation process, shear induces higher volumetric expansion in

soils with larger dilation angles. It should be recognized that due to the large displacements involved with this problem, very large plastic strains develop, in some locations exceeding 30%. With such large plastic strains, the constant dilation angle may exaggerate expansion, leading to an over-prediction of the heave response. However, as illustrated in Figure 6.15, the model is moderately sensitive to ψ .

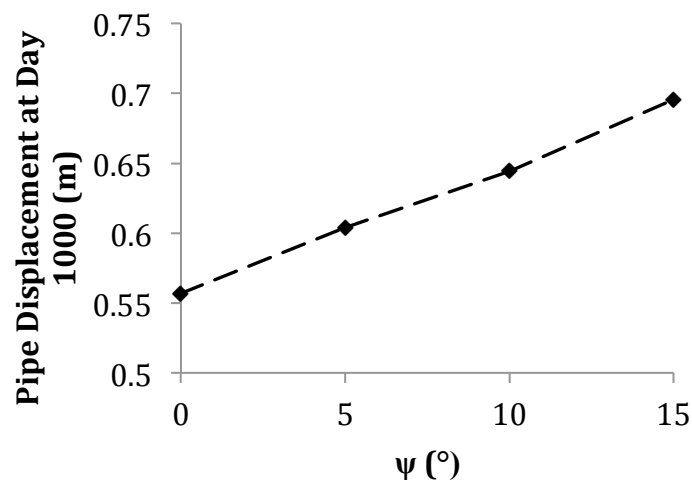


Figure 6.15: Variation in the simulated pipe displacement with the dilation angle of soil for the control configuration.

6.3.3 Operational Parameters

The influence of the surcharge magnitude on the displacement response was briefly explored. Applied across a constant width of 3.0 m, the surcharge was increased from 0 to 30 kPa for the three simulated configurations. As illustrated in Figure 6.16, pipe displacements decreased significantly with increasing surcharge pressures. These findings are consistent with the segregation potential formulation, as the heave rate is negatively

correlated to the stress level. The deep burial section appears to be the least sensitive to the surcharge effect as it displays the lowest relative change in pipe displacement. This is attributed to the deeper position of the frost front in this section; the deeper position will experience a lesser change in stress due to the surcharge.

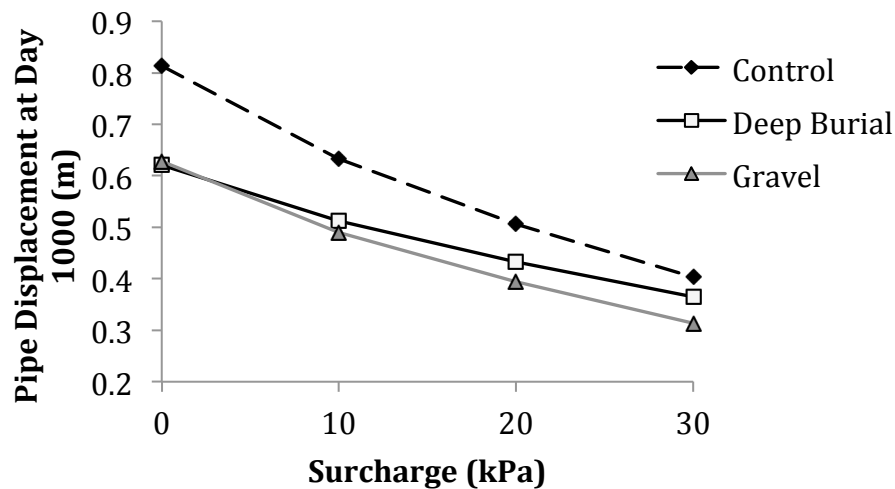


Figure 6.16: The variation in simulated pipe displacement with the applied surcharge.

The sensitivity of the predicted displacement response to the pipe temperature was considered through changing the pipeline temperature in the simulations, presented in Figure 6.17. As may be expected, warmer pipe temperatures produce less heave for all configurations and vice-versa for colder temperatures. The gravel configuration exhibited dramatically less displacement at -5°C as compared to the base analysis of -10°C . However, this result may overstate temperature sensitivity for this case, as the frost front takes a considerable amount of time to pass through the non-susceptible gravel. If the duration of the simulation was extended, the temperature sensitivity of the gravel and

control configuration would likely be comparable. Qualitatively, pipe displacements appear to be less sensitive to pipe temperature than surcharge.

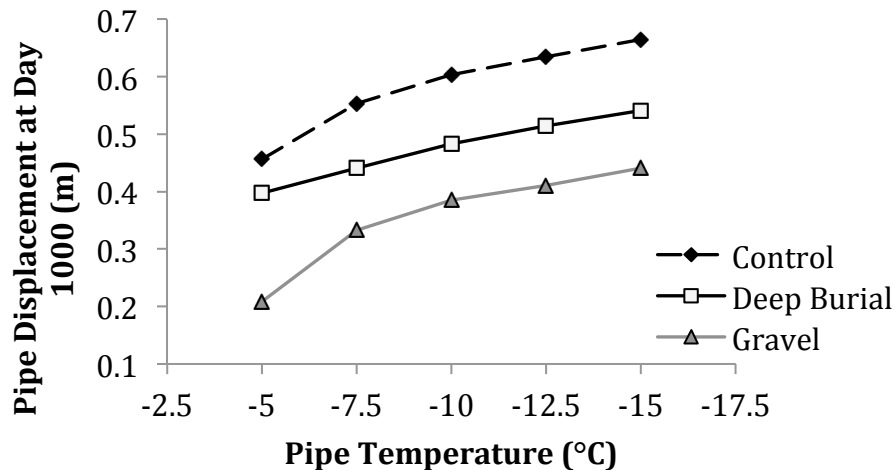


Figure 6.17: The variation in the simulated pipe displacement with pipe temperature.

6.4 SUMMARY AND CONCLUSIONS

The thermal-mechanical couple model for frost heave presented in Chapter 5 was applied to a two-dimensional chilled natural gas pipeline problem. The model was compared to reported results of a series of full-scale pipe heaving experiments, referred to as the Calgary pipeline tests. Three unique pipe burial configurations were examined. The objective was to evaluate the model performance and explore its parametric sensitivity.

The model predicted displacement and thermal responses that are generally in good agreement with measured results for the three pipe configurations. The model also demonstrated a capacity to predict the change in soil porosity due to ice lens growth in the vicinity of the pipe. The simulations indicate the presence of a large mobilized plastic

zone adjacent to the pipeline due to the large displacements and strain caused by the frost heave process. This illustrates the importance of accounting for plastic soil behavior in such problems, as a linear elastic mechanical constitutive expression would have severely under-predicted the pipe displacement.

The simulations demonstrated significant sensitivity to certain model parameters, specifically SP_0 , ζ , and the shear strength of soil. Sensitivity to shear strength was due to the resistance of the pipe-soil system to upward displacement and the stress sensitivity of frost heave rate, where large uplift resistance resulted in higher stresses at the frost front. Though material, the sensitivity of the simulations to the fraction anisotropy factor, ζ , was determined to be non-physical in nature and may be considered to be more of a modelling characteristic. Moderate sensitivity was observed with regards to the elastic modulus, E , frost front advance rate factor, β , or the dilation angle, ψ .

The parametric sensitivity of the model and the general assumptions made regarding the model and material parameters should be taken into account when considering the close agreement between the predicted and observed displacement behavior. More specifically, the simulated results displayed significant sensitivity to the shear strength parameters, particularly cohesion.

Finally, the simulations provide some insight into the performance of techniques to mitigate pipe displacement, specifically the berm size and pipe temperature. While the simulations are qualitatively consistent with previously established behavior (Slusarchuk et al. 1978), they also provide a quantitative analysis of these techniques.

CHAPTER 7 CONCLUSION

The research presented in this thesis explored the numerical modelling of frost heave. This work focused on three primary tasks. First, the mass transport mechanism associated with ice lens growth was characterized, as well as the thermal properties of frozen soil. Second, a numerical model capable of utilizing these characterizations to simulate the frost heave process was formulated. And finally, the developed model was evaluated and verified through a comparative analysis between the simulated predictions and the observed physical response of multiple systems.

The mass transport mechanism was explored through one-dimensional laboratory frost heave tests. Segregation potential (Konrad and Morgenstern 1980) was used to characterize the frost heave. Segregation potential offers a compromise between a physically comprehensive description and practical utility when modelling frost heave. The results demonstrated that the segregation parameter, SP , of a particular material is not a constant value. Instead, this parameter was found to be sensitive to the overburden stress level and the frost penetration rate. The influence of the frost front advance rate on SP was attributed to the hydraulic dynamics in the unfrozen soil. An expression was proposed to account for this influence, equation 3.9. The expression allows for a better characterization of the frost heave rate under highly transient freezing conditions. Without accounting for this effect, frost heave models may significantly under predict the heave rate or SP values may be incorrectly inferred from experimental results.

The frost heave tests also demonstrated a notable physical phenomenon during the initiation of freezing. Observations suggest that the phase change in the pore water does

not first initiate when the soil temperature decreases below the bulk freezing point, 0 °C. The temperature associated with initiation was found to be as low as approximately -2.0 °C. This delay in the onset of phase change, or pore water freezing, strongly influenced the total frost heave displacement in the tests conducted under ramped thermal conditions. Consequently it was concluded that ramped freezing frost heave tests introduce additional complications when conducting comparative analysis.

Thermal conductivity of frozen soil was the primary thermal property investigated, as heat capacity is a relatively simple property to define. Seven relevant models were evaluated for their effectiveness in describing the thermal conductivity of frozen soils. It was demonstrated that the Maxwell and Rayleigh models can be applied to soils so long as a multi-level homogenization is utilized to account for the pore phase. This investigation also proposed a framework for accounting for the inherent anisotropy in frozen soils containing segregated ice. However, it was also found that there is little practical advantage in accounting for this anisotropy. An empirical approach using a volume weighted, geometric mean of the constituent phase conductivities offers an reasonable approach in representing the composite thermal conductivity.

A fully coupled thermal-mechanical and implicitly hydraulic frost heave model was derived from thermodynamic principles. The characterizations of the thermal properties (explored previously in this work) were incorporated into the definition of the heat transport process of the model. Similarly, mass transport was characterized through the segregation potential concept, using the proposed modified format. The model was implemented into a two-dimensional, plain-strain, FEM scheme, utilizing the commercial

software ABAQUS/Standard. Simulations of the one-dimensional frost heave tests were conducted in this study. Good agreement was found between the physical observations and the simulations. This agreement was used to validate the function of the model.

After formulation and validation in one-dimension, the model was applied to a full-scale problem involving a chilled natural gas pipeline undergoing substantial frost heave. Physical observations of the pipeline section were obtained from the reported literature. Good agreement was found between both the observed pipe displacements and the thermal profiles within the soil, and the simulated values. In future investigations, similar simulations could be conducted to explore design variables for chilled gas pipelines. This study briefly considered two particular variables: the surcharge magnitude and pipeline temperature.

The simulation results, particularly the pipe displacement, were found to be sensitive to input parameters other than those characterizing the frost heave process. For example, varying the inputted cohesion from 5 to 15 kPa yielded a 50 – 80% variation in displacement depending on the other simulation variables. It is important to acknowledge that regardless of how technologically sophisticated a model is, the results are only as meaningful as the quality of the input parameters. This was found to be particularly true for frost heave modelling.

7.1 RECOMMENDATIONS

Based on the findings of this study, the following topics appear to provide opportunity for further examination:

1. As previously discussed, the frost susceptibility of a soil is, if not dictated, at least influenced by the hydraulic conductivity at temperatures associated with the frozen fringe. Perhaps due to the challenges associated in its physical measurement, the frozen hydraulic conductivity has not been thoroughly examined in the reported literature. A more detailed exploration of this property may provide valuable insight into the frost susceptibility of soils.
2. The experimental investigation indicated that the segregation potential parameter, SP , is influenced by the frost penetration rate. It has been postulated in this work that this influence (quantified as the material parameter β in equation 3.9) may be related to the rate at which the unfrozen soil dissipates pore pressure. Consequently, it may be possible to relate β to the permeability of the unfrozen soil.
3. The frost heave model can be further extended to explicitly describe the pore water transport process in the soil. The segregation potential characterization of frost heave only explicitly defines the mass flux in the frozen fringe; mass flux elsewhere in the soil is determined implicitly. An additional parallel hydraulic analysis, possibly based on Darcy's law, could be introduced into the frost heave model. This approach would allow for the determination of the effective stress profile in this soil, allowing for the model to account for consolidation due to ice lens growth.

Additionally, this may also provide for the consideration of thaw-weakening and cyclic freeze-thaw behaviour.

4. While experimental observations indicate qualitatively that ice lens growth predominantly occurs in one direction, to date the anisotropic behaviour of frost heave not been thoroughly explored in a quantitative manner. The model formulated in this work uses a fractional anisotropic parameter (ζ in equation 5.20) when defining frost heave expansion. The value of ζ was ultimately assumed from experimental experience with little physical justification. The simulations of the chilled pipeline problem highlighted the sensitivity of the model to this parameter when applied to two dimensions. Ultimately, the modelling of frost heave could benefit from an improved physical understanding or characterization of this parameter.

APPENDIX A FROST HEAVE TEST RESULTS

This appendix provides the full results on the one-dimensional frost heave experiments discussed in Chapter 3. The following tables outline the parameters associated with each test and the corresponding figure label in this appendix.

Table A.1: Step-freezing testing matrix.

Figure Number	Test Name	Material	Overburden (kPa)	Initial Temp (°C)	Top Temp (°C)	Bottom Temp (°C)	Duration (hrs)
A.1	FS-3	FHC	20	5.5	-2.0	4.2	120
A.2	FS-7	FHC	15	4.0	-2.5	3.0	120
A.3	FS-8	FHC	45	4.0	-2.5	3.0	120
A.4	FS-9	FHC	125	4.0	-2.5	3.0	120
A.5	FS-10	FHC	75	4.0	-2.5	3.0	120
A.6	BS-1	BSM	20	4.5	-3.0	3.2	212
A.7	BS-2*	BSM	20	4.5	-3.0	3.2	72
A.8	BS-3*	BSM	20	4.5	-3.0	3.2	212

*Note: BS-4 and BS-5 were conducted without an external water supply.

Table A.2: Ramped-freezing testing matrix.

Figure Number	Test Name	Material	Overburden (kPa)	Temperature Gradient (°C/m)	Rate of Cooling (°C/hr)	Duration (hrs)
A.9	FR-1	FHC	20	20.0	0.018	220
A.10	FR-2	FHC	20	20.0	0.027	165
A.11	FR-3	FHC	20	20.0	0.036	110
A.12	BR-1	BSM	20	20.0	0.072	55
A.13	BR-2	BSM	20	20.0	0.036	110

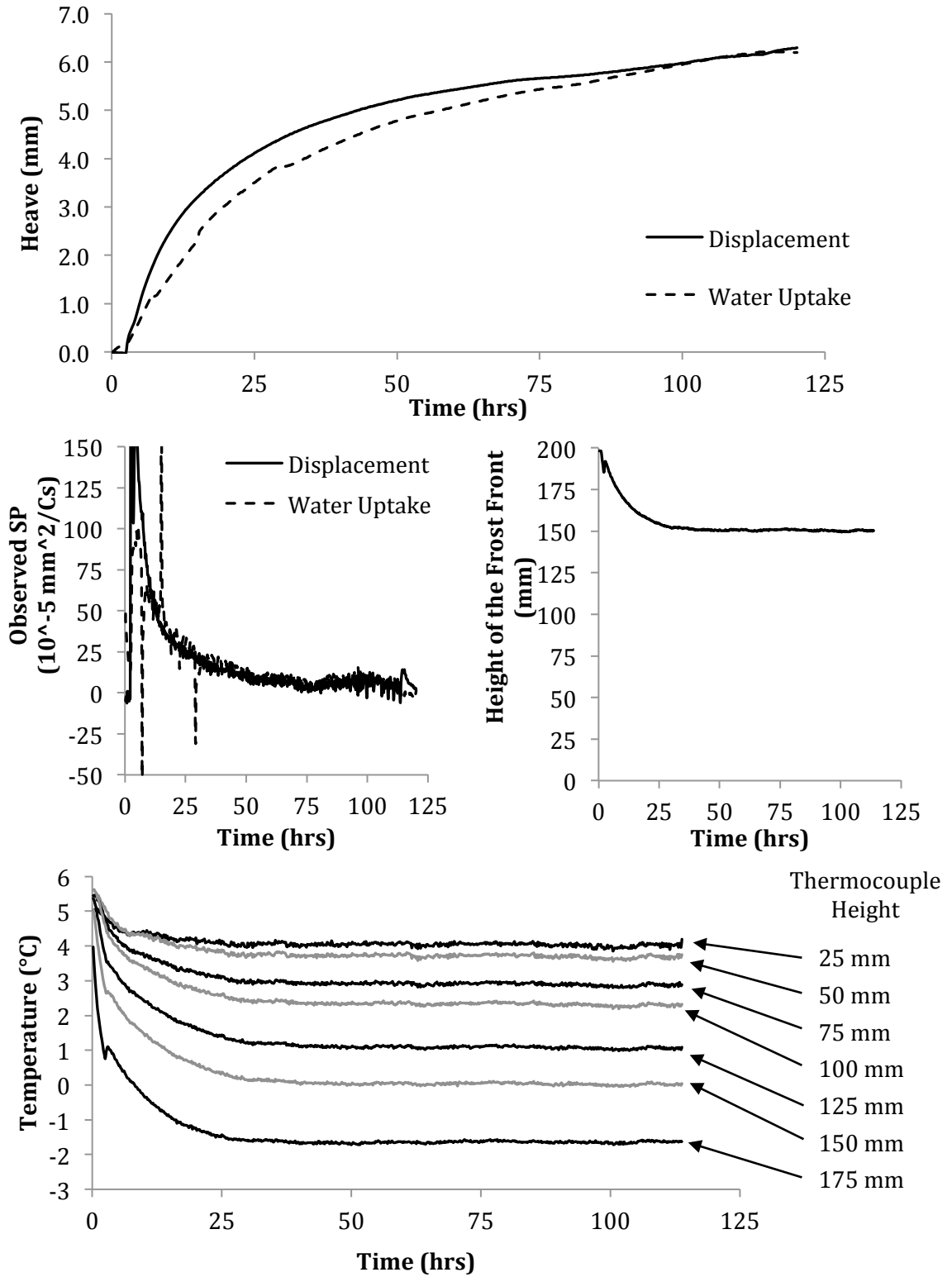


Figure A.1: FS-3 results.

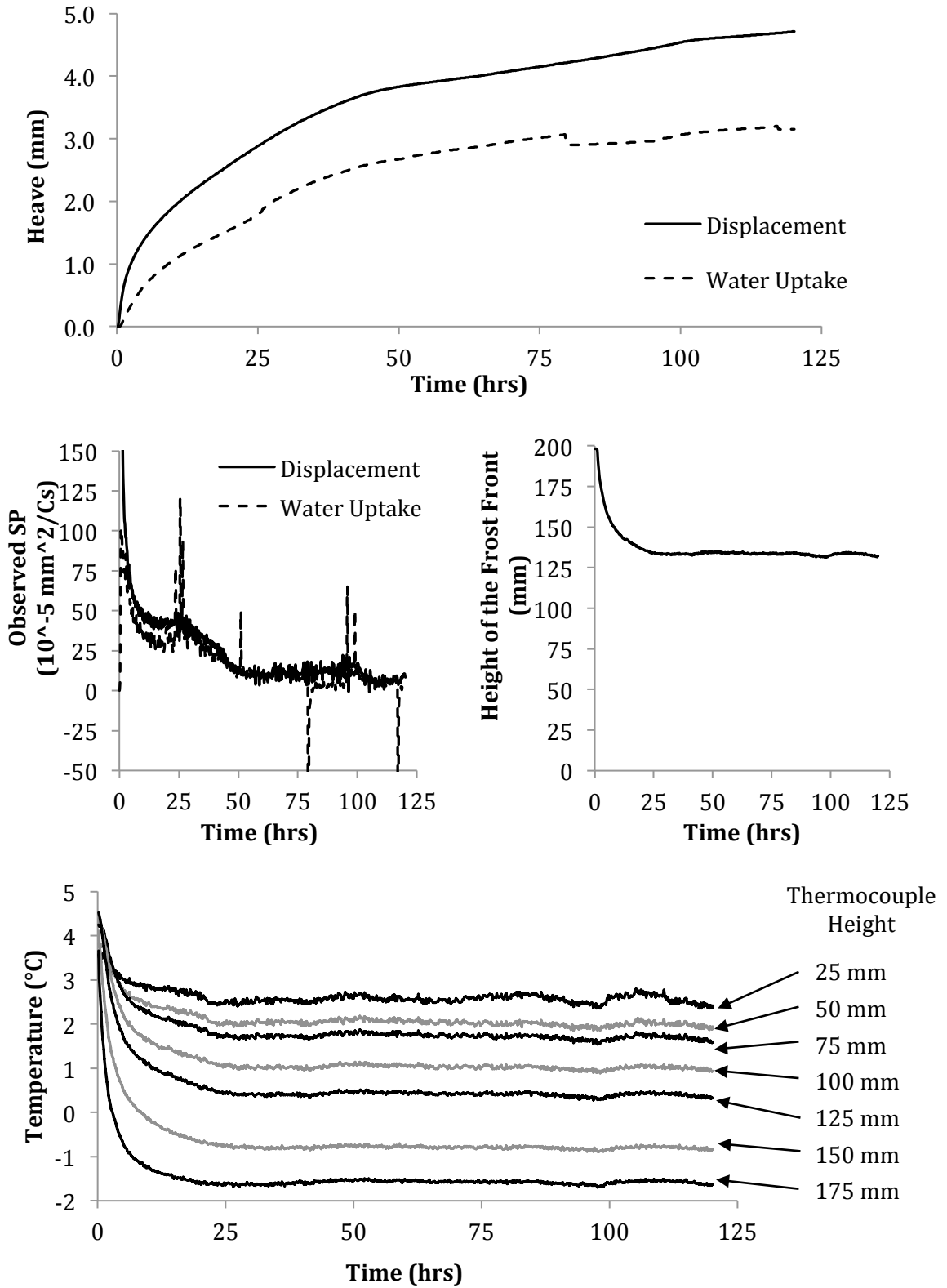


Figure A.2: FS-7 results.

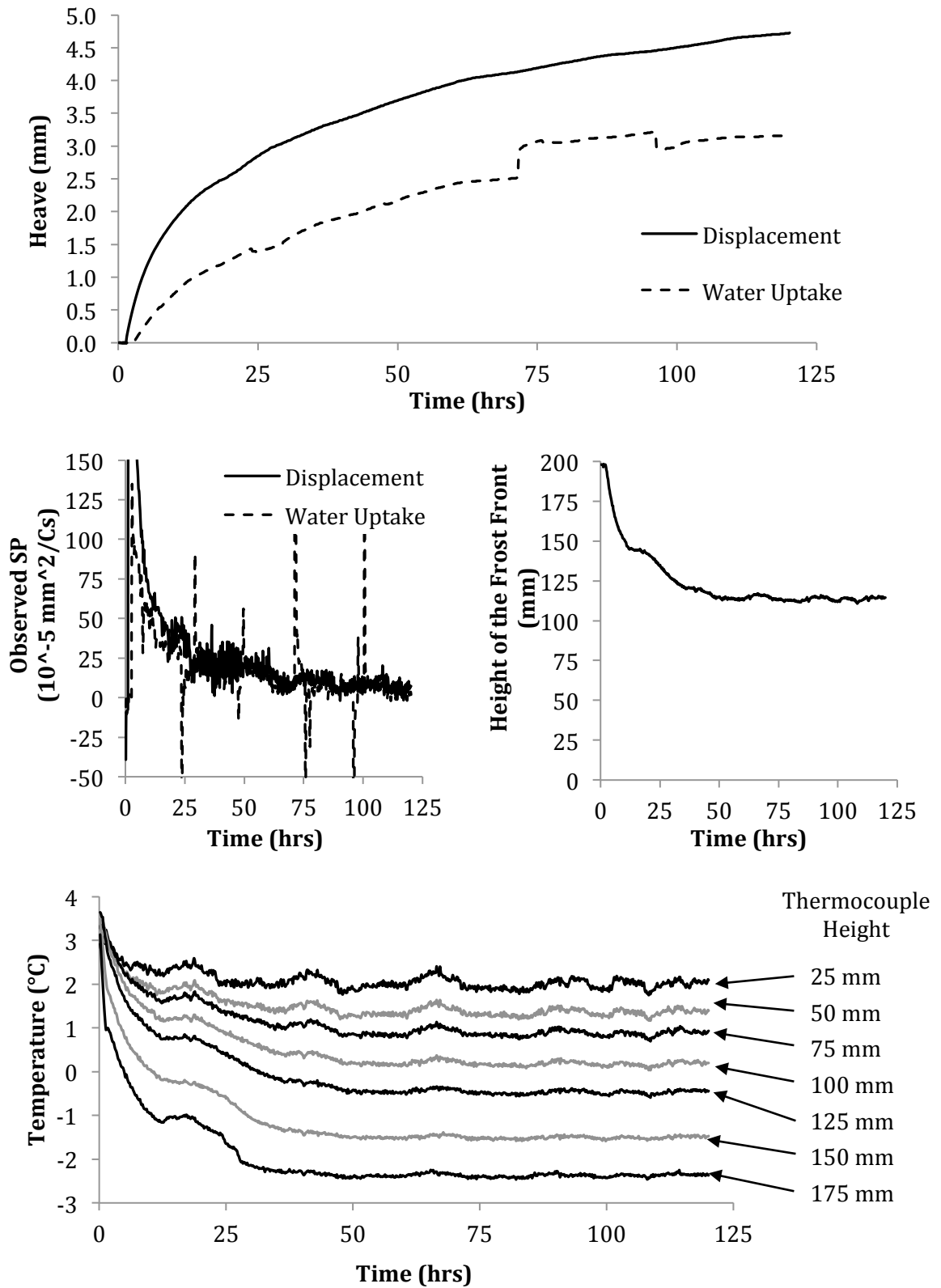


Figure A.3: FS-8 results.

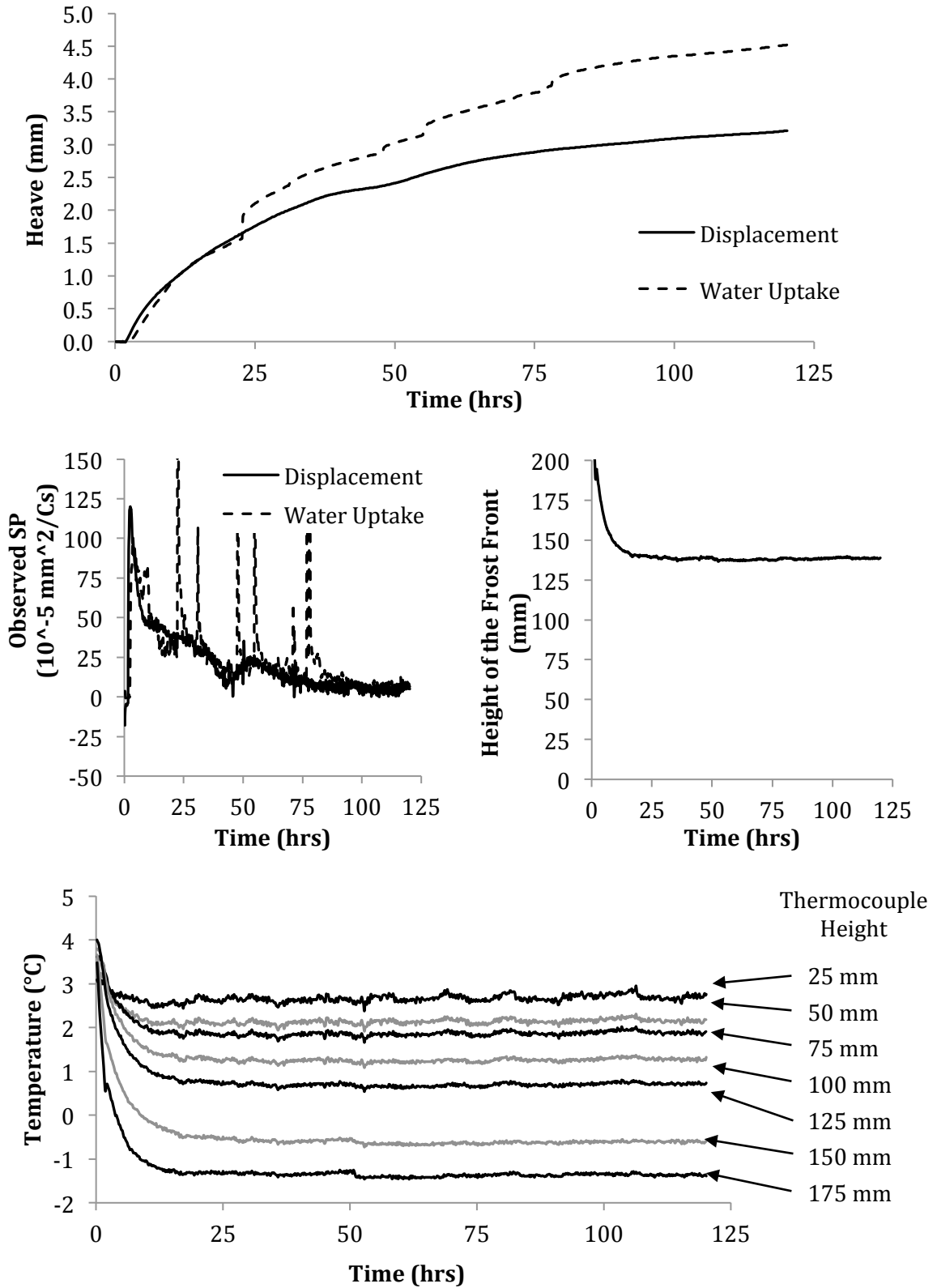


Figure A.4: FS-9 results.

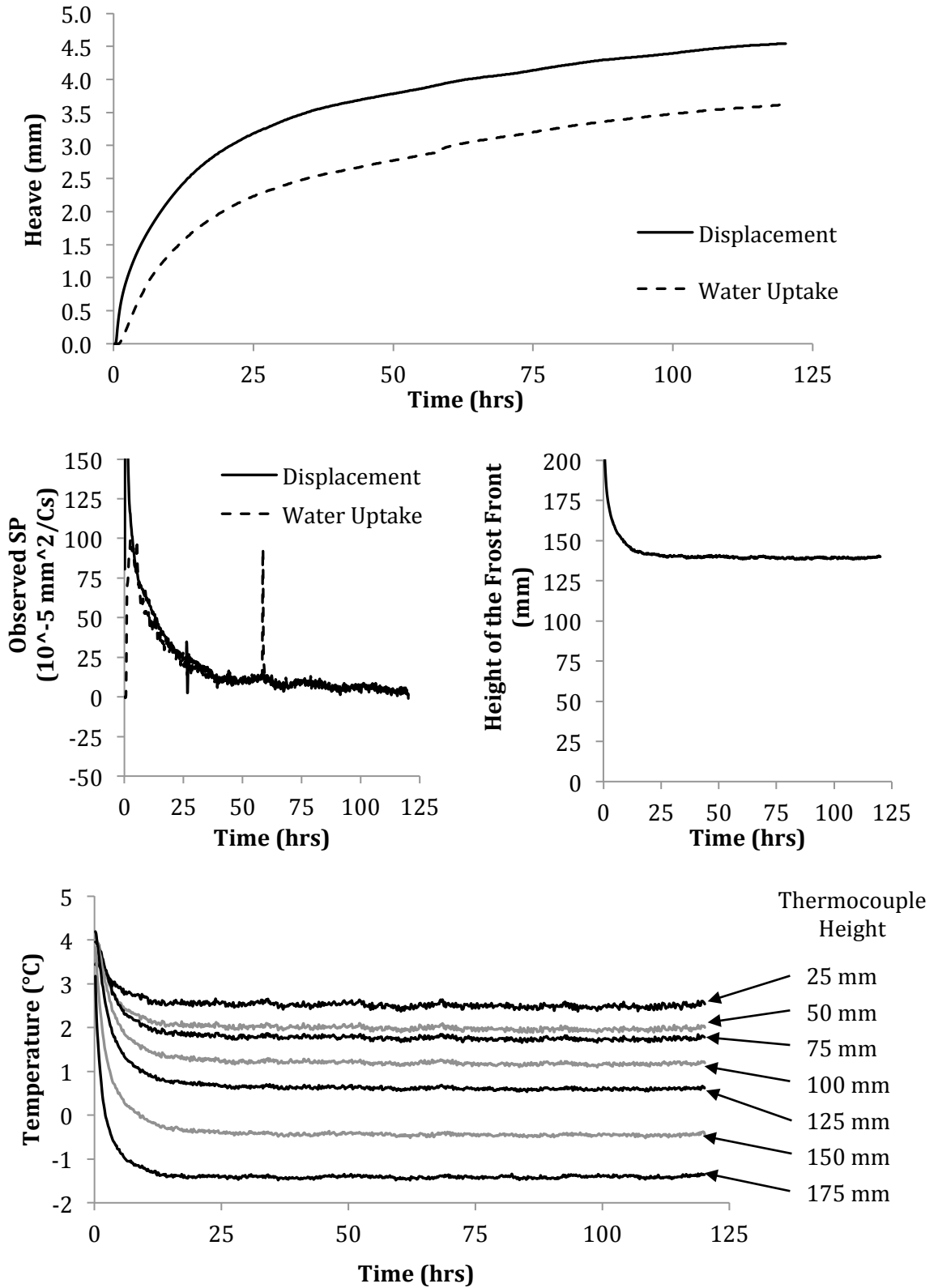


Figure A.5: FS-10 results.

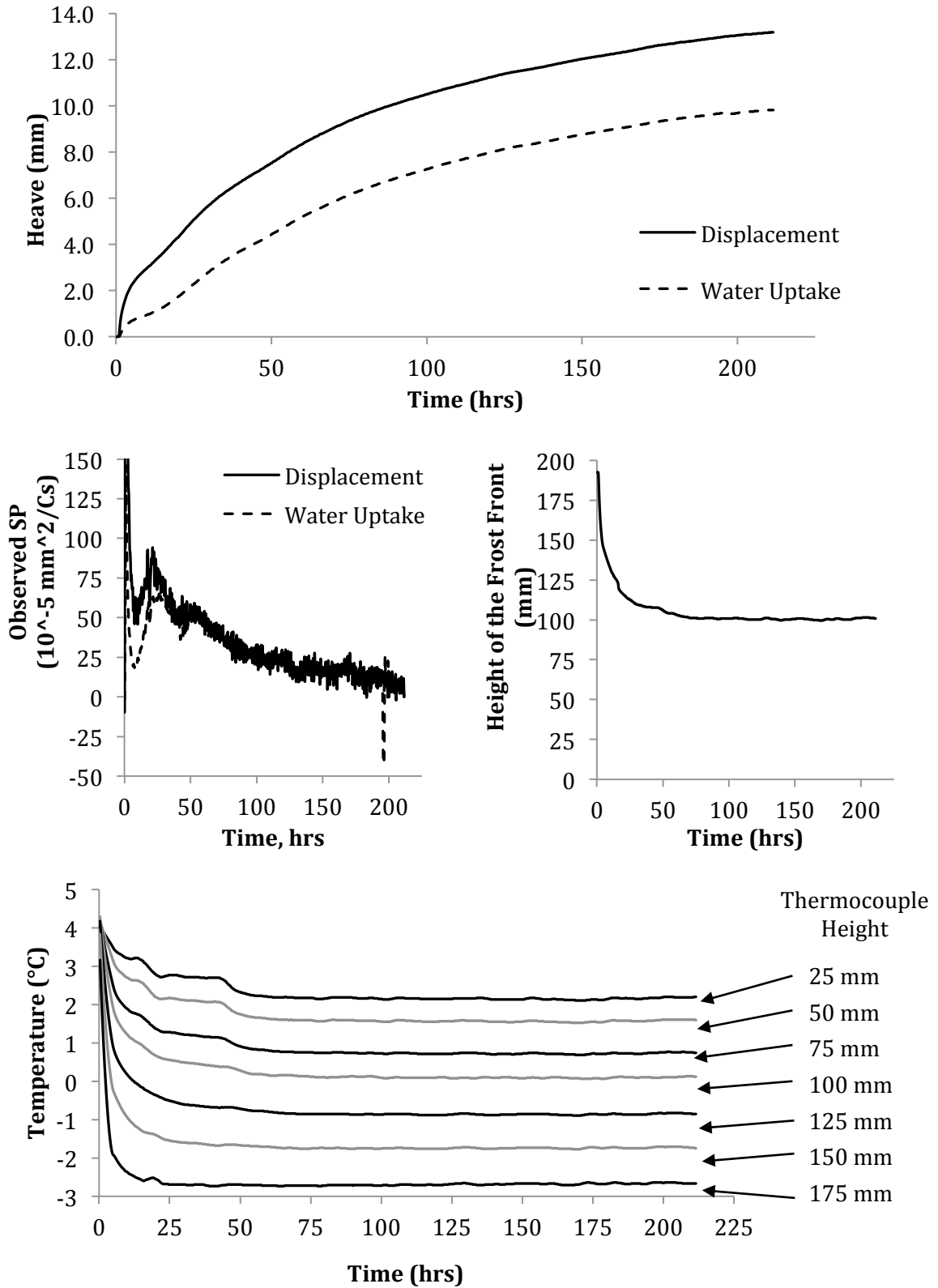


Figure A.6: BS-1 results.

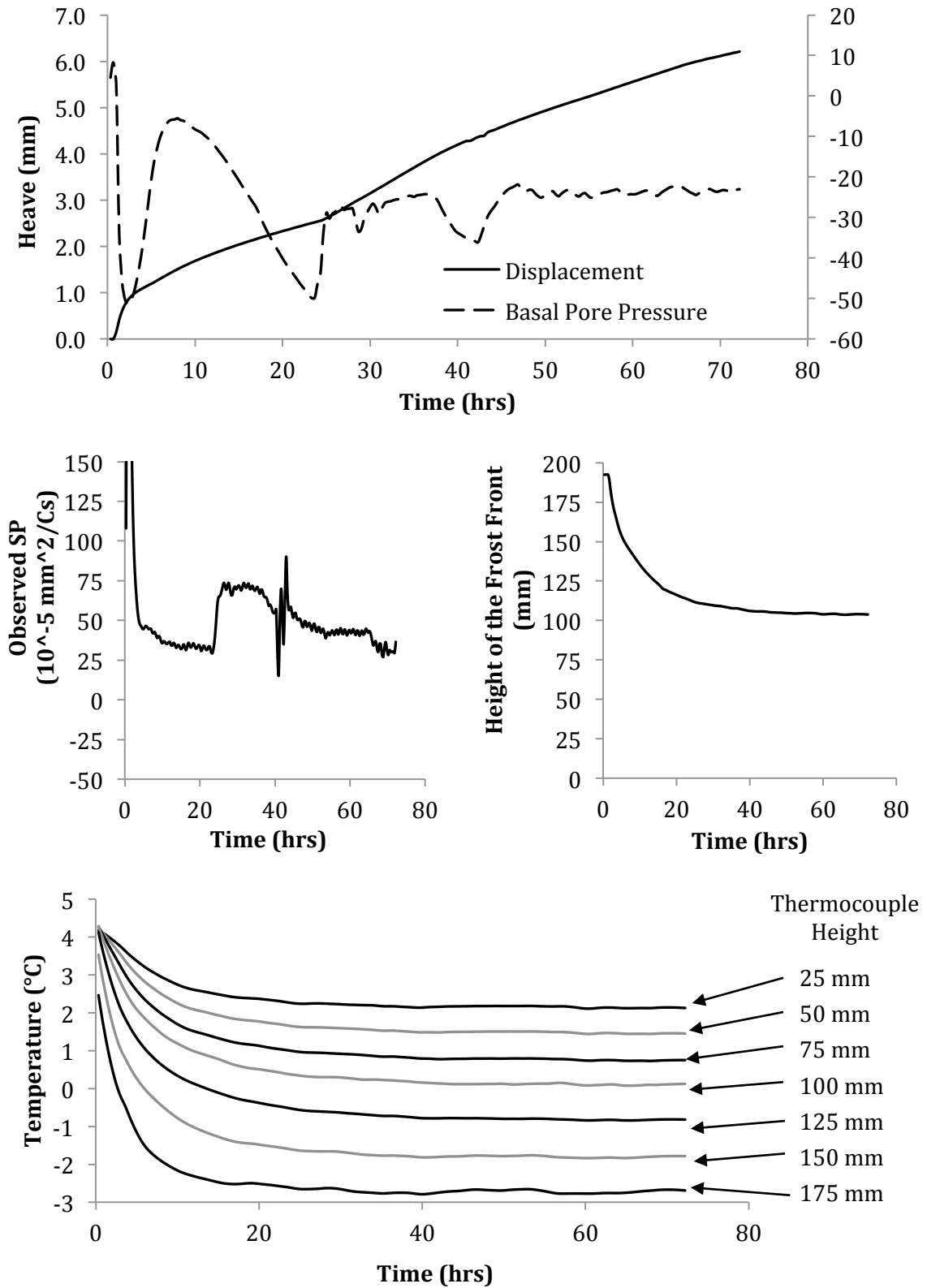


Figure A.7: BS-2 results.

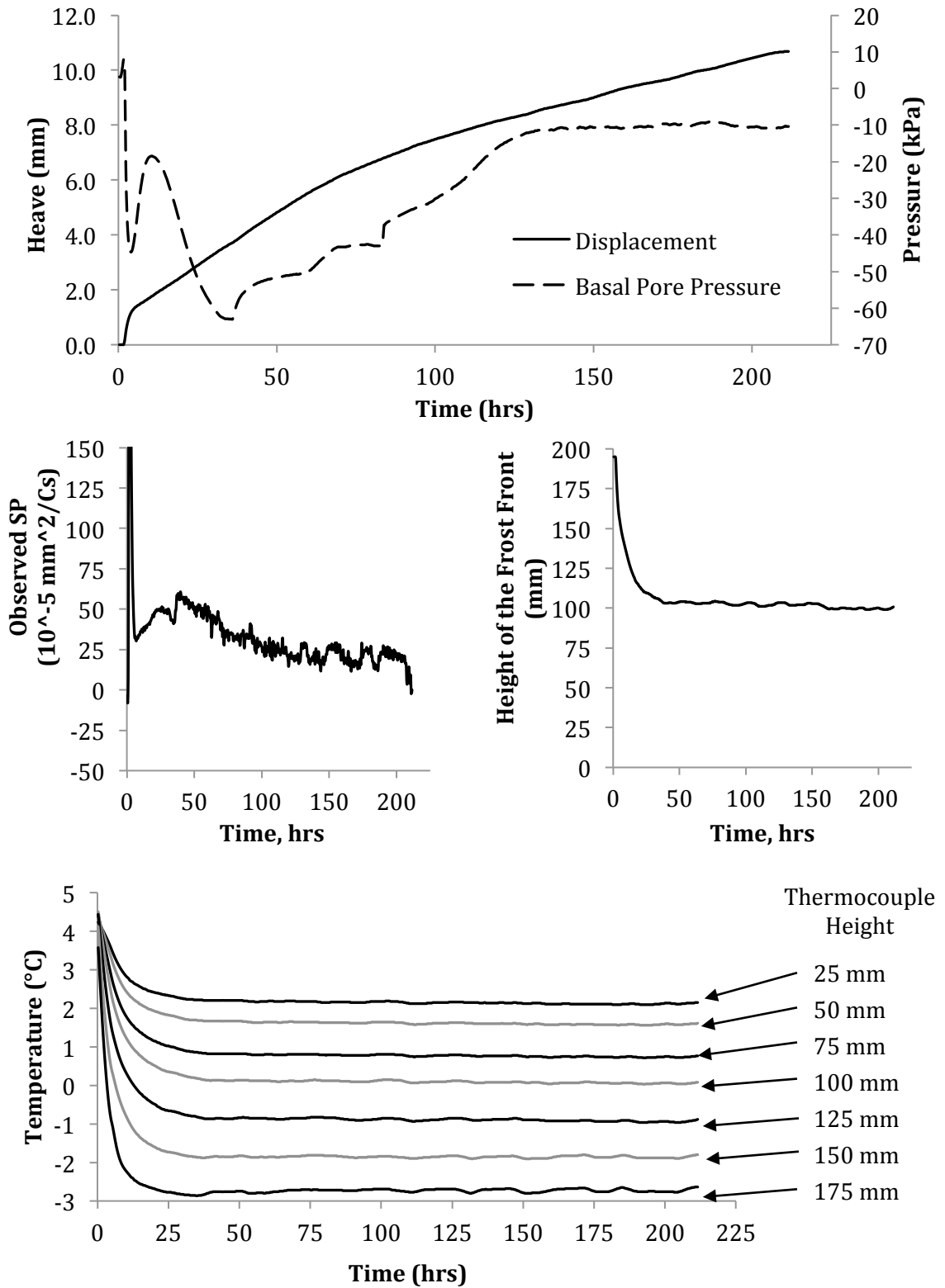


Figure A.8: BS-3 results.

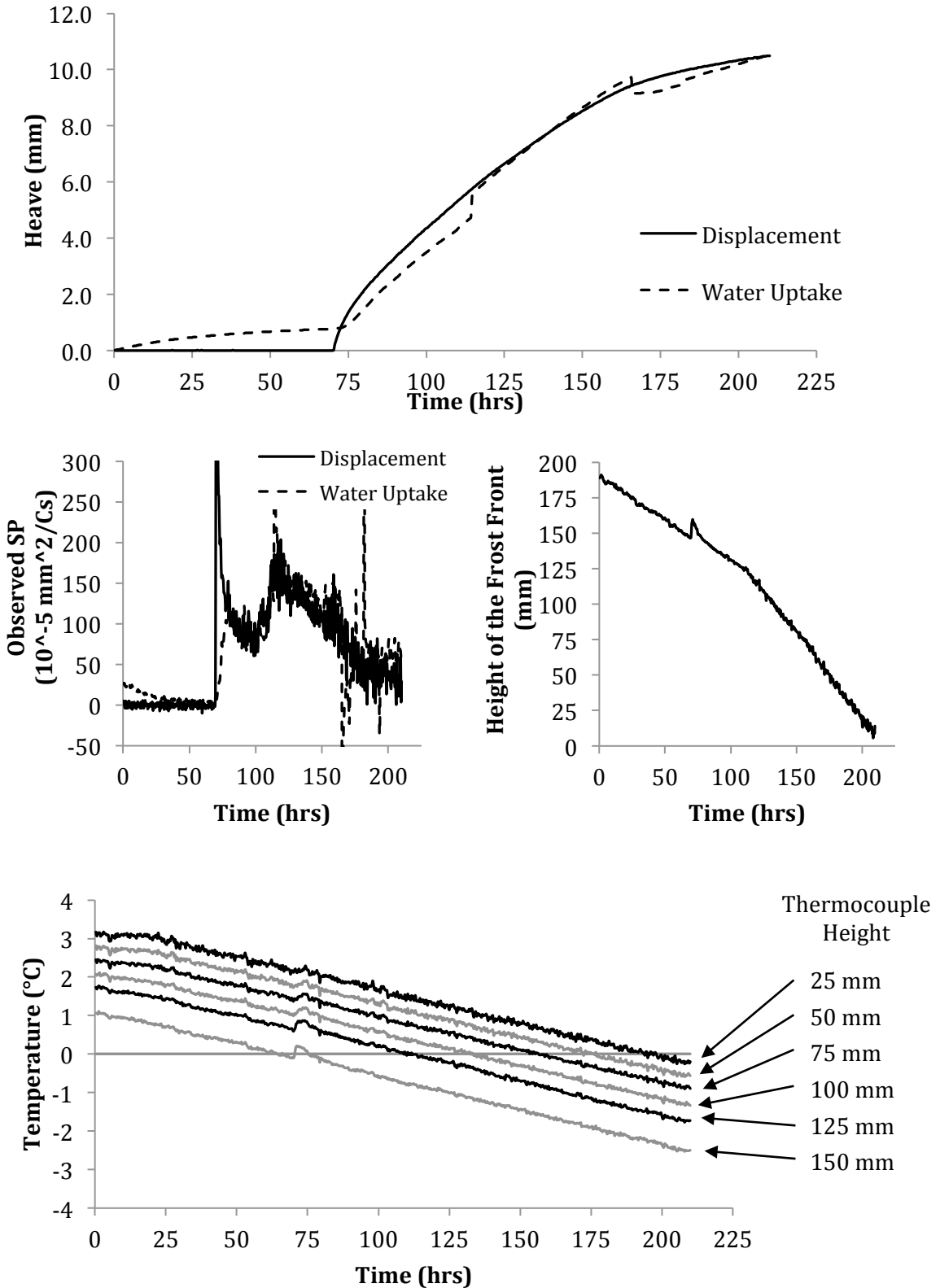


Figure A.9: FR-1 results.

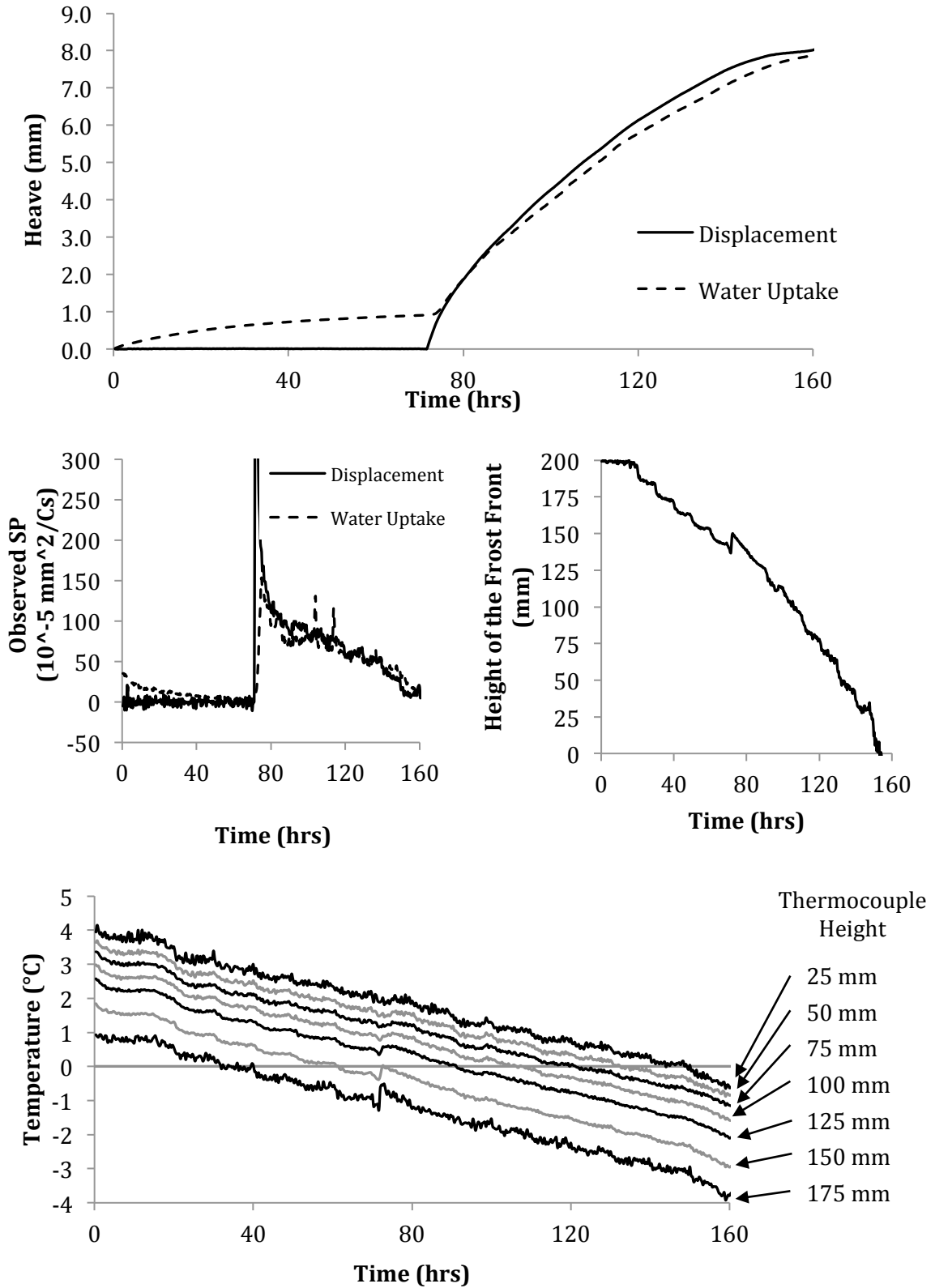


Figure A.10: FR-2 results.

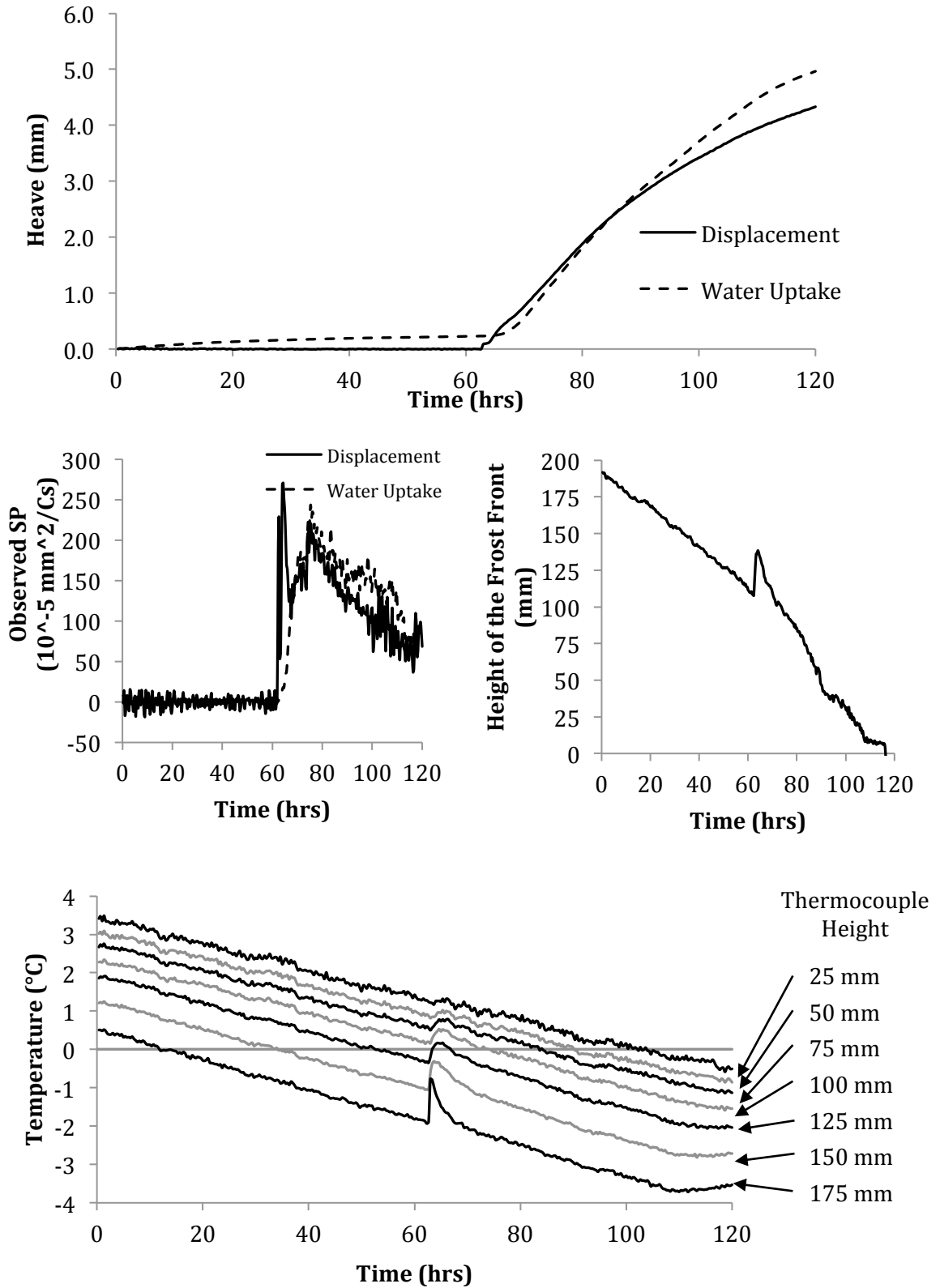


Figure A.11: FR-3 results.

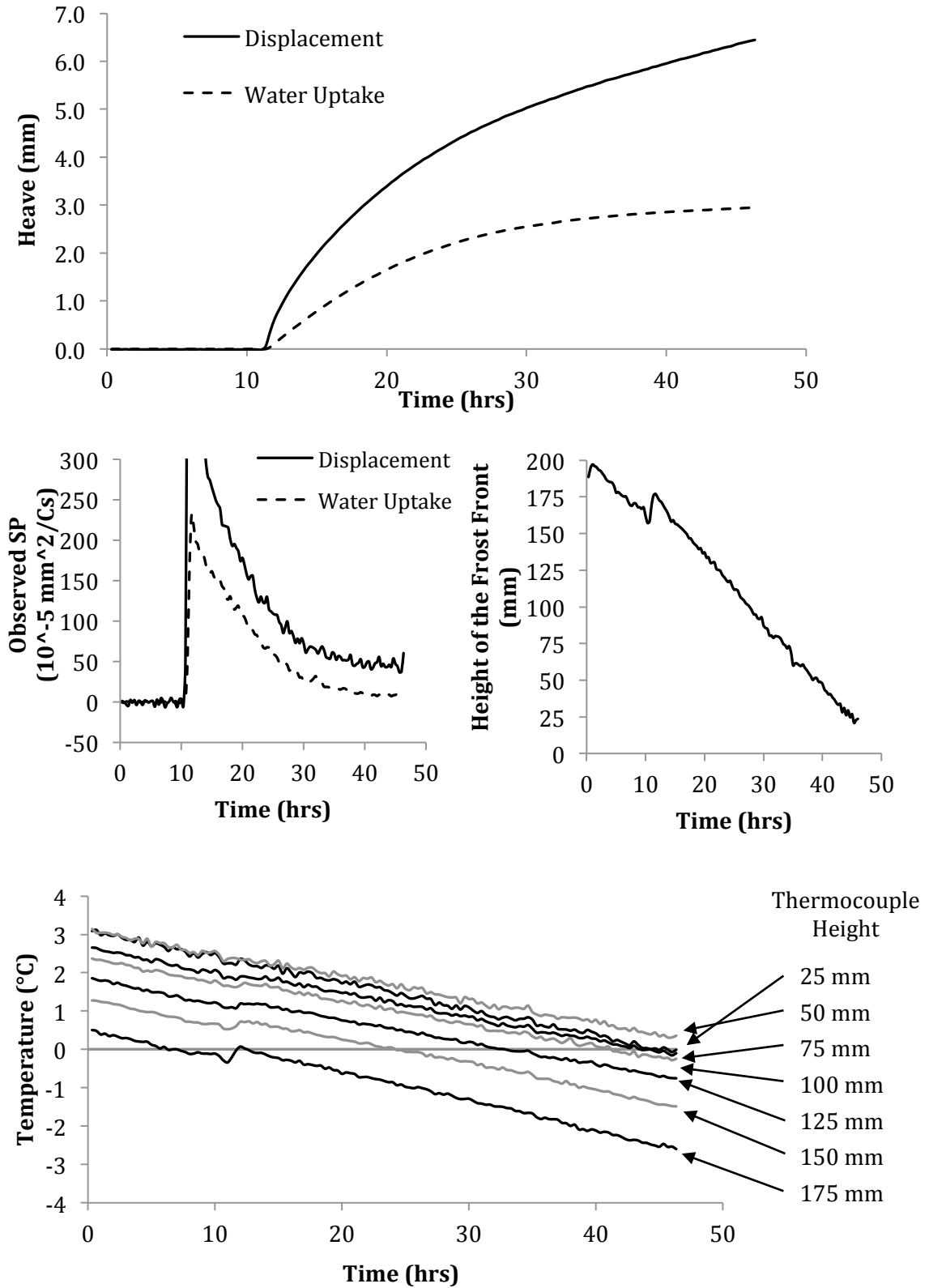


Figure A.12: BR-1 results.

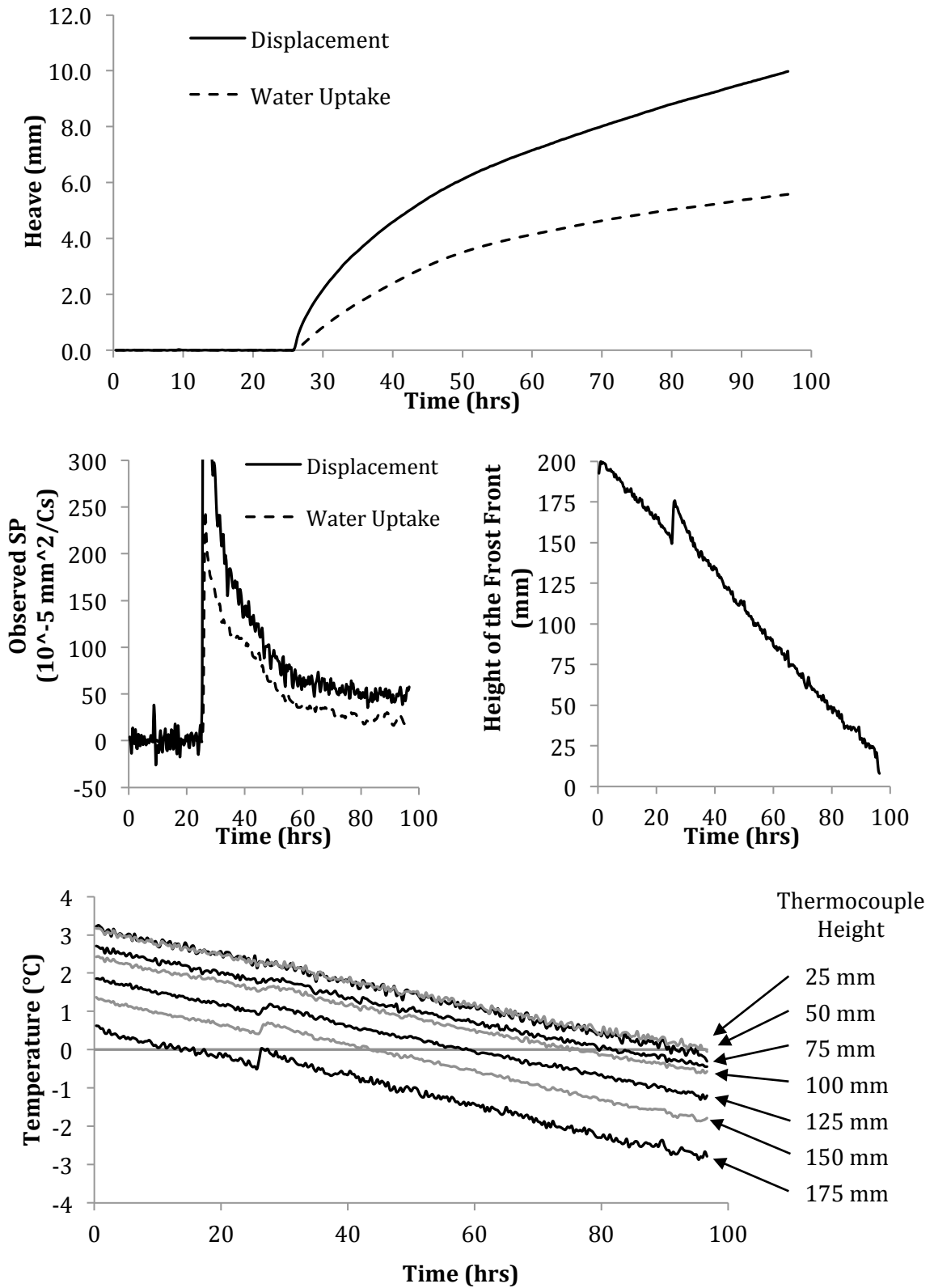


Figure A.13: BR-2 results.

APPENDIX B THERMAL CONDUCTIVITY OF DISCRETE PARTICLE COMPOSITES

B.1 ABSTRACT

The influence of particle shape and orientation on the thermal conductivity of low volume discrete particle composites was examined through two-dimensional numerical simulations using the finite element method, FEM. The simulations demonstrate that the conductivity of such composites is influenced by not only the relative volume and conductivity of the embedded particles, but also their general shape, elongation, and orientation relative to the direction of global heat flow. The Halpin-Tsai equation was utilized to characterize the composite thermal conductivity through the use of a derived expression of the geometric distribution factor, δ . The proposed expression of δ differs from commonly assumed values and is shown to be highly dependent on the shape of the embedded particles. It was further demonstrated that this approach is capable of explicitly characterizing the anisotropic behaviour of composites containing randomly distributed particles of a uniform size and shape based on their relative orientation.

B.2 INTRODUCTION

Discrete particle composites provide the opportunity for the development of sophisticated and advanced materials for numerous applications. Additive materials can enhance the performance of existing materials in a cost effective and efficient manner. Common properties of interest include thermal, electrical, and hydraulic conductivities as

well as mechanical characteristics such as stiffness and toughness. This work focuses on the thermal conductivity of discrete particle composites containing a low conductivity matrix with an embedded discrete phase of high conductivity. The objective is to explicitly characterize the influence of particle shape, elongation and orientation on the overall composite thermal conductivity. The anisotropic behaviour of such materials due to particle shape and orientation is of particular interest in this pursuit.

B.3 COMPOSITE THERMAL CONDUCTIVITY MODELS

When combining materials with differing properties, the resulting composite's material properties will be a function of three factors: the relative properties of each constituent, the corresponding volumetric fractions, and the geometric distribution of all constituents within the whole composite. The properties of a two-phase composite material with any geometric distribution of constituents are known to exist within two theoretical bounds, the Voigt upper bound (1889) and the Reuss lower bound (1929). The upper bound is provided by the parallel model and can also be referred to as the rule of mixtures, while the lower bound corresponds to the series model, or inverse rule of mixtures.

Voigt upper bound:
$$X_E = X_1\theta_1 + X_2\theta_2 \quad (\text{B.1})$$

Reuss lower bound:
$$\frac{1}{X_E} = \frac{\theta_1}{X_1} + \frac{\theta_2}{X_2} \quad (\text{B.2})$$

where θ_j and $X_{j(j = 1, 2)}$ are the volumetric fraction and property of interest of the constituents, respectively and the subscripts refer to the constituents and the effective composite material. As these two models diverge greatly when the properties of the two phases are significantly different, they are of limited practical utility in many applications.

Many models have been developed to estimate various composite material properties (Hill 1965, Kuster and Toksöz 1974, Maxwell 1881, O'Connell and Budiansky 1974, Wand et al. 2006). Regarding discrete particle composites, the effective medium theorem, EMT, is a conceptual approach to describe the global composite behaviour through analysing individual constituent particles. Maxwell used such an approach to derive models capable of describing the thermal conductivity and electrical permittivity (Maxwell 1881) of composites with a low concentration of spherical particles. Eshelby (1957) and Hatta and Taya (1985) expanded on this approach by considering composites composed of ellipsoidal particles. Hatta and Taya's work is capable of describing anisotropic behaviour, but relies on particle shape tensors, which have only been determined for specific particle shapes.

Refined theoretical bounds of composite properties were proposed by Hashin and Shtrikman (1962, 1968). These bounds offer a more narrow range of predictions as compared to the Voigt-Reuss bounds. For the thermal conductivity of a two-phase composite where $\lambda_2 > \lambda_1$, the HS bounds have the following functional forms:

$$\text{HS upper bound:} \quad \lambda_E = \lambda_2 + \frac{\theta_1}{\frac{1}{\lambda_1 - \lambda_2} + \frac{\theta_2}{D\lambda_2}} \quad (\text{B.3})$$

$$\text{HS lower bound:} \quad \lambda_E = \lambda_1 + \frac{\theta_2}{\frac{1}{\lambda_2 - \lambda_1} + \frac{\theta_1}{D\lambda_1}} \quad (\text{B.4})$$

where D is equal to either 2 or 3 depending on whether a two-dimensional or three-dimensional formulation is used, respectively (Szymkiewicz 2005).

A model of particular interest in this research is the Halpin-Tsai equation (Halpin and Kardos 1976). Originally proposed to determine the elastic moduli of two-phase composite materials, this model was derived as an extension of self-consistent micromechanics method developed by Hill (1965) and Hermans (1967). For a two-phase composite the HT equation has the following functional form:

$$\frac{X_E}{X_1} = \frac{1 + \zeta\eta\theta_2}{1 - \eta\theta_2} \quad (\text{B.5})$$

$$\text{with,} \quad \eta = \frac{X_2/X_1 - 1}{X_2/X_1 + \delta} \quad (\text{B.6})$$

In the above expression X is the composite property of interest, for example the bulk or shear moduli. The term δ accounts for the influence of the geometric distribution of the two phases and can be any positive real number. Halpin and Kardos (1976) presented values of δ corresponding to specific mechanical properties and select geometric distributions based on both theoretical derivations and empirical observations. For materials where the values of δ are well defined, the HT expression is an effective model for composite materials. However in many situations the δ parameter must be more generally approximated, which significantly degrades the effectiveness of this approach.

It is interesting to note that when δ approaches ∞ , the HT equation approaches the Voigt upper bound and likewise when the parameter equals 0 the equation yields the Reuss bound.

Lewis and Nielsen (1970) proposed a thermal and electrical conductivity model for composite materials based on the Halpin-Tsai equation by using the mathematical analogies between mechanical properties and the generalized transport processes.

$$\frac{\lambda_E}{\lambda_1} = \frac{1 + AB\theta_2}{1 - B\psi\theta_2} \quad (\text{B.7})$$

with,

$$B = \frac{\lambda_2/\lambda_1 - 1}{\lambda_2/\lambda_1 + A} \quad (\text{B.8})$$

and,

$$\psi = 1 + \left(\frac{1 - \theta_m}{\theta_m^2}\right)\theta_2 \quad (\text{B.9})$$

Here θ_m is the maximum packing fraction of the particles. The authors provided values of θ_m for select orientations and packing types. Generally, this term is empirically based. In the above equation A and B are analogues to δ and η , respectively, in the Halpin-Tsai equation. In general, δ and A depend upon the shape and orientation of the dispersed particles. Examples of proposed values of δ and A are outlined in Table B.1 (Lewis and Nielsen 1970, Progelhof et al. 1976). Progelhof et al. (1976) presented a further review of existing composite thermal conductivity models.

Table B.1: Select values of δ used to predict the bulk modulus of discrete particle composites using the Halpin-Tsai equation.

Condition	δ or A
Non-interacting Spheres	1.5
Interacting Spheres	$2.5/\theta_2 - 1$
Non-interacting Cubes	2
Parallel Fibres	$2(L/D)$
Perpendicular Fibres	0.5

B.4 APPROACH

Most existing composite models explicitly account for the geometric distributions of the constituent phases in some form. The characterization is based on either empirical observations or theoretical solutions of physical processes. The empirically based methods ultimately yield approximate descriptions, while the theoretical approaches are limited by the necessary simplifying assumptions in their formulations. The advent of advanced numerical simulation techniques, specifically FEM, allows for the examination of composites with more complex constituent geometries. With these simulations it is possible to obtain close approximations of the temperature field, allowing for the derivation of more robust composite models in a manner similar to the theoretical approaches. This approach sacrifices a minimal degree of accuracy for the quantification of a broader range of geometries.

The focus of this study is on specific types of composite materials: two-phase, discrete particle composites where the thermal conductivity of the particle phase is greater than the matrix phase. It will be assumed that the particles are non-interacting in nature.

This assumption limits the application of this model to composites with relatively low particle concentrations. Furthermore, only particles with easily quantifiable shapes are examined, specifically rectangular, ellipsoidal, and rhomboidal, as opposed to irregular shaped particles. The numerical simulations will be conducted in a two dimensional framework, the advantages and implications of this will be discussed herein.

Following the conceptual approach used by Lewis and Nielsen (1970), the functional form of the Halpin-Tsai equation is utilized to model the composite thermal conductivity. In this equation the influence of geometry is characterized by a single parameter, δ , which will be further examined through the numerical simulations.

B.4.1 Numerical modelling of Composite Thermal Conductivities

The numerical model simulated two-dimensional steady-state heat transport in a two-phase composite material. The composite was represented by a unit square domain containing one or more discrete particles with a total volume fraction of θ_2 and a thermal conductivity of λ_2 . A continuous medium phase with a conductivity λ_1 occupies the remaining volume. A one-dimensional global temperature gradient was applied across the element through fixed temperature boundary conditions on two opposing sides while imposing a zero flux boundary condition on the remaining sides. As illustrated in Figure B.1, at the x_0 and x_l boundaries the temperature is a fixed T_0 and T_l , respectively. The global thermal gradient can be defined as follows:

$$\nabla u_{global} = \frac{T_1 - T_0}{x_1 - x_0} \quad (\text{B.10})$$

Additionally, the total heat flux passing through the composite in the x-direction can be defined as follows:

$$Q = \int_L \lambda \cdot \nabla T \, dy \quad (\text{B.11})$$

where k and ∇u are the local conductivity and gradient, respectively. The average thermal conductivity of the composite material in the direction of thermal gradient, λ_E , can be determined as:

$$\lambda_E = \frac{Q}{\nabla T_{global}} \quad (\text{B.12})$$

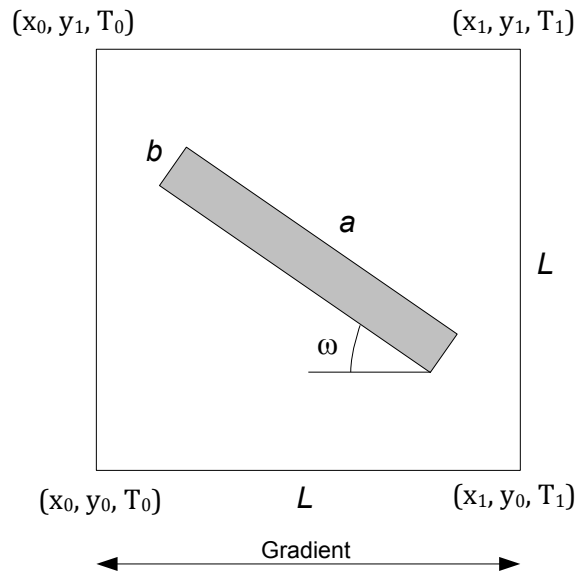


Figure B.1: Schematic representation of a single, rectangular particle composite simulation.

Two general categories of geometries were examined: single particle and multiple particle composites. For the single particle simulations the unit cell element contained a particle with a geometric center coinciding with the center of the element, see Figure B.1. Three different particle shapes were examined: rectangular, elliptical, and rhomboidal. The elongation was characterized by the aspect ratio, AR , defined as the ratio of the largest particle dimension to the smallest and the orientation of the particle was characterized by the angle ω between the long particle axis and the direction of the globally imposed thermal gradient. Due to the square shape of the domain, geometry limits the maximum volume fraction and aspect ratio of the particle, i.e. $\theta_2 \cdot AR = (a/L)^2 \leq 1$ for a rectangular particle. However, substantial boundary effects were observed when the surface of the particle approached the boundary of the element and consequently, the volume fraction and aspect ratio were further limited in order to ensure a minimum spacing of 10% between the particle and domain boundary. For each particle shape examined, the single particle simulations had four variables influencing the relative composite thermal conductivity, λ_E/λ_I , specifically: λ_2/λ_1 , θ_2 , AR , and ω . The specific range of variables examined in these simulations is outlined in Table B.2.

Table B.2: The range of variables examined in the single particle composite simulations.

Rectangular, Elliptical, & Rhomboidal
$0.01 \leq \theta_2 \leq 0.1$
$1 \leq AR \leq 60$
$1 \leq \lambda_2/\lambda_1 \leq 1000$
$0 \leq \omega \leq \pi/2$

In order to examine the influence of the distribution of particles on the composite thermal conductivity, a Monte Carlo scheme is used in the multiple particle composite simulations. In this approach, composites consisting of a series of unique, randomly generated particle distributions are simultaneously analyzed. If a sufficient number of distributions are analyzed, a Monte Carlo scheme yields the mean of the composite property that is a function of λ_2/λ_1 , θ_2 , and the particle shape. Due to practical constraints, this investigation was limited to multiple particle composites containing only rectangular particles.

The simulated multi-particle composites are further subcategorized based on the methods used to generate the particle distributions, specifically periodic and random distributions. Periodic distributions involve assigning particle positions using a prearranged 6 by 6 square grid within the unit square domain. The centroid position of twelve uniform particles was assigned randomly by selecting twelve grid cells, see Figure B.2. The orientation angle of each particle was assigned using a uniform random distribution. The size and shape of the particles was limited to $\theta_2 \cdot AR \leq 2$ so there would be no contact with adjacent particles or the domain boundaries. This distribution method allowed for particles with different sizes and elongations to be analyzed in the same position and orientation. In total, 50 distributions were analyzed, each with the global thermal gradient aligned with both the x and y axes to investigate the directional dependency of thermal conductivity related to particle orientations. It is important to recognize that this generation approach yields distributions with well-dispersed particles.

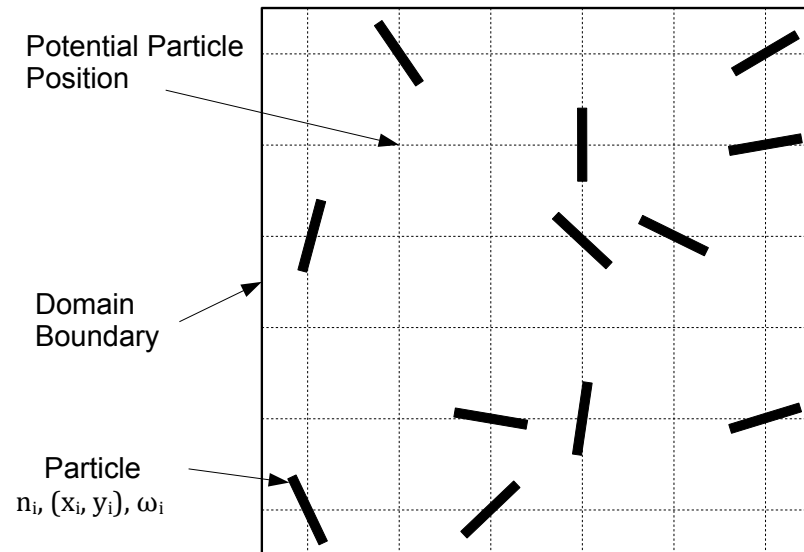


Figure B.2: Illustration of the periodic particle distribution scheme.

In the random distribution scheme the constituent particles are assigned positions and orientations within the composite using a uniform random distribution. The only requirement is that particles do not contact either adjacent particles or the domain boundaries, which was achieved through iterative position assignment. This scheme avoided any partial particles in the simulated composite and allowed for constant and precise volume fractions. The particle distribution scheme allowed for less dispersion between particles, though particles of different dimensions could not be applied to the same distribution. Each distribution contained 100 particles and 30 distributions were analyzed for thermal gradients along the x and y axes for each combination of variables.

B.4.2 Finite Element Analysis

The simulations were conducted with *FlexPDE*. An h-type adaptive mesh refinement method was used to improve numerical accuracy. In this method, the local mesh densities and sizes are adjusted based on a predefined error tolerance, which was 0.2% in this study. The meshes contained six-node quadratic elements with a maximum aspect ratio of 2.0. The number of nodes used varied between 10^3 and 10^6 , depending on the composite geometry and other input variables. A mesh sensitivity analysis was conducted to examine the influence of discretization on the solution. For select composites, the temperature field was determined using meshes of various densities. It was observed that the numerically determined λ_E/λ_I is generally insensitive to mesh size and mesh refinement. Figure B.3 illustrates the variation in the simulated composite conductivity with the number of nodes in the mesh of a reference composite with the following input variables: $\lambda_2/\lambda_1 = 100$, $\theta_2 = 0.05$, $AR = 5$, $\omega = 45^\circ$.

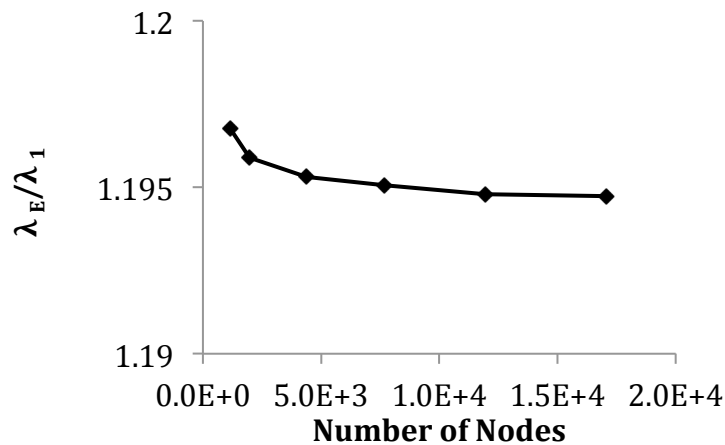


Figure B.3: The variation of the simulated composite conductivity, λ_E/λ_I , with the number of nodes of a reference composite.

B.5 RESULTS AND ANALYSIS

B.5.1 Single Particle Simulations

Figure B.4 presents the variation of composite thermal conductivities for select simulations, more specifically a rectangular particle with a volume fraction $\theta_2 = 0.1$ and conductivity ratio of $\lambda_2/\lambda_1 = 1000$. When the AR exceeds 1 the composite is inherently anisotropic and the properties are dependent on the particle orientation. More specifically, when the orientation of the particle is parallel to the global gradient (i.e., $\omega = 0$), the value of λ_E in the direction of the global thermal gradient increases with the aspect ratio, AR , while for particles perpendicular to the global thermal gradient (i.e., $\omega = \pi/2$), λ_E tends to decrease with increasing AR . However, the magnitude of change is not equal between orientations and the mean composite conductivities (averaged across orientations) increase with AR . Figure B.5 illustrates the variation in the mean composite conductivity with AR corresponding to $\lambda_2/\lambda_1 = 1000$ and $\theta_2 = 0.05$; however, similar behaviour was observed for all conductivities and volume fractions simulated. For a given AR and volume fraction, the variation of λ_E with the particle inclination angle reflects the anisotropy of the composite. As the aspect ratio increases there is a corresponding increase in the degree of anisotropy. In addition to elongation, the general particle shape also has some influence on the composite conductivity. For a particular particle volume fraction and aspect ratio, the elliptical and rhomboidal particle shapes were associated with greater mean composite conductivities as compared to rectangular particles.

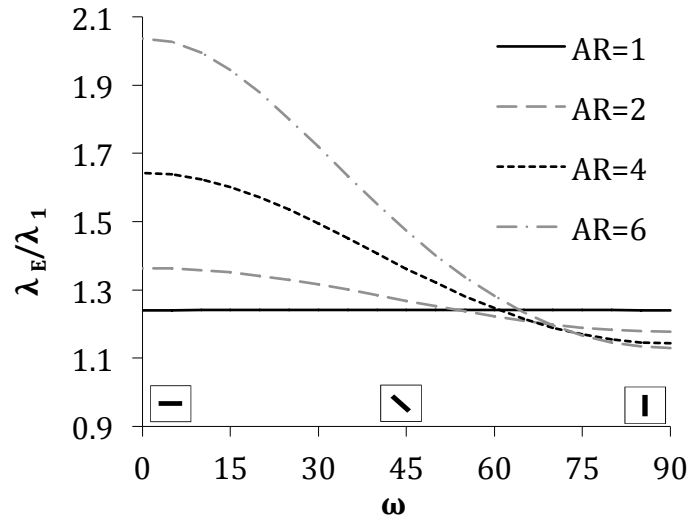


Figure B.4: Variation of composite thermal conductivity of a single rectangular particle composite with relative orientation and elongation.

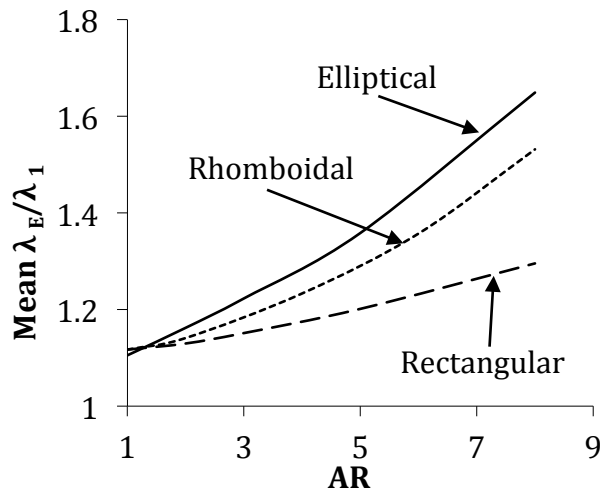


Figure B.5: Variation of the composite thermal conductivity of a single particle composite averaged across all orientations.

When using the framework of the Halpin-Tsai equation to describe the thermal conductivity of composites, the geometric distribution factor, δ , can be regressed for each case

from the modelling results. For the range of variables examined, δ varies with particle shape, elongation, and orientation, while at the same time there was effectively no variation with volume fraction θ_2 or the relative conductivity of the particle inclusions, see Figures B.6 and B.7. Larger values of δ were generally associated with higher particle AR and each particle shape has a unique relationship between δ and orientation.

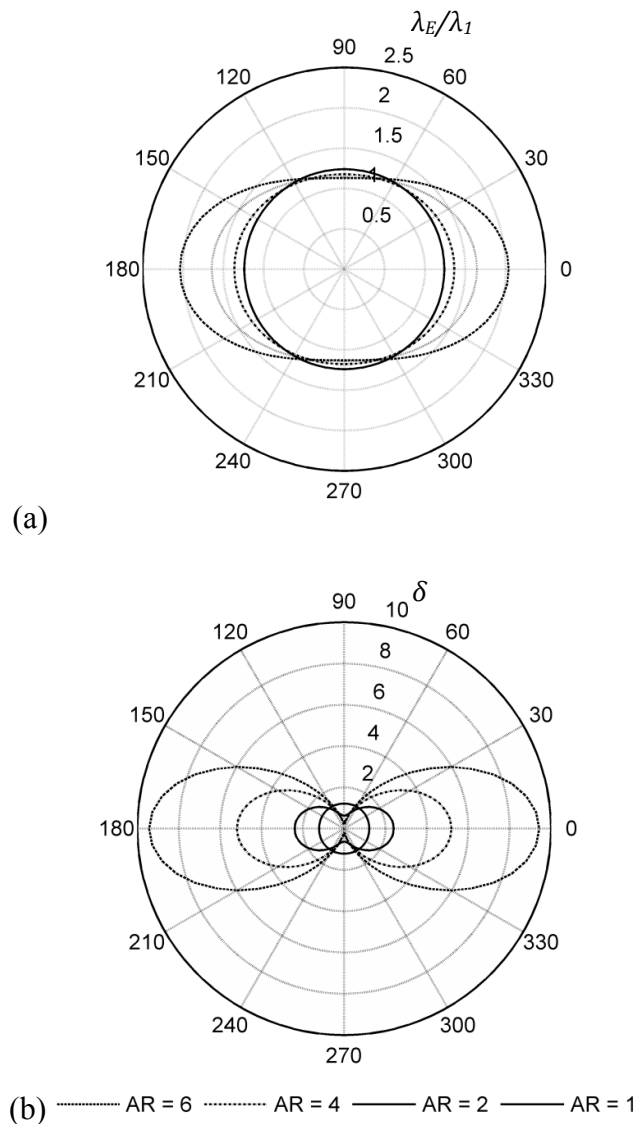


Figure B.6: The variation of the effective thermal conductivity, λ_E/λ_I , and the geometric distribution factor, δ , with AR and orientation for a single, rectangular, particle composite with $\theta_2 = 0.01$ and $\lambda_2/\lambda_1 = 100$.

Similar to the simulated composite conductivities, the values of δ were greatest at particle orientations parallel to the thermal gradient and least at perpendicular orientations. As illustrated in Figure B.7, the variation of δ with AR was observed to follow a linear relation in log-log space at these orientations. Since the 2D particles examined are symmetric about both axes, a particle oriented parallel to the global gradient with a specific AR is equivalent to a perpendicular particle with an elongation of AR^{-1} . The line of best fit in equation B.7 is a characterization of $\delta_{(0\&90)}$ based on the AR for a particular shape and can be expressed as equation B.13. The coefficients in the equation can be determined through regression analysis of multiple simulated results. Although the rectangular, elliptical, and rhomboidal shaped particles all followed the same general behaviour, different coefficients were found for each inclusion shape through regression analysis over a broad range of input variables and are presented in Table B.3. Generally, rhomboidal particles were associated with larger δ values and conductivities, followed by ellipsoidal and rectangular particles.

$$\delta_{(0 \& 90)} = j_1 AR^{j_2} \quad (\text{B.13})$$

Table B.3: The shape parameters in equation B.13 for the three different particle shapes.

Particle Shape	Shape Parameter, j_1 & j_2
Rectangular	$a_1 = 1.2754$ $a_2 = 0.8717$
Ellipsoidal	$b_1 = 0.9987$ $b_2 = 1.0208$
Rhomboidal	$c_1 = 1.2319$ $c_2 = 1.2237$

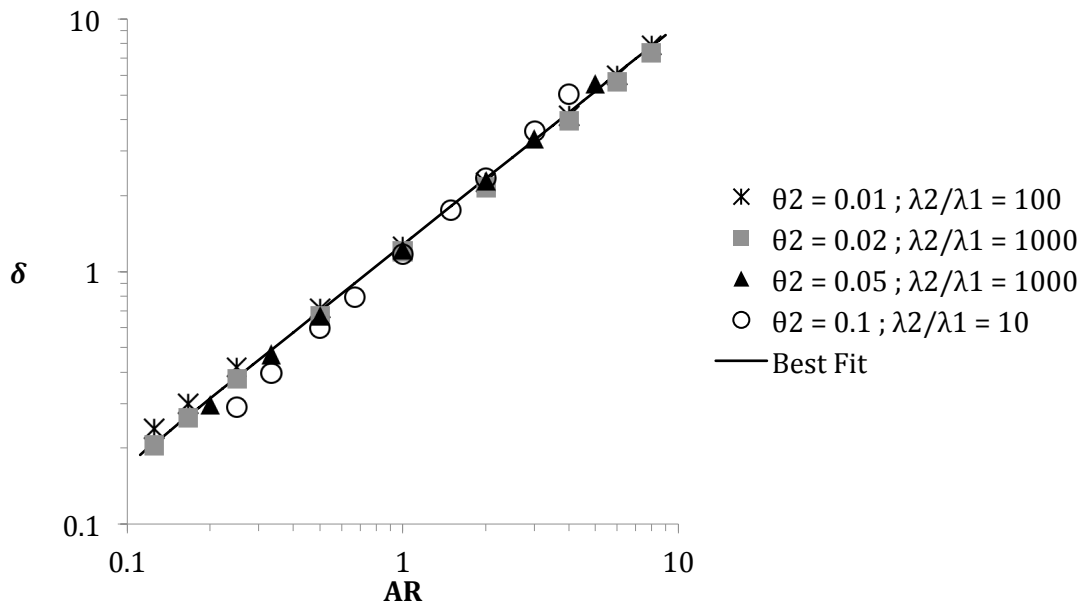


Figure B.7: Select results of the variation of δ with AR for perfectly aligned rectangular particles. The line of best fit in this equation corresponds to equation B.13.

For an orientation angle ω between the global gradient and the major axis of the particle, δ was observed to closely follow the following relation:

$$\delta(\omega) = \delta_0 Fx + \delta_{90} Fy \quad (\text{B.14})$$

where,

$$Fx = \cos^2 \omega; \quad Fy = 1 - Fx \quad (\text{B.15})$$

The subscripts 0 and 90 in equation B.14 refer to δ corresponding to a specific particle shape at parallel and perpendicular orientations, respectively. Figure B.8 illustrates the variation of δ with the orientation parameter Fx for select results of the three particle shapes corresponding to $\theta_2 = 0.01$ and $\lambda_2/\lambda_1 = 100$.

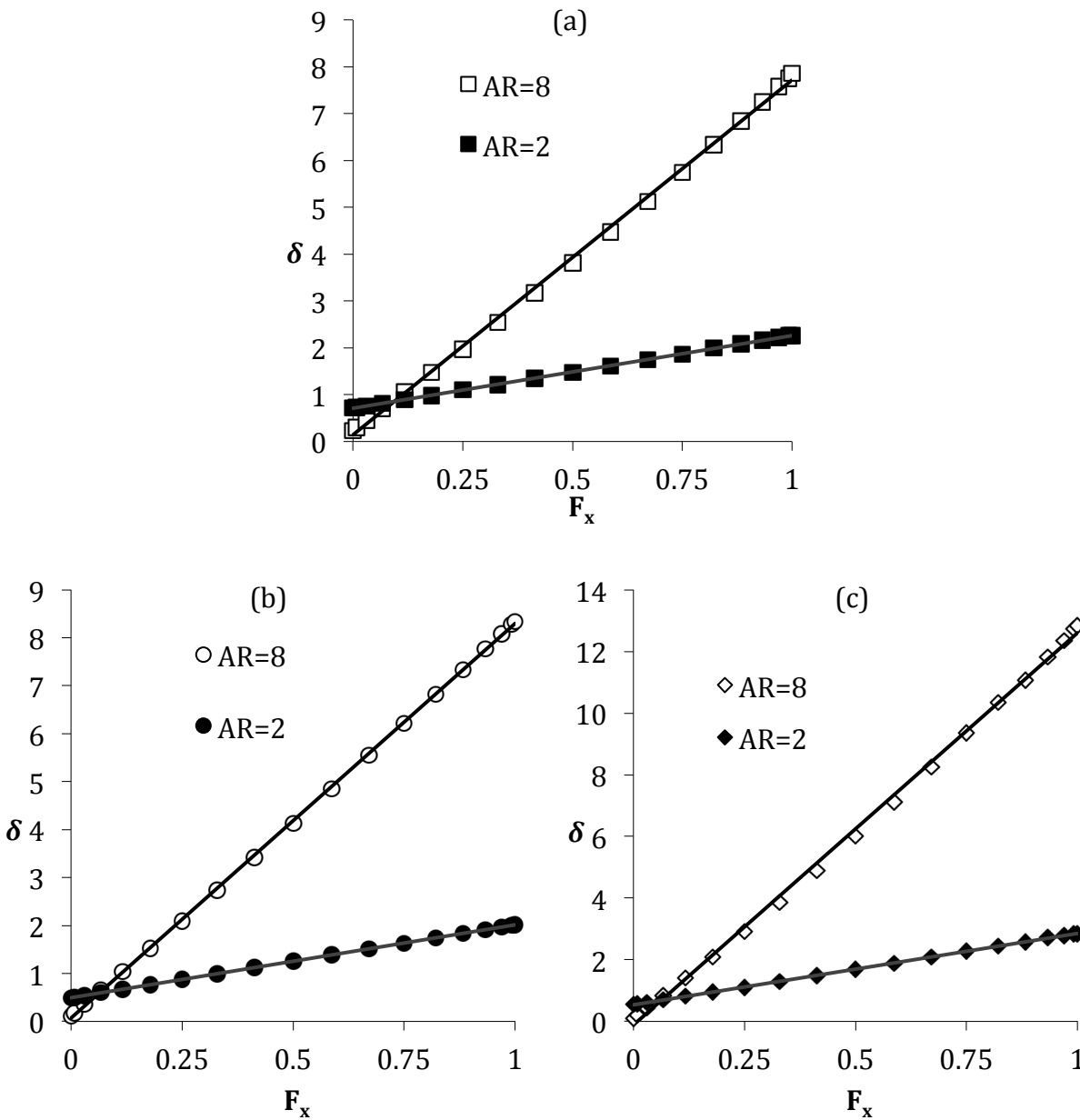


Figure B.8: Variation of δ with F_x for select aspect ratios. Figures (a), (b), and (c) correspond to rectangular, elliptical and rhomboidal particles, respectively.

Combining equations B.13 and B.14 yields a generalized expression of δ as a function of the particle shape, aspect ratio and orientation relative to the global thermal gradient:

$$\delta_{(AR,\theta)} = j_1(AR^{j_2}F_x + AR^{-j_2}F_y) \quad (\text{B.16})$$

B.5.2 Multiple Particle Simulations

The multiple particle simulations indicate that composites with a single particle type, i.e. containing particles of a constant size and shape, the homogenized thermal conductivity is positively correlated with λ_2/λ_1 , θ_2 , and AR , see Figure B.9. The noted influence of particle elongation on the composite properties is generally consistent with the findings of the single particle simulations, increasing AR values corresponded to increasing mean conductivities. The observations further indicated that the influence of AR on the composite properties was more pronounced at larger particle volume fractions.

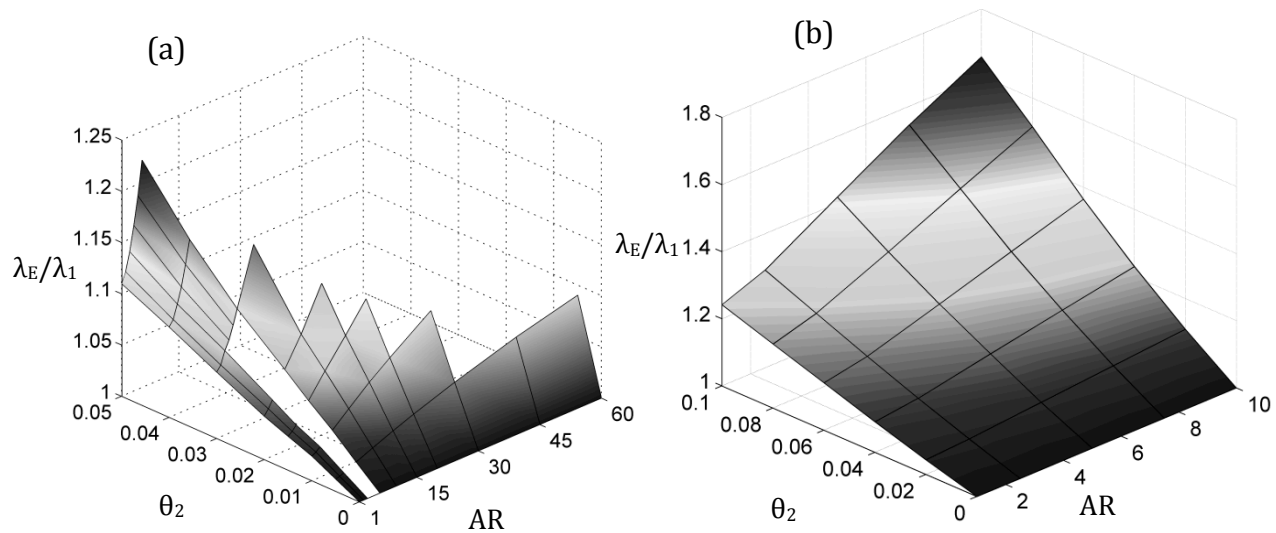


Figure B.9: Variation of the mean relative composite thermal conductivity, λ_2/λ_1 , with aspect ratio and volumetric fraction for multi-particle composites. Figure (a) corresponds to a periodic particle distribution while (b) corresponds to a random distribution. For both cases the composite contained mono-sized rectangular particles with a conductivity ratio of $\lambda_2/\lambda_1 = 100$.

Simulations for composites consisting of multiple particles were conducted with a ratio of constituent thermal conductivity of up to $\lambda_2/\lambda_1 = 1000$. As illustrated in Figure B.10, the observed composite conductivities approach constant values when λ_2/λ_1 was sufficiently large,

approximately three orders of magnitude. Examining larger conductivity ratios was deemed unnecessary.

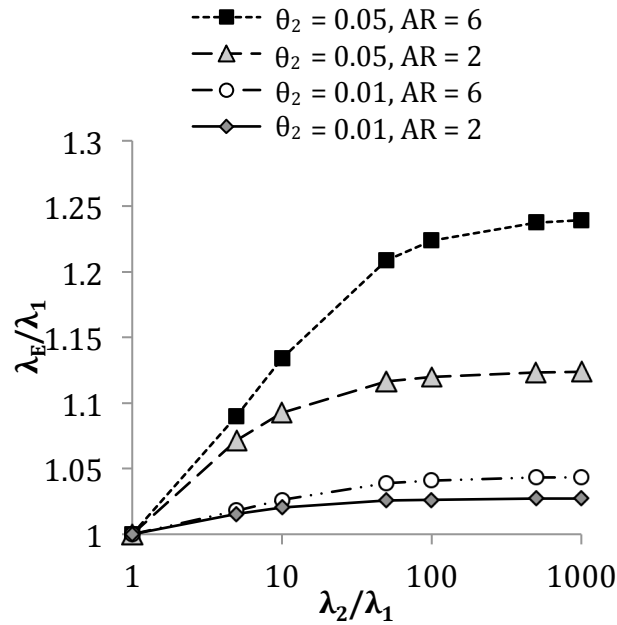


Figure B.10: Variation of the mean composite thermal conductivity with the constituent conductivity ratio for select results of the multiple particle simulations using a periodic particle distribution.

B.5.3 Influence of the relative particle size

For a given volume fraction θ_2 , the number of particles in the composite is directly related to the size of each particle. The ratio, L/a , can be used to quantify the relative particle size, with a being the particle length, defined in equation B.17 for a rectangle.

$$a = \sqrt{\frac{\phi_2 AR}{n}} \quad (\text{B.17})$$

Figure B.11 examines the influence of the relative particle size on the results of select multi-particle simulations. The larger the L/a ratio the more particles the distributions contained. For 30 unique distributions analyzed about the x - and y -axes, the particle size generally does not materially influence the mean conductivities. Instead the particle size effects the deviation of the simulated distributions from the mean. These observations are consistent with reported findings of similar simulations (Iorga et al. 2008, Kari et al. 2007, Michel et al. 1999).

The objective of the multi-particle simulations was to determine the effective, or homogenized, conductivity of composites consisting of randomly distributed and well dispersed particles. In order to achieve this goal, simulations must include either a sufficient number of individual particles, or a sufficient number of particle distributions must be examined, or both. Increasing the number of particles per distribution increases the geometric complexity of the composite, necessitating more elements per simulation and increasing computational effort. The results demonstrate that statistical homogenization was achieved with 100 particles per distribution and 30 distributions per particle shape for the random distributions.

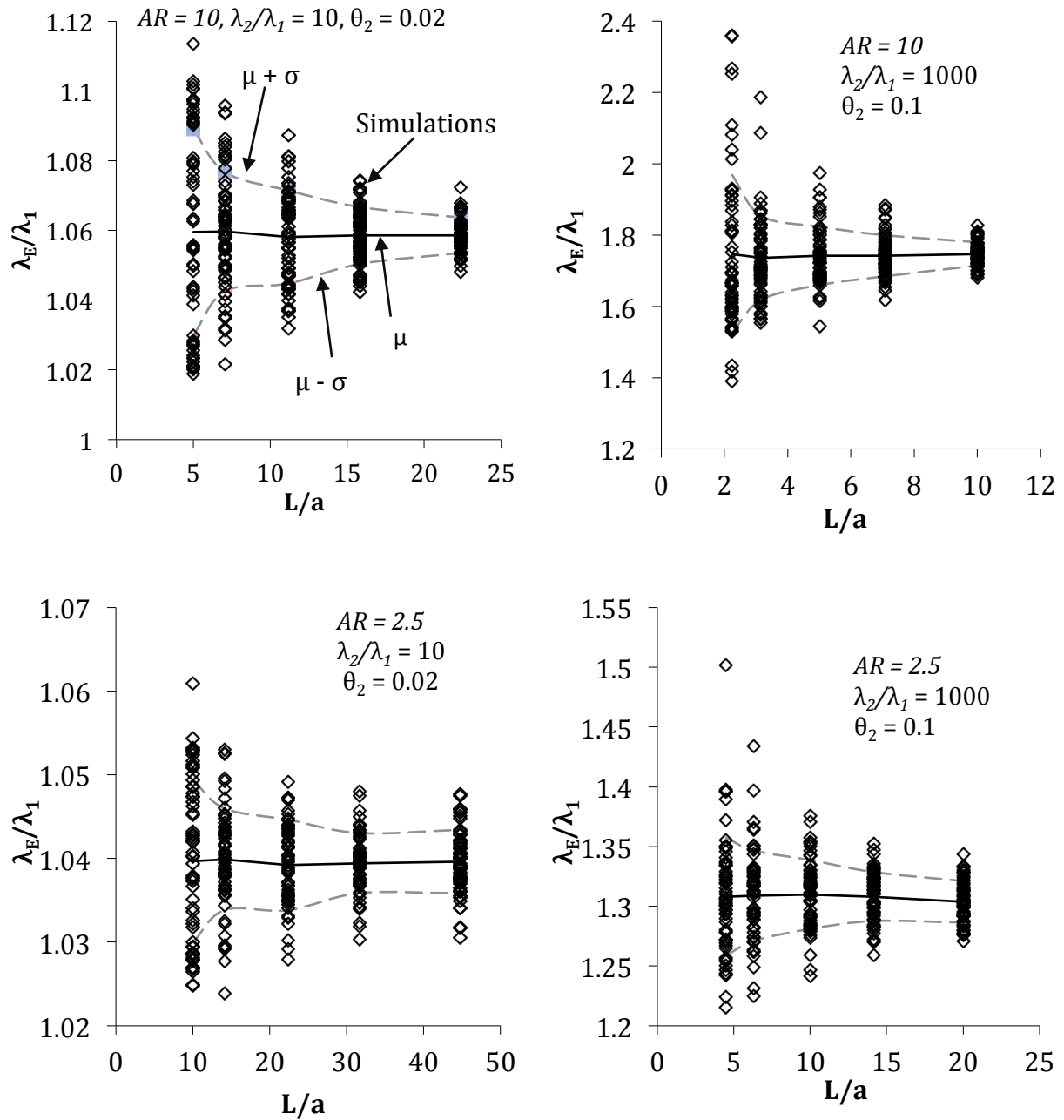


Figure B.11: Variation of the simulated composite thermal conductivities with relative particle size for the random distributions. The symbols μ and σ refer to the arithmetic mean and standard deviation, respectively.

B.5.4 Thermal conductivity anisotropy of multiple particle composites

Since elongated particles are fundamentally anisotropic, composites containing such particles have potential for anisotropic behaviour. For the multi-particle simulations, regardless of the uniform distribution used to assign orientations, due to the finite number of particles involved, there will inevitably be some degree of orientation bias associated with each distribution. Following Oda et al. (1985), a second-rank tensor is introduced to characterize the anisotropy induced by the directional distributions of particles:

$$\mathbf{F}_{ij} = \frac{1}{N} \sum_N n_i n_j \quad (\text{B.18})$$

with,

$$\mathbf{F}_{ii} = 1 \quad (\text{B.19})$$

where N is the number of particles in a unit volume of composite and n_i is the x_i component of the unit normal vector parallel to the longer particle axis.

As illustrated in Figure B.12, the results of the numerical simulations indicate that a linear relation can be used to correlate the directional composite thermal conductivity λ_{Ex}/λ_l and λ_{Ey}/λ_l with the corresponding components F_x and F_y of the fabric tensor, respectively. The results in this figure correspond to $\theta_2 = 0.02$, $AR = 6$, and $\lambda_2/\lambda_l = 100$. The scatter of the data is attributed to the influence of particle positions within the composite, which is not characterized by the fabric tensor.

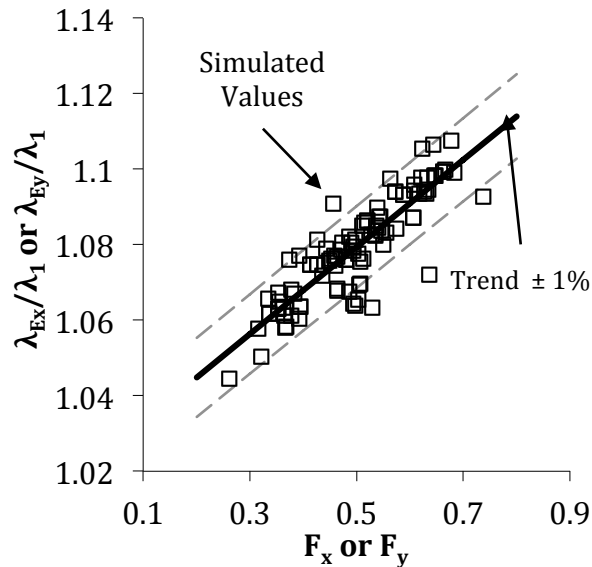


Figure B.12: Variation of relative composite properties with associated components (F_x or F_y) of the fabric tensor orientation parameter for multi-particle simulations using the periodic distribution method.

Similar to the single particle simulations, there is a geometric distribution factor δ associated with the simulated composite conductivity of each unique particle distribution and corresponding direction of thermal gradient. The variation of δ with F_x and F_y for select results is presented in Figure B.13. There is generally good agreement between the single particle correlation, as expressed by equation B.17, and the multi-particle simulation results. Figure B.14 presents the variation of anisotropy, quantified as the ratio of composite conductivity in the x and y directions, with the corresponding F_x/F_y ratios for the periodic simulations. In addition, the observed anisotropy of the simulations is compared to predictions derived from the single particle behaviour. Similar to Figure B.13, there is good agreement between the predictions and simulations when θ_2 is relatively small, while larger volume fractions are associated with greater

deviation. It is noted that there is only minor anisotropy in the composite thermal conductivity at smaller particle volume fractions and aspect ratios.

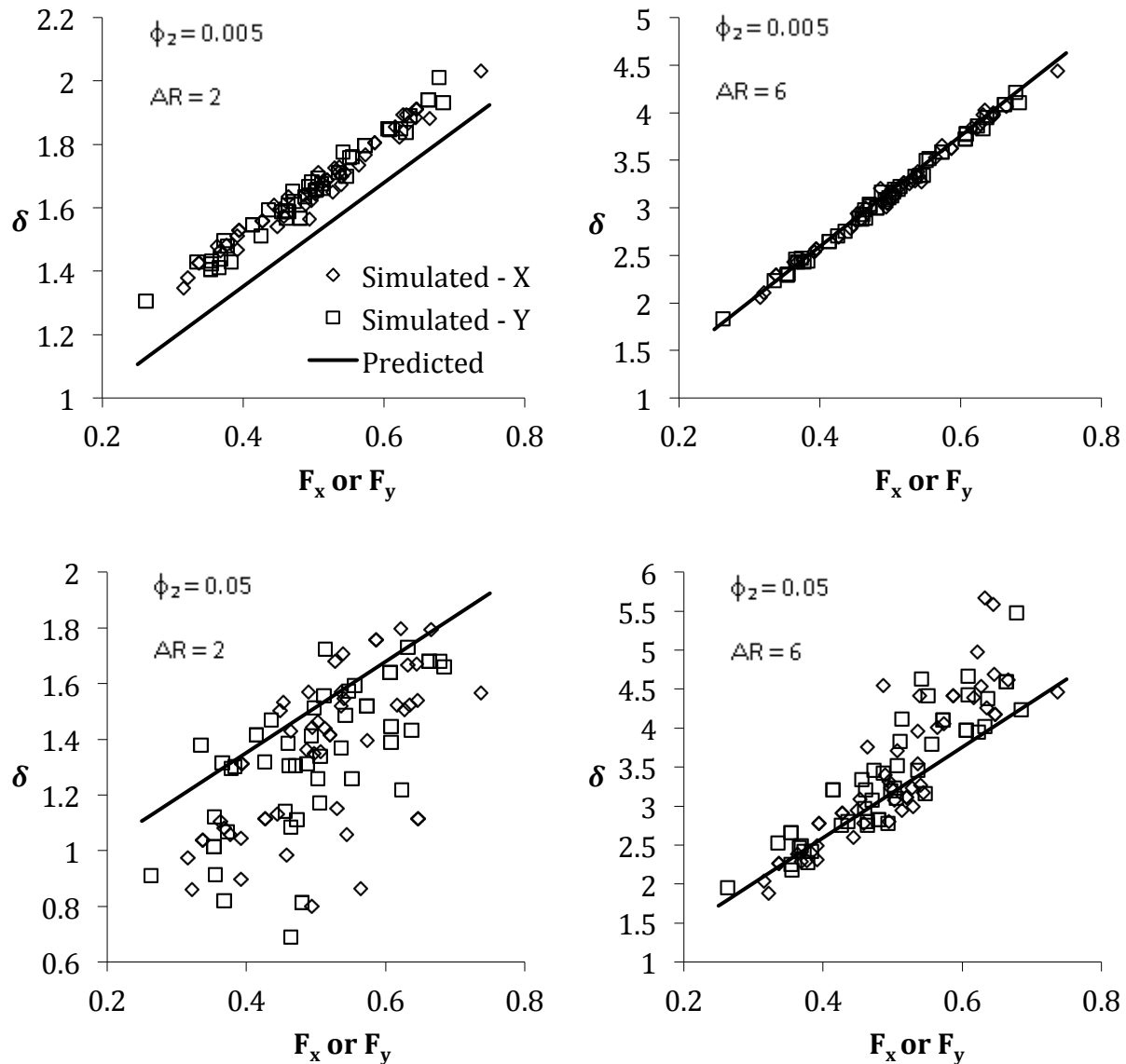


Figure B.13: Comparison of the simulated variation of δ with F_i and equation B.16. In all figures the periodic particle distribution method was used and $\lambda_2/\lambda_1 = 100$. In total 50 unique distributions were analyzed with the global gradient in both the x and y axes.

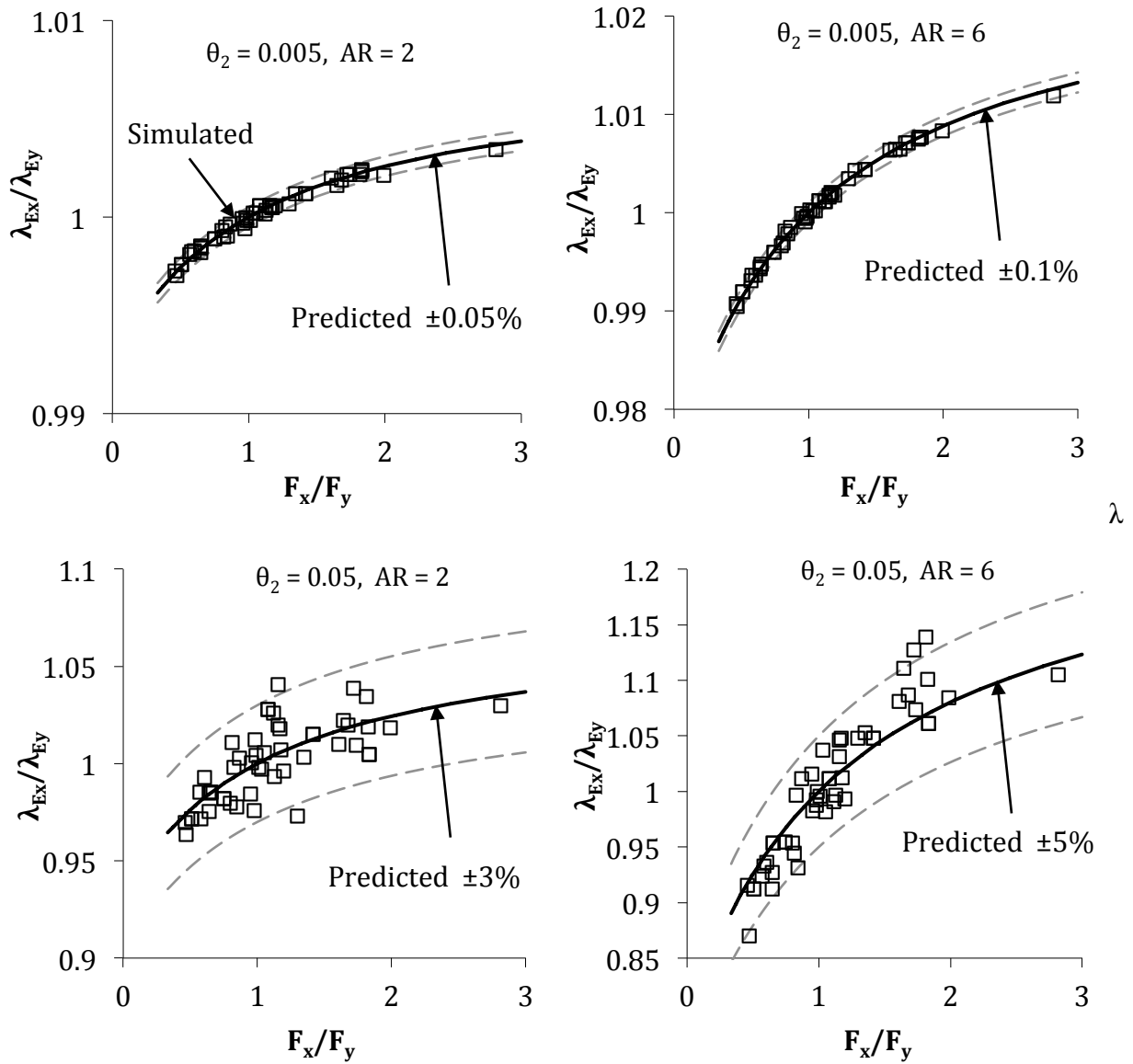


Figure B.14: Thermal conductivity anisotropy in the multi-particle simulations. In this case 50 periodic distributions were analyzed with the global gradient in both the x and y directions at $\lambda_2/\lambda_1 = 100$.

B.5.5 Isotropic Multiple Particle Composites

For a composite containing a series of particles with random orientations, as the size of the representative element volume increases, the fabric tensor F_{ij} approaches isotropic conditions with $F_x = F_y = 0.5$. For this case, equation B.18 reduces to:

$$\delta = \frac{j_1}{2} (AR^{j_2} + AR^{-j_2}) \quad (\text{B.20})$$

Figures B.15 and B.16 compare the predictions utilizing equation B.20 with the mean results of the multi-particle simulations using the periodic and random particle distribution methods, respectively. Included for comparison in the figures are the Voigt-Reuss and Hashin-Shtrikman bounds. Generally, good agreement is observed between the mean simulated values and the predictions, particularly at low AR values. At higher values of AR and θ_2 the predictions yield lower conductivities than the simulations. At an AR of one, both the simulations and predictions indicate slightly higher composite conductivities than the HS lower bound. This can be attributed to the variance in behaviour between the square particles simulated and the circular particles used in the 2D HS formulation.

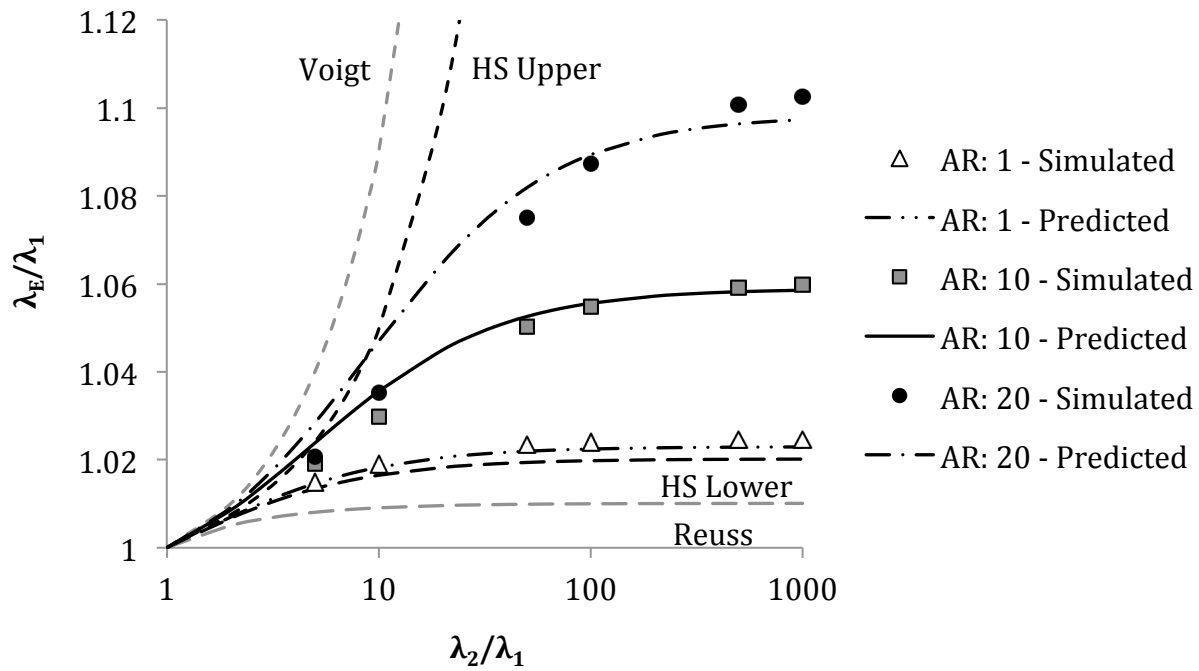


Figure B.15: Comparison of the mean results of the multi-particle simulations with periodic distributions and $\theta_2 = 0.01$ to the predictions utilizing equation B.20.

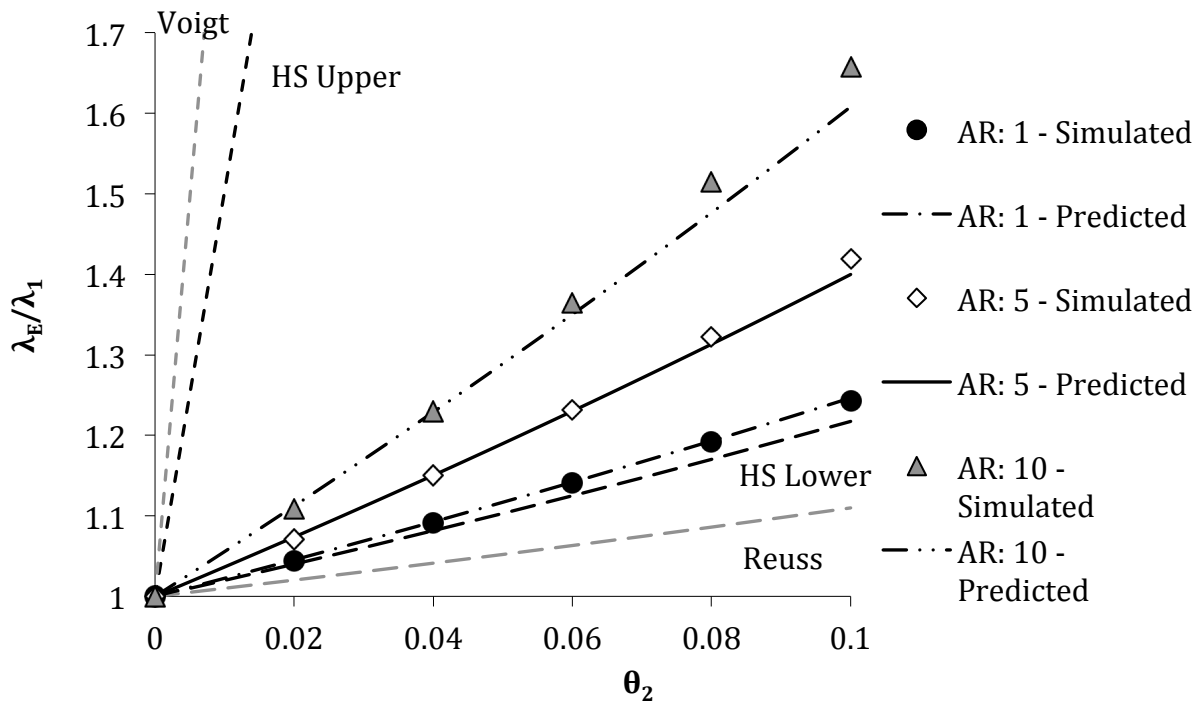


Figure B.16: Comparison of the mean results of the multi-particle simulations with random distributions and $\lambda_2/\lambda_1 = 100$ to the predictions utilizing equation B.20.

B.6 CONCLUSIONS

The homogenized properties of composite materials are highly dependent on the geometric distributions of the constituent phases. Modern numerical tools, such as FEM, allow for the determination of temperature fields of geometrically complex composites. Although these solutions are approximate by nature they can be used to generate more specific descriptions than have previously been developed.

The thermal conductivity of two-dimensional composites containing discrete, elongated, particles was examined. Using the results of FEM simulations of single particle composites, an expression of the geometric distribution factor, δ , in the Halpin-Tsai equation was proposed for select particle shapes based on elongation and orientation. The expression was compared to simulated composites containing multiple randomly distributed particles. These composites were limited to materials containing particles of a uniform rectangle. Including particle orientation in the formulation of δ allows the HT equation to explicitly characterize the anisotropic nature of such composites through the use of a second order tensor describing the directional distribution of particles.

This work focussed on non-interacting particles, which implies small discrete phase volume fractions and moderate AR values. Considering non-interacting particles is consistent with the conceptual approach used by Maxwell (1881) and others (Eshelby 1957, Hatta and Taya 1985). Because of this important assumption, the proposed composite description effectively provides the far-field bound (Bonnecaze and Brady 1990) (which is similar in concept to the

lower Hashin-Shtrikman bound) associated with a particular particle shape and orientation. If the approach were to be extended to large discrete-phase volume fractions, it would be expected that the expression would systematically under-predict true values, as the assumption of non-interaction would no longer be valid. The description of the near-field bound or the threshold at which the non-interacting particle assumption is valid is beyond the scope of the research.

While the numerical simulations were limited to only three particle shapes for the single particle composites (rectangular, elliptical and rhomboidal) and one shape (rectangular) in the extended multi-particle simulations, the conceptual approach will likely be valid for any axially symmetric two-dimensional shape. Irregular shapes can be easily simulated, however, the derived functional form of δ (equation B.13) may not be relevant. It is apparent that this concept can be readily extended into a three dimensional framework, though at present time this has not been sufficiently explored by the authors.

APPENDIX C THE THERMAL CONDUCTIVITY OF BENTONITE GROUT CONTAINING GRAPHITE OR CHOPPED CARBON FIBRES

C.1 ABSTRACT

The effectiveness of chopped carbon fibres to enhance the thermal conductivity of bentonite based grout was examined. Fibres of 3mm and 150 μ m in length were added to sodium bentonite and silica sand mixtures at different volumetric concentrations. The thermal conductivity of the resulting composite material was then measured using a non-steady-state needle probe technique. The conductivities of the fibrous materials were compared to bentonite and sand mixtures containing natural flake graphite and milled, compressed exfoliated graphite at corresponding volumetric concentrations. The resulting conductivities for all tested materials increased with the volumetric fraction of additive. However, the 3mm carbon fibres were more effective as compared to either granular graphite; at a volume fraction of 0.68% the 3mm fibres were approximately twice as effective as either form of graphite.

C.2 INTRODUCTION

Ground source heat exchangers (GSHEs) allow for the heating and cooling of buildings while consuming less energy compared to conventional systems. It has been well established, from both numerical models (Delaleux et al. 2012) and field observations (Lee et al. 2012), that the thermal conductivity of the bentonite grout used in vertically-bored GSHEs has a significant impact on the overall system performance. More

specifically, the higher the conductivity of the grout the more heat can be transferred per unit length of borehole.

Due to environmental concerns about the potential for contamination of underlying ground water, jurisdictions commonly require vertical boreholes be filled with nearly impervious bentonite grout. In these systems the grout also functions as a thermal contact between the heat exchanger, typically a loop of polyethylene tubing, and the surrounding soil. Bentonite grout is a composite material typically containing sand and montmorillonite clay, which has a high affinity towards absorbing water and possesses little hydraulic conductivity. This material typically has a modest thermal conductivity of between 0.7 and 2 W/mK. Numerical simulations indicate the performance of GSHEs could be significantly improved by increasing the thermal conductivity of the grout to as high as 8 W/mK (Delaleux et al. 2012). This introduces the potential benefit of enhancing the thermal conductivity of bentonite grout.

Currently, the most common approach taken toward thermal conductivity enhancement is a highly conductive additive material. Recent research has focused on various forms of graphite due to its high conductivity, relative inertness, and comparable cost with bentonite powder. Studies have shown that adding granular graphite to bentonite grout successfully increases the overall conductivity (Lee et al. 2010; Lee et al. 2012; Delaleux et al. 2012). To date the focus has been on the relative conductivity and volumetric concentration of the additive graphite. However, the effect of the size and shape of the additive has not been as thoroughly explored.

At low concentrations the graphite particles are essentially suspended in a continuous phase of grout, composed of sand and clay particles which have significantly lower conductivity. In this case the size and relative conductivity of the graphite particles are less important in the overall heat flow through the material than the distance between particles. Consider a series of spherical particles uniformly dispersed and suspended in a matrix. In this case the distance between particles is large and consequently the potential for heat flow is minimal. Next, consider the same number and volume of particles except with a highly elongated shape, i.e. ellipsoids or cylinders with large aspect ratios which are randomly oriented. In this case the average distance between particles is substantially less leading to greater potential for heat transfer. Consequently, for composite materials with dispersed particles at low volumetric concentrations, the greater the particle aspect ratio the greater the overall thermal conductivity of the material (Agari et al. 1991).

This principal has long been recognized and successfully applied to various composite materials (Bigg 1979; Demain and Issi 1993; Fukai et al. 2000; Karaipekli et al. 2007). For example the thermal and electrical conductivity of polymers can be increased by the introduction of carbon nano-tubes, small carbonic fibres with large aspect ratios (Agari et al. 1991). In these applications it has been observed that the aspect ratio of such particles significantly influences the properties of the resulting composite material (Nan et al. 2003).

The objective of this work is to investigate how the aspect ratio of the additive particles can influence the composite thermal conductivity of bentonite grout.

C.3 EXPERIMENTAL STUDY

C.3.1 Materials

The effectiveness of various materials in enhancing the thermal conductivity of bentonite grout is examined by direct measurement of various compositions of grout. A baseline mix was developed to approximate the composition of a typical bentonite grout used in engineering practice. Four different materials, each with high thermal conductivities, were added to the grout at low volumetric concentrations.

The sodium bentonite used in this study was an industrial grade powder marketed for use in vertical ground source heat exchangers. Guidelines are available from the manufacturer for enhancing the thermal conductivity of the grout by blending the bentonite powder with common silica sand.

The sand used in the grout mixes was an industrially available, clean, uniformly graded, silica or quartz sand. The particle size distribution, the coefficient of uniformity C_C and the coefficient of curvature C_U values are presented in Figure C.1 and Table C.1, respectively.

Two forms of graphite were examined: a natural flake graphite and a milled, compressed, expanded, graphite (CENG). The flake graphite is a lightly processed graphite with a carbon content (LOI) of 95.7%. Alternately, CENG is a more processed form of graphite with a higher thermal conductivity. The carbon content of the CENG examined was 98.8%. Both materials have been previously documented to enhance the

conductivity of bentonite grouts, but CENG was found to be generally more effective than flaked graphite (Delaleux et al. 2012). The size and distribution of the graphite particles can be found in Figure C.1, with the mean particle size, the coefficients of uniformity and curvature being provided in Table C.1.

Two sizes of chopped carbon fibres were used: ‘short’, milled 150µm nominally long fibres and ‘long’, chopped 3mm nominally long fibres. Both fibres have a specified diameter of 7.5µm indicating a particle aspect ratio of 20 and 400, respectively. The thermal conductivity of the individual fibres was not measured directly and is assumed from reported values to be between 100 and 1000 W/mK.

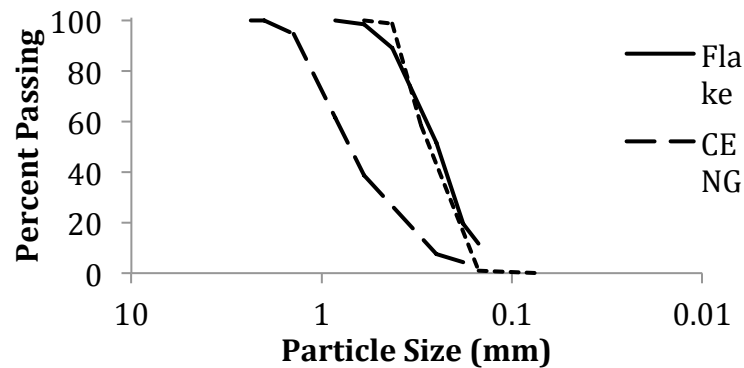


Figure C.1: Particle size distribution of the two forms graphite and the silica sand.

Table C.1: The coefficients of curvature and uniformity as well as the mean particle sizes (D_{50}) of the grout constituents.

	Flake Graphite	CENG	Silica Sand
C_U	1.0	1.1	1.0
C_C	2.0	3.0	1.8
D_{50} (mm)	0.24	0.74	0.27

Note: $C_U = D_{30}^2 / (D_{60}D_{10})$, $C_C = D_{60} / D_{10}$, in which D_{60} , D_{30} and D_{10} are characteristic sizes such that 60%, 30% and 10% (by weight) of particles are smaller than them.

C.3.2 Thermal Conductivity Measurements

The thermal conductivity of the grout was measured using a thermal needle probe as outlined in ASTM D5334-08 and illustrated in Figure C.2. This transient technique provides relatively quick measurements with an accuracy of between 5 and 10% in the range of 0.5 to 5 W/mK. The needle probe method follows the same line-source principal as the hot wire method used in other studies of similar materials (Fukai et al. 2000; Karaipekli et al. 2007; Lee et al. 2010). The probe was modified slightly from the ASTM specifications, the needle length was elongated to 120mm and a lower amperage of approximately 0.10A was used. The accuracy of the probe was validated through measuring the thermal conductivity of glycerine; conductivities within 5% of the reported values were consistently obtained.

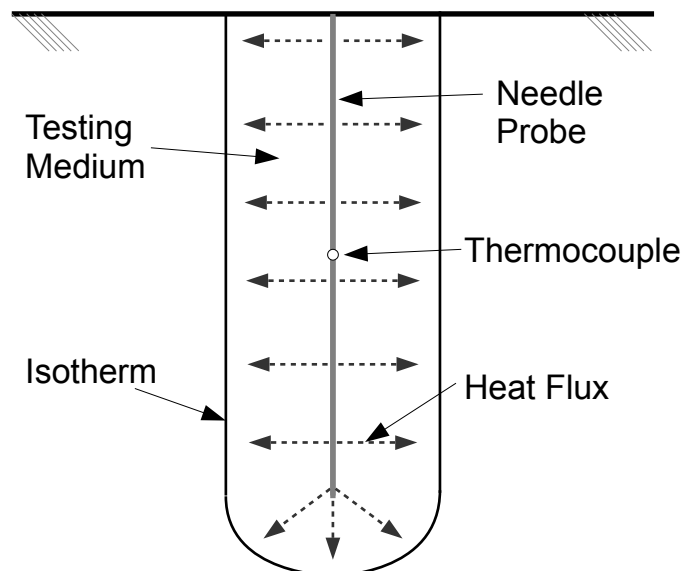


Figure C.2: Illustration of the needle probe used to measure the thermal conductivity of the grout

C.3.3 Grout Mix Preparation Method

The volumetric compositions of the grout mixes examined are outlined in Table 2. The baseline mix was composed of bentonite, silica sand, and water. As outlined in the following section, the samples were prepared in a manner to minimize air intrusion. While it is possible that the samples did contain a small amount of air, it is assumed that any air in grout did not significantly affect the thermal conductivity and the degree of saturation was consistent between samples.

When designing grout mixes containing additional additive materials, the volumetric concentrations were selected in order to maintain a consistent total solid content between samples. For any volume of additive introduced, the volume of sand was decreased by the same amount while the volume of bentonite remained constant. The objective of this was to minimize the difference in grout viscosity between mixes in order to maintain a consistent degree of saturation and degree of mixing.

Table C.2: The volumetric composition of the various grout mixes examined in this study. For each volumetric composition, aside from the baseline case, four samples were produced corresponding to each additive material examined.

Composition Number	Volume Fraction, V/V_{total}			Additive Material
	Water	Bentonite	Sand	
Baseline	0.730	0.135	0.135	0.000
1	0.730	0.135	0.134	0.001
2	0.730	0.135	0.132	0.003
3	0.730	0.135	0.128	0.007

The grout mixes were produced as follows. First the solid components, bentonite, silica sand, and the additive, were dry mixed together thoroughly. A specific volume of water was added forming a slurry which was subsequently mixed using a power operated paddle mixer for 2 minutes. The water used was de-aired, with a conductivity of 0.36 mS/cm. The slurry was then placed under a vacuum of approximately 80kPa for one hour to minimize the amount of entrained air. The slurry was then poured into cylindrical PVC sample moulds of 100mm in diameter and 150mm long. Enough slurry was produced for each mix to make two samples. Prior to measuring the thermal conductivity, the samples were sealed and placed in a temperature-controlled water bath, maintained at 27°C, for at least 24 hours. Measurements were obtained with the samples in the bath. Although it is assumed that the thermal conductivity of the grout does not vary significantly with time, the measurements were conducted within 72 hours of the sample being produced. Two cylindrical samples were produced for each grout mix and three measurements were obtained from each sample from uniformly spaced locations, providing a total of six recorded thermal conductivity values per mix.

C.4 RESULTS

The mean thermal conductivity of the control samples, containing only bentonite, water, and silica sand, was 0.99 W/mK, which is consistent with the manufacturer's specification of 0.94 W/mK at a 1:1 ratio of bentonite to sand. As illustrated in Figure C.3, for all additive materials involved, the mean grout conductivity generally increased with additive content. The mean conductivities of the samples containing 3mm long

chopped carbon fibres were larger than those of samples containing either form of graphite or the 150 μ m fibres at a volume of additive of 0.68% and 0.27%. Alternately, at the 0.14% volume of additive there was no significant difference between the 3mm fibres and the CENG.

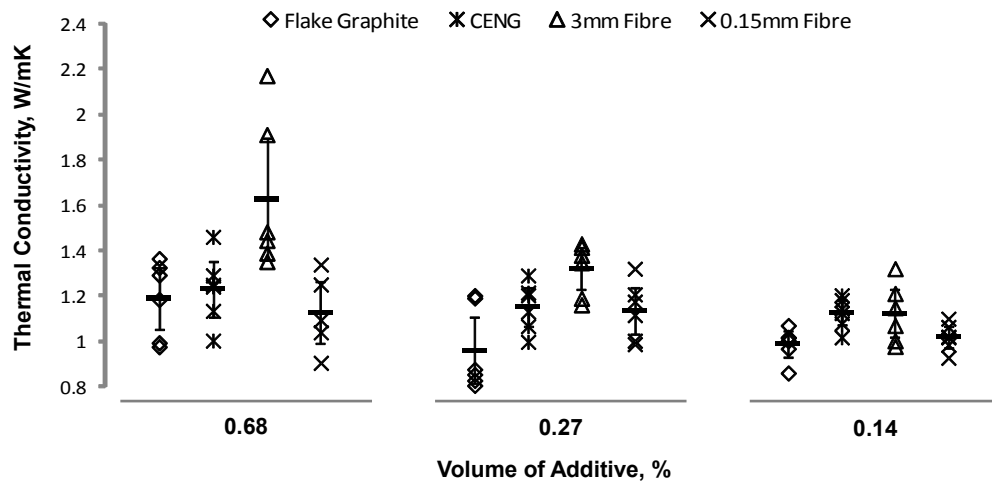


Figure C.3: Variation of thermal conductivity of bentonite grout with additive concentration for the four materials examined; the error bars indicate the 95% confidence interval assuming a normal distribution.

It should be noted that there was a significant degree of variations in the thermal conductivity values, particularly at higher measured conductivities. Regardless, at an additive volume of 0.68%, the difference in mean conductivity between the samples containing 3mm fibres and all other additives was greater than the respective 95% confidence bounds, indicating a statistically significant effect.

C.5 DISCUSSION

The results, as illustrated in Figure C.3, demonstrate that adding chopped carbon fibres is a viable and effective approach to enhance the thermal conductivity of bentonite

grout. The influence of the chopped carbon fibres, specifically the 3mm long fibres, had a significant impact on the overall grout conductivity. These fibres increased the mean conductivity by approximately 50% at a total volumetric fraction of only 0.68%, which corresponds to 22g of fibres per kilogram of bentonite and sand. Compared to the 150 μ m fibres or either type of granular graphite, the 3mm fibres were more effective at enhancing the thermal conductivity. Such effectiveness is attributed to the higher aspect ratio of the longer fibres, 400 compared to 20 and approximately 1 for the shorter fibres and granular graphite, respectively. These findings do not imply that either flake graphite or the CENG are ineffective materials for thermal conductivity enhancement, but rather more enhancement was achieved for the same volume fraction using 3mm chopped carbon fibres. The findings have further implications for thermal conductivity enhancement of other composite materials. Specifically, chopped carbon fibres could be used to enhance the conductivity of portland cement concrete for applications such as energy foundations.

Also illustrated in Figure C.3 is the high degree of variability associated with the measured conductivity values. This variation is attributed to the nature of the line source technique used to measure thermal conductivity, which has a specified accuracy of approximately 5-10%. Furthermore, the high degree of heterogeneity of the various grout mixes may have further degraded the technique's precision. In order to mitigate the variability six measurements were taken from each mix and based on the statistical significance of the findings this was determined to be sufficient.

This study did not measure the impact of the fibres on the viscosity of the grout. Visual observations indicate that the viscosity increased with the presence of the 3mm long fibres while both the granular graphite and the 150 μ m fibres were not observed to influence the viscosity. This is a potential challenge for the application of fibres and will likely limit the maximum volume fraction and fibre length that can be practically used. Further investigations may lead to an optimal combination of granular graphite and chopped fibres.

It is possible that the presence of carbon fibres could provide additional benefits to the performance of bentonite grout that were not within the scope of the current study. Fibres have been shown to mitigate the formation of shrinkage micro-cracks in clay materials that can arise due to hydraulic conductivity (Allan and Kukacka 1995; Miller and Rifai 2004).

Acknowledgements

This research was funded by the Natural Sciences and Engineering Research Council of Canada. The authors wish also to acknowledge the support of Mr. Peter Koudys in the development of the thermal needle probe and the experimental technique. Both the carbon fibres and the granular graphite used in this study were provided by *Asbury Carbons*.

APPENDIX D FROST HEAVE MODEL SUBROUTINE

```

C*****
C USER SUBROUTINES FOR MODIFEID SP FROST HEAVE FUNCTION
C BY: ERIC TIEDJE, PH.D. CANDIDATE
C DEPARTMENT OF CIVIL ENGINEERING, MCMASTER UNIVERSITY
C 2014
C*****
C
C NOTE:    COUPLED THERMAL-MECHANICAL, IMPLICIT, PLANE STRAIN,
C          ANALYSIS USING CPE8RT ELEMENTS
C
C LIST OF STATE VARIABLES:
C STATEV(1)    VOLUMETRIC HEAVE, NU
C STATEV(2)    POROSITY, NU
C STATEV(3)    ACTIVE THERMAL GRADIENT, C/m
C STATEV(4)    INTIAL CHARACTERISTIC ELEMENT LENGTH, m
C STATEV(5)    THERMAL GRADIENT IN X, C/m
C STATEV(6)    THERMAL GRADIENT IN Y, C/m
C STATEV(7)    SIGMA11, Pa (MAY VARY)
C STATEV(8)    SIGMA22, Pa  "
C STATEV(9)    SIGMA12, Pa  "
C STATEV(10)   CHARACTERISTIC ELEMENT LENGTH, m
C STATEV(11)   SEGREGATION POTENTIAL, C/m^2*s
C STATEV(12)   CHANGE IN ICE CONTENT
C STATEV(13)   HEAT FROM HEAVE COMPONENT
C STATEV(14)   SIGMA NORMAL, Pa
C STATEV(15)   ...
C STATEV(16)   ICE LENS VOLUME
C
C-----
C USER SUBROUTINE USDFLD
C-----
      SUBROUTINE USDFLD(FIELD, STATEV, PNEWDT, DIRECT, T, CELENT,
1  TIME, DTIME, CMNAME, ORNAME, NFIELD, NSTATV, NOEL, NPT, LAYER,
2  KSPT, KSTEP, KINC, NDI, NSHR, COORD, JMAC, JMATYP, MATLAYO,
3  LACCFLA)
      INCLUDE 'ABA_PARAM.INC'
      CHARACTER*80 CMNAME, ORNAME
      CHARACTER*3  FLGRAY(15)
      DIMENSION FIELD(NFIELD), STATEV(NSTATV), DIRECT(3,3),
1  T(3,3), TIME(2)
      DIMENSION ARRAY(15), JARRAY(15), JMAC(*), JMATYP(*), COORD(*)
C
C - INCLUDE HEAVE-HEAT EFFECTS ON C* -
      FIELD(1) = STATEV(13)
C
C CHARACTERISTIC ELEMENT LENGTH
      IF (KINC.LE.1.0D0) THEN

```

```

        STATEV(15) = CELENT
        ENDIF
        STATEV(10) = CELENT
C
C - DETERMINE THE THERMAL GRADIENT -
        CALL GETVRM('HFL',ARRAY,JARRAY,FLGRAY,JRCD,JMAC,JMATYP,
        1 MATLAYO,LACCFLA)
C HEAT FLUX IN X AND Y
        HFLX = ARRAY(2)
        HFLY = ARRAY(3)
C COND: THERMAL CONDUCTIVITY AT T0
        COND = 1.631D0
        STATEV(5) = HFLX/COND
        STATEV(6) = HFLY/COND
C
C - DETERMINE STRESS COMPONENTS -
        CALL GETVRM('S',ARRAY,JARRAY,FLGRAY,JRCD,JMAC,JMATYP,
        1 MATLAYO,LACCFLA)
        STATEV(7) = ARRAY(1)
        STATEV(8) = ARRAY(2)
        STATEV(9) = ARRAY(4)
C
        STATEV(16) = STATEV(16) + STATEV(1)*CELENT**2.0D0
C
C IF ERROR, WRITE COMMENT TO .DAT FILE
        IF(JRCD.NE.0)THEN
            WRITE(6,*) 'REQUEST ERROR IN USDFLD FOR ELEMENT NUMBER ',
            1 NOEL,'INTEGRATION POINT NUMBER ',NPT
        ENDIF
C
        RETURN
        END
C-----
C USER SUBROUTINE UEXPAN
C-----
        SUBROUTINE UEXPAN(EXPAN,DEXPANDT,TEMP,TIME,DTIME,PREDEF,
        1 DPRED,STATEV,CMNAME,NSTATV,NOEL)
        INCLUDE 'ABA_PARAM.INC'
        CHARACTER*80 CMNAME
        DIMENSION EXPAN(*),DEXPANDT(*),TEMP(2),TIME(2),PREDEF(*),
        1 DPRED(*),STATEV(NSTATV)
C
        C=STATEV(10)
        IF (TIME(1).LT.1000D0) THEN
            STATEV(4) = C
            STATEV(16) = 0.0D0
            ENDIF
        ETEMP=TEMP(1)
        HEAVE=0.0D0

```

```

      HEAVEMAX=1.0D0
C SP0: BASE SEGREGATION POTENTIAL VALUE
      SP0 = 26.5D-11
C BBB: STRESS REDUCTION PARAMETER ON HEAVE
      BBB =5.0D-06
C BETA: RATE OF COOLING INFLUENCE
      BETA = 5.95d6
C ICE GROWTH PARAMETER: 0.33 = ISOTROPIC <-> 1.00 = 1D
      ZETA = 0.9D0
C - DEFINE THERMAL GRADIENT IN X AND Y SPACE -
      GX = STATEV(5)
      GY = STATEV(6)
      IF (ABS (GX) .LE. 1.0E-7) THEN
        THETA = 3.14159265358D0/2.0D0
      ELSE
        THETA = ATAN (GX/GY)
      ENDIF
      ST = SIN (THETA)
      S2T = SIN (2.0D0*THETA)
      CT = COS (THETA)
      C2T = COS (2.0D0*THETA)
      SK = SIN (3.14159265358D0/2.0D0 - THETA)
      CK = COS (3.14159265358D0/2.0D0 - THETA)
C MAX THERMAL GRADIENT, DICTATES FROST HEAVE
      GRADD = SQRT (GY**2.0D0+GX**2.0D0)
      STATEV(3) = GRADD
C - DETERMINE HEAVE RATE -
C TSTAR: ASSUMED HEAVE TEMPERATURE
      TSTAR = -0.25D0
      T1 = TSTAR-GRADD*C
      T2 = TSTAR+GRADD*C
C
      IF ((ETEMP.GE.T1) .AND. (ETEMP.LT.TSTAR)) THEN
        ETA = (T1-ETEMP)/(T1-TSTAR)
      ELSEIF ((ETEMP.GE.TSTAR) .AND. (ETEMP.LE.T2)) THEN
        ETA = (T2-ETEMP)/(T2-TSTAR)
      ELSE
        ETA = 0.0D0
      ENDIF
      IF ((ETA.GT.0.0D0) .AND. (TEMP(2) .LE.0.0D0)) THEN
C***
        SG11 = STATEV(7)
        SG22 = STATEV(8)
        SG12 = STATEV(9)
C DETERMINE THE STRESS NORMAL TO THE FROZEN FRINGE
        SIGNORM = (SG11+SG22)/2.0D0-(SG11-SG22)*C2T/2.0D0-SG12*S2T
        STATEV(14) = SIGNORM
C
C - DETERMINE THE MODIFIED SP VALUE -

```

```

C CALCULATE THE RATE OF COOLING (m/s)
  DTDI = -1.0D0 * TEMP(2) / DTIME
  ZDOT = DTDI/GRADD
  IF (ZDOT.LT.1.0D-08) THEN
    ZDOT = 0.0D0
  ENDIF
  HREDUC = EXP(BBB*SIGNORM)
  IF (HREDUC.LT.0.1D0) THEN
    HREDUC = 0.1D0
  ELSEIF (HREDUC.GT.1.0D0) THEN
    HREDUC = 1.0D0
  ENDIF
  HINC = (1.0D0+BETA*ZDOT)
  IF (HINC.GT.15.0D0) THEN
    HINC = 15.0D0
  ENDIF

C
  SP = SP0*HINC*HREDUC
C***
C
  VEL = ETA*1.09D0*SP*GRADD
  HEAVE = VEL*DTIME/C
  ENDIF

C
  IF ((TEMP(2).GT.0.0D0).AND.(ETEMP.GT.1.0D-01)) THEN
    HEAVE = -0.1*STATEV(16) / (C**2.0D0)
  ENDIF

C
  STATEV(1) = HEAVE
  STATEV(11) = SP
C - DETERMINE INSITU FREEZING/HEAVE -
C NOTE: SPECIFIED NUMERIC VALUES REFLECT
C SOIL-FREEZING CHARACTERISTIC
  SIT = 0.0D0
  PNL = 0.346D0*((STATEV(4)/STATEV(10))**2.0D0)
  DIDT = 0.0D0
  IF (ETEMP.LT.-1.5D0) THEN
    DIDT = 175D0*EXP(3.25D0*ETEMP)*PNL
  STATEV(12) = DIDT
  SIT = -STATEV(12)*TEMP(2)*0.09D0
  ENDIF

C
C - UPDATE MODIFIED SPECIFIC HEAT -
  SPECH = 1440.0D0
  HEAT = 3.337D05
  STATEV(13) = SPECH + HEAT*(-HEAVE/TEMP(2)+DIDT)

C
C - ASSIGN HEAVE COMPONENTS -
  H1 = HEAVE*ZETA

```

```

      H2 = HEAVE*(0.5D0*(1.0D0-ZETA))
      H1Y = H1*ABS(CT)
      H1X = H1*ABS(ST)
      H2Y = H2*ABS(SK)
      H2X = H2*ABS(CK)
C
      EXPAN(1) = H1X+H2X + SIT/3.0D0
      EXPAN(2) = H1Y+H2Y + SIT/3.0D0
      EXPAN(3) = H2 + SIT/3.0D0
C
C - UPDATE POROSITY -
      PORI = 0.346D0
      IF (STATEV(2).EQ.0D0) THEN
      POR = PORI
      VLENS = 0.0D0
      ELSE
      POR = STATEV(2)
      ENDIF
C
      DPOR=(1.0D0-POR)*(STATEV(1)/(1.0D0+STATEV(1)))
      STATEV(2)=POR+DPOR
C
      RETURN
      END
C-----
C USER SUBROUTINE UVARM
C-----
C - UVARM VALUES ARE USED IN POST-PRCOESSING ANALYSIS -
      SUBROUTINE UVARM(UVAR,DIRECT,T,TIME,DTIME,CMNAME,ORNAME,
1  NUARM,NOEL,NPT,NLAYER,NSPT,KSTEP,KINC,
2  NDI,NSHR,COORD,JMAC,JMATYP,MATLAYO, LACCFLG)
      INCLUDE 'ABA_PARAM.INC'
      CHARACTER*80 CMNAME,ORNAME
      DIMENSION UVAR(*),TIME(2),DIRECT(3,3),T(3,3),COORD(*),
1  JMAC(*),JMATYP(*)
      CHARACTER*3 FLGRAY(15)
      DIMENSION ARRAY(15),JARRAY(15)
C
      CALL GETVRM('SDV',ARRAY,JARRAY,FLGRAY,JRCD,
1  JMAC,JMATYP,MATLAYO, LACCFLG)
      UVAR(1)=ARRAY(1)
      UVAR(2)=ARRAY(2)
      CALL GETVRM('TEMP',ARRAY,JARRAY,FLGRAY,JRCD,
1  JMAC,JMATYP,MATLAYO, LACCFLG)
      UVAR(3)=ARRAY(1)
      UVAR(4)=COORD(1)
      UVAR(5)=COORD(2)
      RETURN
      END

```

APPENDIX E NUMERICAL SENSITIVITY OF THE ONE-DIMENSIONAL MODEL IMPLEMENTATION

This appendix provides a brief examination of the sensitivity of the one-dimensional simulations utilizing the proposed frost heave model, presented in Chapter 5, to numerical parameters. All numerical models are influenced to varying degrees by a series of qualitative and quantitative factors and this sensitivity ultimately impacts the utility of such approaches. In this section select model details are explored.

Table E.1 outlines the model parameters considered. The influence of these factors was examined through comparison to a reference simulation of test FH-7. This particular test was conducted on FHC under step-freezing thermal boundary conditions, as outlined in Chapter 3, The total surface displacement and the terminal heave rate were utilized for comparative purposes. The baseline parameters associated with the reference simulation are presented in Table E.1.

Table E.1: Numerical parameters examined in the sensitivity analysis.

Parameter	Baseline Value
dT_{\max}	0.1 °C
Element Size	0.02 m
Element Aspect Ratio	~1.0
ζ	0.9

The sensitivity of the model to the time step was first considered. Two time-stepping schemes were examined: an adaptive, temperature differential controlled time

step and a fixed time step. In the former, the time step is continuously adjusted so that the maximum temperature change throughout the model is within a specified tolerance. This time stepping scheme offers the advantage of computational efficiency as it typically requires fewer model iterations as compared to a fixed step. The time step was further constrained to a maximum value of 2000 s.

Figure E.1 illustrates the sensitivity of the model to the fixed time step. For a fixed step, there was significant deviation in the simulated results at values greater than approximately 500 s, with larger time steps appear to be associated with smaller simulated heave values. The model utilizes an implicit time stepping scheme, implying the solution is unconditionally stable with regards to the time step size. However, due to the inherent complexity in the governing partial differential equations, small time steps are required to adequately capture the non-linear behaviour, particularly during the initial, highly transient freezing. The required small steps imply more iterations and increased computational expense as compared to the adaptive scheme.

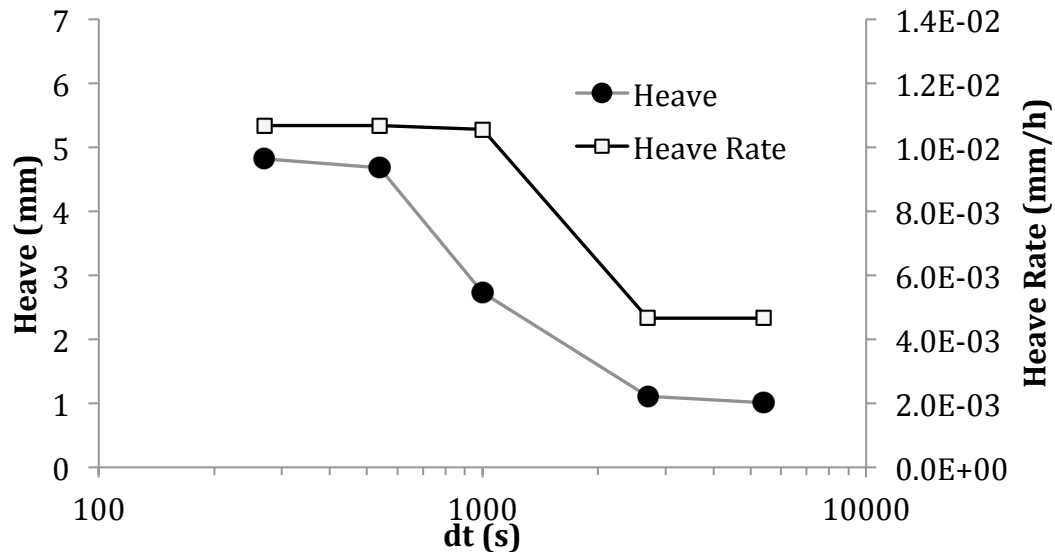


Figure E.1: The variation in the model results of FH-7 with the value of the fixed time step. The reference simulation used an alternate time stepping scheme dictated by dT .

The sensitivity of the adaptive scheme with the prescribed temperature increment is illustrated in Figure E.2. Total heave decreases slightly with increasing dT_{max} , while the final heave rate is virtually constant. These observations imply that the temperature increment predominantly influences the initial phase, as opposed to the final phase. Decreasing the allowable temperature increment effectively reduces the time step during the highly transient initial phase, better capturing the non-linear behaviour. Ultimately, the model does not appear to be particularly sensitive to the temperature increment.

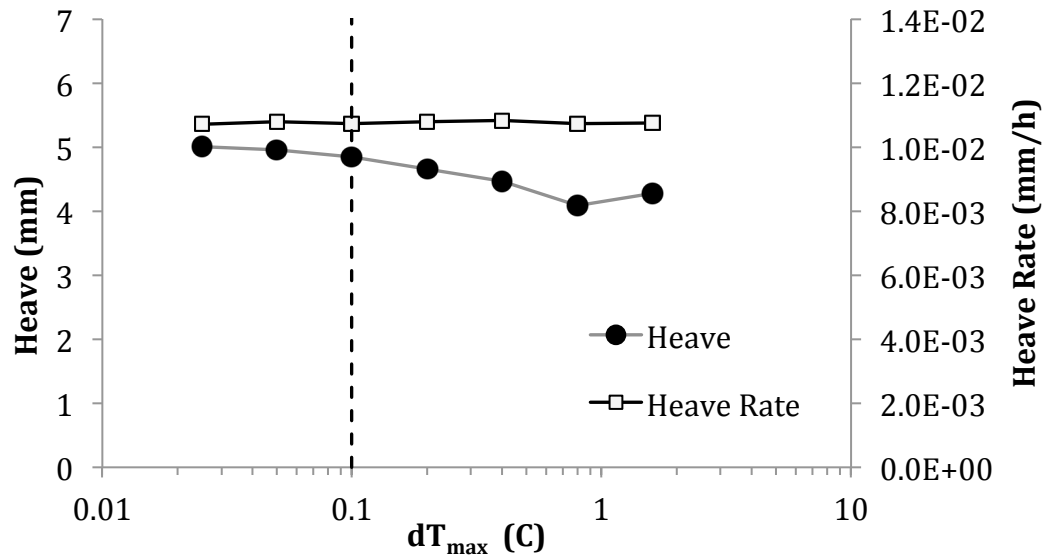


Figure E.2: The variation in the model results of FH-7 with the size of the maximum allowable temperature increment. The dashed line corresponds to the reference case of 0.1 °C.

The influence of two element geometric parameters, absolute element size and aspect ratio, on the model response was explored. As illustrated in Figure E.3, the final heave rate is moderately sensitive to element size, while the total heave shows little variation. The results show more sensitivity with regards to the element aspect ratio, illustrated in Figure E.4. Generally, at aspect ratio greater than approximately 2 there is significant variation in both the heave and heave rate compared to an aspect ratio of 1.

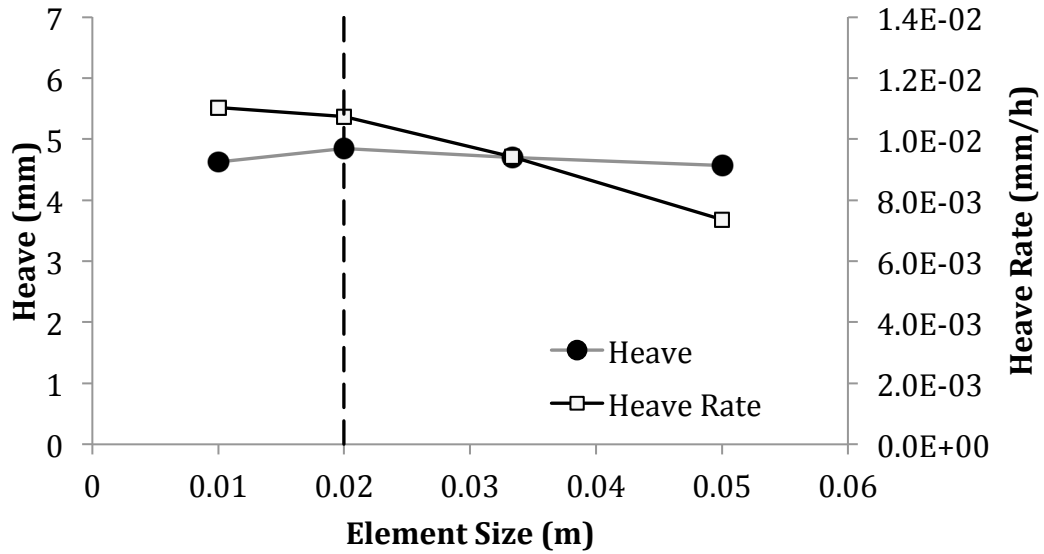


Figure E.3: The variation in the model results of FH-7 with the element size (all elements in these simulations were square). The dashed line corresponds to the reference case of 0.02 m.

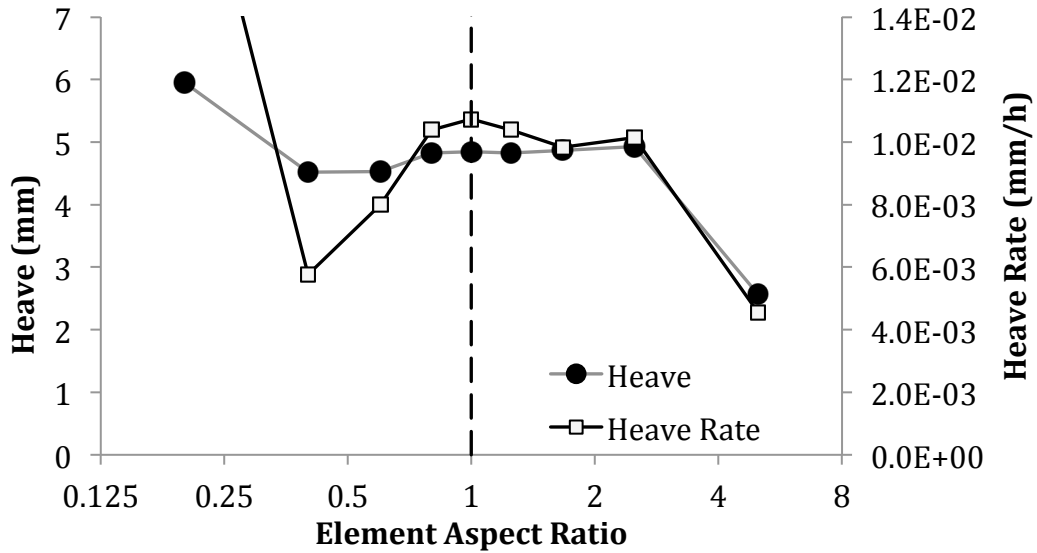


Figure E.4: The variation in the model results of FH-7 with the element aspect ratio, defined as l_y/l_x where heat transfer occurs in the y -orientation. The dashed line corresponds to the reference case of 1.

The fractional anisotropy parameter, ζ , is used to define the frost heave tensor, see Chapter 5. When ζ is 1.0 and 0.333 the volumetric strain due to ice lens growth is unidirectional and isotropic, respectively, relative to the direction of the thermal gradient in the frozen fringe. While this concept has been established in previously proposed numerical models (Michalowski 1993; Konrad and Shen 1996; Kim 2011), it has not been thoroughly characterized and reported efforts to investigate it experimentally are limited. Anecdotally, in situ and experimental observations of ice lens growth indicate the process is close to unidirectional and many existing frost heave models assume ζ values close to 1.0. In the reference simulations, ζ equal 0.9 was assumed. As seen in Figure E.5, the model is moderately sensitive to variation in ζ . More specifically, both the heave and heave rate are positively correlated with ζ . The frozen and unfrozen soil is assumed to be compressible, with a Poisson's ratio of 0.30. Since the soil is laterally confined and plane strain conditions are assumed about the third, z , axis, the lateral volumetric strains induced by frost heave will be translated to the vertical direction, albeit at a magnitude reduced in proportion to ν . A Poisson's ratio of 0.30 implies a 20 % difference in total heave between ζ of 1.0 and 0.333; while the simulations indicate respective heaves of 5.06 and 4.21 mm, or an approximate 16.8% variation. This deviation can be attributed to the complex coupling dynamic between the thermal and mechanical processes. If the soil was assumed to be nearly incompressible, the 1D model would be insensitive to ζ . The influence of ζ is qualitatively influenced by the imposed mechanical boundary conditions. Permitting lateral deformation on one side of the sample will yield lower heaves regardless of the compressibility.

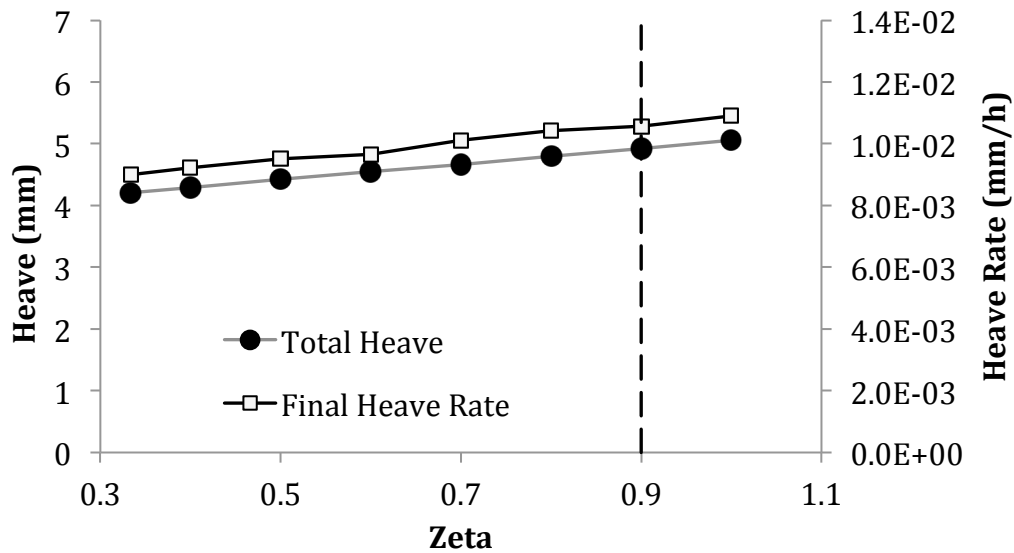


Figure E.5: The variation in the model results of FH-7 with the dimensionless fractional anisotropy parameter. The dashed line corresponds to the reference case of 0.09.

In conclusion, the sensitivity of the model to the time step, element geometry, and the assumed fractional anisotropy (ζ) was examined. Using an adaptive, temperature increment controlled, time step, the simulated results are largely insensitive to the step size. While a fixed step scheme requires an increment no greater than approximately 500 s, significantly increasing the computational effort required for the problem. Generally, element size has a minimal impact on the heave response. Element aspect ratio does not materially influence simulated results when less than approximately 2. At aspect ratios greater than 2 large deviations in the simulations are observed. The fractional anisotropy does influence the simulated results; however this influence can be attributed to the soil compressibility and the geometry of the specific problem.

APPENDIX F CALGARY PIPELINE SIMULATION FIGURES

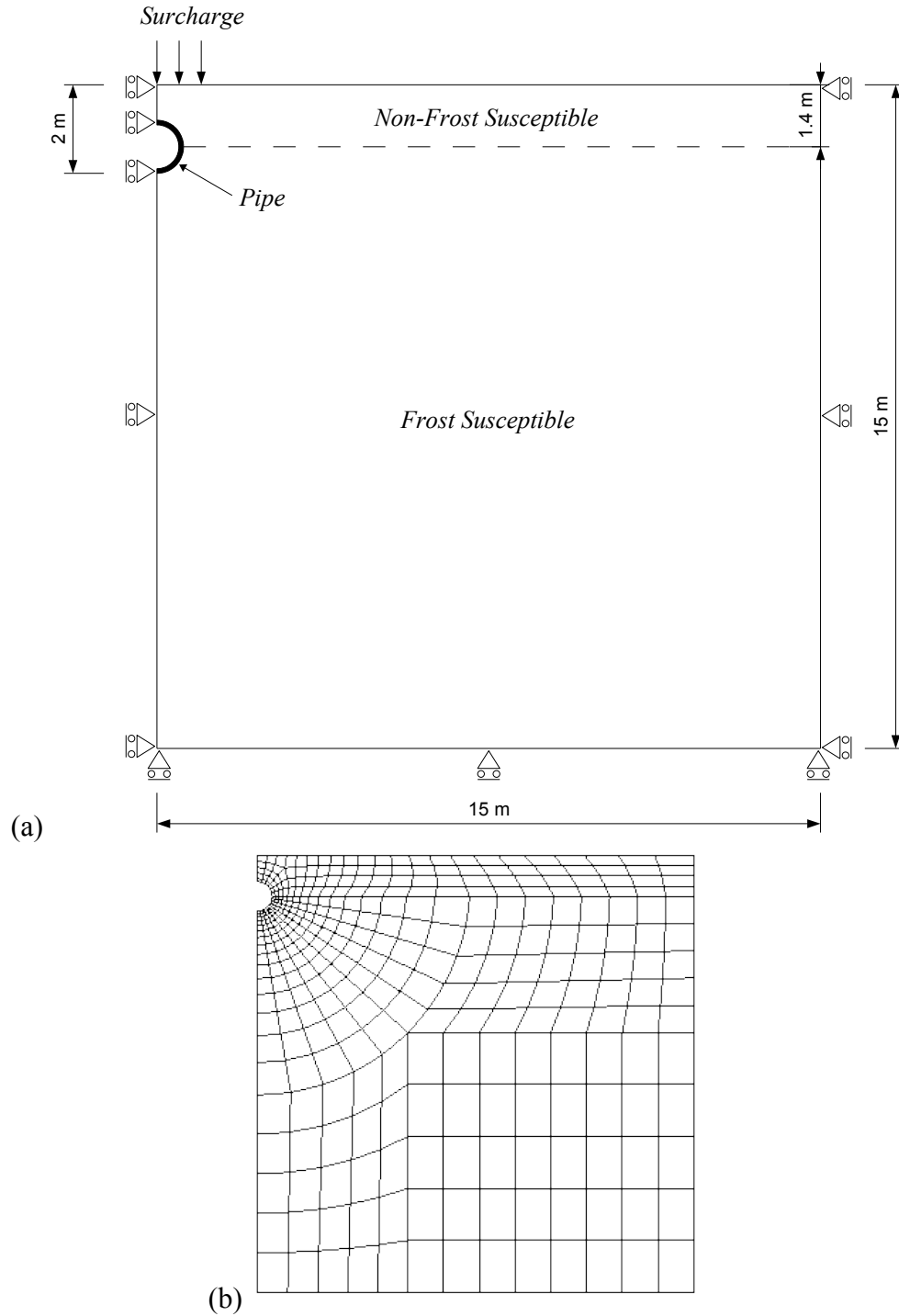


Figure F.1: Control configuration representation (a) and corresponding finite element discretization (b) of the Calgary pipeline problem.

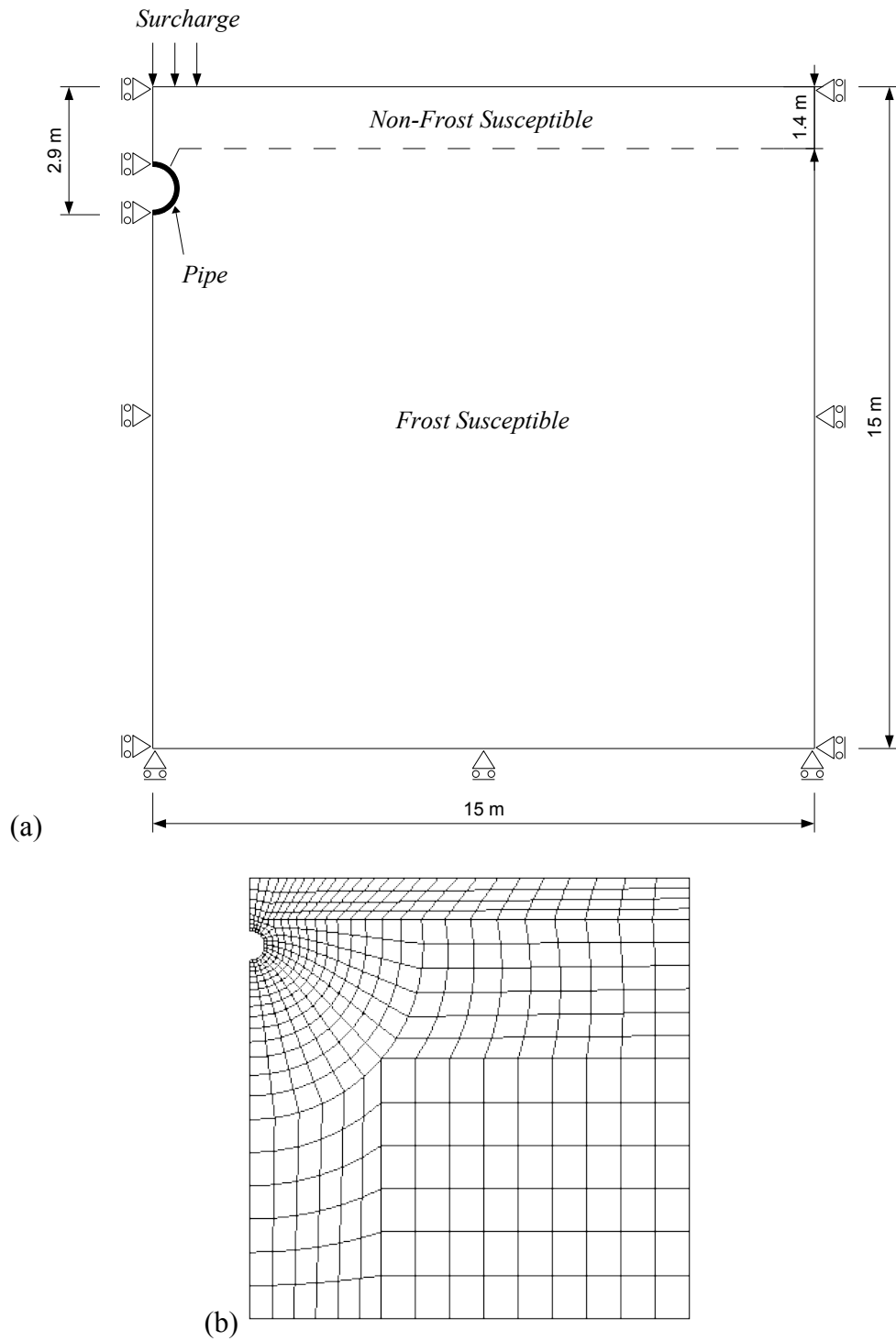


Figure F.2: Deep burial configuration representation (a) and corresponding finite element discretization (b) of the Calgary pipeline problem.

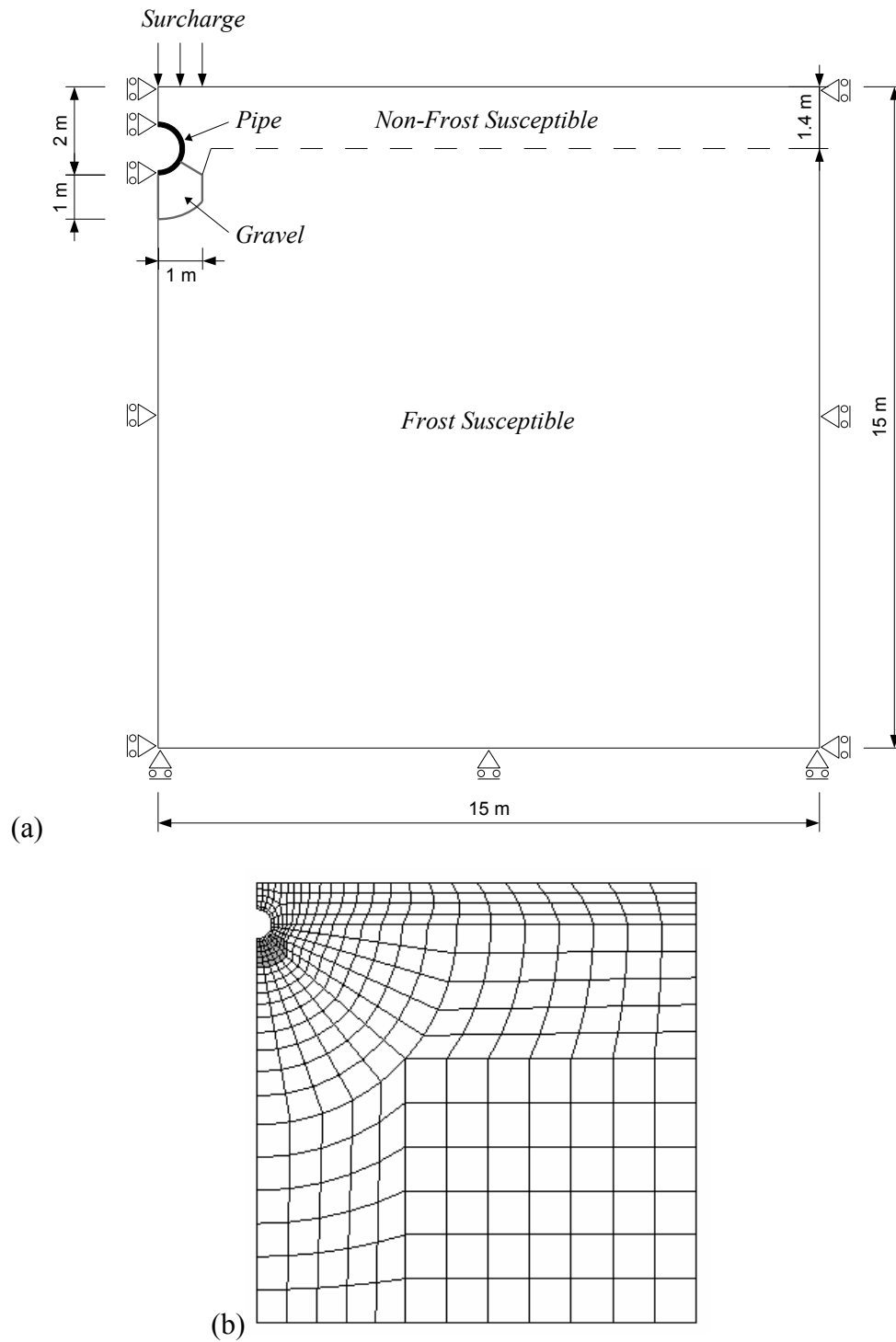


Figure F.3: Gravel configuration representation (a) and corresponding finite element discretization (b) of the Calgary pipeline problem.

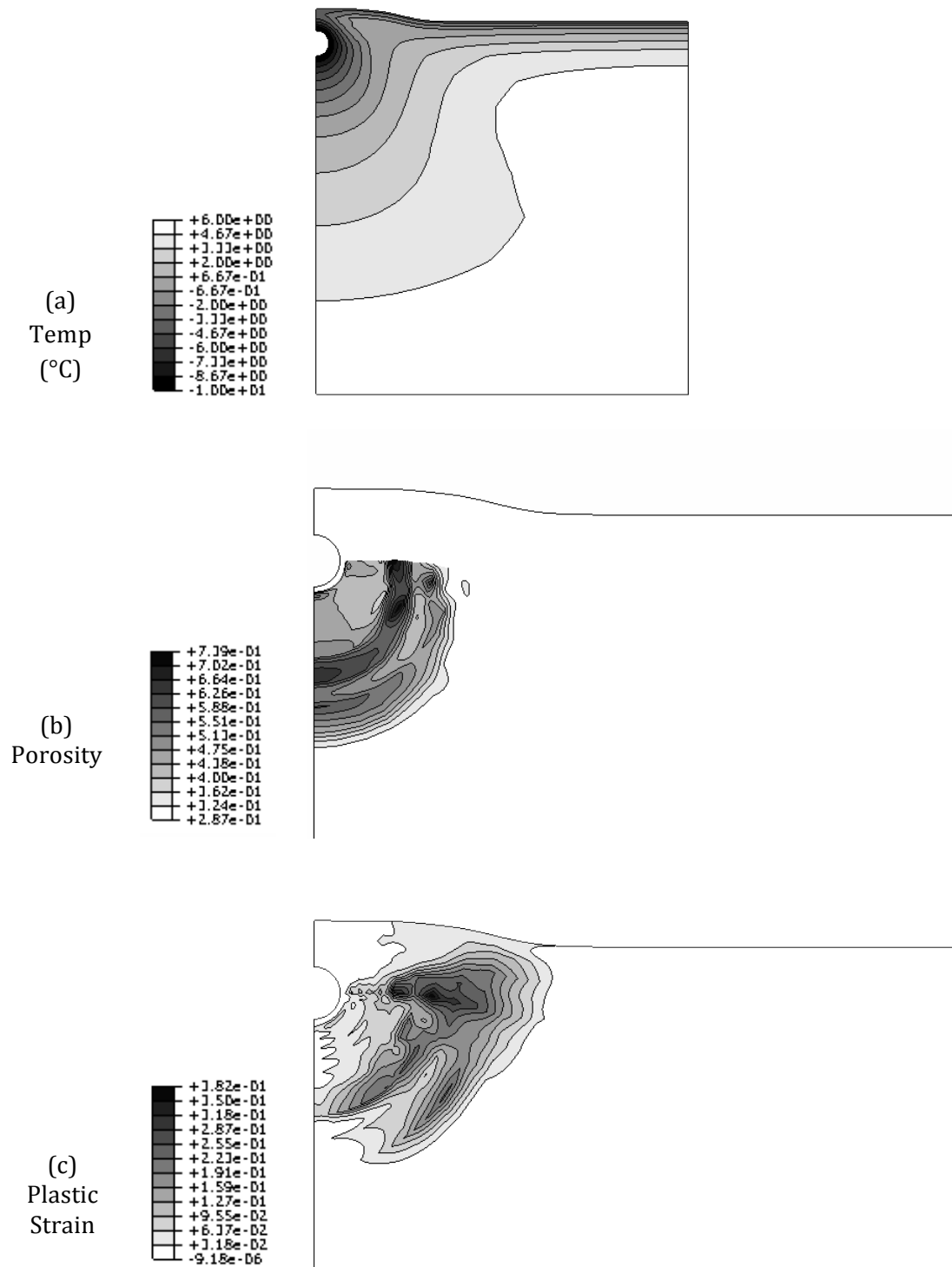


Figure F.4: Temperature profile (a), porosity profile (b), and plastic strain (c) on day 1042 for the control configuration.

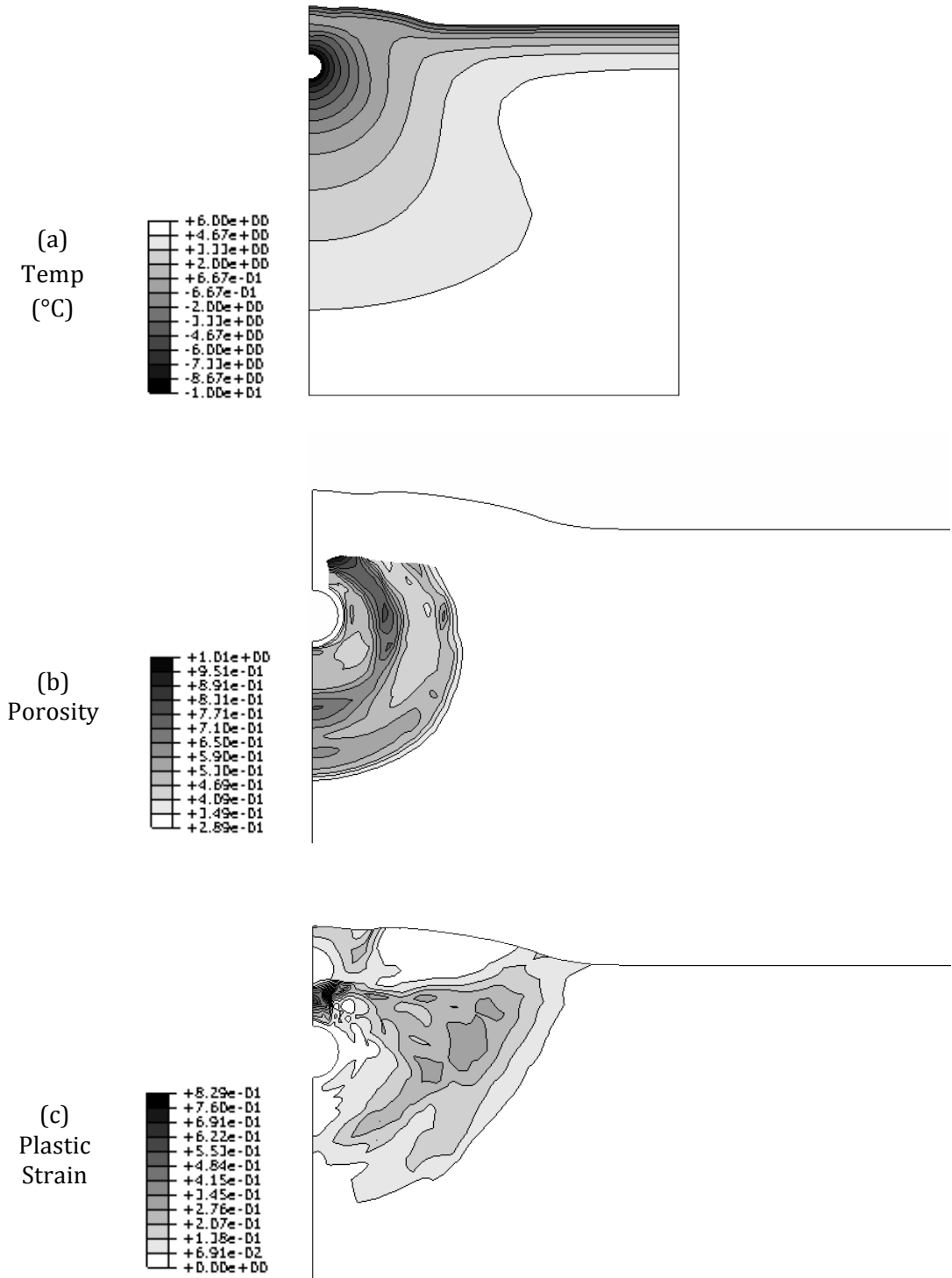


Figure F.5: Temperature profile (a), porosity profile (b), and plastic strain (c) on day 1042 for the deep burial configuration.

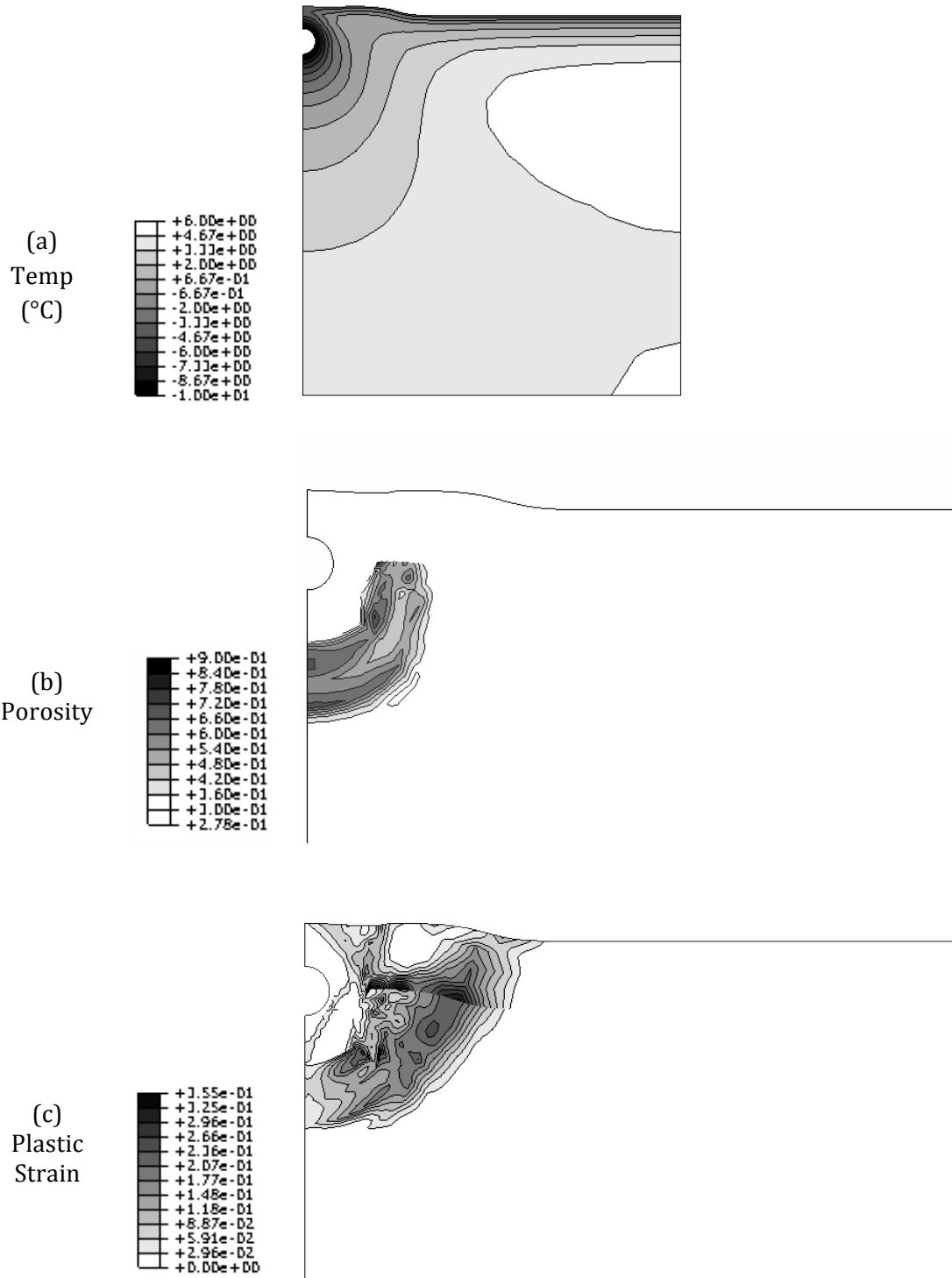


Figure F.6: Temperature profile (a), porosity profile (b), and plastic strain (c) on day 1042 for the gravel configuration.

REFERENCES

- Agari, Y., Ueda, A., & Nagai, S. (1991). Thermal conductivity of polyethylene filled with disoriented short-cut carbon fibres. *Journal of Applied Polymer Science*, 43(6), 1117-1124.
- Allan, M. L., & Kukacka, L. E. (1995). Permeability of microcracked fibre-reinforced containment barriers. *Waste Management*, 15(2), 171-177.
- Andersland, O. B., & Ladanyi, B. (1994). *An introduction to frozen ground engineering*. New York, NY: Chapman & Hall.
- Arenson, L. U., & Springman, S. M. (2005). Mathematical descriptions for the behaviour of ice-rich frozen soils at temperatures close to 0 C. *Canadian Geotechnical Journal*, 42(2), 431-442.
- Azmatch, T. F., Segoo, D. C., Arenson, L. U., & Biggar, K. W. (2011). Tensile strength and stress-strain behaviour of Devon silt under frozen fringe conditions. *Cold Regions Science and Technology*, 68(1), 85-90.
- Bigg, D. M. (1979). Mechanical, thermal, and electrical properties of metal fiber-filled polymer composites. *Polymer Engineering and Science*, 19(16), 1189-1192.
- Beskow, S. (1935) *Soil freezing and frost heaving with special attention to roads and railroads*, transl. Osterberg, J. In The Swedish Geological Society, Ser. C, 375, Year Book No. 3. Evanston, IL, Northwestern University Technological Institute. [Reprinted 1991 CRREL Spec. Rep. 91-23, 37-157.]
- Bishop, A. W. (1966). The strength of soils as engineering materials. *Geotechnique*, 16(2), 89-130.
- Bonnecaze, R. T., & Brady, J. F. (1990). A method for determining the effective conductivity of dispersions of particles. *Proceedings of the Royal Society of London. Series A: Mathematical and Physical Sciences*, 430(1879), 285-313.
- Boyd, D. W. (1976). Normal freezing and thawing degree-days from normal monthly temperatures. *Canadian Geotechnical Journal*, 13(2), 176-180.
- Brown, R. J. E., & Kupsch, W. O. (1974). *Permafrost terminology* (No. 111). Associate Committee on Geotechnical Research. Ottawa: National Research Council of Canada.
- Bruggeman, D. A. G. (1935). Calculation of various physics constants in heterogeneous substances I Dielectricity constants and conductivity of mixed bodies from isotropic substances. *Annalen der Physik*, 24(7), 636-664.

- Burt, T. P., & Williams, P. J. (1976). Hydraulic conductivity in frozen soils. *Earth Surface Processes*, 1(4), 349-360.
- Carlson, L. E., Ellwood, J. R., Nixon, J. F., & Slusarchuk, W. A. (1982, March). Field test results of operating a chilled, buried pipeline in unfrozen ground. In *Proceedings of the 4th Canadian Permafrost Conference, Calgary, Alta* (pp. 2-6).
- Chamberlain, E. J. (1981). *Frost susceptibility of soil, review of index tests* (No. CRREL-81-2). COLD REGIONS RESEARCH AND ENGINEERING LAB HANOVER NH.
- Christ, M., & Park, J. B. (2009). Ultrasonic technique as tool for determining physical and mechanical properties of frozen soils. *Cold Regions Science and Technology*, 58(3), 136-142.
- Clark, J. I., & Phillips, R. (2003, July). Centrifuge modelling of frost heave of arctic gas pipelines. In *Proceedings of the 8th International Permafrost Conference, Zurich, Switzerland* (pp. 21-24).
- Côté, J., & Konrad, J. M. (2005). Thermal conductivity of base-course materials. *Canadian Geotechnical Journal*, 42(1), 61-78.
- Delaleux, F., Py, X., Olives, R., & Dominguez, A. (2012). Enhancement of geothermal borehole heat exchangers performances by improvement of bentonite grouts conductivity. *Applied Thermal Engineering*, 33–34, 92-99.
- Demain, A., & Issi, J. P. (1993). The effect of fiber concentration on the thermal conductivity of a polycarbonate/pitch-based carbon fiber composite. *Journal of Composite Materials*, 27(7), 668-683.
- Doré, G., & Zubeck, H. K. (2009). *Cold regions pavement engineering*. New York, NY: McGraw-Hill.
- Eigenbrod, K. D., Knutsson, S., & Sheng, D. (1996). Pore-water pressures in freezing and thawing fine-grained soils. *Journal of cold regions engineering*, 10(2), 77-92.
- Environment Canada (2013) *Monthly mean air temperature, Calgary intl. airport, 1974 – 1978*. Retrieved from the Environment Canada website: http://climate.weather.gc.ca/climateData/monthlydata_e.html?timeframe=3&Prov=AB&StationID=2205&mlyRange=1881-01-01|2012-07-01&Year=1974&Month=01&Day=01
- Eshelby, J. D. (1957). The determination of the elastic field of an ellipsoidal inclusion, and related problems. *Proceedings of the Royal Society of London. Series A. Mathematical and Physical Sciences*, 241(1226), 376-396.

- Foriero, A., & Ladanyi, B. (1994). Pipe uplift resistance in frozen soil and comparison with measurements. *Journal of cold regions engineering*, 8(3), 93-111.
- Fowler, A. C. (1989). Secondary frost heave in freezing soils. *SIAM Journal on Applied Mathematics*, 49(4), 991-1008.
- Fowler, A. C., & Krantz, W. B. (1994). A generalized secondary frost heave model. *Siam Journal on Applied Mathematics*, 54(6), 1650-1675.
- Fukai, J., Kanou, M., Kodama, Y., & Miyatake, O. (2000). Thermal conductivity enhancement of energy storage media using carbon fibers. *Energy Conversion and Management*, 41, 1543-1556.
- Fukuda, M., Kim, H., & Kim, Y. (1997). Preliminary results of frost heave experiments using standard test sample provided by TC8. In *Proceedings of the International Symposium on Ground Freezing and Frost Action in Soils* (pp. 25-30).
- Gilpin, R. R. (1980). A model for the prediction of ice lensing and frost heave in soils. *Water Resources Research*, 16(5), 918-930.
- Godfrey, K. A. (1978). Trans Alaska Pipeline. *Civil Engineering—ASCE*, 48(6), 59-69.
- Halpin, J. C., & Kardos, J. L. (1976). The Halpin-Tsai equations: a review. *Polymer Engineering & Science*, 16(5), 344-352.
- Hansson, K., Šimůnek, J., Mizoguchi, M., Lundin, L. C., & Van Genuchten, M. T. (2004). Water flow and heat transport in frozen soil. *Vadose Zone Journal*, 3(2), 693-704.
- Hardy Associates (1978) *Report on frost heave testing of Calgary silty clay*. (Department of Energy, Mines and Resources Report No. 83-26) Ottawa, ON.
- Hashin, Z. (1968). Assessment of the self consistent scheme approximation: conductivity of particulate composites. *Journal of Composite Materials*, 2(3), 284-300.
- Hashin, Z., & Shtrikman, S. (1962). A variational approach to the theory of the effective magnetic permeability of multiphase materials. *Journal of applied Physics*, 33(10), 3125-3131.
- Hatta, H., & Taya, M. (1985). Effective thermal conductivity of a misoriented short fiber composite. *Journal of Applied Physics*, 58(7), 2478-2486.

- Haynes, F. D. (1978). Strength and deformation of frozen silt. In *Proceedings of the Third International Conference on Permafrost, Edmonton, Alberta, Canada*(Vol. 1, pp. 655-661).
- Henry, K. S. (2000). *A review of the thermodynamics of frost heave* (No. ERDC/CRREL-TR-00-16). ENGINEER RESEARCH AND DEVELOPMENT CENTER HANOVER NH COLD REGIONS RESEARCH AND ENGINEERING LAB.
- Hermans, J. J. (1967). Elastic properties of fiber reinforced materials when fibers are aligned. *Koninklijke Nederlandse Akademie Van Wetenschappen-Proceedings Series B-Physical Sciences*, 70(1), 1-9.
- Hill, R. (1965). A self-consistent mechanics of composite materials. *Journal of the Mechanics and Physics of Solids*, 13(4), 213-222.
- Hoekstra, P. (1969). Water movement and freezing pressures. *Soil Science Society of America Journal*, 33(4), 512-518.
- Hooke, R. L., Mellor, M., Budd, W. F., Glen, J. W., Higashi, A., Jacka, T. H., ... & Weertman, J. (1980). Mechanical properties of polycrystalline ice: An assessment of current knowledge and priorities for research: Report prepared for the International Commission on Snow and Ice, with support from the US National Science Foundation. *Cold regions science and technology*, 3(4), 263-275.
- Horiguchi, K., & Miller, R. D. (1980). Experimental studies with frozen soil in an “ice sandwich” permeameter. *Cold Regions Science and Technology*, 3(2), 177-183.
- Horiguchi, K., & Miller, R. D. (1983, July). Hydraulic conductivity functions of frozen materials. In *Proc. 4th Int. Conf. Permafrost, Fairbanks, Alaska* (pp. 504-508).
- Huang, S. L., Bray, M. T., Akagawa, S., & Fukuda, M. (2004). Field investigation of soil heave by a large diameter chilled gas pipeline experiment, Fairbanks, Alaska. *Journal of cold regions engineering*, 18(1), 2-34.
- Iorga, L., Pan, Y., & Pelegri, A. (2008). Numerical characterization of material elastic properties for random fiber composites. *Journal of Mechanics of Materials and Structures*, 3(7), 1279-1298.
- Japanese Geotechnical Society (2003) *Test method for frost heave susceptibility of soils* JGS 0172-2003

- Karaipekli, A., Sari, A., & Kaygusuz, K. (2007). Thermal conductivity improvement of stearic acid using expanded graphite and carbon fiber for energy storage applications. *Renewable Energy*, 32, 2201-2210.
- Kari, S., Berger, H., & Gabbert, U. (2007). Numerical evaluation of effective material properties of randomly distributed short cylindrical fibre composites. *Computational Materials Science*, 39(1), 198-204.
- Kim, K. (2011). *Multi-dimensional frost heave modeling with SP porosity growth function* (Doctoral dissertation). University of Alaska Fairbanks, Fairbanks, AK.
- Konrad, J. M. (1987). The influence of heat extraction rate in freezing soils. *Cold Regions Science and Technology*, 14(2), 129-137.
- Konrad, J. M. (1988). Influence of freezing mode on frost heave characteristics. *Cold regions science and technology*, 15(2), 161-175. Seto and Konrad 1994
- Konrad, J. M. (1989a). Physical processes during freeze-thaw cycles in clayey silts. *Cold Regions Science and Technology*, 16(3), 291-303.
- Konrad, J. M. (1989b). Pore water pressure at an ice lens: its measurement and interpretation. *Cold regions science and technology*, 16(1), 63-74.
- Konrad, J. M. (1994). Sixteenth Canadian Geotechnical Colloquium: Frost heave in soils: concepts and engineering. *Canadian Geotechnical Journal*, 31(2), 223-245.
- Konrad, J. M., & Morgenstern, N. R. (1980). A mechanistic theory of ice lens formation in fine-grained soils. *Canadian Geotechnical Journal*, 17(4), 473-486.
- Konrad, J. M., & Morgenstern, N. R. (1981). The segregation potential of a freezing soil. *Canadian Geotechnical Journal*, 18(4), 482-491.
- Konrad, J. M., & Morgenstern, N. R. (1982). Effects of applied pressure on freezing soils. *Canadian Geotechnical Journal*, 19(4), 494-505.
- Konrad, J. M., & Morgenstern, N. R. (1983). Frost susceptibility of soils in terms of their segregation potential. In *Proc.s of the 4th Intl. Conf. on Permafrost, University of Alaska, National Academy Press, Washington DC*.
- Konrad, J. M., & Morgenstern, N. R. (1984). Frost heave prediction of chilled pipelines buried in unfrozen soils. *Canadian Geotechnical Journal*, 21(1), 100-115.
- Konrad, J. M., & Seto, J. T. C. (1994). Frost heave characteristics of undisturbed sensitive Champlain Sea clay. *Canadian Geotechnical Journal*, 31(2), 285-298.

- Konrad, J. M., & Shen, M. (1996). 2-D frost action modeling using the segregation potential of soils. *Cold regions science and technology*, 24(3), 263-278.
- Koopmans, R. W. R., & Miller, R. D. (1966). Soil freezing and soil water characteristic curves. *Soil Science Society of America Journal*, 30(6), 680-685.
- Kozłowski, T. (2009). Some factors affecting supercooling and the equilibrium freezing point in soil–water systems. *Cold Regions Science and Technology*, 59(1), 25-33.
- Kujala, K. (1997, April). Estimation of frost heave and thaw weakening by statistical analyses. In *Proc. Int. Symp. on Ground Freezing and Frost Action in Soils, 7th, Lulea, Sweden* (pp. 15-17).
- Kuster, G. T., & Toksöz, M. N. (1974). Velocity and attenuation of seismic waves in two-phase media: Part I. Theoretical formulations. *Geophysics*, 39(5), 587-606.
- Ladanyi, B. (1972). An engineering theory of creep of frozen soils. *Canadian Geotechnical Journal*, 9(1), 63-80.
- Lee, C., Lee, K., Choi, H., & Choi, H.P. (2010). Characteristics of thermally-enhanced bentonite grouts for geothermal heat exchanger in South Korea. *Science China: Technological Sciences*, 53(1), 123–128.
- Lee, C., Park, M., Nguyen, T. B., Sohn, B., Choi, J. M., & Choi, H. (2012). Performance evaluation of closed-loop vertical ground heat exchangers by conducting in-situ thermal response tests. *Renewable Energy*, 42, 77-83.
- Leonoff, C. E., & Lo, R. C. (1982) Solution to frost heave of ice arenas, *4th Can. Permafrost Conf, Calgary, AB* (pp. 481 -486).
- Lewis, T. B., & Nielsen, L. E. (1970). Dynamic mechanical properties of particulate-filled composites. *Journal of Applied Polymer Science*, 14(6), 1449-1471.
- Lovell Jr, C. W. (1957). Temperature effects on phase composition and strength of partially-frozen soil. *Highway Research Board Bulletin*, (168).
- Lumb, P. (1966). The variability of natural soils. *Canadian Geotechnical Journal*, 3(2), 74-97.
- Lundin, L. C. (1990). Hydraulic properties in an operational model of frozen soil. *Journal of Hydrology*, 118(1), 289-310.
- Lyazgin, A. L., Lyashenko, V. S., Ostroborodov, S. V., Ol'shanskii, V. G., Bayasan, R. M., Shevtsov, K. P., & Pustovoit, G. P. (2004). Experience in the Prevention of Frost

- Heave of Pile Foundations of Transmission Towers under Northern Conditions. *Power Technology and Engineering*, 38(2), 124-126.
- Maxwell, J. C. (1881). *A treatise on electricity and magnetism* (Vol. 1). Clarendon press.
- McCartney, L. N., & Kelly, A. (2008). Maxwell's far-field methodology applied to the prediction of properties of multi-phase isotropic particulate composites. *Proceedings of the Royal Society A: Mathematical, Physical and Engineering Science*, 464(2090), 423-446.
- Meredith, R. E., & Tobias, C. W. (1960). Resistance to potential flow through a cubical array of spheres. *Journal of applied Physics*, 31(7), 1270-1273.
- Michalowski, R. L. (1993). A constitutive model of saturated soils for frost heave simulations. *Cold regions science and technology*, 22(1), 47-63.
- Michalowski, R. L., & Zhu, M. (2006). Frost heave modelling using porosity rate function. *International journal for numerical and analytical methods in geomechanics*, 30(8), 703-722.
- Michel, J. C., Moulinec, H., & Suquet, P. (1999). Effective properties of composite materials with periodic microstructure: a computational approach. *Computer Methods in Applied Mechanics and Engineering*, 172(1), 109-143.
- Miller, R. D. (1970). Ice sandwich: Functional semipermeable membrane. *Science*, 169(3945), 584-585.
- Miller, R. D. (1972). Freezing and heaving of saturated and unsaturated soils. *Highway Research Record*, (393).
- Miller, C. J., Rifai S. (2004). Fiber reinforcement for waste containment soil liners. *Journal of Environmental Engineering*, 130(8), 891-895.
- Milton, G. W. (2002). *The theory of composites* (Vol. 6). Cambridge University Press.
- Mitchell, J., & Soga, K. (2005). *Fundamentals of soil behavior* (3rd ed.). John Wiley and Sons, Inc., Hoboken, NJ.
- Morgan, V., Hawlader, B., & Zhou, J. (2006, January). Mitigation of frost heave of chilled gas pipelines using temperature cycling. In *2006 International Pipeline Conference* (pp. 927-931). American Society of Mechanical Engineers.
- Nan, C. W., Shi, Z., Lin, Y. (2003). A simple model for thermal conductivity of carbon nanotube-based composites. *Chemical Physics Letters*, 375, 666-669.

- Nishimura, S., Gens, A., Olivella, S., & Jardine, R. J. (2009). THM-coupled finite element analysis of frozen soil: formulation and application. *Geotechnique*, 59(3), 159-171.
- Nixon, J. F. (1991). Discrete ice lens theory for frost heave in soils. *Canadian Geotechnical Journal*, 28(6), 843-859.
- Noon, C. (1996). *Secondary frost heave in freezing soils* (Doctoral dissertation), University of Oxford, Oxford, UK.
- O'Connell, R. J., & Budiansky, B. (1974). Seismic velocities in dry and saturated cracked solids. *Journal of Geophysical Research*, 79(35), 5412-5426.
- Oda, M., Nemat-Nasser, S., & Konishi, J. (1985). Stress-induced anisotropy in granular masses. *Soils Found*, 25(3), 85-97.
- O'Neill, K., & Miller, R. D. (1982). *Numerical solutions for a rigid-ice model of secondary frost heave* (No. CRREL-82-13). COLD REGIONS RESEARCH AND ENGINEERING LAB HANOVER NH.
- Ozawa, H. (1997). Thermodynamics of frost heaving: A thermodynamic proposition for dynamic phenomena. *Physical Review E*, 56(3), 2811.
- Patterson, D. E., & Smith, M. W. (1981). The measurement of unfrozen water content by time domain reflectometry: Results from laboratory tests. *Canadian Geotechnical Journal*, 18(1), 131-144.
- Penner, E. (1970). Thermal conductivity of frozen soils. *Canadian Journal of Earth Sciences*, 7(3), 982-987.
- Penner, E. (1974). Uplift forces on foundations in frost heaving soils. *Canadian Geotechnical Journal*, 11(3), 323-338.
- Penner, E., & Ueda, T. (1977). The dependence of frost heaving on load application-preliminary results. In *Proceedings of an international Symposium on Frost Action in Soils* (Vol. 1, pp. 92-101).
- Petrovic, J. J. (2003). Review mechanical properties of ice and snow. *Journal of materials science*, 38(1), 1-6.
- Piercey, G., Volkov, N., Phillips, R., & Zakeri, A. (2011). Assessment of frost heave modelling of cold gas pipelines. In *Pan-Am CGS Geotechnical conference*.

- Progelhof, R. C., Throne, J. L., & Ruetsch, R. R. (1976). Methods for predicting the thermal conductivity of composite systems: a review. *Polymer Engineering & Science*, 16(9), 615-625.
- Rayleigh, L. (1892). LVI. On the influence of obstacles arranged in rectangular order upon the properties of a medium. *The London, Edinburgh, and Dublin Philosophical Magazine and Journal of Science*, 34(211), 481-502.
- Rempel, A. W. (2007). Formation of ice lenses and frost heave. *Journal of Geophysical Research: Earth Surface (2003–2012)*, 112(F2).
- Rempel, A. W., Wettlaufer, J. S., & Worster, M. G. (2001). Interfacial premelting and the thermomolecular force: Thermodynamic buoyancy. *Physical review letters*, 87(8), 088501.
- Rempel, A. W., Wettlaufer, J. S., & Worster, M. (2004). Premelting dynamics in a continuum model of frost heave. *Journal of Fluid Mechanics*, 498, 227-244.
- Reuss, A. (1929). Berechnung der Fließgrenze von Mischkristallen auf Grund der Plastizitätsbedingung für Einkristalle. *ZAMM □ Journal of Applied Mathematics and Mechanics/Zeitschrift für Angewandte Mathematik und Mechanik*, 9(1), 49-58.
- Sayles, F. H., & Haines, D. (1974). *Creep of Frozen Silt and Clay* (No. CRREL-TR-252). COLD REGIONS RESEARCH AND ENGINEERING LAB HANOVER NH.
- Schulson, E. M. (1999). The structure and mechanical behavior of ice. *JOM*, 51(2), 21-27.
- Selvadurai, A. P. S., Hu, J., & Konuk, I. (1999). Computational modelling of frost heave induced soil–pipeline interaction: I. Modelling of frost heave. *Cold regions science and technology*, 29(3), 215-228.
- Shibata, T., Adachi, T., Yashima, A., Takahashi, T., & Yoshioka, I. (1985, August). Time-dependence and volumetric change characteristic of frozen sand under triaxial stress condition. In *Proceedings of the 4th International Symposium on Ground Freezing, Sapporo, Japan* (pp. 5-7).
- Slusarchuk, W. A., Clark, J. I., Nixon, J. F., Morgenstern, N. R., & Gaskin, P. N. (1978, July). Field test results of a chilled pipeline buried in unfrozen ground. In *Proceedings of the 3rd International Permafrost Conference, Edmonton, Alta* (pp. 10-13).
- Spaans, E. J., & Baker, J. M. (1996). The soil freezing characteristic: Its measurement and similarity to the soil moisture characteristic. *Soil Science Society of America Journal*, 60(1), 13-19.

- Szymkiewicz, A. (2005). Calculating effective conductivity of heterogeneous soils by homogenization. *Arch Hydro-Eng Environ Mech*, 52(2), 111-130.
- Taber, S. (1929). Frost heaving. *The Journal of Geology*, 428-461.
- Taber, S. (1930). The mechanics of frost heaving. *The Journal of Geology*, 303-317.
- Tice, A. R., Anderson, D. M., & Banin, A. (1976). The prediction of unfrozen water contents in frozen soils from liquid limit determinations. Cold Regions Research & Engineering Laboratory. *US Army Corps of Engineers*.
- Tice, A. R., Burrous, C. M., & Anderson, D. M. (1978, July). Determination of unfrozen water in frozen soil by pulsed nuclear magnetic resonance. In *Proceedings of the Third International Conference on Permafrost* (Vol. 1, pp. 149-155).
- Tiedje, E., & Guo, P. (2013). Thermal Conductivity of Bentonite Grout Containing Graphite or Chopped Carbon Fibers. *Journal of Materials in Civil Engineering*, 26(7).
- Tiedje, E. W., & Guo, P. (2014). Modeling the influence of particulate geometry on the thermal conductivity of composites. *Journal of Materials Science*, 49(16), 5586-5597.
- Van Genuchten, M. T. (1980). A closed-form equation for predicting the hydraulic conductivity of unsaturated soils. *Soil science society of America journal*, 44(5), 892-898.
- Voigt, W. (1889). Ueber die Beziehung zwischen den beiden Elasticitätsconstanten isotroper Körper. *Annalen der Physik*, 274(12), 573-587.
- Vyalov, S. S., & Shusherina, E. P. (1970). Resistance of frozen soils to triaxial compression. *Merzlotnye Issled*, 4, 340-375.
- Wang, J., Carson, J. K., North, M. F., & Cleland, D. J. (2008). A new structural model of effective thermal conductivity for heterogeneous materials with co-continuous phases. *International Journal of Heat and Mass Transfer*, 51(9), 2389-2397.
- Wang, J., Carson, J. K., North, M. F., & Cleland, D. J. (2006). A new approach to modelling the effective thermal conductivity of heterogeneous materials. *International Journal of Heat and Mass Transfer*, 49(17), 3075-3083.
- Watanabe, K., & Flury, M. (2008). Capillary bundle model of hydraulic conductivity for frozen soil. *Water Resources Research*, 44(12).
- Watanabe, K., & Wake, T. (2008). Hydraulic conductivity in frozen unsaturated soil. In *Proc. 9th Int. Conf. Permafrost* (pp. 1927-1932).

- Williams, P. J. (1964). "Unfrozen water content of frozen soils and soil moisture suction." *Geotechnique* 14.3: 231-246.
- Williams, P. J. (1986). *Pipelines and permafrost: science in a cold climate*. McGill-Queen's Press-MQUP.
- Woodside, W. (1958). Calculation of the thermal conductivity of porous media. *Canadian Journal of Physics*, 36(7), 815-823.
- Zhu, Y., & Carbee, D. L. (1984). Uniaxial compressive strength of frozen silt under constant deformation rates. *Cold Regions Science and Technology*, 9(1), 3-15.